Development of solid state thick film zirconia oxygen gas sensors

A thesis submitted to the Council for National Academic Awards in partial fulfilment of the requirements for the degree of Doctor of Philosophy.

Andreas Stylianou IOANNOU

June 1992

Energy Technology Centre

Middlesex University

Bounds Green Road, London N11 2NQ

in collaboration with

British Gas Research and Technology

DEDICATION

To my parents, Stelios and Anastasia.

A PLEA

I love Cyprus for her poets and her heroes.

Under the present circumstances and in the face of turbulent, dramatic political changes, I felt the need to remind those within and outside Greek boundaries of the tragedy of the Greek-Cypriot nation.

A nation which has strived for over four thousand years with sacrifices and blood to retain its Greek identity, its national consciousness, its cultural heritage.

I appeal to you known and unknown friends, with the desire to challenge both your interest and sensitivity.

Seventeen and a hall years ago, the troops of our "friends and allies" Turkey invaded Cyprus occupying forty percent of the island, and boorishly trampling every meaning of International Human Rights and Culture, every known principle of Freedom and Democracy, ignoring still to date all the resolutions of the United Nations (for Cyprus produces olive oil and not crude).

The victims of this war for the independence of Cyprus are the hundred thousand of Cypriot refugees, the misplaced, the thousands of dead and the thousands of missing patriots.

Peace is the supreme possession of nations. In Greek mythology the Goddess of peace is the daughter of Justice and the God of Welfare is the son of Peace. However in order to restore and secure Peace and Welfare we must institute Justice first.

And it is for this Justice that the Cyprus people will continue their struggle.

Andreas Stylianou Ioannou, January 1992

ACKNOWLEDGEMENTS

This work would not have been possible without the collaboration of many people.

Foremostly I would like to say a warm thank you to Dr W.C. Maskell for not only directing this study, but also for his persistent interest, encouragement and valuable comments and discussions, all which I thoroughly enjoyed.

For their role as second supervisors I also thank Dr J. Spears and Mr K. Pitt.
I would like to thank the following for granting access to equipment: Dr J. Spears and Mr P. Kershaw for use of the scanning electron microscope, Mr K. Pitt for microelectronics clean room facilities, Mr K. Hargreaves for facilities used at the British Gas Watson House Research Station, Mr R. Rudkin for use of facilities at the Department of Materials at Imperial College.

British Gas is acknowledged for their financial assistance in the form of a three year Scholarship and numerous conference attendances in the UK and abroad.

Financial support from my parents throughout the years is also gratefully acknowledged.

Finally I would like to thank all my colleagues at the Energy Centre for their support, challenges and for providing a stimulating working environment. These include Dr M. Benammar, Mr R. Copcutt, Mr J. Jones, and Dr J. Larcin.

ABSTRACT

Aspects relating to and including the development of thick film amperometric zirconia oxygen sensors were investigated. These devices, which were operated in the range 550-950°C, had a laminated structure in which a cathode, an electrolyte and an anode were printed, in that order, onto a planar alumina substrate. The anode and electrolyte were porous and during sensor operation also acted as a diffusion barrier, restricting the rate of oxygen diffusion to the cathode. A thick film platinum heater was also developed to maintain the sensor at its operating temperature while acting simultaneously as a resistance thermometer; it was screen-printed onto the substrate on the reverse side to the sensor. The individual components were characterised and optimised prior to assembly of complete sensors.

Zirconia films were deposited by screen-printing onto alumina substrates. Careful attention was paid to formulation of zirconia inks, drying and firing procedures. Temperatures above 1350°C were necessary to sinter the zirconia to a low (<0.1%) though not zero porosity. The high sintering temperatures were found to result in the diffusion of impurities from the 96% alumina substrate into the zirconia film which accelerated grain growth. X-ray diffraction showed that the grain growth resulted in transformation of the metastable tetragonal zirconia to the monoclinic form: where this occurred frequency response analysis of the films showed the expected decrease in ionic conductivity. These effects were absent on high purity (99.6%) alumina substrates.

Platinum-zirconia cermets were investigated as possible electrodes. When screen-printed and fired at 1000°C for 1 hour and operated in the range 500-700°C, electrode activity was orders of magnitude greater than for pure porous platinum electrodes and increased substantially with increasing zirconia fractions provided electronic continuity was maintained within the film. High firing temperatures (> 1000°C), which were necessary for preparing a sensor with co-fired electrolyte and electrodes, decreased electrode activities although cermets remained greatly superior to pure platinum.

Planar amperometric zirconia oxygen sensors were prepared using thick-film technology exclusively. When a voltage (0.5-1.4 V) was applied between the electrodes, a current flowed which was directly proportional to the oxygen concentration in the range up to 21%; this has not previously been achieved with such sensors. Characteristics were shown to be dependent upon firing temperature and substrate purity. Interestingly, temperature coefficients of the output were positive and negative for sensors fired at temperatures up to 1400 and above 1450°C respectively. Operation in the combustion products of a gas-burning flue demonstrated linear dependence upon calculated oxygen concentration.

Heaters, printed using either fritted or unfritted platinum inks, were given extended treatments in a furnace at elevated temperatures (1000-1300°C) to accelerate ageing effects. Measurements were made of resistance (at 20°C), platinum evaporation rate and film cross-sectional area and these were correlated with the microstructure. The variation of resistance (at 20°C) of the films was analysed using effective medium theory invoked in order to quantify the blocking effect of the non-metallic fractions. During the initial phase (resistance decreasing) the governing factor was probably the high resistance of necks between contacting platinum particles. During the subsequent phase (resistance increasing) the resistance was controlled principally by the formation and growth of voids.

CONTENTS

(Chapter 1, cont...)

(Chapter 2, cont...)

(Chapter 5, cont...)

LIST OF MAJOR SYMBOLS USED

A_{el}	geometric electrode overlap area
C	capacitance
C_1	empirical constant to Eq. (6.17) (Archie's law)
c_{O2}	oxygen concentration
D_{O2}	oxygen diffusion coefficient
d_p	pore diameter
E	EMF
E_A	Activation energy
F	faraday constant (9.64846×10^4 C mol^{-1})
f	volume fraction occupied by the non-conducting phase
f_p	percent of connected through porosity of ceramic
G_F	longitudinal gauge factor
I	current passed
I_{lim}	limiting current
J	rate of diffusion of oxygen
k, k_1	constant
L	effective length of the diffusion barrier
ℓ	thickness of solid electrolyte film
M_g	molecular weight of gas
n	number of moles of oxygen
P	barometric pressure
P_F	packing fraction
p_{O2}	oxygen partial pressure
p	probability function
Q_1	electric charge
Q	ratio of the resistance of a heterogeneous mixture to that of the conducting medium
q	flow behaviour index
R	gas constant (8314.41 J K^{-1} $kmol^{-1}$)
R_x	resistance (where x represents any subscript)
r_N	normalised resistance
S	total cross sectional area of the diffusion pores

s critical exponent of percolation theory

T temperature in kelvin (unless otherwise indicated)

t time

t_N normalised time

V_c critical volume or area fraction of conducting phase required for electrical continuity

V_f volume fraction of conducting phase

V_m volume fraction of monoclinic phase

v_i internal volume of the sensor

Greek letters

α temperature coefficient of resistance

α_ρ temperature coefficient of resistivity

γ shear rate

ε thermal expansion coefficient

ζ fluid consistency index

η viscosity of fluid

θ tortuosity factor

λ_m mean free path of the gas

μ_v kinematic viscosity of gas

π constant of value 3.14159

ρ resistivity

σ conductivity

τ shear stress

ω angular frequency

CHAPTER 1

INTRODUCTION

1.1 BACKGROUND

1.1.1 General

The measurement of the concentration of a variety of gases has become increasingly important because of the finite nature of fossil fuel reserves and because of increasing public awareness concerning health and safety and environmental pollution. Miniature sensors have particular advantages with regard to speed, selectivity, convenience, reliability and low cost. Much recent research effort has focused on solid state technologies resulting in devices producing an electrical signal related to the concentration of species of interest. Such devices can be readily interfaced with appropriate electronics for signal conditioning and data handling.

1.1.2 Oxygen gas sensors

Oxygen sensors are used for the detection and control of oxygen partial pressure / oxygen concentration in such places as aircraft cabins, life support breathing systems [1,2], mines, glove boxes, metallurgical heat treatment furnaces [3], sputtering machines [4], gas purity control etc. However the most widespread use for such sensors has been in closed–loop electronic control systems for the optimisation of combustion processes (automobile engines, boilers etc...) with respect to efficiency and emissions [5,6,7,8]. Major influences towards precise combustion control were antipollution legislation during the late 1970s in California and sharp rises on the price of crude oil during 1973 (referred to as the "energy crisis").

1.2 TYPES OF OXYGEN SENSORS

1.2.1 Paramagnetic

These devices use the high paramagnetic susceptibility of oxygen as compared to other gases. Paramagnetic substances are attracted toward the stronger parts of a magnetic field; this physical property of oxygen is used in a number of ways to measure the oxygen partial pressure of a gas mixture [9]. A successful marketed device is based on a magnetic auto–balance [10,11] and incorporates an electromagnet on a dumb-bell shaped test body (filled with a non-paramagnetic gas)

suspended in a non-uniform magnetic field. The test body is displaced by the attraction of oxygen to the stronger parts of the magnetic field; displacement is detected by an optical system. A current is applied to the electromagnet to keep the test body in a fixed (zero) position; the value of this current is directly proportional to the volume magnetic susceptibility of the gas mixture surrounding the test piece. Other substances such as NO, NO_2 and ClO_2 are also paramagnetic albeit to a much smaller degree than oxygen; the presence of such substances in the sample gas can introduce errors in the measurement of the oxygen partial pressure.

1.2.2 Aqueous electrochemical

These sensors generally comprise an aqueous electrolyte solution (such as potassium chloride) and two electrodes (usually precious metal such as Pt, Au, Ag etc) in contact with the solution [9,12]. This enables the use of a variety of techniques for oxygen concentration / partial pressure measurement. The most common and well known technique is termed the polarographic method and is identical to the amperometric method (discussed in more detail in § 1.2.4.3). The polarographic method involves the use of a thin porous membrane (usually polytetrafloroethylene) to limit the rate of diffusion of oxygen in the sample gas to one electrode acting as the cathode. The application of a sufficiently high applied voltage (around 900 mV) between the anode and the cathode induces redox reactions that are limited only by the rate of oxygen diffusion to the cathode [13,14]. The limiting current obtained is then proportional to the oxygen concentration in the sample gas.

1.2.3 Semiconducting oxides

The principle of operation of the semiconducting oxygen sensor is that the electrical resistance (R_o) of a non–stoichiometric oxide in an oxygen partial pressure p_{O2} can be represented by an expression of the form

$$R_o = k \exp\left(-\frac{E_A}{RT}\right) (p_{O2})^n \qquad (1.1)$$

where E_A is the activation energy for conduction, R is the gas constant, T is the

temperature (in kelvin) and k is an empirical constant. The sign and value of u varies according to the defect chemistry of the metal oxide. Semiconducting devices have been constructed using a variety of materials such as TiO_2 [15], CeO_2 [16], $SrTiO_3$ [17], Ga_2O_3 [18], ZnO [19] and CoO [20,21]. These sensors operate at elevated temperatures, some as high as 1000°C.

1.2.4 Solid electrolyte

1.2.4.1 General

Electrochemical sensors utilise the oxygen ion conducting properties of bulk solid electrolytes e.g. zirconia (§ 1.4.2). The use of zirconia–based electrolytes for oxygen monitors developed from space–craft technology [22] and was first demonstrated by Kiukkola and Wagner [23]. Since then several relevant reviews have been published [12,24,25,26,27]. Electrochemical devices traditionally used for oxygen sensing, have also been adapted for detecting gases which can be oxidised or reduced electrochemically [28,29,30].

1.2.4.2 Potentiometric

A galvanic cell is depicted in Fig. 1.1 and consists of an oxygen ion conductor between two electronic conductors. This cell can be used as a *"gauge"* detecting differences in the oxygen concentration of two atmospheres separated by the cell. Provided the electronic conductivity of the electrolyte is low with maximum permissible levels normally being around 1% of the total conductivity [12], the cell develops an EMF according to the Nernst equation:

$$E = \frac{RT}{4F} \ln \left(\frac{P_{O2}(b)}{P_{O2}(a)} \right) \qquad (1.2)$$

where R,T and F are the gas constant, the operating temperature (kelvin) and the faraday respectively. This cell forms the basis of the potentiometric sensor for measurement of the ratio of the oxygen partial pressure of the sample gas and that of a stable reference gas. The reference gas used is normally air. In order to avoid the problems associated with providing a stable reference gas some authors [31] have described sensors utilising oxygen partial pressures generated in situ by a redox couple such as Pd/PdO.

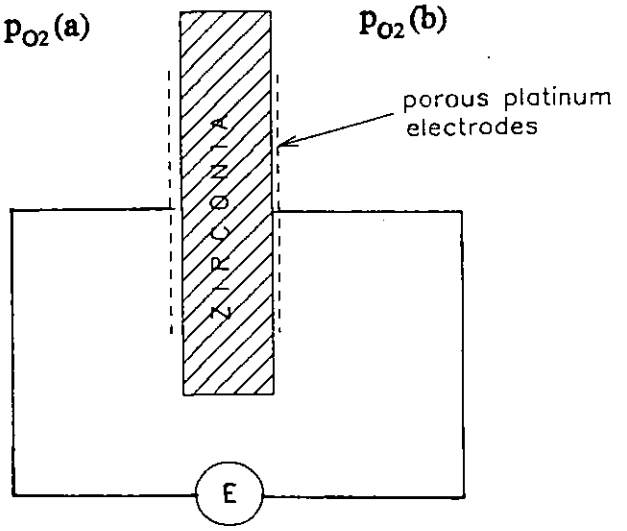

Figure 1.1 *Schematic representation of a galvanic cell*

1.2.4.3 Amperometric

The application of a voltage across the cell of Fig. 1.1 (see Fig. 1.2) causes oxygen to be electrochemically pumped from one side of the cell to the other; oxygen is reduced at the cathode side and evolved at the anode side according to the reaction (in Kroger-Vink notation):

$$O_2(g) + 2V_O^{\cdot\cdot} + 4e' \underset{\text{anode}}{\overset{\text{cathode}}{\rightleftharpoons}} 2O_O^{x} \qquad (1.3)$$

$V_O^{\cdot\cdot}$ - oxygen ion vacancy

O_O^{x} - oxygen ion on a lattice site

This electrochemical process is referred to as oxygen pumping [32]. The oxygen ion flux is in the opposite direction to the direction of conventional current flow. The number of moles of oxygen transferred (n) through the electrolyte is related to the charge passed (Q_1) by Faraday's Law:

$$dn = -\frac{dQ_1}{4F} \qquad (1.4)$$

A schematic representation of a solid-state amperometric oxygen sensor is shown in Fig. 1.3 [33]. Oxygen is electrochemically removed from the vicinity of the cathode by an applied voltage. The porous barrier, normally fixed in front of the cathode, restricts the transport of oxygen to the electrode. If a sufficient voltage is

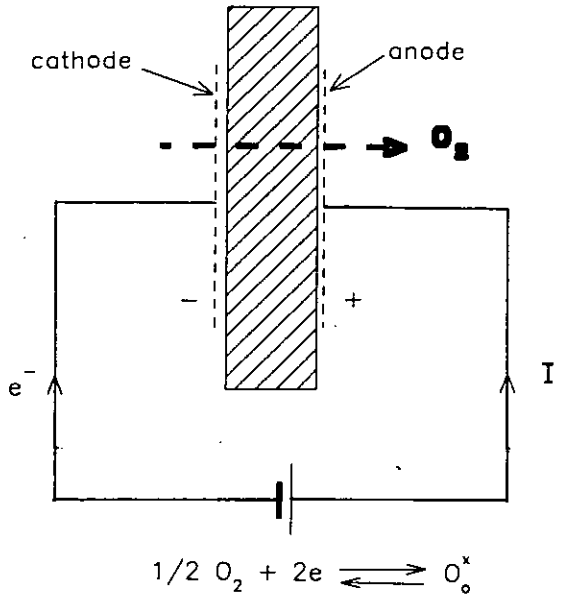

Figure 1.2 *Oxygen pumping across an electrolyte cell.*

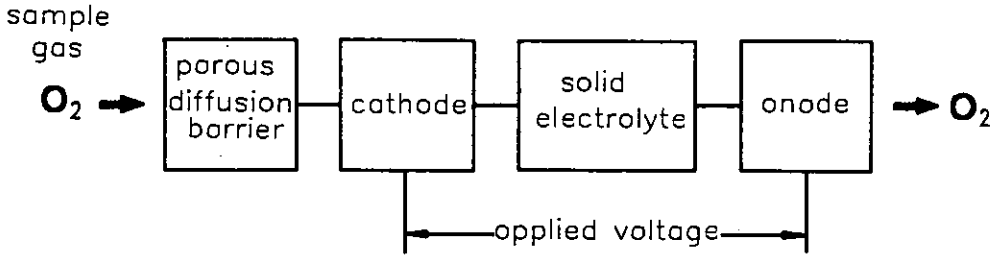

Figure 1.3 *Schematic diagram of an amperometric device.*

applied between the anode and the cathode then the partial pressure of oxygen at the cathode is reduced to a value close to zero; this is the limiting condition. An oxygen concentration gradient is set up in the restricting barrier. The current then flowing between the electrodes (I_{lim}) (Fig. 1.4) is controlled by the diffusion of oxygen through the porous barrier according to Fick's first law,

$$I_{lim} = 4FD_{O2}(S/L)\, p_{O2}(sg) \qquad (1.5)$$

where D_{O2} is the diffusion coefficient of oxygen which is inversely proportional to the barometric pressure [12], S is the cross–sectional area of the pores of the diffusion barrier of effective length L and $p_{O2}(sg)$ is the partial pressure of oxygen

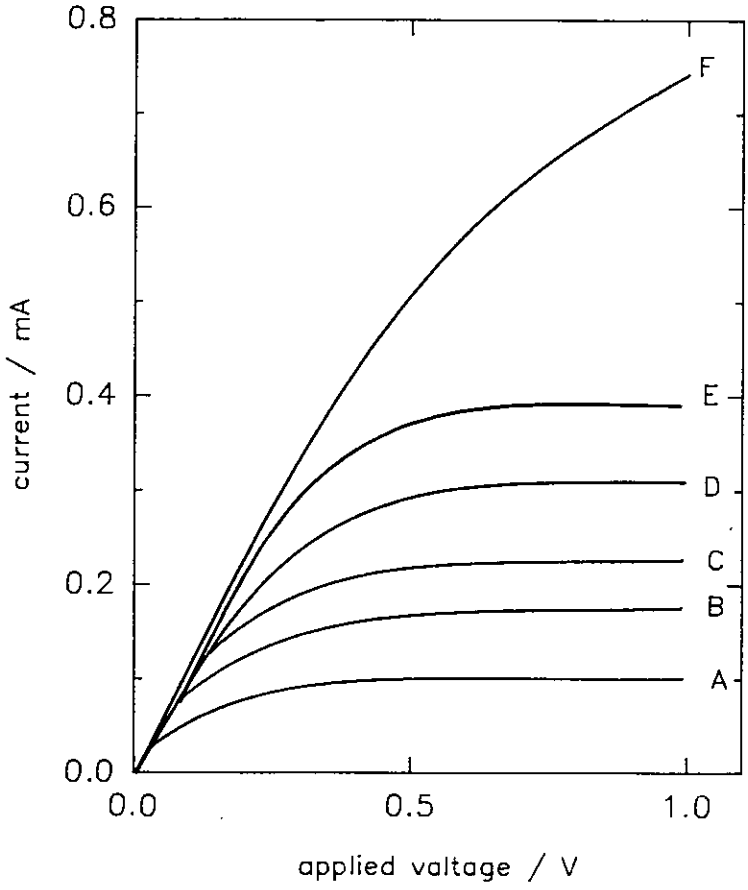

Figure 1.4 *Characteristics of a limiting-current sensor where the diffusion barrier was a laser drilled hole, 100μm in diameter, filled with porous ceramic (Dietz* [33]*). Pecentage O_2 in N_2: A,1%; B,2%; C,3%; D,4%; E,5%; F,10%.*

in the sample gas. The above equation shows that at a fixed barometric pressure (and value of S/L), the limiting current is proportional to the oxygen concentration in the sample gas surrounding the sensor [12,24,33]; (the value of this current will depend upon the rate of diffusion of oxygen gas to the cathode only). Solid state amperometric sensors are normally operated above 500°C where the ionic conductivity of the electrolyte and the electrochemical reaction kinetics at the electrodes are adequate to allow passage of a current sufficient to achieve the limiting condition.

If a change in the oxygen concentration of the sample gas occurs when an amperometric sensor is operating in the current-limiting condition, then the oxygen concentration profile within the diffusion barrier (varying from the sample gas value at one end to zero at the other) must change. This is time-dependent manifested as

a response time of the sensor [34]. The theoretical current-time characteristic derived from data presented by Crank [35] predicts a 90% response to a step change in p_{O2} according to the equation

$$t_{90} = 0.3L^2/D_{O2} \qquad (1.6)$$

where L is the pore length and D_{O2} is the diffusion coefficient of oxygen. Thus at fixed operating conditions the response time is mainly dependent upon the length of the diffusion barrier.

1.2.4.4 Coulometric

These devices involve the measurement of the charge passed when a given volume of a gas is quantitatively converted by electrolysis. One device used in this mode was similar in construction to the amperometric device [36], incorporating an internal volume between the diffusion barrier and the cathode. This device operated as follows. A constant current was applied to the pump to remove electrochemically almost all of the oxygen within the internal volume much faster than the leakage rate through the diffusion barrier. An indication that all the oxygen was removed from the internal volume was given by a sharp rise in the voltage of the pump. The current was then discontinued allowing oxygen to leak into the enclosed volume. For a constant applied current (I), the oxygen partial pressure p_{O2} is given by the following equation derived by invoking Faraday's law and the ideal gas equation

$$p_{O2} = \frac{RTI}{4Fv_i}t \qquad (1.7)$$

where v_i is the internal volume and T the operating temperature. The measured value of the time, t, is directly proportional to the oxygen partial pressure. It is essential that the time between measurements be greater than the diffusion time which should be much greater than the pumping time. It is interesting that the calibration is dependent only upon I, v_i and T and is independent of the capillary characteristics. Unlike the amperometric sensor the coulometric sensor measures oxygen partial pressure rather than oxygen concentration.

1.2.4.5 Pump-gauge

These sensors consist of an enclosed volume and two ionically conducting materials each in contact with both the external and internal gases (Fig. 1.5). The internal volume can be hermetically sealed or connected to the external gas by a pore or porous material. These sensors are operated by using one ion conductor as an oxygen pump and the other as a gauge; the effect of oxygen generation or extraction by the pump can be monitored by the gauge [37,38]. These arrangements allow

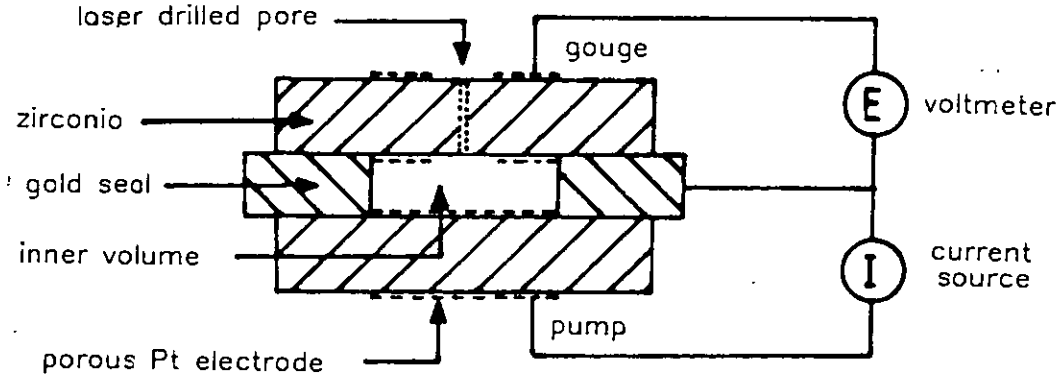

Figure 1.5 *Schematic representation of the cross-section of a pump-gauge device (Maskell*[24]*).*

the measurement of oxygen partial pressures in a number of operating modes such as coulometric [39,40,41] amperometric without fixed reference [40], amperometric with fixed reference [7,33], potentiometric with monitored internal reference [24], and various implementations in the AC mode [42,43,44, 45,46].

1.2.4.6 Impedance based

A device consisting of an oxygen-ion conducting wafer coated on each side with a thin layer of Pd has been described by Badwal and De Bruin [47]. Oxygen partial pressure was determined by measuring the large reversible changes (approximately 2 orders of magnitude) in the electrode impedance of the cell as the Pd was oxidised to PdO. The temperature at which the transition between Pd and

PdO occurred depended upon the oxygen partial pressure. This technique for the determination of oxygen partial pressure is absolute and does not require the use of a reference gas. Measurements were made by applying an AC signal at low frequencies (5-100 Hz) as shown in Fig. 1.6.

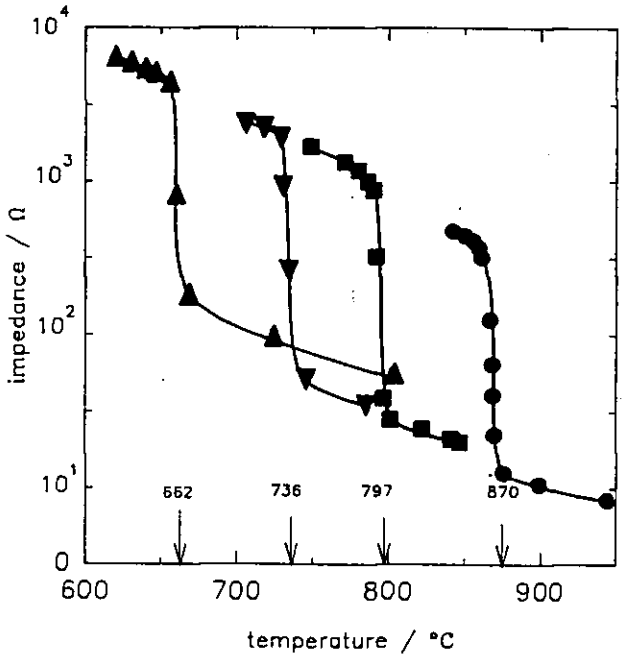

Figure 1.6 *Impedance-temperature behaviour at 10 Hz for a Pd/Zirconia/Pd cell. Sample gas oxygen partial pressure / kPa:* ●,100; ■,20.8; ▼,4.9; ▲, 0.46 *(De Bruin and Badwal*[47])

Another impedance based sensor has been described. It was prepared using a mixture of Pt and zirconia [48,49] and was operated by measuring the DC resistance across the cermet when exposed to the sample gas. Current traversed the cermet via oxygen ions in the ceramic and electrons in the metal [50]; thus there was an interfacial impedance between each contact point of the ceramic and metal. The electrode impedance has been shown to vary with p_{O2} [51] and consequently with calibration allowed determination of p_{O2}

1.2.5 Comparison of the various types of oxygen sensors

1.2.5.1 General

Disadvantageous features of the devices that have been described are given in point form below:

Paramagnetic: The output of these devices is sensitive to the temperature of the sample gas and they have a slow response (20 seconds) to changes in oxygen concentration. They also have complex hardware.

Aqueous electrochemical: These devices have volatile electrolytes which may prematurely end sensor life when operating in gases at temperatures above ambient.

Semiconducting: These devices suffer from cross–sensitivity with other gases and reproducibility as well as high operating temperatures. Some of the cross–sensitivity problems have been overcome by analyzing the outputs of sensor arrays using a microprocessor [52]. The sensors also suffer from a slow response and irreversible behaviour (by reduction of the oxide) upon exposure to reducing gases (i.e combustion gases during fuel rich burning).

Solid electrolyte: Elevated temperatures of operation are required.

Solid state electrochemical oxygen sensors are the most likely candidates to satisfy performance and life requirements in appliances such as gas boilers and automobile internal combustion engines. In such applications, solid electrolyte devices have, within the last 15 years, established a position of market dominance. They have the following advantages:

i) High selectivity to oxygen and fast response.

ii) Their elevated temperature of operation (when using platinum electrodes) can facilitate the catalysis of reactive gases (such as combustible gases in a flue) so that the sensor measures the nett oxygen concentrations after gases have equilibrated.

1.2.5.2 Comparison of solid electrolyte devices

Solid electrolyte sensors operated in the AC, coulometric and impedance modes require relatively complex instrumentation. The potentiometric devices have a logarithmic response to changes in oxygen concentration. Amperometric devices offer a combination of advantages not shared with any of the other devices described; for most applications these outweigh the disadvantages. Both advantages and

disadvantages of amperometric devices compared with other solid electrolyte devices are given below:

Advantages of amperometric devices

i) The supply of a reference is gas not necessary.

ii) Their output is linearly related to the oxygen concentration.

iii) Measurements are taken in the steady state enabling the use of simple low cost instrumentation.

iv) The output signal is fairly insensitive to temperature fluctuations and consequently precise temperature control is not required.

v) They generally do not suffer from sluggish electrode response because they operate at high electrode overvoltages; consequently they can be operated at lower temperatures.

vi) Characteristics of the device do not alter with small changes in electrolyte conductivity and electrode activity.

Disadvantages of amperometric devices

i) The dimensions of the diffusion path(s) determine the output; changes in these can bring a change in the characteristics of the device. Further if the dimensions of the diffusion barrier are not reproducible individual devices may require calibration.

ii) In combustion systems they do not allow the two sides of stoichiometry to be distinguished; this is because the normal operating voltage becomes sufficiently cathodic to reduce H_2O and CO_2 resulting in a current flow when in the sub-stoichiometric region. This problem can be overcome by using devices with a double chamber [33,53].

1.3 FABRICATION TECHNOLOGIES FOR MINIATURE SOLID ELECTROLYTE SENSORS

1.3.1 Discrete components

Cost has been reduced substantially compared to conventional potentiometric sensors [25,54,55,56] by constructing miniature amperometric zirconia oxygen sensors from discrete components [57,58]. This involves ceramic technologies including powder preparation, pressing, high temperature sintering, machining, grinding and polishing to provide ceramic discs. Metal to ceramic hermetic sealing

(using gold or platinum) [59,60,61] and more recently glass to ceramic seals [62,63] have been used to assemble devices. Electrodes are deposited on the discs by painting or screen–printing of a paste of the material, or by sputtering techniques. The assembly of one solid electrolyte device, the pump–gauge, is shown in Fig. 1.7 [42]. In cases where a physical leak is required to the internal volume of the device, this can be provided by laser drilling a pore in one of the electrolyte discs

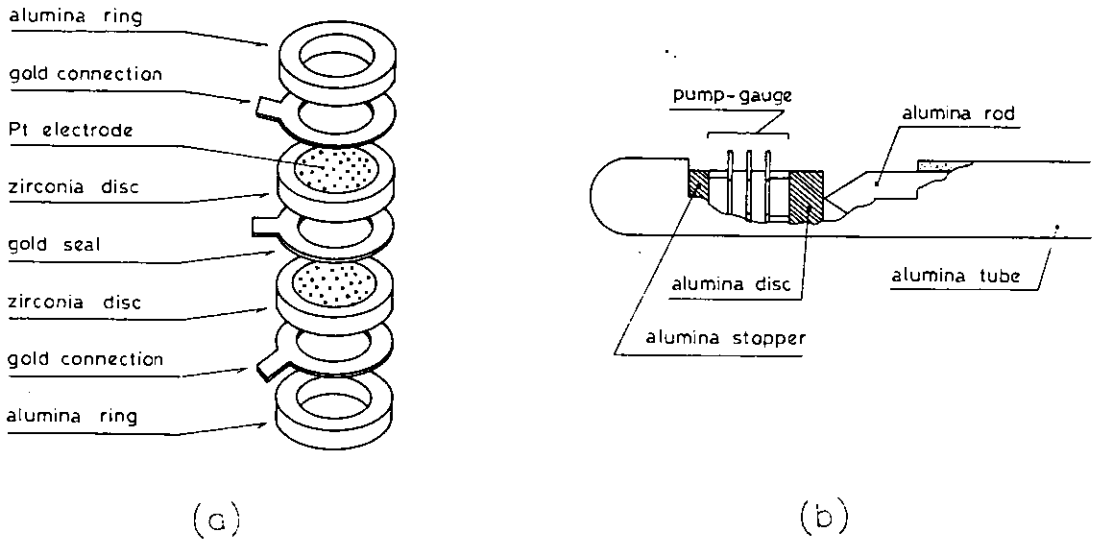

Figure 1.7 *Assembly of solid electrolyte pump-gauge device from discrete components (Source: Benammar* [42]*). (a) exploded view of components, (b) assembly of components by pressing together in an alumina jig and firing at 1040°C for 16 hours.*

[57]. There are advantages to minimising this pore diameter; the minimum diameter that can be reproduced by laser drilling at present is ~30 μm and is related to the focusing of the laser and the wavelength of the radiation.

1.3.2 Thin film

Various arrangements for planar potentiometric devices fabricated by sputtering, evaporation, ion implantation or chemical vapour deposition onto alumina substrates have been reported [7,64,65,66,67]. Two examples of this "microionic" approach are given in Fig. 1.8 [64]; these devices were fabricated by the sputtering of layers having thickness in the nanometre range. Such devices were not very successful as they suffered from very short working lives.

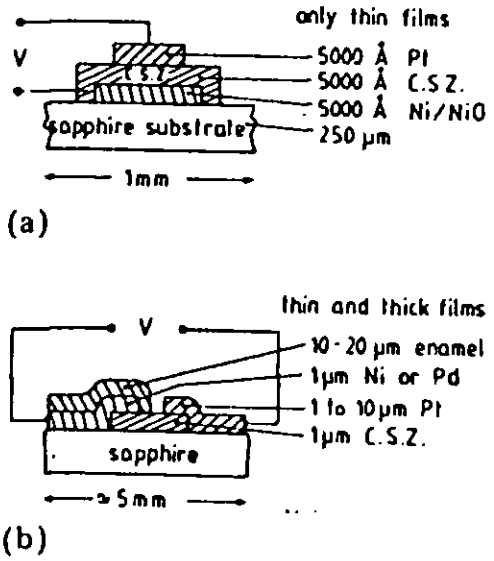

Figure 1.8 Thin film potentiometric devices (Source: Velasco et al[64]).

A thin film amperometric sensor consisting of a platinum cathode, a zirconia solid electrolyte and a platinum anode was produced by sputtering layers of the materials in succession on a porous alumina substrate [68]. The low porosity of the substrate used provided diffusion limitation of the gases. Device characteristics were similar to those of devices made using discrete components.

1.3.3 Thick film

Screen printing techniques have been used to replace thin film techniques in potentiometric arrangements [69]. These have met with problems relating to the gas tightness of the electrolyte layer [69,70]; an unsatisfactory method to overcome this consists of successive depositions and firings (the latter layers fill up the defects and open pores of the previous films [71]).

A planar device constructed using thick film technology and operated amperometrically, has recently been reported [70]. This could detect oxygen levels only in the range up to 0.1%. The sensor construction was similar to that of the thin film amperometric device of Kondo *et al* [68], the sole difference being that in the thick film device a non porous substrate was used. The porous electrolyte acted as the diffusion barrier.

Another technique that can be used to deposit planar thick films is that of plasma spraying. This technique has very recently been used to fabricate working potentiometric and amperometric sensors of identical construction to that of Chu *et al* above [72].

1.3.4 Comparison of the various fabrication technologies

1.3.4.1 General

The need for cost reduction and further miniaturisation has provided the recent impetus for the adaptation of planar technologies to sensor manufacture. These offer the possibility of functional advantages that may be achieved by the reduction of ceramic thickness [64] and also enable simpler mounting and the incorporation of integral heating.

1.3.4.2 Ease of manufacture and cost considerations

Discrete components: Fabrication from discrete components normally involves a large number of costly and time consuming manufacturing steps and comparatively high precious metal content [57]. However robust and reliable devices can be easily produced and the technology is well proven.

Thin film: This microelectronic mass manufacture technology can require lengthy time periods to build up a material layer of sufficient thickness. Furthermore there is a high capital cost presently associated with thin film deposition equipment.

Thick film: Screen printing technology is by far the simplest, cheapest and easiest of the presently available techniques; thus it has received recognition in the last decade as an important technology for sensor manufacture [73]. This technology offers a combination of conveniences not shared with other integrated technologies. These include high productivity, flexibility of design, fast modifications, a short time to pass from prototypes to products and low capital expenditure. These advantages along with the good extent of miniaturisation can realise inexpensive sensors irrespective of economies of scale.

1.3.4.3 Likely technological difficulties

Discrete components: A difficulty in sensor construction from discrete components is the provision of an hermetic metal–ceramic seal that can withstand temperature cycling.

Thin film: Thin film structures were found to be sensitive to stresses which induced cracks in the solid electrolyte film. These stresses were caused by thermal expansion mismatch between dissimilar materials [64].

Thick film: Thick film technologies were met with difficulties in reducing the porosity of the electrolyte layer [70]; a further anticipated problem is that this porosity may not be within tolerable limits of reproducibility.

1.3.5 The chosen fabrication route

In applications requiring operation at elevated temperatures it is likely that zirconia-type sensors will continue to dominate the oxygen sensor market [74]. Widespread application in domestic appliances such as gas boilers and automobile internal combustion engines depends upon achieving satisfactory performance and life of the sensor at low cost; performance and life requirements are likely to be met by zirconia electrochemical sensors. Of these amperometric devices are the cheapest to implement.

If the implementation of screen–printing as a fabrication technology for solid state amperometric devices can be perfected, it should reduce the cost per device by at least an order of magnitude compared with existing sensors constructed from discrete components. Furthermore the response time of an amperometric oxygen sensor could be greatly decreased by a reduction of the diffusion path length (according to Eq. (1.6) § 1.2.4.3) which can be provided by this planar technology.

1.4 OXYGEN-ION CONDUCTORS

1.4.1 General

Many ceramics have been used over the years as oxygen ion conductors. These include Bi_2O_3, ThO_2, CeO_2 and ZrO_2 doped with aliovalent cations so as to introduce a relatively high concentration of oxygen vacancies. Some of the oxygen ion conductors crystallise in a cubic fluorite structure. The electrical and physical properties of these oxides have been the subject of many reviews [75,76,77]. Thoria is difficult to manufacture due to its high melting point (3300°C) and being slightly radioactive is little used. A disadvantage to the use of a stabilised bismuth oxide is the reducibility by unburned combustion fuel (e.g. CH_4) [78,79]; furthermore it has a low melting point (~850°C) and thus is not used for high temperature applications such as fuel cells. Doped CeO_2 exhibits some undesirable properties including primarily electronic conductivity at high temperatures and low oxygen partial pressures [80]. The most widely used solid electrolytes for oxygen ion conduction have been zirconias particularly those doped with yttria. This is because they offer very low electronic transport number and one of the highest ionic conductivities amongst zirconia electrolytes coupled with good chemical stability [81] and little deterioration of its electrical properties with time.

1.4.2 Zirconia electrolytes

1.4.2.1 General

Zirconium dioxide, ZrO_2, is crystallographically monoclinic at room temperature, transforming to the tetragonal form at 1170°C with a volume shrinkage of ~3% [82], transforming again to the cubic form at 2370°C and becoming a liquid above 2680°C [83]. These transitions cause pure ZrO_2 to crumble upon thermal cycling due to the volume changes. It has been found that the inclusion of a proportion of aliovalent oxides stabilises the tetragonal and cubic structures at room temperature. Stabilisers form solid solutions with the ZrO_2 and include CaO, MgO, Y_2O_3, and rare earth oxides. Stabilised ZrO_2 is referred to by the collective term zirconia. The addition of a sufficient amount of stabiliser causes the material to retain the cubic phase at room temperature and is referred to as fully-stabilised zirconia (FSZ). Materials which do not contain sufficient stabiliser to effect full stabilisation are

referred to as partially-stabilised zirconia (PSZ). Recently an all-tetragonal material was developed known as tetragonal zirconia polycrystal (TZP). This material has high strength (> 1 GPa) and fracture toughness and recent work suggests improved electrochemical behaviour [84]. TZP is metastable provided that the crystallite size is sufficiently small (0.2-1.0 μm depending upon dopant content) and does not transform to the monoclinic form upon cooling [85,86]. Zirconia doped with 3 mol% Y_2O_3 remains fully tetragonal provided the ceramic grain size does not exceed a critical value. This critical value has been reported as 0.45 μm [87] and also as 0.3 μm [88].

1.4.2.2 Ionic conductivity

Stabilised zirconia exhibits significant oxygen ion mobility above about 300°C due to the high vacancy concentration introduced by the stabilising additions. This is a consequence of the lower valency of the substituted cation and may be represented in Kroger-Vink notation as follows:

$$CaO \longrightarrow Ca_{Zr}^{''} + O_O^{x} + V_O^{\cdot\cdot} \qquad (1.8)$$

$V_O^{\cdot\cdot}$ represents an oxygen ion vacancy into which an adjacent oxygen ion (O_O^{x}) is able to move (Fig. 1.9). Zirconia can then act as an electrolyte with oxygen ions able to drift in an applied electric field. The oxygen ions and vacancies in the ceramic are analogous to electrons and holes respectively in a semiconductor. The cations have diffusion coefficients 6 orders of magnitude lower than that for the oxygen ions [83]; hence they may be regarded as motionless at the normal operating temperature of 700°C. The ionic conductivity, σ, is generally described by an Arrhenius equation which can be written as:

$$\sigma = \sigma_o \, e^{(-\frac{E_A}{RT})} \qquad (1.9)$$

or:

$$\sigma T = \sigma_o \, e^{(-\frac{E_A'}{RT})} \qquad (1.10)$$

where σ_o (σ'_o) is the pre-exponential factor, E_A (E'_A) the activation energy for ionic motion, R and T are the gas constant and absolute temperature respectively.

Equations (1.9) and (1.10) are both used in the literature, the latter providing a better fit to the data because of the slight temperature dependence of E_A [89]. For practical reasons Eq. (1.9) is used in this thesis.

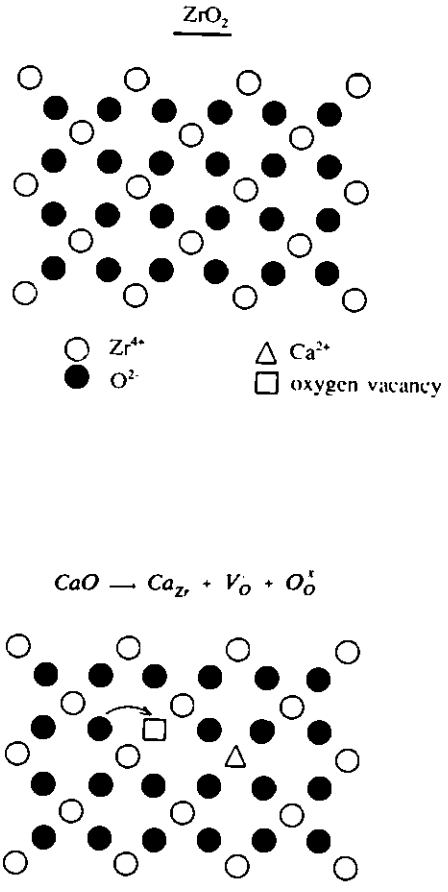

Figure 1.9 *Schematic diagram of the zirconia lattice and the effect of doping.*

1.4.2.3 Electronic conductivity

Zirconia ceramics, though principally ionic conductors, can exhibit some electronic conductivity due to electronic carriers generated by the following processes [90]

$$O^x_O \rightleftharpoons \tfrac{1}{2}O_2 + V^{\cdot\cdot}_O + 2e' \qquad (1.11)$$

$$V^{\cdot\cdot}_O + \tfrac{1}{2}O_2 \rightleftharpoons O^x_O + 2h^{\cdot} \qquad (1.12)$$

Thus electrons and holes tend to be generated at low and high oxygen partial pressures respectively. The degree of electronic conductivity of solid electrolytes often determines their usefulness for various galvanic cell arrangements; the range in which zirconia satisfies this criterion is shown in figure 3 of the paper by Maskell and Steele [25].

1.4.2.4 Fabrication processes

Bulk zirconias

Modern ceramics can be easily fabricated by traditional process routes. In stabilised zirconia the calcination temperatures must be high (>1300°C) to promote the inter–diffusion of the cations; the achievement of high density by traditional process routes has often required the use of high firing temperatures (>1700°C) [91]. A zirconia is generally found to be gas impermeable if it has a density of more than 92% of theoretical [92].

Alternative routes in which zirconia powders can be prepared by wet chemical methods have received considerable attention [93,94]. The objective of this approach is to prepare ultrafine powders of uniform particle size which are free from hard agglomerates; such powders may sinter to full density more rapidly and at lower temperatures and provide more precise and homogeneous compositions [95]. Wet chemical methods such as metal alkoxide [96,97], citrate [98], sol-gel [99], a combination of sol-gel and emulsion [100] and chloride [101,102] processes have all been used successfully for stabilised zirconias. The sintering behaviour of powders having large active surface areas is sensitive to the atmosphere [103], to washing media [102,104], and to residual chemical species [105].

Planar zirconia films

Recently a number of studies have been reported on thin films of zirconia; these demonstrate that a great variety of solid electrolytes having ionic conductivities similar to bulk materials can be deposited or synthesized on a substrate by various thin film techniques. These include chemical vapour deposition [106,107] electrochemical vapour deposition [108], and sputtering [109,110]. Layer thickness was typically in the nm–μm range. A likely major future application is the high temperature solid oxide fuel cell (SOFC) [111] as thin films can provide high ionic conductance and can satisfy the requirements of high power to weight ratios.

Thick films of fully stabilized zirconia have previously been produced by plasma spraying [112,113], and screen-printing techniques [114,70,69]. These can

provide major cost advantages but very little has yet been reported on the material science of such layers and their interaction with the supporting substrate. Detailed systematic studies on the required processes for producing screen-printed films have not been cited. Recently zirconia/binder sol systems have begun to be studied with work investigating rheological characteristics of dip-coating [115] and slip casting processes [116]. Rheological properties and carrier inclusions for the above-mentioned processes differ from those required for printing pastes; such pastes in conjunction with appropriate processing information are not commercially available to date.

1.5 SINTERING OF CERAMIC POWDERS

1.5.1 General

Sintered ceramics are normally prepared by compressing the powder followed by firing. However, an alternative route is the screen–printing of a paste of the ceramic onto a suitable substrate followed by drying and firing.

The driving force for sintering is a decrease in the surface free energy arising from a tendency in the powder compact towards a reduction of the solid-vapour surface area: this creates compaction forces in three dimensions of a material in the bulk state [92,117]. It is well known that neck formation and shrinkage, fissure formation and growth, pore growth, grain growth, pore rearrangement and pore entrapment can occur during the sintering of powders [127]. These processes may take place throughout the period of sintering but there is generally a dominant mechanism in a given period. Dominating mechanisms are dependent upon the physical state of the powder and hence may change with sintering time and temperature.

Pores in the ceramic can be characterised by a coordination number CN, and growth occurs if this is larger than a critical number CN_c. Only pores with $CN<CN_c$ can disappear during sintering [118]. As grain growth proceeds CN decreases. The processes of grain growth and rearrangement reduce the coordination number of pores enabling further densification [119].

It is thought that the most important factor in achieving a dense ceramic is the ultimate homogeneity of the particle dispersion and the use of fine and unagglomerated particles [120,121,122,123,124]. Additives that may form liquids at the sintering temperature have been used as sintering aids to increase the density or reduce the sintering temperature of ceramics.

Successful solid state densification requires that the energy reduction be achieved by pore contraction rather than by particle growth [125] and that the microstructure be stabilised so that the pores are attached to the grain boundaries [126]. A detailed characterisation of the sintering behaviour of highly agglomerated and ultrafine compacted zirconia powders into bulk ceramics has been undertaken by Wu and Wu [127].

Sub-micron particles tend to agglomerate due to Van der Waals adhesion forces that are about six times gravitational ones [128]. The bonding mechanisms of agglomerates in increasing order are thought to be [128], electrostatic, Van der Waals, liquid bridges, capillary liquid, viscous binders and solid bridges.

1.5.2 Zirconia

Fundamental kinetic studies on the sintering of stabilised zirconia [91,129, 130,131] have mainly concluded that the densification mechanism is controlled by lattice diffusion of the cations; the rate controlling process is the movement of the cation by an interstitial rather than by a vacancy mechanism. The diffusion coefficient of the cation is determined by the concentration of the stabilising dopant. Maximum density values are obtained at specific dopant concentrations for each stabiliser; additional dopant contents are accompanied by a decrease in density. In the case of Y_2O_3 the optimum content for maximum densification has been suggested to be 6-7 mol% [132,133,134]. More recently Gnoheim and Hanna [135] found an optimum value of 4 mol % and suggested that their lower value was due to an oxide homogeneity on a smaller (atomic) scale than in previous work which reduced the amount of Y_2O_3 needed for maximum densification.

Conductivities of stabilised zirconias depend upon the particular dopant cation chosen and the oxygen vacancy concentration, exhibiting maxima when the sizes of the cation of the dopant and host lattice are closely matched [136,137] and when the amount of stabiliser is the minimum amount for full stabilisation.

Bulk stabilised zirconia ceramics (with the absence of sintering aids) of high density are attainable if adequate attention is given to powder preparation and subsequent handling processes [92,133,138]. Additives such as glassy phases and α–alumina powders have been purposely introduced into zirconia to lower the sintering temperature and increase mechanical strength respectively. However deleterious effects have been reported on the ionic conductivity by both glassy phases [139,140,141,142], and α–alumina inclusions [143] in silica–free zirconias. Despite an increasing sintering inhibition in zirconia with increasing alumina additions [144,145,146] some authors report improvements in ionic conductivity of zirconia with low levels of alumina additive. This may be due to some residual glassy phase present in their alumina-free zirconia; Butler and Drennan [147] suggested that alumina in cubic stabilised zirconia acts as a scavenger for the silica.

Generally ionic conductivities of zirconias depend upon the physical and chemical properties of the sample such as composition, porosity, grain size and purity.

1.6 Thick-film technology

1.6.1 General

Screen printing is a craft first known to have been used by the Chinese some 3000 years ago using silk screens for pattern design, later adopted for printing text. Designs are delineated on fine-weave cloths as sealed and open areas. These are then used as masks which are placed onto the surface to be printed; ink is spread across and prints through the open zones only.

Thick film technology applied in the semiconductor industry consists of the screen printing of a viscous paste in a definite pattern on a rigid surface (substrate) and the subsequent drying and firing of this deposit at appropriate temperatures for

a suitable time to produce a set of usually passive, planar components and interconnections such as conductors, resistors or dielectrics in microelectronic applications.

"Thick-Film" is a misleading term. The distinctive features are not related to the layer thickness but to the deposition method, i.e the print-dry-fire technology. Reproducible "thick-films" can be deposited down to a thickness of 1 μm using newly developed organometallic inks; however the fired thickness of a thick film is usually in the range 10-50 μm.

1.6.2 Properties of screen-printing pastes

Pastes are formulated to have the necessary flow properties for printing, to bind together and to the substrate when dry and normally contain ingredients to fuse onto the substrate when fired. Four components are normally present, namely fluid, binder, powdered glass and the functional material. The fluid evaporates soon after printing and the binder is burned off in the early stages of firing. Firing sinters the remaining finely divided components into a solid. A deflocculant (or dispersant) is sometimes included (a 5th ingredient) to suppress agglomeration of the powders and to aid wetting to the substrate and/or to obtain a suspension as thick as possible whilst retaining fluidity.

Pastes are generally proportioned to have a treacle-like viscosity with pseudoplastic properties (decreasing viscosity with increasing shear rate) and thixotropic properties (changing viscosity with time) [148]. The important rheological properties of pastes are the viscosity and the surface tension and the dependence of these on shear rate and time. For many fluid systems the relation between the shear stress τ and the shear rate γ can be expressed according to an empirical relation known as the power law [149]

$$\tau = \zeta \gamma^{q} \qquad (1.13)$$

The parameters ζ and q are termed the fluid consistency index and the flow behaviour index respectively. Newtonian flow is characterised by q = 1. If η_a is the apparent viscosity, then

$$\eta_a = \tau/\gamma = \zeta \gamma^{q-1} \qquad (1.14)$$

An equation was proposed by Casson [150] to relate the viscosity and shear rate of printing inks:

$$\eta^{½} = \eta_{\infty}^{½} + \tau_0^{½}\,\gamma^{½} \qquad (1.15)$$

where η is the viscosity, η_{∞} is the limiting high shear viscosity and τ_0 is the yield point. This equation is generally applicable for thixotropic materials and has previously been used for their characterisation [151].

1.7 DIFFUSION OF GASES THROUGH POROUS SOLIDS

Diffusion of gases to the cathode must be severely restricted in solid state amperometric sensors. This is due to the high diffusion coefficients of gases (4–5 orders of magnitude higher than ions in aqueous solutions), and to the fact that pump currents are restricted by the resistance imposed by the solid electrolyte cell and the rate of the electrode reactions. Various forms of diffusion barrier which were successfully employed on working devices were described by Dietz [33]. More recently a device was constructed that used the pores of the platinum cathode as a diffusion barrier [152]. The mechanisms of diffusion through porous solids in general are considered below.

When there exists a concentration difference across a porous solid a diffusional flow of the species takes place. This may occur in gases by one or more of three mechanisms: these are bulk (or ordinary), Knudsen and surface diffusion. The principal mechanism of diffusion is conditional upon the size, shape, and tortuosity of the pores of the diffusion barrier. The various types of diffusion through a pore may all be described with reference to the Knudsen number (K_n) defined as the ratio between the mean free path of the gas λ_m, and the pore diameter d_p, [153].

$$K_n = \lambda_m / d_p\,, \qquad (1.16)$$

Figure 1.10 is a schematic diagram of some the various diffusion mechanisms.

The value of λ_m is estimated by the following equation [154]

$$\lambda_m = \frac{3.2\mu_v}{P}\sqrt{\frac{RT}{2\pi M}} \qquad (1.17)$$

where μ_v is the viscosity, M the molecular weight, P the pressure, T the temperature of the gas and R is the universal gas constant.

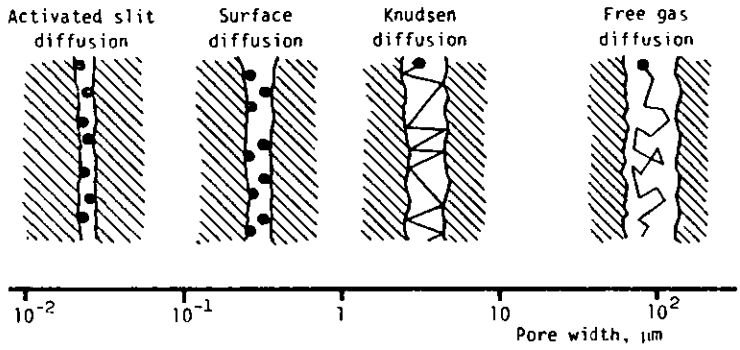

Figure 1.10 *Schematic representation of various diffusion mechanisms in porous solids as a function of pore width at atmospheric pressure.*

Bulk diffusion is dominant where K_n is small i.e the pore size is larger than the mean free path of the gas (typically 10 microns at atmospheric pressure). Here the molecule-molecule collisions are more frequent than molecule–wall collisions.

The Knudsen diffusion coefficient D_K, is a function of the molecular weight of the gas and can be found from [155]

$$D_K = 97 r_p \left(\frac{T}{M}\right)^{1/2} \qquad m^2\ s^{-1} \tag{1.18}$$

where r_p is the capillary radius. Consequently the components of a gas mixture will pass through a porous solid barrier at different rates. Knudsen diffusion dominates where K_n is large.

A further possible transport mechanism is surface diffusion. Surface diffusion on the walls of the pores is relatively fast compared with bulk diffusion [156]; it includes solute adsorption, diffusion while adsorbed, and solute desorption. This

physical mechanism has been used to explain diffusion rates in porous solids which are greater than can be explained by other mechanisms [153]. It can explain the observation of decreased diffusion with increasing temperature (adsorption decreases as the temperature is increased).

In a given capillary gaseous diffusion (in the absence of) will occur according to both bulk and Knudsen processes; one or other mechanism may be rate controlling,

$$D_T = \left(\frac{1}{D_B} + \frac{1}{D_K} \right)^{-1} \tag{1.19}$$

where D_T is the resultant diffusion coefficient through the capillary, D_K is the oxygen diffusion coefficient through a capillary where Knudsen diffusion is predominant, and D_B is the bulk diffusion coefficient of oxygen in nitrogen. If in surface diffusion the adsorbed layer can be assumed to be sufficiently thin that the volume of the pore available for gas diffusion is not greatly reduced, surface diffusion can then occur in parallel with gaseous diffusion and the fluxes are additive [157] hence

$$D_T = - \left(\frac{1}{D_B} + \frac{1}{D_K} \right)^{-1} + k_1 D_S \tag{1.20}$$

where D_S is the surface diffusion coefficient of oxygen on the capillary wall, and k_1 is an empirical constant. If however the gas is strongly adsorbed the adsorbed layer may be thick enough to reduce the gas diffusion appreciably, or even fill the pore [158]. In cases of both bulk and Knudsen the rate of diffusional flow is proportional to the pressure difference and inversely proportional to the diffusion path length. The effect of temperature, T, and total barometric gas pressure, P, on the limiting current, I_{lim} of solid state amperometric oxygen sensors on both types of diffusion was considered by Dietz [12]. For bulk diffusion I_{lim} should be independent of P but proportional to $T^{0.7}$. For Knudsen diffusion I_{lim} should be proportional to both $T^{-0.5}$ and to P. Surface diffusion has not yet been reported to occur in practical amperometric devices.

1.8 AIMS AND OBJECTIVES

The overall objective was to demonstrate the feasibility of fabricating practical miniature zirconia amperometric oxygen gas sensors, including integral heating, using planar thick-film technology exclusively.

The achievement of this necessitated investigations of the following aspects:

(i) Screen printing of electronically conducting electrodes (platinum and platinum–zirconia cermets) capable of withstanding firing temperatures in excess of 1300°C and characterisation by electrical tests.

(ii) Preparation and screen printing of zirconia pastes, drying and firing to sinter to very low, though not zero, porosity: characterisation of the sintered film by scanning electron microscopy (SEM), X–ray diffraction and AC impedance spectroscopy.

(iii) Preparation of complete sensors comprising an electrode layer, an electrolyte layer and a second electrode layer and cofiring where appropriate: characterisation of these sensors in air–nitrogen mixtures and in the flue gases from a gas burning system.

(iv) Printing of thick film platinum heaters: characterisation after treatment at temperatures above 800°C for extended periods of time using SEM, resistance measurements, cross–sectional area and platinum loss measurements.

CHAPTER 2

EXPERIMENTAL

" A Scientist is like a traveller without a map "

2.1 GENERAL

The major items of equipment, materials and procedures with general application are discussed in this chapter. Details of techniques, where specific to a particular chapter, are provided in the relevant chapter.

2.2 EXPERIMENTAL MATERIALS

2.2.1 Zirconia powders

The zirconia powders used were 3 mol% and 8 mol% (Y_2O_3) yttria stabilised zirconias, referred to as 3Y and 8Y zirconias respectively prepared using a hydrolysis method by Toyo-Soda (Japan) and obtained via Whitfield & Son (U.K).

2.2.2 Screen printing vehicles

The organic vehicles used for the preparation of the screen printable zirconia pastes were obtained from Electro Science Laboratories (ESL) UK Ltd and were of the type:

400 : resistive cermet screening vehicle

401 : thinner; very slow drying

403 : dielectric vehicle

2.2.3 Platinum inks

The platinum inks used were commercially available 5544 fritted and 5542 fritless compositions purchased from ESL. The detailed compositions of the pastes are considered proprietary information by the manufacturer; ink 5544 is known to contain an admixture of a glass whereas 5542 is guaranteed to contain platinum only, after burnout of the organic constituents.

2.2.4 Substrates

The substrates used were ceramic squares (25 mm edge and 700 μm thick) from Coors Ceramics Electronics containing nominally 96 and 99.6% by weight of alumina. The chemical constitution of the substrate is given in Table 2.1. The physical, mechanical, and thermal characteristics of the substrate are summarised in Table 2.2. Substrates were used as supplied by the manufacturer without any further cleaning, abrading or polishing processes.

Material	Substrate Type	
	Coors ADS 96	Coors ADS 996
Al_2O_3	95.1	99.2
SiO_2	2.3	0.52
CaO	0.01	0.07
MgO	1.9	0.23

Table 2.1 *Chemical Analysis (weight %) of the alumina substrates. (Source: Pitt [159]).*

Property	Substrate Type	
	Coors ADS 96	Coors ADS 996
Bulk density / g cm^{-3}	3.75	3.88
Thermal conductivity at 20°C / W m^{-1} K^{-1}	34.7	26
Coefficient of thermal linear expansion (per °C in the range 25–1000°C)	$8x10^{-6}$	$8.3x10^{-6}$
Resistivity at 20°C / Ω cm.	$>10^{14}$	$>10^{14}$
Surface finish–CLA* / µm	0.72	0.19

*Centre Line Average

Table 2.2 *Substrate characteristics (Source: Manufacturer's data sheet)*

2.3 APPARATUS AND PROCEDURES

2.3.1 Profiles

Dimensions and profiles of the thick–films were obtained using a Tencor Instruments Alpha-Step 200. The force applied by the traversing stylus was 8 mg. The tip of the needle was rounded with a radius of 2.5 µm. The vertical and horizontal resolutions of the instrument were 0.5 nm and 40 nm respectively. The

instrument was calibrated using a 850 nm standard step supplied by the manufacturer. The software in the Alpha-Step provided a graphical output of the trace and calculated the average height, the width and area relating to the film profile.

2.3.2 Weight measuring scales

The balance used was a Precisa analytical balance model 300A reading to 0.1mg.

2.3.3 Triple roll mill

This was a Model 1 from Pascall Engineering, fitted with porcelaine rollers and a PVC take-off blade.

2.3.4 Viscometer & viscosity standard fluids

A digital cone and plate type viscometer, model HBTDCP (Brookfield Engineering Laboratories, USA) was used. The viscosity of the pastes and liquids was measured on the plate whilst this was held at a constant temperature of 25°C using water from a constant temperature water bath.

The viscometer calibration was checked using the following calibrated viscosity standard Newtonian liquids obtained from BDH.
Viscosity at 25°C (cPs) / Lot number :i) *5060 / 121889*; ii) *29520 / 091289*; iii) *95200 / 082989*

2.3.5 Chemicals

The following chemicals supplied by BDH Chemicals were used:
i) SpectrosoL platinum standard solution (1000 ± 5ppm) in a matrix of 0.5 mol l^{-1} hydrochloric acid containing chloroplatinic acid as the solute.
ii) AnalaR nitric acid with a specific gravity of 1.42
iii) AnalaR hydrochloric acid.

2.3.6 Screen-printing

Pastes were printed onto the alumina ceramics using a model 1202 DEK screen-printer. The ambient temperature during printing was 19°C. The printing

screens were obtained to given specifications (Table 2.3) from DEK Screens Division.

The pattern of the print was formed using the Autocad computer–aided design package. A 20:1 scale copy of the pattern was then transferred onto Rubulith (a two layered plastic sheet material comprised of a red and a clear layer) using a modified Ferranti flat bed plotter with the pen replaced by a scalpel. The scalpel cut only through the red layer of the Rubulith. Removal of the appropriate part of the red layer of the Rubulith formed the pattern. This was photographically reduced down to final size onto copyproof sheet using an Agfa-Gevaert (RPS 2024 Mk4) exposure unit. The copyproof sheet was developed using an Agfa-Gevaert (CP 530) developer.

The screen, masked by the full scale pattern, was exposed to ultra violet light with the aid of a screen exposure unit (DEK model 107). The screen emulsion was hardened where the radiation fell upon it leaving the areas delineated by the pattern soft enough to wash away with water and expose the screen mesh from both sides.

Screen function	Screen specification			
	Mesh count per inch	Mesh angle / degrees	Open area / %	Emulsion thickness / μm
Platinum–heater films	325	90	40	25
Electrode and Cermet films	200	90	42.5	13
Zirconia films	200 100	90 90	42.5 68.0	50 50
	Ethed metal mask			50

Table 2.3 *Specification of screens used.*

2.3.7 Drying and firing

The printed inks were dried using an infra-red dryer (model DEK 1209). All higher temperature treatments were given using a Carbolite muffle furnace (model RHF 16/3) of the fast heating type, able if required to reach a maximum of 1600°C from room temperature, in less than 1 hour. This furnace was equipped with a Eurotherm model 818P temperature controller providing three term (PID) temperature control.

2.3.8 Resistance measurement

All room temperature electrical resistance measurements were made using a four point probe technique to eliminate contact resistances. A constant current source (Fig. 2.1), adopted from Horowitz and Hill [160] was constructed to apply a current I_{out}, of 1000μA, adjusted using a 10 turn trimmer R_2, through the sample; the resistance was obtained from a measurement of the resulting voltage across the sample. The low applied current avoided any significant resistive heating during measurement. The magnitude of the applied current was regularly checked using a Solartron (Type 7150) digital multimeter.

2.3.9 Scanning electron microscopy and image analysis equipment

Samples were examined using either of two scanning microscopes. One was a Cambridge Instruments Stereoscan 240 equipped with a Link Analytical AN 1085 energy dispersive X-ray system. The other was a JEOL 733 superprobe electron microscope used for feature analysis and image digitisation with the aid of Link Analytical image analysis software.

2.3.10 Chemical analysis

Wet-chemical analysis was performed with a Pye-Unicam SP9 atomic absorption spectrometer (AAS) burning an air-acetylene mixture (burner width 10 cm). The hollow cathode lamp (for detecting Pt) was supplied by SJ electronics and was operated with a current of 10 mA. Class A calibrated glassware were used to prepare the standard solutions.

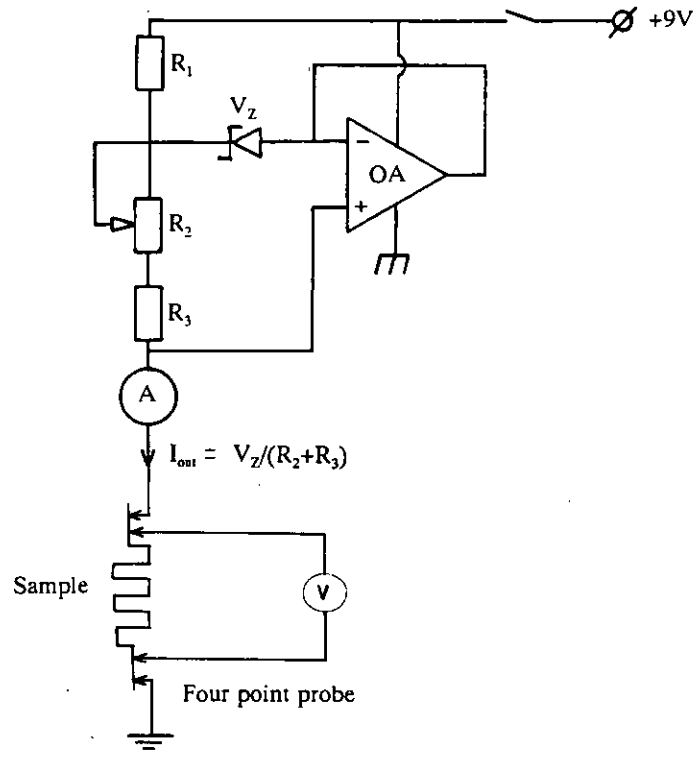

Figure 2.1 Electrical resistance measurement using a current source and a four point probe.

The technique involved dissolution of the platinum on the surface of a substrate in a solution of aqua regia (3 volumes hydrochloric to 1 nitric acid) and comparison of the absorbance value (output of AAS) with those of previously prepared standard solutions of known platinum concentrations.

Sample preparation

The samples (substrates incorporating printed platinum films, having been given the appropriate thermal treatment) were placed in a small beaker containing 20 ml aqua regia. The beaker was subsequently covered and heated using a bunsen burner, thus allowing the contents to boil gently for 15 minutes. The contents were continuously agitated by gentle swirling of the beaker. The bare substrate was removed and washed into the beaker with distilled water. The contents from the beaker were transferred to a 100 ml measuring flask. To ensure maximum transfer of the dissolved platinum from the beaker to the flask, the beaker was rinsed thrice with

distilled water directly into the measuring flask. Prior to obtaining the absorbance value the flask was filled to its 100 ml marker point, stoppered and the contents thoroughly mixed.

Preparation of the standards

A series of standards was prepared with known Pt concentrations by diluting the platinum standard solution. Absorbance values were obtained for these standards using the atomic absorption spectrometer (AAS). This established a relation for converting absorbance values to platinum concentrations.

Care was taken to ensure that the standard solutions were prepared in the same way as the sample solutions. The required amount of Pt standard solution was added to a beaker using a class A burette, together with 20 ml of aqua regia and a blank alumina substrate. The beaker contents were gently heated for 15 minutes prior to transfer of the contents to a measuring flask which was filled to 100 ml with distilled water and thoroughly mixed. To check the effect of the acid concentration on the absorbance values, standards of the same concentration were prepared using no aqua regia.

2.3.11 Temperature and gaseous environment control for sensor testing

Gas mixing arrangement

The sensor was mounted in an enclosed environment where oxygen concentration was controlled (Fig. 2.2a) by mixing flows of oxygen–free nitrogen (British Oxygen Company) and air using mass flow valves (Type 5850TR and 5850E) from Brooks Instruments. These valves controlled flows in the ranges of 0-10, and 0-100 ml min^{-1}. A control unit (Brooks Instruments, Type 5878) was used to allow setting and digital reading (3½ digits) of the flows to be achieved. The total gas flow rate to the sealed environment enclosing the sensor was always maintained at 100 ml min^{-1}. A regular check of the calibration of this equipment was conducted by measuring the time taken for a soap bubble sealing the flowing gases from the atmosphere to travel through a fixed volume of a calibrated burette. The checks of the calibration correlated to within ±1% of the flowmeter setting.

Temperature control

The furnace used consisted of an alumina tube with a non-inductive winding; temperature was controlled to better than ±3°C using a remote-setpoint three-term controller (Eurotherm model 810) with a type K thermocouple located adjacent to the sample.

Sample placement

The sample was mounted in the furnace within a silica tube; this enabled control of the gaseous atmosphere around the sample using the gas mixing apparatus. Electrical connections to the sample were made using platinum wire (150 μm in diameter); these were screened to within 10 mm of the sample using a stainless steel sheath rod. The experimental set–up is shown in Fig. 2.2.

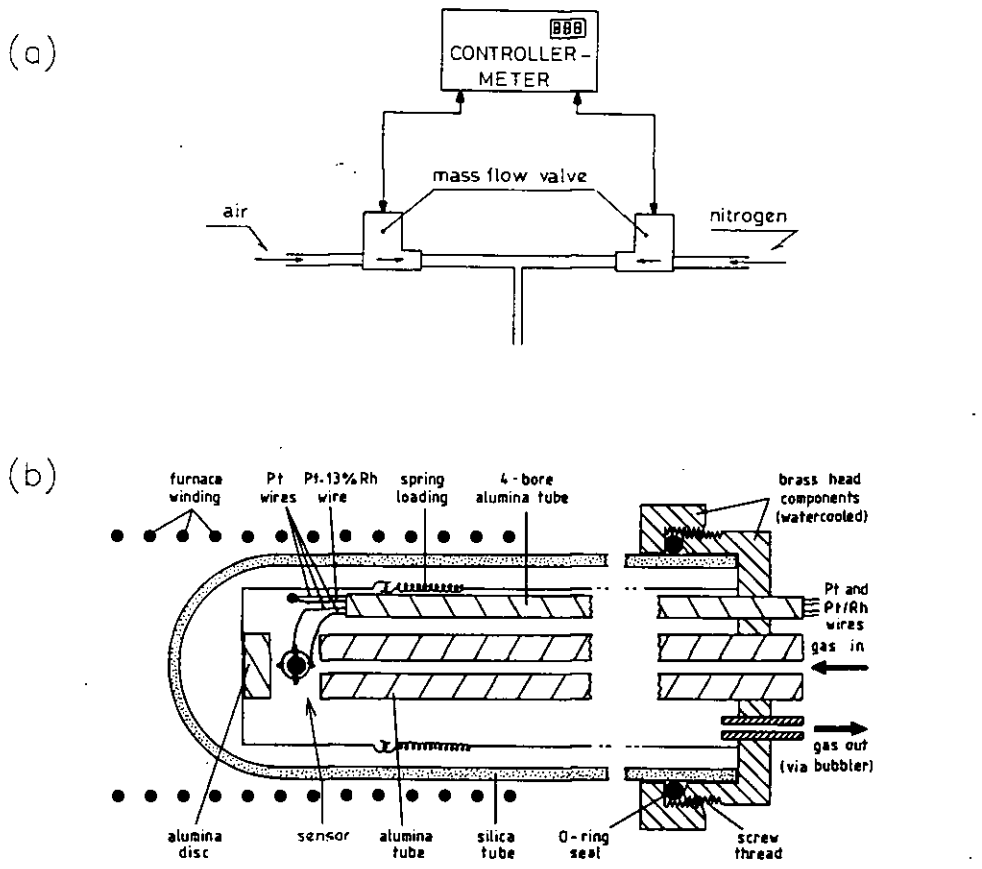

Figure 2.2 Experimental arrangement for measurement of sensor characteristics. (a) gas mixing arrangement, (b) furnace arrangement.

2.3.12 A-C impedance analysis

The system used for impedance analysis was a commercial arrangement made and interfaced to a computer by Hewlett Packard Ltd. This had a facility for inputting the area/length ratio for each sample and provided complex plane impedance plots of the data. The measurement system was checked using dummy R-C circuits containing components of known values.

2.3.13 X-ray analysis

This was carried out with the following automated equipment supplied by Philips: PW 1730/10 high performance 4kW 60kV constant potential generator; PW 2253/20 broad focus copper anode X-ray tube; PW 1752/00 graphite monochromator; PW 1711/10 xenon proportional counter; PW 1050/81 goniometer and step motor; PW 1710/00 automated diffractometer control. Measurements were performed by the step–scanning method at a goniometer scan speed of 0.1 degrees of 2θ per second and generator settings of 45kV and 55 mA. The patterns were outputted on a Tectronics terminal and subsequently on a graphics plotter.

All samples for X-ray diffraction were flush-mounted into the aluminium sample holders by backfilling with plasticine against glass slides.

CHAPTER 3

THICK ZIRCONIA FILMS

3.1 INTRODUCTION

Thick film technology has not commonly been used to prepare dense high purity ionically conducting ceramics. The technology requires that sintering be performed without high pressure compaction. Ionic conductivity considerations dictate the absence of inclusions such as sintering aids which remain as impurities in the sintered films. Furthermore the films are constrained from sintering (and consequently shrinking) normally in three dimensions by their adhesion to the substrate. Thus careful optimisation of the process was required to prepare dense, high purity layers sintering at relatively low temperatures. It was essential that films adhered well to the substrate and consequently interactions with the substrate were also important.

In this chapter the preparation of low porosity zirconia thick films is first considered in detail. This is followed by the characterisation (physical, electrical and crystallographic) of these films.

3.2 EXPERIMENTAL

3.2.1 Fabrication of dense zirconia layers by screen printing

The stabilized zirconia powders were first calcined at various temperatures and their tap density measured. The tap density is that corresponding to the maximum packing achieved by gently tapping a container of the powder until there was no observable change in the volume occupied by the powder.

Prior to paste manufacture the powders were calcined at 700°C for 30 minutes in order to remove any adsorbed moisture and combustible impurities. The powders were then mixed with a range of organic vehicles in various proportions (Table 3.1) in a pestle and mortar followed by more intimate mixing using the triple roll mill. Samples were taken from the resulting pastes and characterised using a viscometer to determine their rheological properties and dispersed nature. The precise composition of the pastes was measured by ashing the paste (evaporating the vehicle at low temperature followed by a 700°C firing for 10 minutes) and measuring the weight loss. Insignificant vehicle loss by the mixing procedure was indicated.

The pastes were screen printed using a DEK Model 1202 machine onto 96 and 99.6% alumina substrates. The films were allowed to settle for 10 minutes prior to drying slowly in an infra-red dryer at 150°C to remove solvent and at 400°C to remove organic binders. Repetition of the print and dry (at both 150 and 400°C) procedures was used to build up the thickness of the zirconia films. The dried films were then subsequently fired for 1 hour at a temperature in the range 1300°C to 1600°C. Where an intervening layer of platinum (between the substrate and the film) was incorporated this was printed using a fritless ink (Type 5542 from ESL).

3.2.2 Scanning electron microscopy

Fracture edges were generated for examination by scribing the back face of the substrate and snapping. Microstructure of the films was investigated using the Cambridge Instruments Stereoscan 240 scanning electron microscope.

3.2.3 Examination using X-ray diffraction

X-ray diffractometer traces were obtained for the as-received zirconia powder, the zirconia films as printed and dried and as sintered on 96 and 99.6% alumina substrates at temperatures up to 1600°C for 1 hour. Diffractometer traces of both types of alumina substrate were also obtained so that peaks relating to the alumina could be eliminated. Line traces were obtained over a range of 2θ from 20° to 90°. Emphasis was placed on the part of the profile where 2θ = 25°–33° as this contained the strongest peaks for the monoclinic phase (~28.3° for (111̄) and 31.7° for (111)) and for the metastable tetragonal phase (30.5° for (111)). The volume fraction of the monoclinic phase, V_m, was estimated according to the Equation [161]

$$V_m = \frac{1.311\ X_m}{1 + 0.311\ X_m} \tag{3.1}$$

where X_m is the integrated intensity ratio defined as

$$X_m = \frac{Ip_m(111^-) + Ip_m(111)}{Ip_m(111^-) + Ip_m(111) + Ip_t(111)} \tag{3.2}$$

calculated using the intensities (peak height), of the monoclinic (Ip_m) peaks (111̄) and (111) and the tetragonal (Ip_t) peak (111) from which the background radiation had already been subtracted.

3.2.4 Electrical characterisation of the films

Electrical characterisation was performed using the Hewlett Packard frequency response analysis equipment. The technique, referred to as impedance spectroscopy was first applied to measure the conductivity of ceramic ionic conductors by Bauerle [162]. Its principal advantage over DC measurements is that it enables the contribution of the grain interiors and grain boundaries to the total conductivity to be separated. Baurle used zirconia with platinum electrodes and showed that the resistances due to the grain interior, grain boundaries and electrode-electrolyte interface could be resolved in the complex admittance plane. Subsequent workers chose to work in the impedance plane obtaining a graphical representation that was more readily analyzed [163,164].

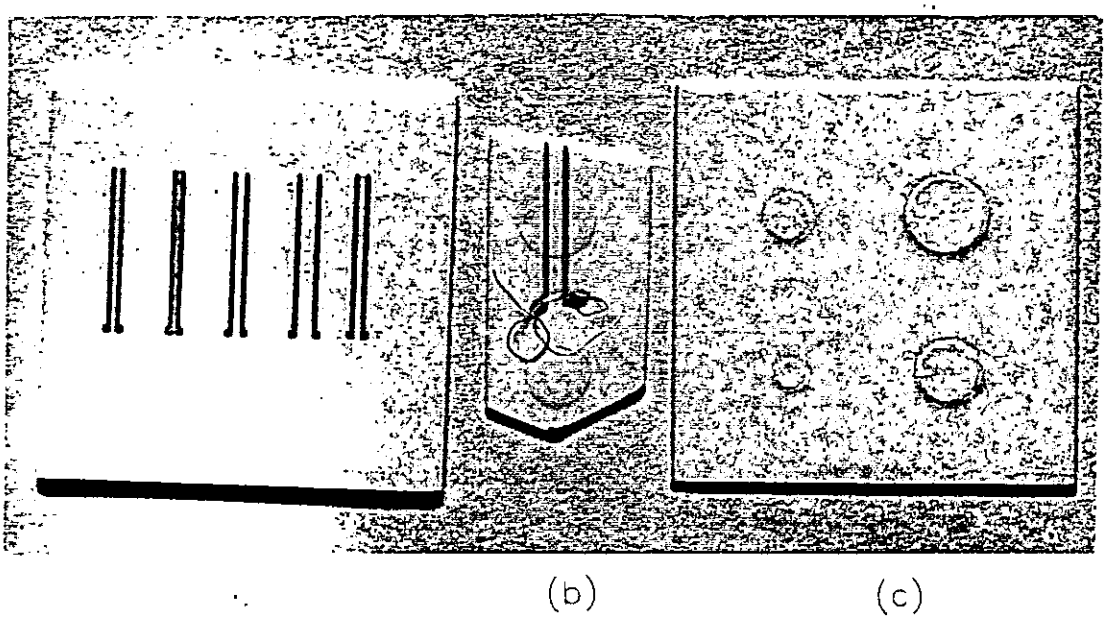

Figure 3.1 (a) Printed platinum strips used for electrical connection to the sample, (b) Photograph of a sample on an alumina substrate used for A-C impedance measurements (c) Zirconia thick-films (circular).

A-C impedance measurements were made perpendicular to the plane and transversely across the surface of the zirconia films. Measurements, made transversely across the surface of the film, were facilitated by two parallel platinum strips (Fig. 3.1) which were printed (using fritless platinum paste, Type 5542) following thermal treatment of the zirconia films. Platinum wires (100 μm in

diameter) were attached to the strips (using the previously-mentioned paste) and subsequently fired at 1000°C for 30 minutes; the resulting platinum strips were 5 μm thick. The separation of the strips was measured using calibrated optical microscope slides and verified by Alpha–step measurements. The thickness of the zirconia films was measured by the Alpha-step. The separation of the platinum strips and the thickness of the zirconia films enabled the electrical characteristics of the zirconia thick–films to be normalised to unit dimensions. In order to eliminate end effects the separation of the electrodes was chosen to be large (typically 1 mm) compared to the thickness of the electrolyte layer (<30 μm).

3.3 RESULTS AND DISCUSSION

3.3.1 General

This discussion is presented in two parts. In the first part (§ 3.3.2), studies related to the preparation of low porosity sintered zirconia layers on alumina substrates is discussed. In the second part (§ 3.3.3) characterisation of the electrical, microstructural and crystallographic properties of the films, with film thickness, firing temperature and alumina substrate purity as variables are discussed. Such characterisation is important and the techniques powerful because the electrical properties of stabilised zirconia depend strongly upon the microstructure, crystallographic form and grain boundary effects [165].

3.3.2 Studies related to the production of low porosity zirconia thick films

3.3.2.1 Powder treatment

Scanning electron micrographs of the as-received powders (Fig. 3.2) show that dense agglomerates of 40-160 microns in diameter (but mostly of 110 microns existed). These were composed of particles of 0.3-1.0 microns in diameter. Crushing of the loose powder in a pestle and mortar may have broken up the agglomerates but these presumably reformed due to large interparticle attraction forces. Firing of the as-received uncompacted powders at temperatures normally sufficient for sintering did not result in the formation of a compact ceramic. Intra–agglomerate sintering was observed but there was no sign of the agglomerates fusing to form a compact body. The mean agglomerate size (average of 100 agglomerates intercepted by a single

straight line drawn across a micrograph) and the "tap" density, both as a function of the sintering temperature are shown in Fig. 3.3; the bulk density of the zirconia was quoted by the manufacturer to be 6.05 g cm^{-3}. The agglomerates began to sinter at around 1000°C as shown from tap density measurements. High tap densities have previously been associated with high agglomerate densities [166]; this is supported by figure 3.3. These results indicate that the 3Y began to compact during sintering about 50°C below the 8Y powder. This may have been due to a smaller particle size of the 3Y compared to the 8Y powder. Figure 3.3 shows that there was a large volume decrease (~95%) within the agglomerates (3Y powder) upon sintering the as received loose powder (mean agglomerate size of 110 μm diameter) to 1450°C (40 μm diameter). Tap density measurements at 600°C show that the as received powder had a porosity of ~80%; the porosity within agglomerates was thus expected to be less than this value. The large observed decrease in the agglomerate size suggests that they began to break down to smaller diameters during firing (it is not expected that break-up continued when they began to sinter). Further decreases in the agglomerate diameter were due to sintering.

(a)

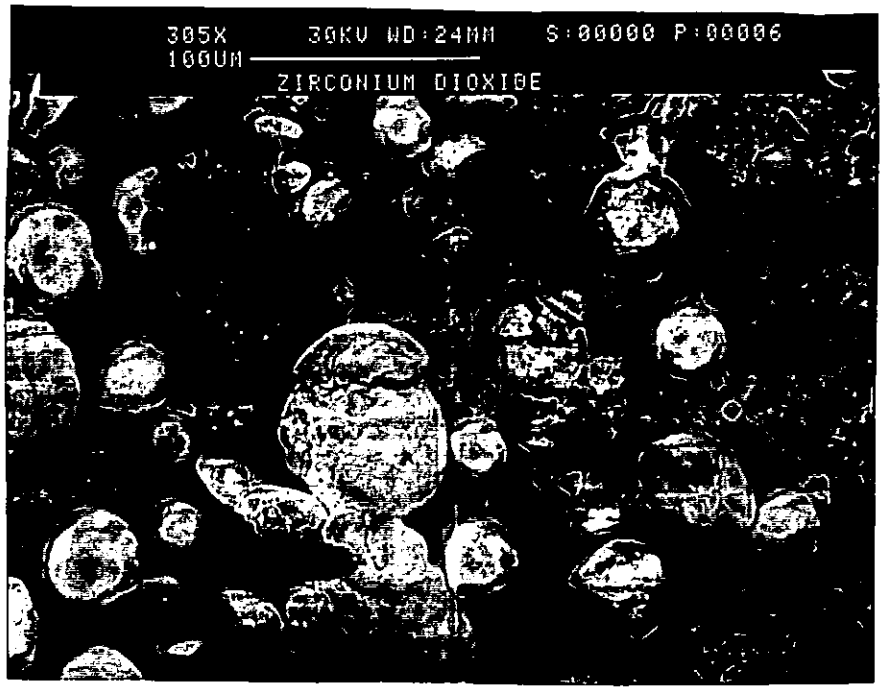

(b)

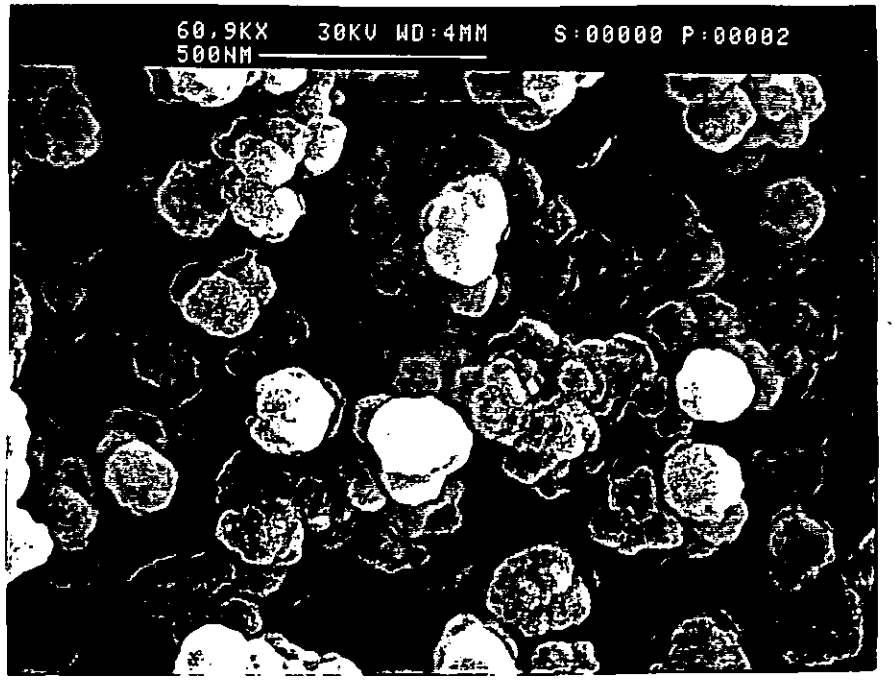

Figure 3.2 *Scanning electron micrographs at two magnifications of the as received 3Y zirconia powders. Cursor lengths show the magnifications.*

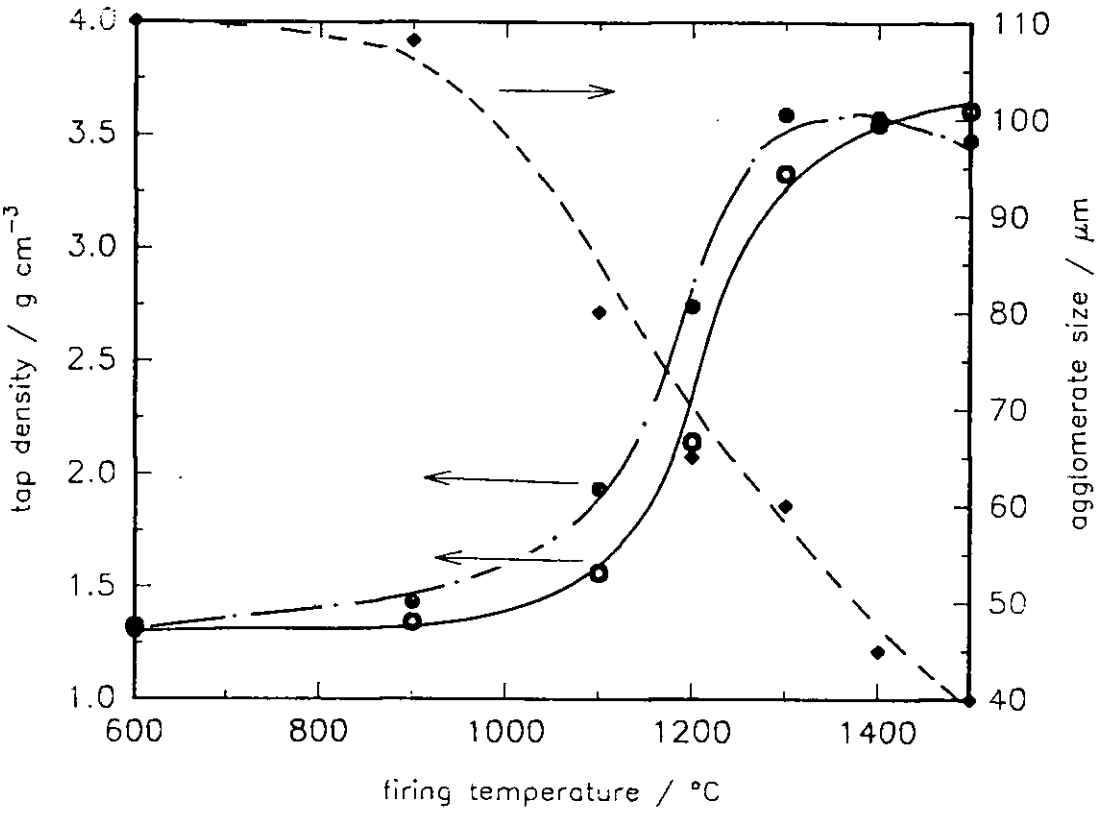

Figure 3.3 *Firing temperature (held for 1 hour) vs tap density and mean agglomerate size.* ○*;8Y tap density,* ●*; 3Y tap density,* ♦*; 3Y mean agglomerate size.*

3.3.2.2 Paste characterisation

Composition

Compositions of the various pastes prepared are shown in Table 3.1.

Paste Number	Vehicle / % wt		
	ESL 400	ESL 401	ESL 403
3c	---------	25	---------
3d	---------	28	---------
3b	---------	30	---------
3	---------	34	---------
3e	---------	38	---------
4	34	---------	---------
4a	40	---------	---------
4b	45	---------	---------
4c	50	---------	---------
4d	60	---------	---------
4e	70	---------	----------
5a	---------	---------	30
5	---------	---------	34
5b	---------	---------	40

Table 3.1 *Zirconia paste compositions; the remaining percentage was made up of 3Y zirconia powder.*

Rheological behaviour

Typical examples of the flow behaviour of the various pastes prepared are described below with reference to the paste number 4d. The decreasing viscosity with increasing shear rate (Fig 3.4) and shear stress dependence on the shear rate (Fig. 3.5) demonstrate the pseudoplastic properties of the paste.

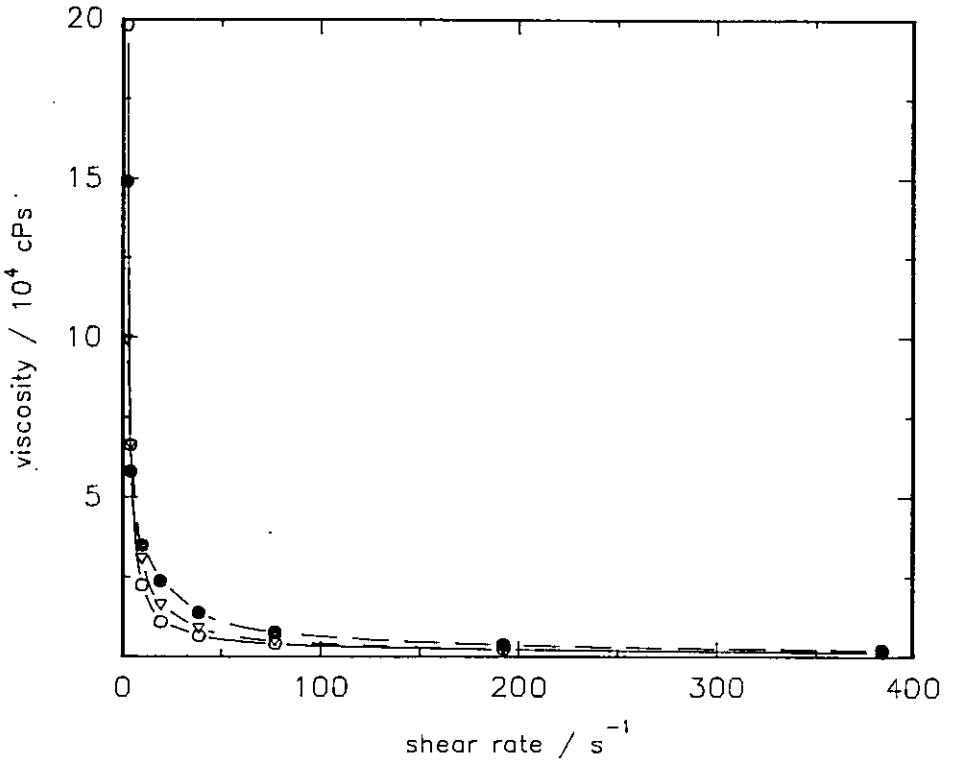

Figure 3.4 *Viscosity dependence on shear rate for paste number 4d; ○, mixed in pestle and mortar: ●, roll milled for 10 minutes; ▯, roll milled for 1 hour.*

Plots of the data according to the following expression: $\tau = \zeta\gamma^{q}$ (Eq. (1.13)) (Fig. 3.6) show the index q to be in the range of 0.7 and 0.9; a value less than one is expected for pastes with pseudoplastic behaviour [167]. Pseudoplasticity was exhibited by all the pastes made and was important as the pastes were required to exhibit low viscosity during printing but high viscosity once deposited. Low viscosity allowed the pastes to be readily forced into the mesh apertures to wet the substrate and then to be pulled through the screen without leaving a significant amount of paste in the screen "fabric". After printing, the paste no longer under shear reverted to a high viscosity; the time available before the deposit dried had only to be sufficient for a localised levelling between adjacent undulations resulting from the mesh of the screen so that the deposit could hold its form during the drying and firing processes.

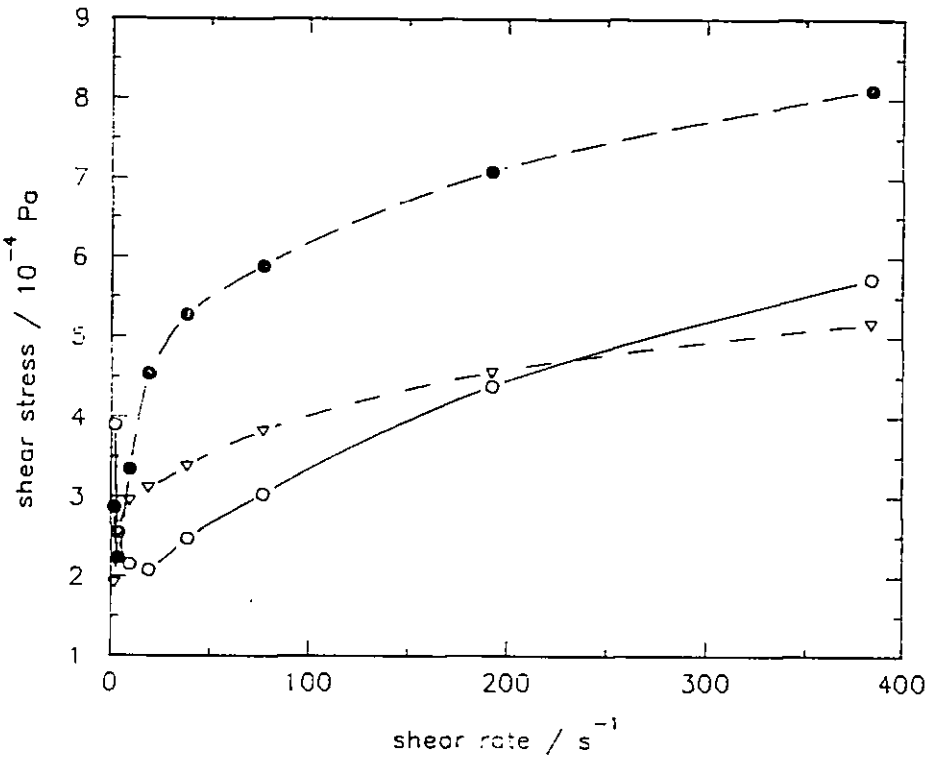

Figure 3.5 Shear stress vs shear rate for one zirconia paste containing 40% by wt 3Y zirconia dispersed in ESL 400 vehicle. ○; mixed in pestle and mortar, ●; roll milled for 10 minutes, ▽ roll milled for 1 hour.

The decreasing torque with time at a fixed shear rate (Fig. 3.7) show that roll-milling of the paste reduced the degree of thixotropy (remember that thixotropy refers to the property of changing viscosity with shearing time). A high degree of thixotropy often is not a desirable feature when pseudoplastic behaviour is important. If the paste viscosity were to remain low immediately after deposition, the advantages of high viscosity at low shear rates would be lost. A rapid recovery (<1 second) of high viscosity with reducing shear rate was essential and seemed to be exhibited by the pastes although it was not measured.

Screen printing normally subjects the pastes to shear rates of around 100-200 s^{-1} [168] whilst the ink is passing through the mesh opening. Screen printing inks are normally considered to print best [168] when viscosities are around 400-500 poise at shear rates of 100 s^{-1} and above 30,000 poise at a shear rate of 0.1 s^{-1} to

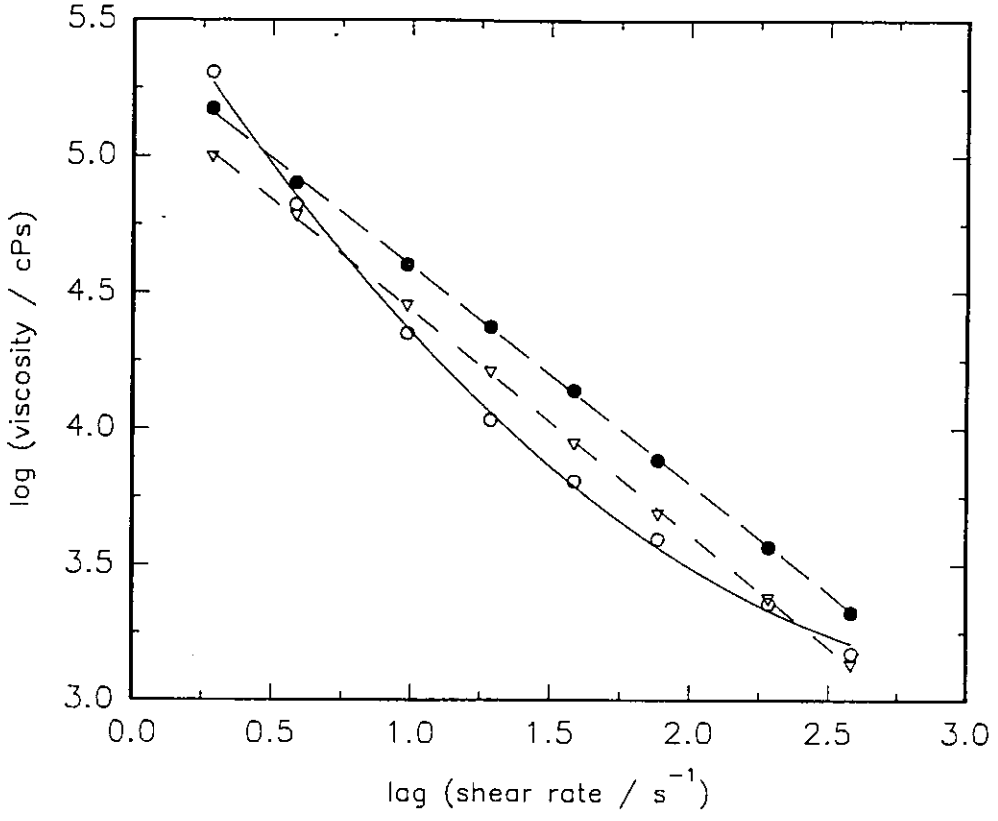

Figure 3.6 *Log_{10} of viscosity vs log_{10} of shear rate for paste number 4d. ○, mixed in pestle and mortar; ●, roll milled for 10 minutes; ▽, roll milled for 1 hour.*

prevent excessive flow during levelling. These criteria were satisfied by most of the pastes prepared.

Dispersed state of the pastes

Cassons equation, $\eta^{½} = \eta_{\infty}^{½} + \tau_0^{½}\,\dot{\gamma}^{½}$ (Eq. (1.15)), suggests that if the square root of viscosity is plotted against the reciprocal of the square root of the shear rate, a straight line should be obtained with an intercept of $\eta_{\infty}^{½}$ and slope of $\tau_0^{½}$. Depending upon the shear history of the paste, viscosity-shear rate data have been shown [151] to exhibit a varying value of $\tau_0^{½}$, and a common value of $\eta_{\infty}^{½}$ for well dispersed thixotropic materials. Flocculated (non-dispersed) materials show ill defined values of $\eta_{\infty}^{½}$. Such parameters can be used to identify a flocculated or dispersed state in a paste and its shelf stability. Figure 3.8 shows that pastes mixed in a pestle and mortar had a flocculated nature as a common value of $\eta_{\infty}^{½}$ was not

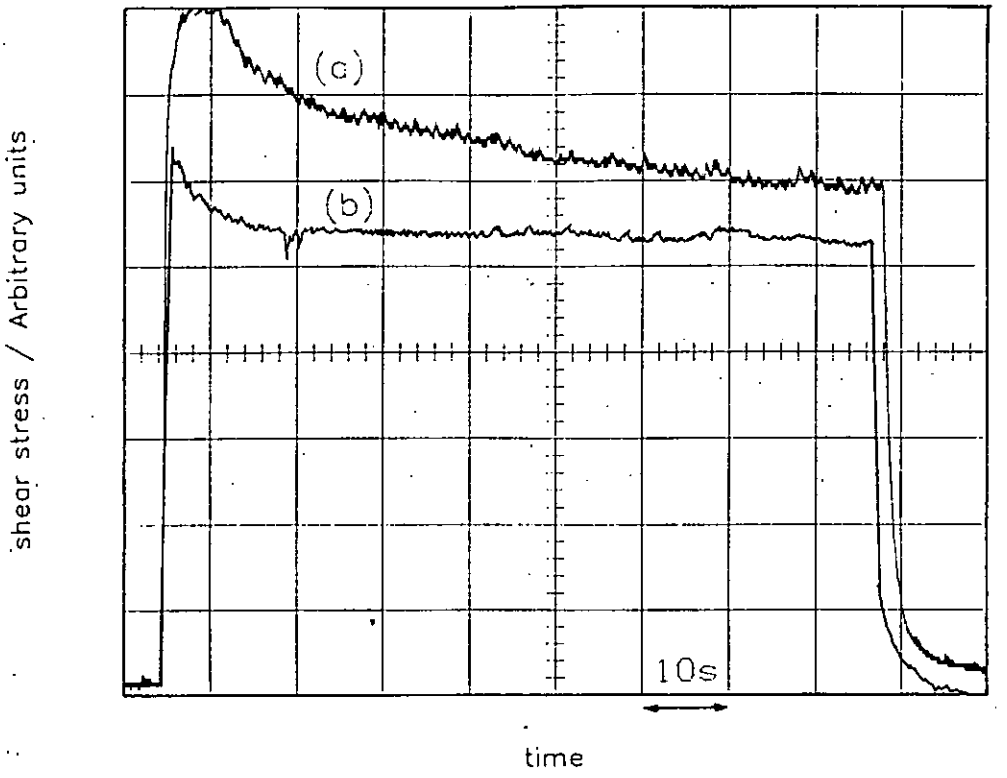

Figure 3.7 *Real time measurement of torque at a fixed shear rate for paste containing 40% wt 3Y zirconia and ESL 400 vehicle (a) mixed in a pestle and mortar, (b) roll milled for 1 hour.*

obtained between the agitated (sheared) and non-agitated (unsheared) pastes. Subsequent mixing of the paste for 30 minutes in a triple–roll mill showed a common value of η_{∞}^{*} between sheared and unsheared pastes confirming their well–dispersed state.

Figure 3.9 shows the relationship between solids loading and viscosity of the zirconia pastes made with ESL-400 screening vehicle; the use of this vehicle provided very good dispersion. Viscosities of the pastes, made by mixing in a pestle and mortar, were lower than those obtained after roll milling for all solid loadings. This was presumably because the vehicle was not uniformly mixed with the powder. The high shear action created by roll milling resulted in a more uniform mixing in the paste by dispersing the particles within the agglomerates.

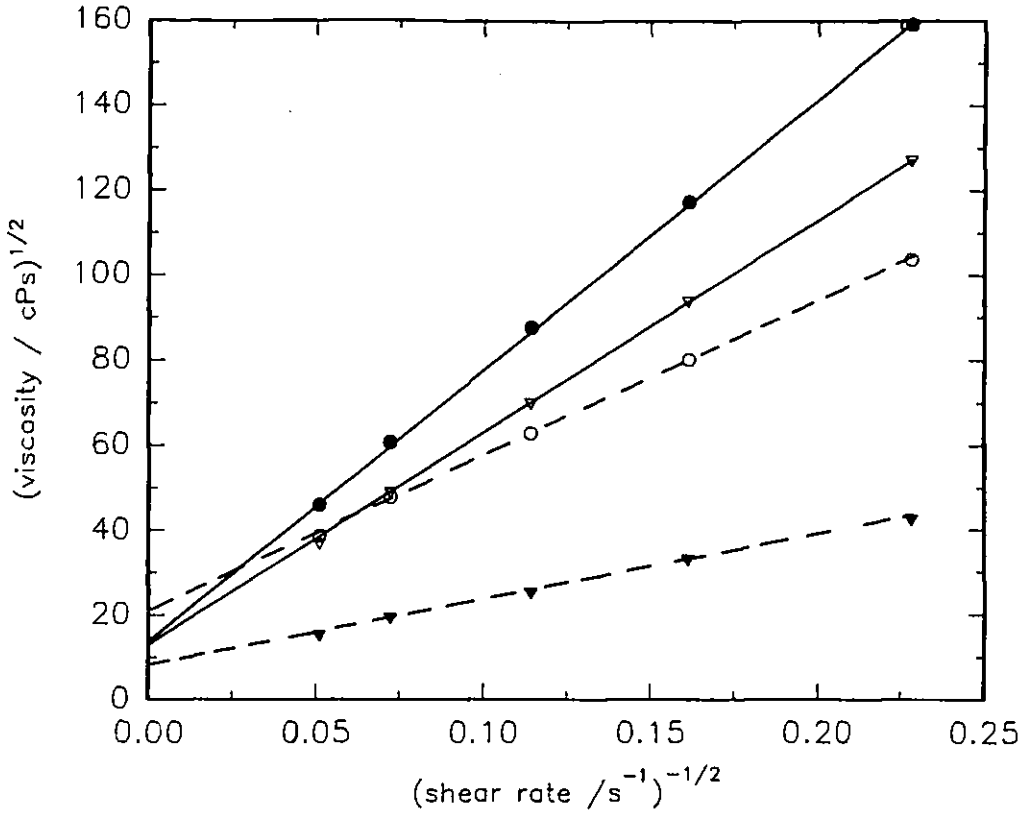

Figure 3.8 *Square root of (viscosity vs reciprocal shear rate). Paste mixed in pestle and mortar: ○,unsheared; ▽,sheared. Paste roll-milled: ●,unsheared; ▼,sheared.*

3.3.2.3 Printing and drying of the pastes

Attainment of the correct rheology of the zirconia pastes was an important factor in obtaining homogeneous green microstructures. Very viscous pastes did not allow the deposit to level sufficiently after deposition leaving the imprint of the mesh marks of the screen; this provided a source of film inhomogeneity. The printing of fairly viscous pastes was improved by using an etched metal mask screen. It was thought that the printing of viscous pastes would facilitate higher green densities of the dried deposits. However no such advantage was obtained. Very low viscosity pastes, on the other hand, slumped upon deposition losing film definition.

During storage minimal settlement or agglomeration of the particles held in suspension was desirable. Excessive (~70% and above) or insufficient (~40% and

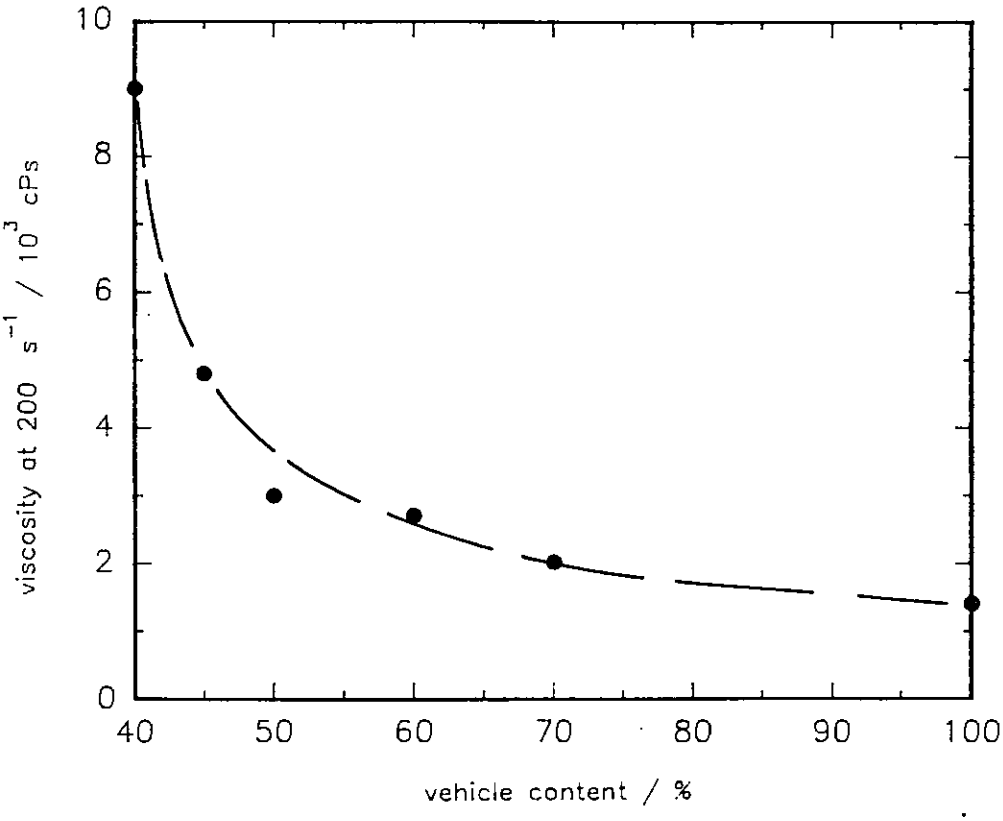

Figure 3.9 *Viscosity dependence with vehicle content (ESL 400) in the 3Y zirconia pastes after roll-milling for 1 hour.*

below) amounts of vehicle (ESL 400) in the pastes both resulted in an inhomogeneous mix and segregation of the solid and liquid phases upon storage. Such pastes could not easily be printed to defined patterns and severely agglomerated upon drying. The consistency of the composition and rheology of the paste were important for reproducible results.

The most desirable green microstructures were obtained with paste 4d, which contained 40% by weight solids in the paste as this provided optimum dispersion and an appropriate viscosity for a screen printing paste. Consequently this composition was selected for all further experimentation.

Air drying in a furnace particularly at high rates of temperature ramp, caused the surface of the deposit to become, at least in part, sealed against further removal of the vehicle. This resulted in a build up of gas pressure within the deposit which

disrupted the homogeneity of the green microstructure and caused the film to crack. Slow drying with the use of an infra-red drier produced the most homogeneous green bodies for a given paste. The infra-red heat source caused slow and homogeneous heating throughout the film and hence promoted homogeneous vehicle removal without sealing the surface.

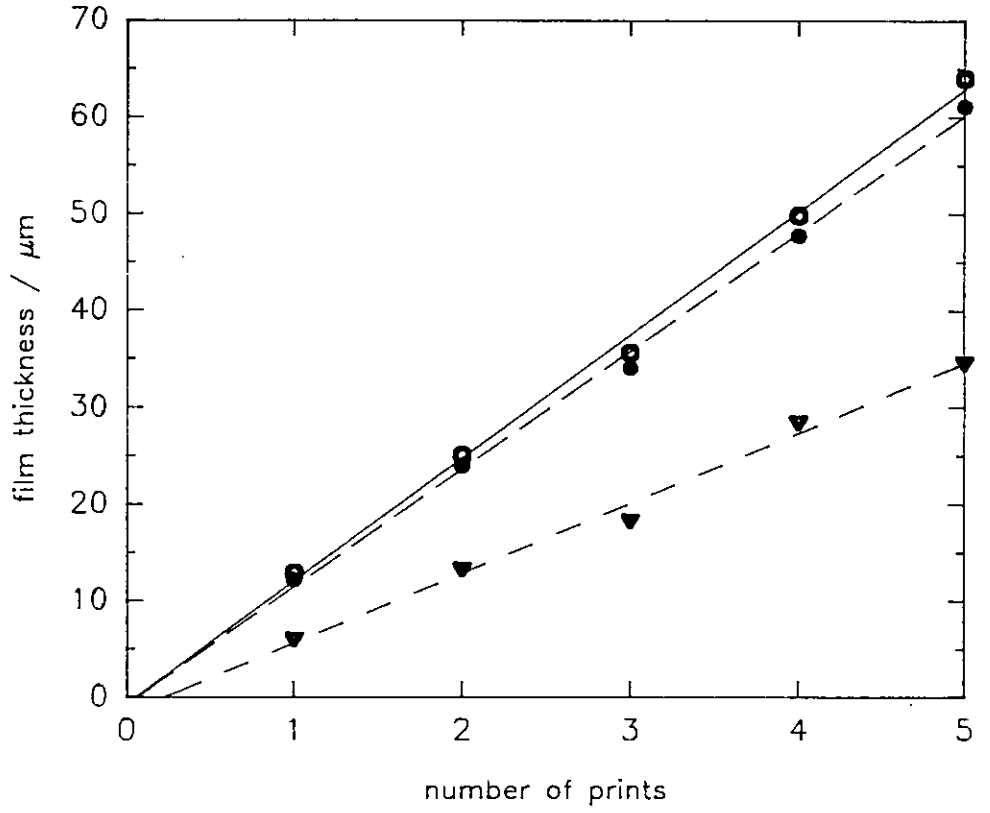

Figure 3.10 *Variation of dried deposit thickness with number of prints*: O; *mixed in pestle and mortar*, ●;*roll milled*, ▾;*following firing at 1400°C for 1 hour.*

Non-dispersed (after mixing in a pestle and mortar) and dispersed (after roll milling of the same paste) were printed onto 99.6% alumina substrates using paste 4d. A single screen and pattern were used under identical printing conditions and a number of successive print–dry cycles provided progressively thicker deposits; each successive print was dried for 10 minutes at 150°C, at 450°C and at 700°C. The deposit thickness was in direct proportion to the number of prints in both cases (Fig. 3.10) but the thickness of the resulting films was lower for the dispersed than the non-dispersed pastes. This is presumably due to the presence of agglomerates in the

latter pastes that create large pockets of porosity limiting the attainable density. These observations are consistent with those of Fennelly and Reed [169] who also achieved higher packing densities with well dispersed slurries.

A major advantage provided by the preparation of a paste with solids well–dispersed in a medium was that upon printing, the powder remained in this well–dispersed state. This aided packing of the deposit upon drying resulting in compact bodies of high density upon sintering as opposed to the sintering of a loose powder which did not form a unified body (§ 3.3.2.1).

3.3.2.4 Sintering

General observations

Screen printed materials are required to bond to the substrate upon sintering. Adhesion of the film to the substrate constrains the shrinkage during sintering to one dimension; it would be expected that this would result in strain in the plane of the deposit. If cracking is to be avoided it would seem that the adhesion force should become operative before the beginning of compaction by sintering. This force would need to be great enough during sintering in order to prevent the screened layer from becoming detached. A tendency to sinter in 3 dimensions caused the film to crack and peel off the substrate demonstrating the "cracked-mud" appearance of Fig. 3.11 (sintered at 1400°C for 1 hour; the ramp rate to the sintering temperature and back to room temperature was 30°C min^{-1}). There was a limit on the thickness of the films that could be produced by a single print-dry-sinter cycle without cracking and peeling from the substrate. An explanation for this could be that the thicker films had a greater tendency to sinter in 3 dimensions than did the thinner films. The part of the film adjacent to the substrate adhered sufficiently well to the substrate to be constrained from shrinking in the plane of the deposit; the free surface and the remainder of the film on the other hand, provided some unconstrained sintering. This caused cracking and localised bowing of the film with a consequent loss of adhesion.

The maximum thickness of a film (printed using a well-dispersed paste) which sintered without cracking after a single sintering cycle (irrespective of the number of print-dry cycles) was around 30 μm after sintering. Thicker deposits could be

(a)

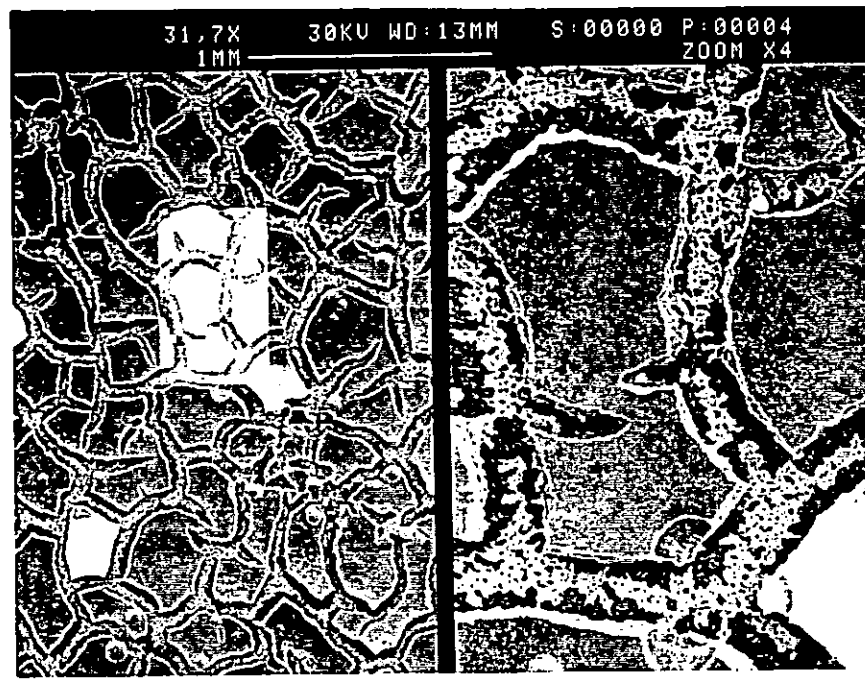

(b)

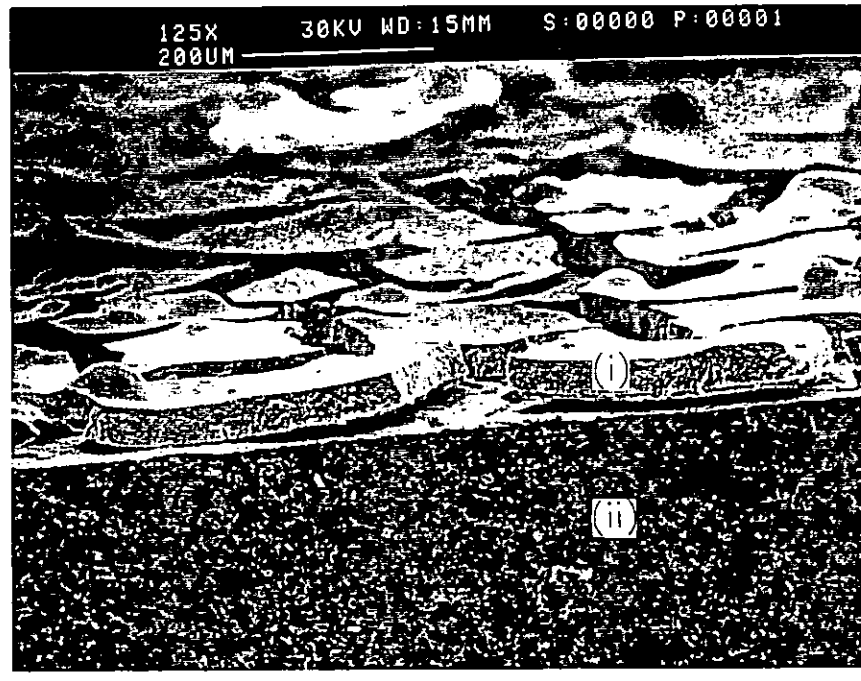

Figure 3.11 *(a) Top view and (b) perspective view of "cracked mud" appearance in a 3Y zirconia thick-film (shown as (i)) sintered on 96% alumina (shown as (ii)). The cursor length in (a) refers to the left half, the highlighted area on the left is shown to the right at fourfold magnification.*

produced by the successive print-dry-sinter of additional layers. The inter-adhesion of such layers was good but was not further investigated in this work. Crack-free

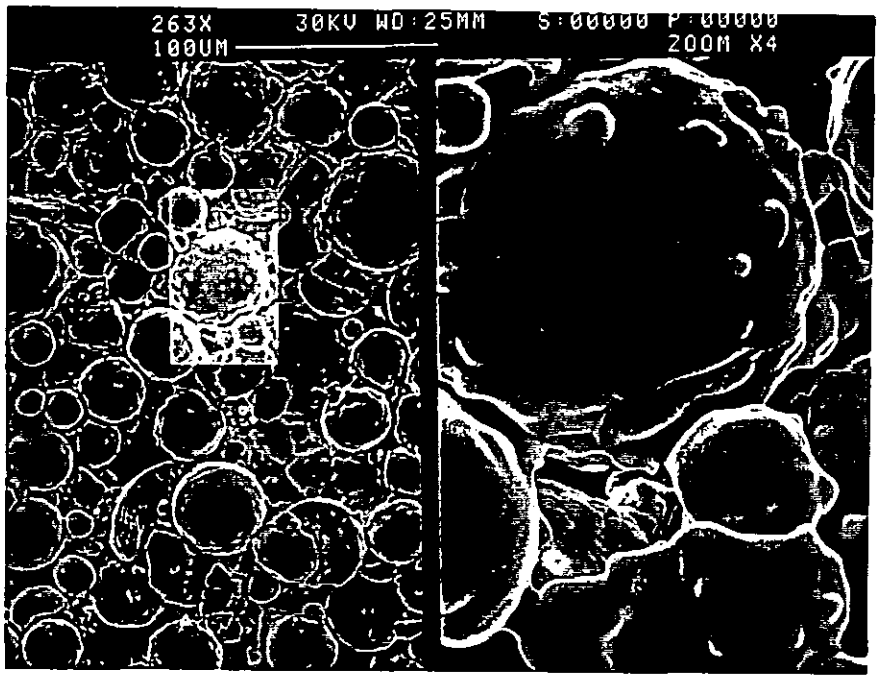

Figure 3.12 *Result of depositing a paste made of a powder presintered at 1400°C for 1 hour and subsequently firing at 1500°C for 1 hour. Cursor length shows the magnification.*

layers were more difficult to achieve as the green deposit became thicker. Firing of the as-received powders caused intra-agglomerate sintering producing strong aggregates. Pastes made with such aggregated powders were used to build up crack-free layers thicker than those possible using non-aggregated powders by reducing shrinkage and hence compaction forces upon sintering. Consequently the maximum deposited thickness producing crack-free layers was dependent upon the density of the green deposit. However such layers even though crack-free were highly porous (Fig. 3.12). These deposits were composed of sintered aggregates and pockets of porosity between these aggregates. The reduced surface free energy that presumably resulted from the larger particle size (resulting from sintering) of the aggregates meant that it was almost impossible to close the pores within such layers; this required excessively high treatment temperatures as further densification could only be achieved by particle growth [125].

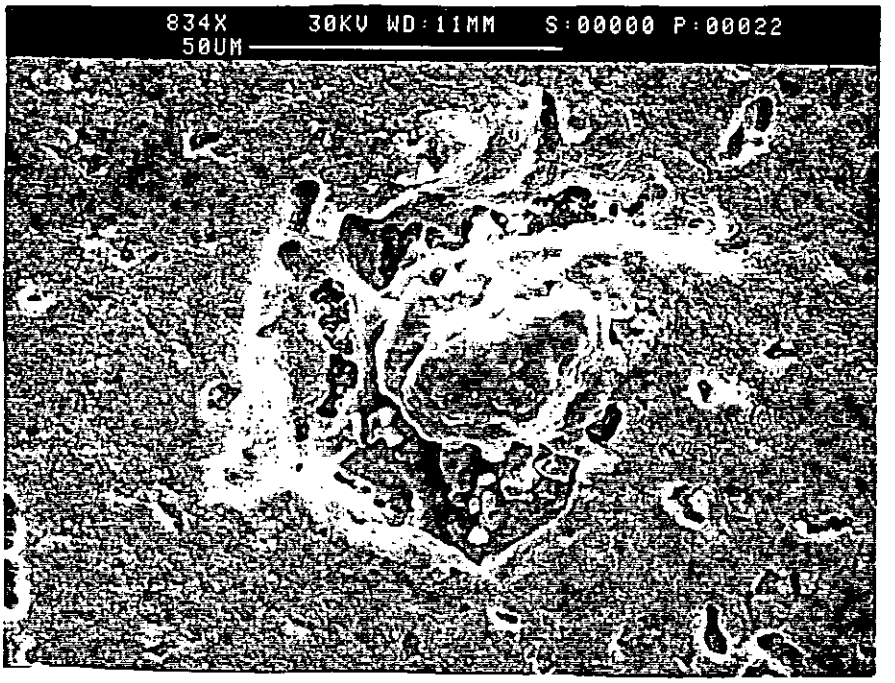

Figure 3.13 *Microstructural inhomogeneities after firing. The magnification is shown by the cursor length.*

Green microstructures obtained from pastes prepared by mixing the as–received powder with vehicle in a pestle and mortar showed cracking upon sintering. This is attributed to the existence of agglomerates in such pastes (§ 3.3.2.2) leading to the formation of rather strong aggregates during the sintering step [132] of the print–dry–sinter cycle; these agglomerates were not broken down during the mixing process and may have been the cause of the observed microstructural inhomogeneities during the firing process (Fig. 3.13). Porosity inhomogeneities were a source of inhomogeneous sintering providing coarse grained regions in the sintered compact. Hence the use of monosized and unagglomerated powders in the green deposit were important for producing films of low porosity.

Dried deposits heated rapidly (~10–50°C min^{-1}) to temperatures above 1400°C showed severe cracking. Defect-free layers were produced in two ways: these involved the use of slow ramp rates of 3°C min^{-1} to reach the sintering temperature

or prefiring of the deposit at a lower temperature such as 1100°C for one hour prior to the higher temperature sintering. Prochazka and Coble [170] were also able to avoid crack formation by prefiring at a temperature lower than the sintering temperature when sintering bulk alumina (it should be noted here that both alumina and zirconia sinter by a solid state diffusion process [171]). It is postulated that high temperature sintering caused rapid densification giving rise to stresses exceeding those of interparticle bonding. Prefiring at lower temperatures (lower than those resulting in cracking, ~1400°C) caused the interparticle necks to grow with time [170] and thus build up sufficient strength to overcome the stresses caused by fast densification rates at the higher temperatures, thus avoiding cracking. At a temperature of 1300°C the two competing processes may have been occurring at rates such that the size of the interparticle necks was sufficiently large to prevent cracking.

Fast ramp rates to the sintering temperature also caused temperature gradients within the film due to radiant heating of the film's surface. Temperature gradients were detrimental as regions at the higher temperatures sintered before the remainder creating stresses that disrupted the homogeneity of the green microstructure.

Influence of agglomerates

The agglomerate size of the as-received zirconia powders used (~110 μm) was larger than the dimensions of the thick–films produced (3–30 μm). Thick–film processing involves sintering under no external forces such as compaction; such forces can break up the agglomerates and hence reduce their effects during sintering. Therefore dispersion of the agglomerates within the paste was important as they have a more negative influence on the gas tightness of planar films than of bulk materials.

When the agglomerates were not totally dispersed prior to firing, then intra-agglomerate sintering formed aggregates so reducing the surface free energy of the compact and as a result required high sintering temperatures to remove pores between agglomerates. Lange and Metcalf [172] have reported that differential shrinkage brought about by various sized agglomerates having different bulk densities caused cracking in bulk ceramics. The same effects could explain cracking observed

upon sintering of films deposited using pastes that were not well dispersed.

Some obvious defects caused by large particle agglomerates that existed within the zirconia pastes were as follows. When the agglomerate size was similar to the deposit thickness, the evaporation of the carrier vehicle led to a decreased deposit thickness around the agglomerate but not within it resulting in a crack around the agglomerate. When agglomerates were buried within the film the air they contained expanded during the drying creating a defect in the film just above the agglomerate. The different densification rates of the agglomerates relative to the surrounding matrix caused them to pull away from the matrix, leaving a large pore where the agglomerate was partially detached from the matrix (Fig. 3.13) again resulting in a defect. The same effects have been observed in bulk ceramics [132,119]. This type of porosity was almost impossible to close due to the undesirably large co-ordination number of the pores. Large voids are thermodynamically stable and do not shrink during the firing process [118,173]. Large pockets of porosity also acted as critical flaws for fracture initiation.

It has been demonstrated in this work that no advantages can be gained by partial sintering of the agglomerated powder prior to deposition and further sintering if the requirement is a film of very low porosity. The higher the pre-baking temperature of the powder, the lower its surface free energy will be thus reducing the driving force for sintering. Consequently, higher temperatures are then required for further densification. In the inter-agglomerate pore region a critical pore size exists that defines the transition from convex to concave surfaces. In general, surfaces tend to move toward their centre of curvature; thus pores with convex surfaces tended to grow.

Summary of requirements for obtaining low porosity zirconia thick-films.

1. Powders should be mixed with a viscous organic binder system in a triple roll-mill to produce a homogeneous paste of the appropriate viscosity and solids content to hold the powders in an unagglomerated state.
2. The paste should be printed under conditions enabling it to settle and smooth out,

and allowed to do so after printing.

3. Drying should be carried out with an infra-red drier using a selected slow drying procedure. (The powder, should now be completely de-agglomerated and thus ready for the firing procedure).

4. Firing temperatures must be achieved using a slow ramp rate ($-<3°C^{-1}$) or a low temperature firing (e.g. ~1100°C for 30 minutes) should first be given prior to the final high temperature firing.

3.3.3 Characterisation of sintered zirconia thick films printed on alumina substrates

3.3.3.1 Microstructural observations

Zirconia thick-films were screen-printed onto alumina substrates and fired for one hour in the temperature range 1300–1550°C. The effects described below were observed at temperatures of 1400°C and above and have been summarised in a recent publication [174].

The microstructure of a zirconia (Toyo-Soda, 3Y) film printed onto a substrate of 96% alumina with a partially intervening layer of platinum (5 μm thick) is shown in Fig. 3.14. A marked difference in zirconia grain size is apparent between that printed directly onto the alumina and that printed over the platinum. The same effects were also observed when platinum-zirconia cermets (with platinum contents as low as 55% by volume) were substituted for the platinum layer. It seemed that platinum was in some way inhibiting grain growth.

The fracture edges of zirconia films of various thicknesses on 96% alumina substrates are shown in Fig. 3.15. Clearly grain growth in this case increased as film thickness decreased. A possible explanation here was that the grain size difference was the result of differing sintering constraints within films of varying thickness: thinner films may have been differently constrained during mono-dimensional sintering due to adhesion with the substrate. A model has been described by Scherer and Garino [175] which predicts a decrease in the densification rate of constrained films, the decrease being proportional to the stress that develops. Alternatively, contamination by components of the substrate may have been responsible for the accelerated grain growth effect.

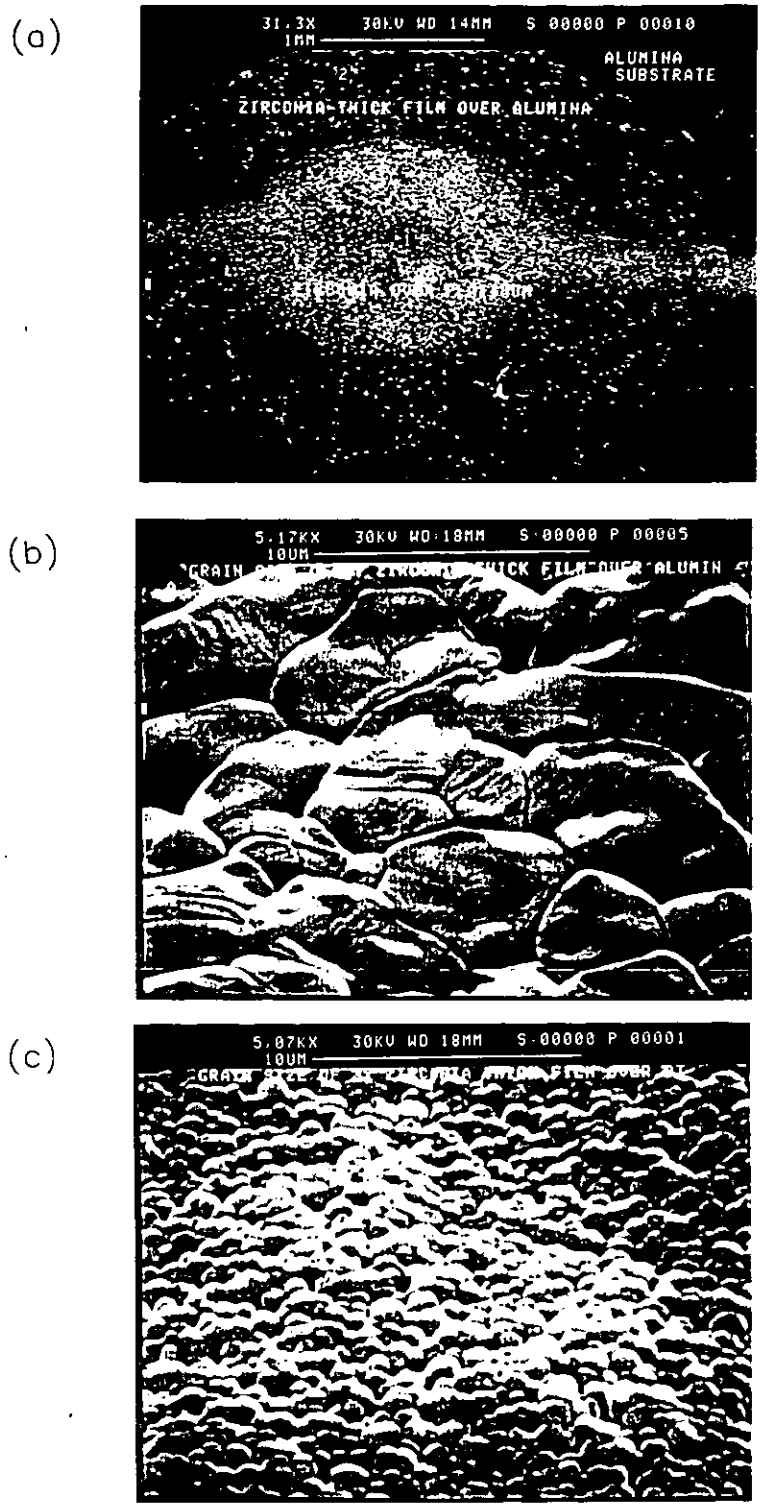

Figure 3.14 *Microstructure of a 3Y zirconia thick–film printed over a platinum layer residing onto 96% alumina. Cursor lengths show the magnifications. (a) Zirconia over platinum and alumina, (b) Zirconia over alumina only, (c) Zirconia over platinum.*

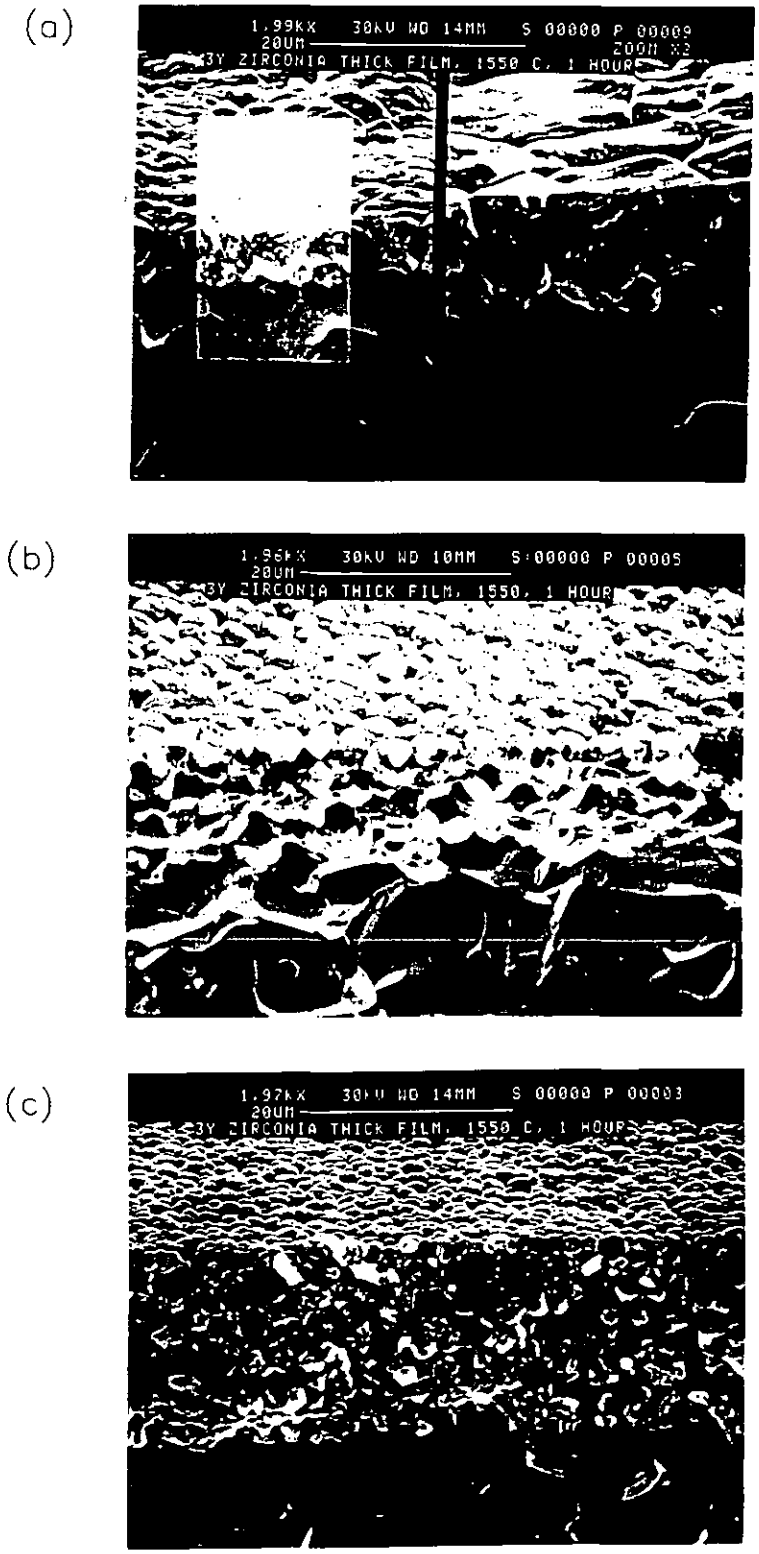

Figure 3.15 *Fracture edge of 3Y zirconia thick-films of various thicknesses fired at 1550°C for 1 hour on 96% alumina. The zirconia and alumina layers are clearly distinct with the zirconia in the upper half of each micrograph. The cursor length in (a) refers to the left half. The highlighted area is shown to the right at double magnification.*

(a)

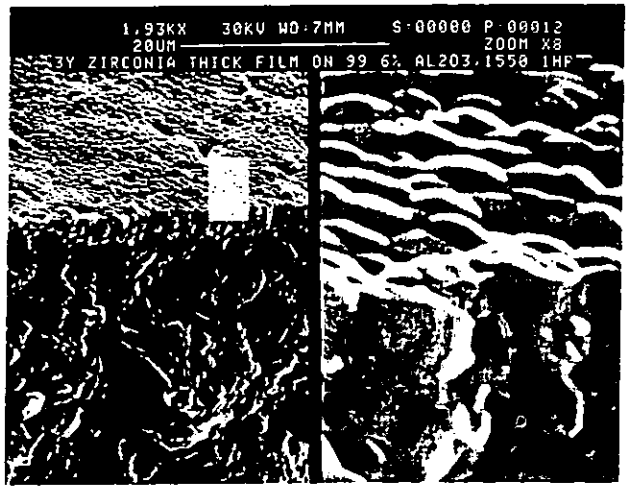

(b)

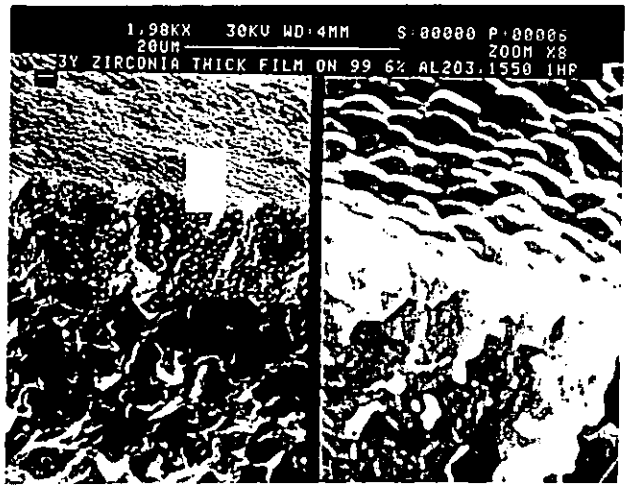

Figure 3.16 *Fracture edge of 3Y zirconia thick-films of two thicknesses fired at 1550°C for 1 hour on 99.6% alumina. The cursor length refers to the left half. The highlighted area is shown to the right at eightfold magnification.*

The latter possibility was investigated by repeating the work with films of various thicknesses on higher purity substrates (99.6% alumina). The results shown in Fig. 3.16 demonstrate no dissimilar grain growth in this case.

Clearly the variations in grain growth were primarily related to the purity of the alumina. The compositions of the substrates are shown in Table 2.1 (§ 2.2.4). Substrate impurities were mainly silica and calcia, added to aid sintering and densification of the alumina. On 99.6% alumina the zirconia grain size remained small in comparison with films on 96% alumina. Clearly the high temperatures required to sinter the zirconia resulted in diffusion of impurities into the thick film and these accelerated grain growth. The uniformity of grain size in a given film indicates uniform distribution of impurities and rapid diffusion in the zirconia. Thicker ceramic layers had a lower impurity concentration and hence slower grain growth.

The result in Fig. 3.14 can now be understood. The presence of the platinum layer impeded the transfer of impurities into the zirconia thick film. The resulting oxide grain size over the platinum layer was similar to that observed when the film was sintered on 99.6% alumina. As the platinum film was porous this suggests that impurity transport from the substrate to the zirconia thick film probably did not occur via the gas phase.

The use of zirconia 8Y powder to prepare films (on both 96 and 99.6% alumina) in the same way to that already described resulted in films of high porosity as seen in Fig. 3.17. Such films also had a tendency to crumble following sintering treatment at 1400°C and above. Because of the previously mentioned effects, films made using the 8Y zirconia were not investigated in further detail. Scanning electron micrographs showed a segregated phase located at the alumina–zirconia interface (Fig. 3.17a). Energy dispersive X-ray analysis has revealed this segregated phase to be yttria–rich. Further work is necessary to establish the nature and cause of the segregated phase observed for the 8Y (made by Toyo-Soda) zirconia films on 96% and 99.6% alumina.

(a)

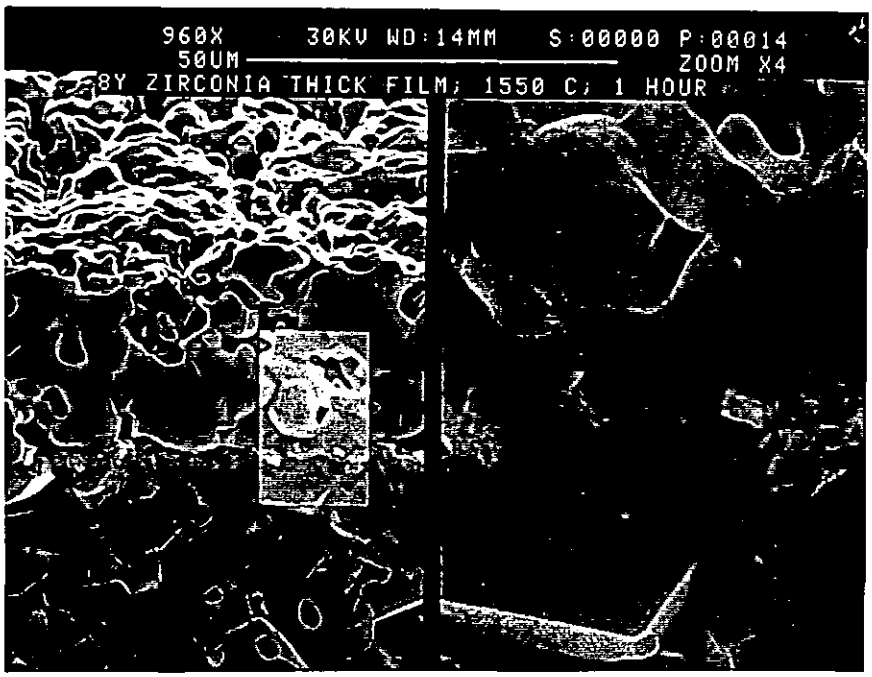

(b)

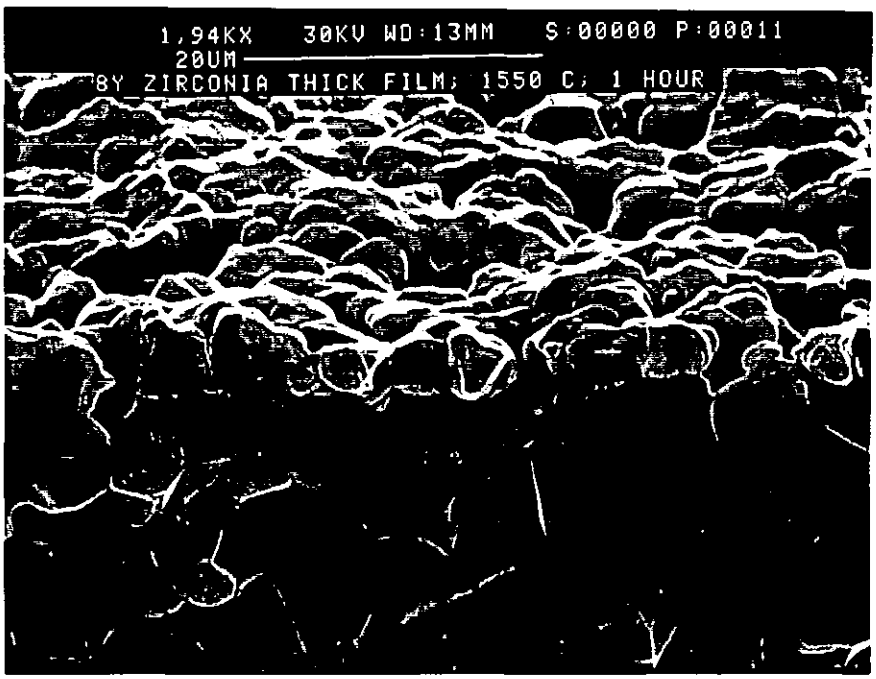

Figure 3.17 *8Y sintered zirconia thick-films of two thicknesses fired at 1550°C for 1 hour on 96% alimina showing their porous nature. The cursor length shown in (a) refers to the left half. The highlighted area to the left in (a) is shown to the right at fourfold magnification to highlight the segregated phase.*

3.3.3.2 X-ray diffraction studies

The X-ray diffractometer traces obtained for the as received 3Y powder (Fig. 3.18) and for the printed and dried films (Fig. 3.19a) are in agreement with spectra reported in the literature for both the powder [176] and for the bulk solid [177,178]. The (111) tetragonal peak showed the highest intensity. Further, the measured value of the "d" spacing of the tetragonal (111) peak was 0.2953 nm, and can be compared with the range 0.2947 to 0.2946 nm reported in the literature [178,176]. Inspection of the peaks did not indicate the presence of cubic phase [179]. There were no peaks present that could be assigned to the monoclinic phase, hence the films were composed almost entirely of tetragonal phase at this stage.

The samples sintered at 1300°C on 96% alumina retained their original structure as the X-ray diffraction patterns were similar to those measured previously on the unsintered zirconia film and powder (Fig. 3.19b). When fired at 1500°C on 96% alumina (Fig. 3.19c) significant changes were observed which indicate that in this case the sample was mainly composed of the monoclinic phase: with reference to Fig. 3.19a it is clearly seen that the strongest peak of the tetragonal phase (at 2θ = ~30.5°) had disappeared. This was associated with the appearance of new peaks at 2θ values of 28.3° and 31.7° relating to the presence of ($11\bar{1}$) and (111) monoclinic planes respectively. Firing at 1500°C on 99.6% alumina did not show the t→m transformation shown by the films fired on 96% alumina (compare figures 3.19b and 3.19c).

An indication of the volume fraction of monoclinic phase present, V_m, was obtained using Eq. (3.1) (§ 3.2.3). The percentage tetragonal phase retained in the film ($1-V_m$) as a function of firing temperature for 3Y zirconia thick-films of similar thickness (6±0.2 μm) sintered on substrates containing nominally 96 and 99.6% alumina is shown in Fig. 3.20. Films sintered on the purer substrate retained over 95% of the tetragonal phase when sintered up to 1600°C. Films sintered on the less pure alumina began to show a transformation to the monoclinic phase when fired at temperatures above 1300°C and were almost completely transformed to monoclinic when fired at 1600°C. The effect of zirconia film thickness when fired at 1400°C for 1 hour is shown in Fig. 3.21. Films sintered on 99.6% alumina were composed of a

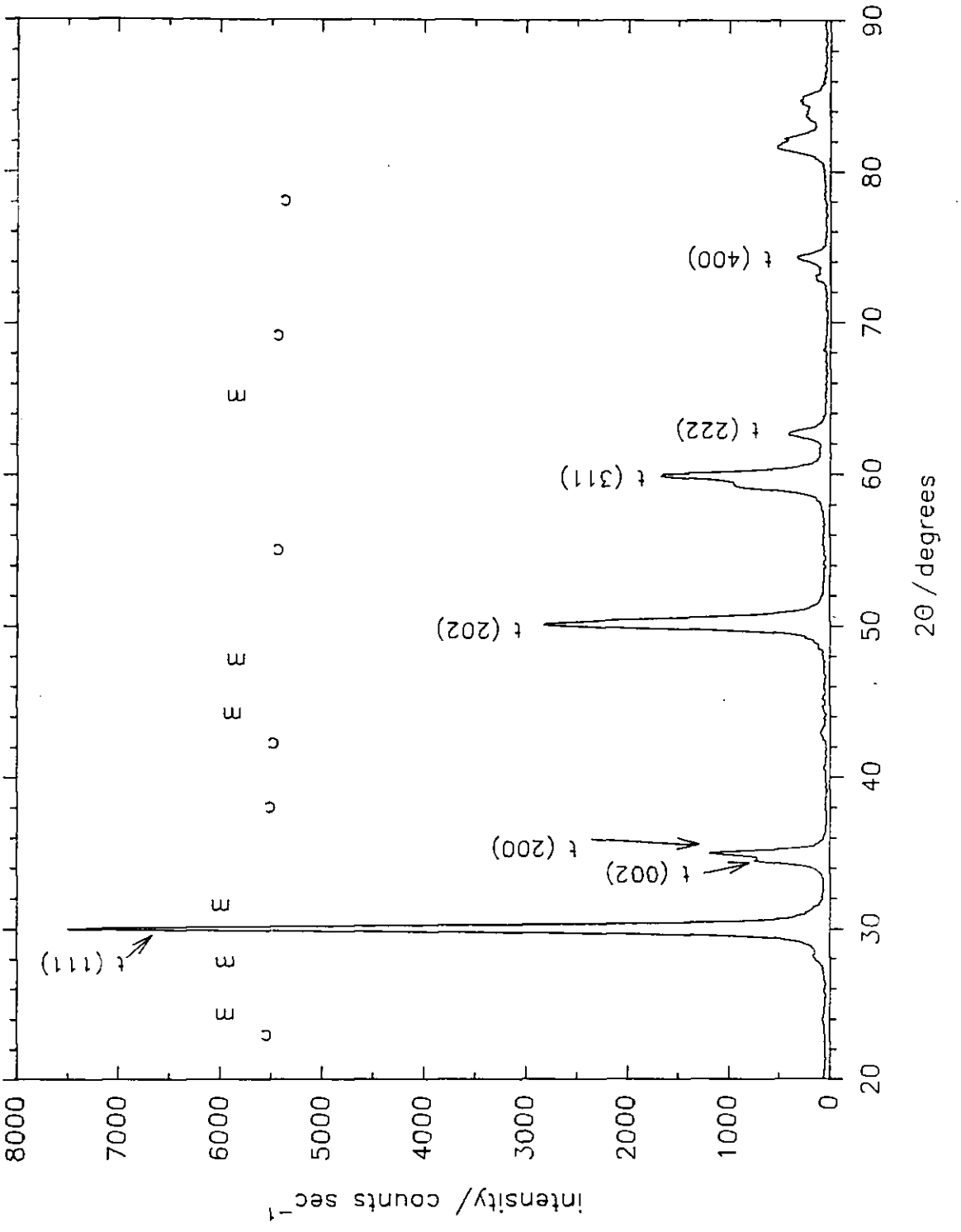

Figure 3.18 *X-ray diffractometer trace of as received 3Y zirconia powder. Also shown are the reported peak positions for cubic, tetragonal and monoclinic phases (c, t and m respectively).*

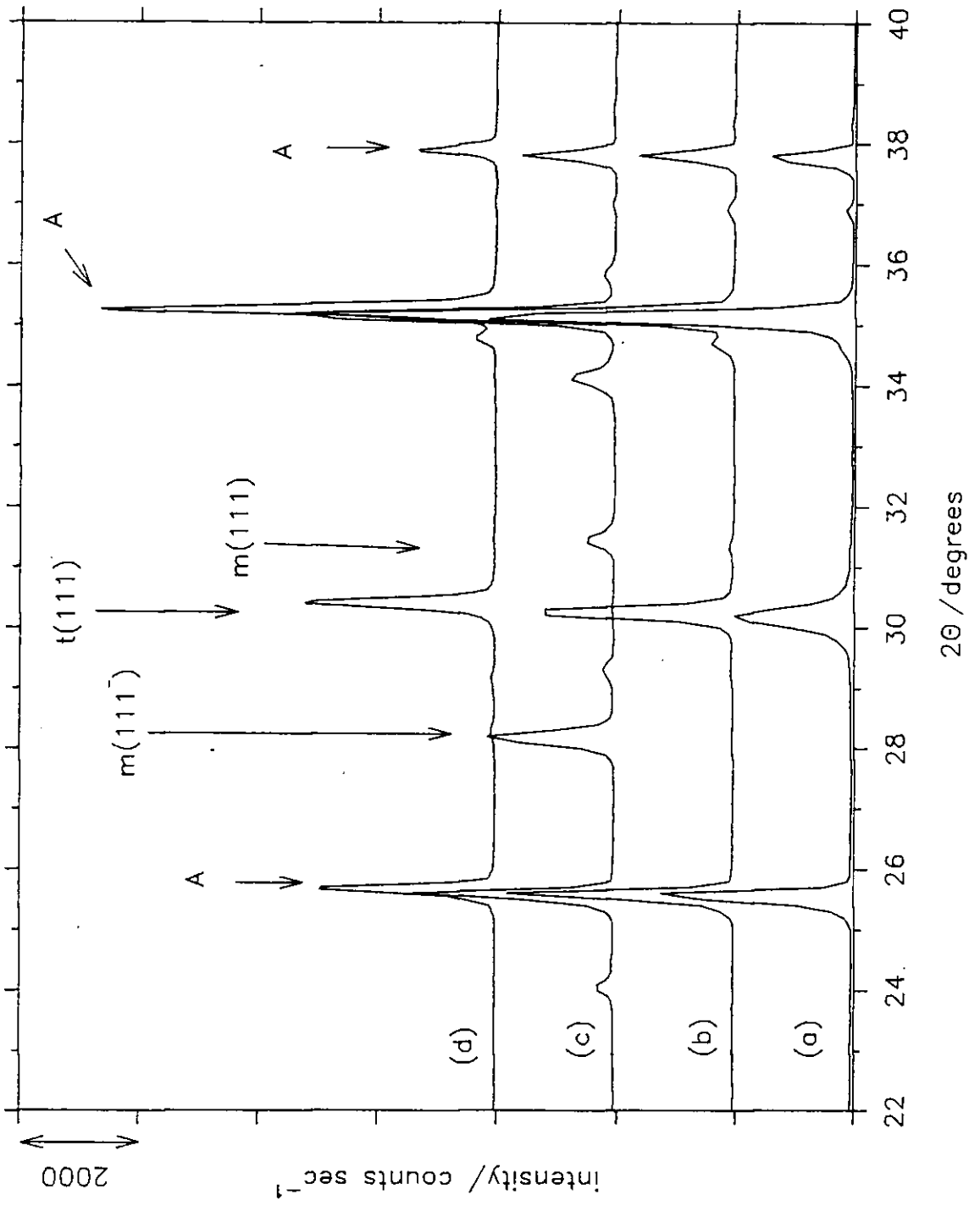

Figure 3.19 *X-ray diffractometer trace of 3Y zirconia thick-films deposited onto alumina substrates. Also shown are the relevant peak positions relating to the tetragonal and monoclinic phases (c and m respectively). Peaks marked A relate to the alumina substrate. (a) printed and dried film on 96% alumina (b) zirconia thick-film fired at 1300°C for 1 hour on 96% alumina, and zirconia thick-films fired at 1500°C for 1 hour on (c) 96% and (d) on 99.6% alumina.*

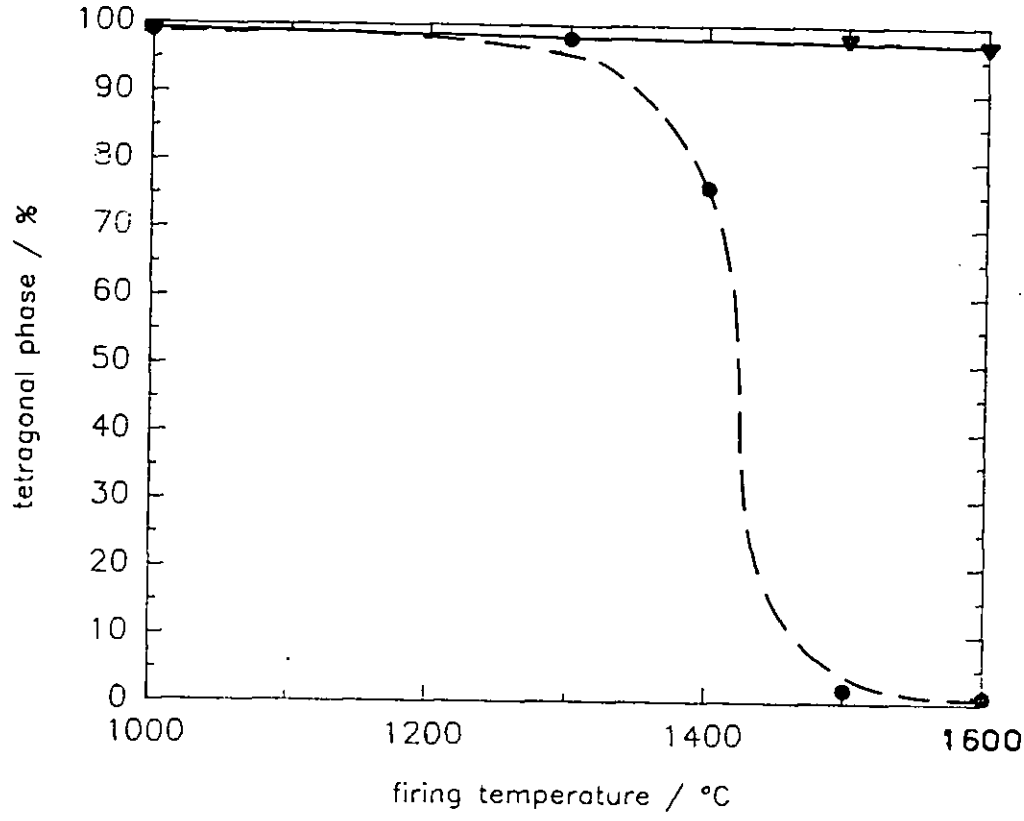

Figure 3.20 *Effect of firing temperature on the amount of tetragonal phase retained in 6μm thick 3Y zirconia thick-films fired on ●, 96% and ▾, 99.6% alumina.*

high fraction of tetragonal phase (above 95%) and showed little influence on film thickness. In comparison films sintered on the less pure alumina showed a marked dependence of the monoclinic content as the film thickness decreased below ~6 μm. It can be concluded that the observed transformation of the tetragonal to monoclinic phase observed in zirconia films sintered on 96% alumina, was primarily related to impurity diffusion from the substrate into the zirconia film. These impurities, which accelerated grain growth, caused the grain size to exceed the critical value in the region of 0.3 - 0.45 μm (Fig. 3.15); it has been reported that a value above this induces the tetragonal→monoclinic (t→m) transformation in 3 mol% Y_2O_3–ZrO_2 [88]. The sharp transition of t→m phase in zirconia films sintered on 96% alumina, evident in figures 3.20 and 3.21, was due to the uniformity of the grain size (Fig. 3.15).

Films sintered on 99.6% alumina did not show an accelerated grain growth effect

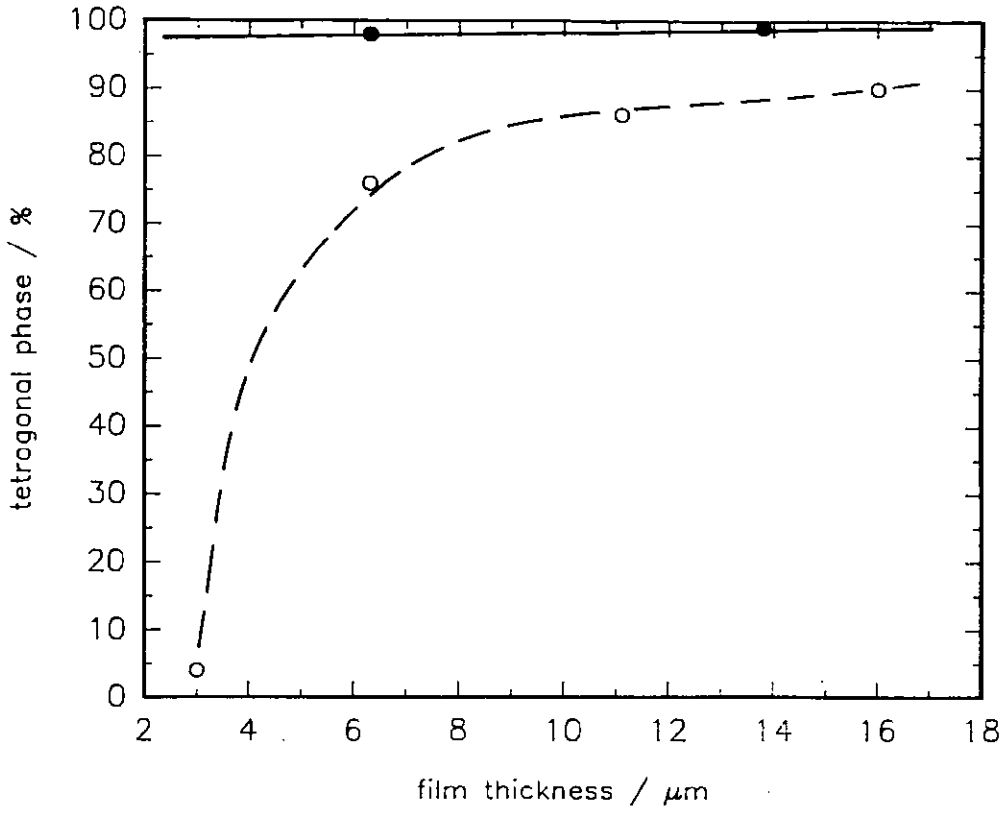

Figure 3.21 *Effect of film thickness on the amount of tetragonal phase retained in 3Y zirconia thick-films fired at 1400°C for 1 hour on* O*; 96% and* ●*; 99.6% alumina substrates.*

(Fig. 3.16) and it is for this reason that they retained the tetragonal phase. By studying the ageing behaviour of 2.3% mol% Y_2O_3–ZrO_2 with varying silica content Lange *et al* [180] concluded that the glassy phase did not play a major role in the degradation of TZP materials. This indicates that, although the glassy impurities caused the accelerated grain growth effect, it was not these impurities, but the grains exceeding a critical size that caused the t→m transformation.

The thermal expansion mismatch between the alumina substrate (8 x10^{-6} °C^{-1}) and the zirconia (10-11 x10^{-6} °C^{-1} [181]) causes a well-adhered film to be under tensile stress upon cooling from the sintering temperature. The difference in volume shrinkage when cooled from 1400°C to room temperature (taking a linear thermal expansion coefficient for zirconia of 10.5 x10^{-6} °C^{-1}) is ~0.35% in a linear dimension. Where a t→m transformation occurs in the thick film this induces a

volume expansion of ~3% [82] i.e a linear expansion of ~1%; this would act to relieve the tensile forces induced by the thermal expansion mismatch. Furthermore the transformation would not take place until the film had cooled below 1170°C [82]. It is interesting that on cooling from the sintering temperature the tensile forces in the film progressively increase until 1170°C where the t→m transformation (if it occurs) causes the film to be under compressive forces which are gradually alleviated with further cooling. This assumes complete transformation (t→m) of the film.

3.3.3.3 Electrical properties

General

The frequency dispersion measurements were analyzed using the equivalent circuit in Fig. 3.22a [162]. Generally complex impedance plane plots of polycrystalline solid ionic conductors show three semicircular arcs corresponding to grain interior, grain boundary and electrode interfaces [182]. The complete diagram is given in Fig. 3.22b. Arcs on typical complex plane impedance plots (Fig. 3.23) were attributed to the grain interior (GI), grain boundary (GB) and electrode (El) (compare figures 3.22b and 3.23). In order of decreasing frequency these plots show a very small (non-existent in some cases) GI arc, a large GB arc and an El arc which extends below the frequency range employed. It is of interest to note that the existence of the electrode arc suggests that the conductivity in the films was essentially ionic (in agreement with previous measurements on pure tetragonal zirconia [183,184]). The relevant conductivity (σ) and capacitance (C) data were calculated for each arc according to the following relations:

$$\sigma_{GI} = 1/\rho_1 \tag{3.3}$$

$$\sigma_{GB} = 1/(\rho_2-\rho_1) \tag{3.4}$$

$$C_{GB} = \frac{1}{(\rho_2-\rho_1)\,\omega_2} \tag{3.5}$$

$$C_{GI} = \frac{1}{\rho_1\,\omega_1} \tag{3.6}$$

where the frequency $\omega = 2\pi f$ (at the zenith of the semicircle) and ρ is the resistivity (estimated from the interceptions of the arcs in the real axis). Capacitance values

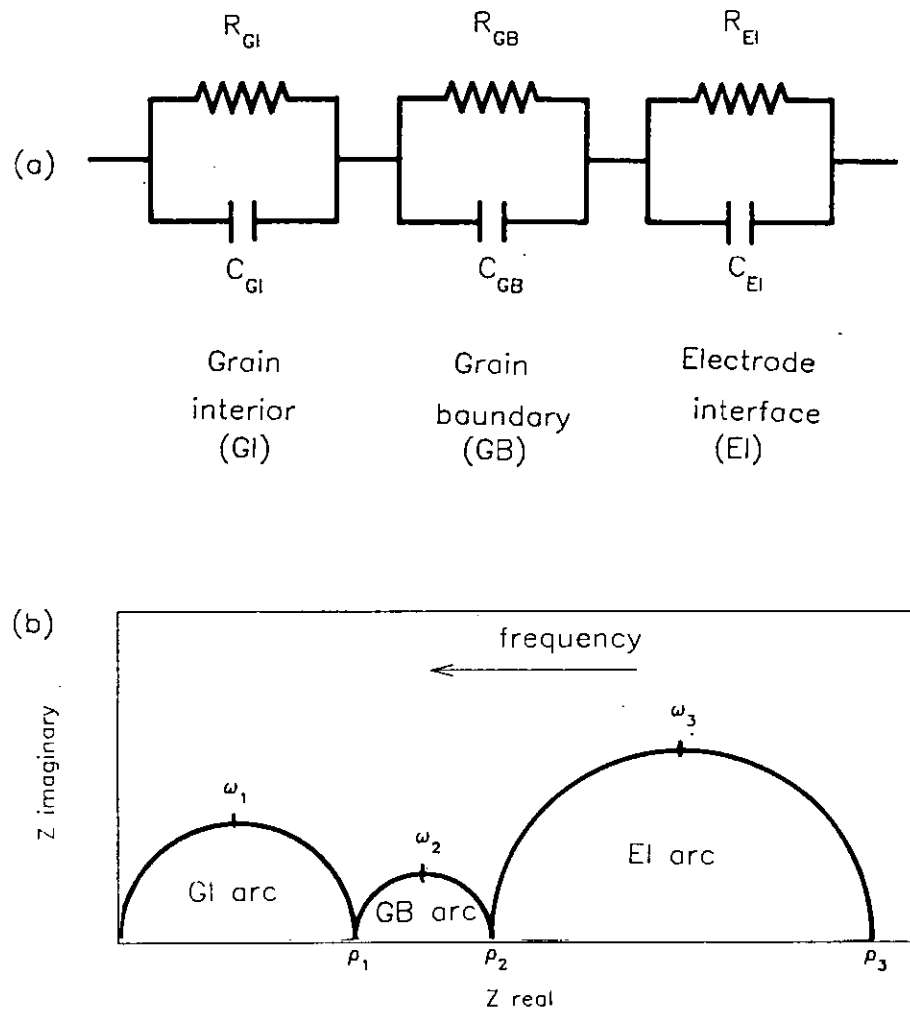

Figure 3.22 *(a) Equivalent circuit used for analysis of AC impedance plots, (b) Idealised complex plane impedance plot for zirconia electrolytes.*

were in accordance to those measured by other investigators [165] i.e GI ≈ $1x10^{-12}$ F, and GB ≈ $1x10^{-8}$ F. Arcs due to GI and GB were not modified by changes in the oxygen concentration whereas the semicircle related to the electrode was, as expected. At 600°C and above (Fig. 3.23), the resistance attributed to the GI for conduction in the plane of the film became an insignificant part of the total resistivity; the resistance was principally due to the grain boundaries. Differences in the specific area of the grain boundary within the zirconia films (arising from differences in the grain size of the films) were expected to influence the value of the grain boundary (GB) conductivity. For a given GB structure the resistivity of the GB should be inversely proportional to the grain size according to the "brick-layer"

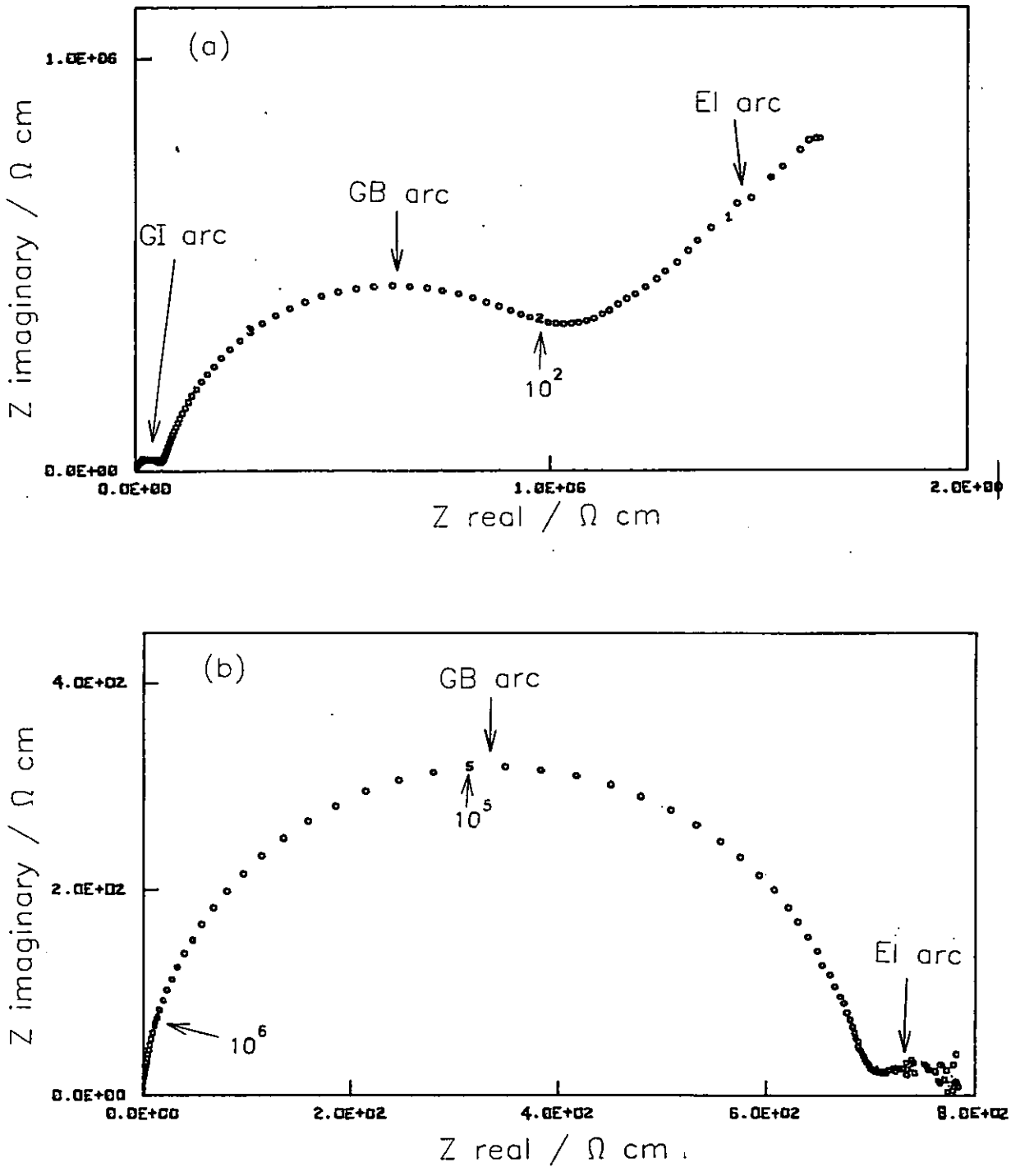

Figure 3.23 *(a) Typical impedance plot obtained for 3Y zirconia films for conduction (a) perpendicular to the plane of the film at 325°C, (b) along the plane of the film at 650°C. Films were sintered at 1400°C for 1 hour on 99.6% alumina. Numbers in powers of 10 denote the frequency in Hz.*

microstructural model [185].

In contrast to the well established behaviour of fully stabilised zirconia (FSZ) the activation energies (E_A) for σ_{GI} and σ_{GB} are not the same for tetragonal zirconia (TZP) [165]. Bonanos *et al* [165] have reported activation energies for σ_{GI} in the range 0.92-0.98 eV and for σ_{GB} in the range of 1.09-1.12 eV (note that 1 eV = 96.485 kJ mol^{-1}).

The conductivity data reported below are the total conductivity σ_T of the ceramic which was derived from the intersection of the grain boundary and electrode arcs (i.e $\sigma_T = (\sigma_{GB} + \sigma_{GI}) = 1/\rho_2$)

Comparison of ionic conductivities measured transversely across the thickness and perpendicular to the plane of the films

It has been reported [182] that as a rule, the observable range shifts from the left (high frequency) to the right (low frequency) of the complex resistivity diagram as the temperature of the sample increases. The high transverse resistance resulting from a high aspect ratio and the limited frequency range of the impedance analyzer meant that conductivity values could not be obtained at low temperatures (typically below 400°C) for conduction in the plane of the film. This was in contrast with measurements made perpendicular to the plane of the films where measurements were made down to 250°C.

A comparison of the ionic conductivities measured *across the plane* (*AP*) and those measured *perpendicular to the plane* (*PP*), of films fired at 1400°C for 1 hour on 99.6% alumina is shown in Fig. 3.24; values measured across the plane were lower by a factor of ~5. The differences in conductivity were too great to be explained by errors in the measurement of the film thickness and electrode area. Significant alterations to the effective film thickness by diffusion of platinum into the zirconia film during co-firing the electrodes with the zirconia layer was not observed (Fig. 5.4, § 5.4.2). Therefore the disagreement was probably due to differences in the extent of sintering of the films. Microstructural studies (§ 3.3.3.1) revealed a smaller grain size of the sintered zirconia when an intervening platinum layer separated it

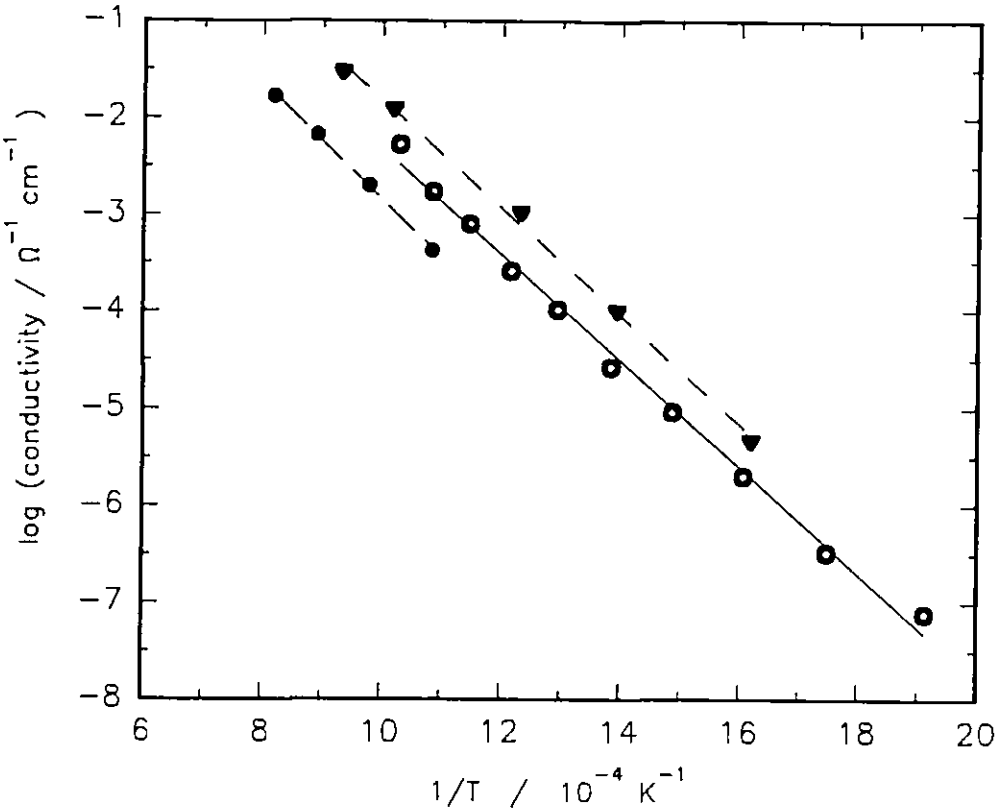

Figure 3.24 *Comparison of total ionic conductivities (measured at 800°C) of 3Y zirconia thick-films fired at 1400°C for 1 hour on 99.6% alumina, ●, measured across the plane of the films, O, perpendicular to the plane of the films, ▾, 3Y zirconia wafer (300μm thick) sintered at 1400°C.*

from the substrate (as was the case when measurements were made *PP*) than without the intervening layer (as was the case when making measurements *AP*). It was shown (Fig. 3.23) that the major contribution to the resistance of the films was related to the grain boundaries. Thus the increased area of grain boundaries per unit volume due to the smaller grain size of films used for *PP* measurements were expected to result in lower ionic conductivities in the zirconia than when measuring *AP*; however the converse was true (Fig. 3.24). This discrepancy may be because the intervening platinum layer present in films whose conductivity was measured *PP*, impeded diffusion of substrate and / or substrate impurities into the zirconia film. It has previously been shown that impurities such as silica tend to locate at grain boundaries and raise the GB resistance [186].

The ionic conductivity measured perpendicular to the plane of the zirconia thick-film sintered on 99.6% alumina was approximately half that measured for a 300 μm thick 3Y zirconia disc (Fig. 3.24). This discrepancy may have been due to porosity in the printed films resulting in tortuosity of the ionic conduction path.

Effect of sintering temperature, substrate composition and film thickness

The ionic conductivity data reported below were obtained from measurements made transversely across the surface of the film as shown in Fig. 3.1.

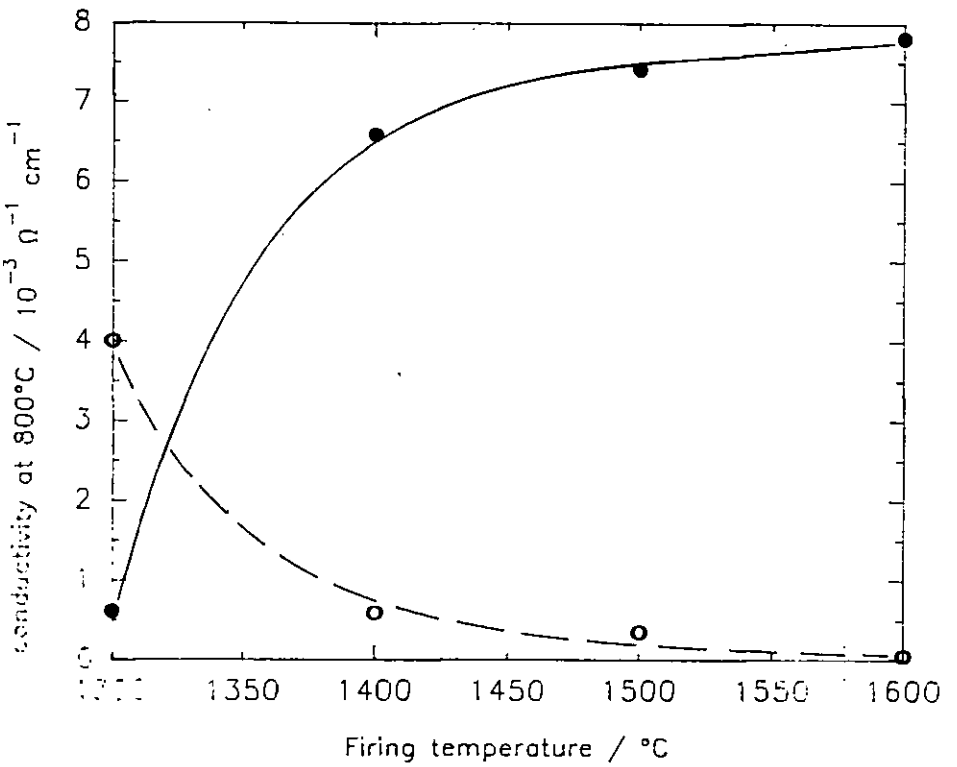

Figure 3.25 *Effect of firing temperature (held for 1 hour) on the ionic conductivities (measured at 800°C) of 6μm thick 3Y zirconia thick-films on:* O,*96% and* ●, *99.6% alumina substrates.*

The effect of sintering temperature on the ionic conductivities of 3Y zirconia thick-films is shown in Fig. 3.25. Films sintered on 99.6% alumina showed a sharp conductivity increase as the firing temperature was increased from 1300°C to 1400°C and a much smaller increase between 1400°C and 1500°C. Furthermore, for films

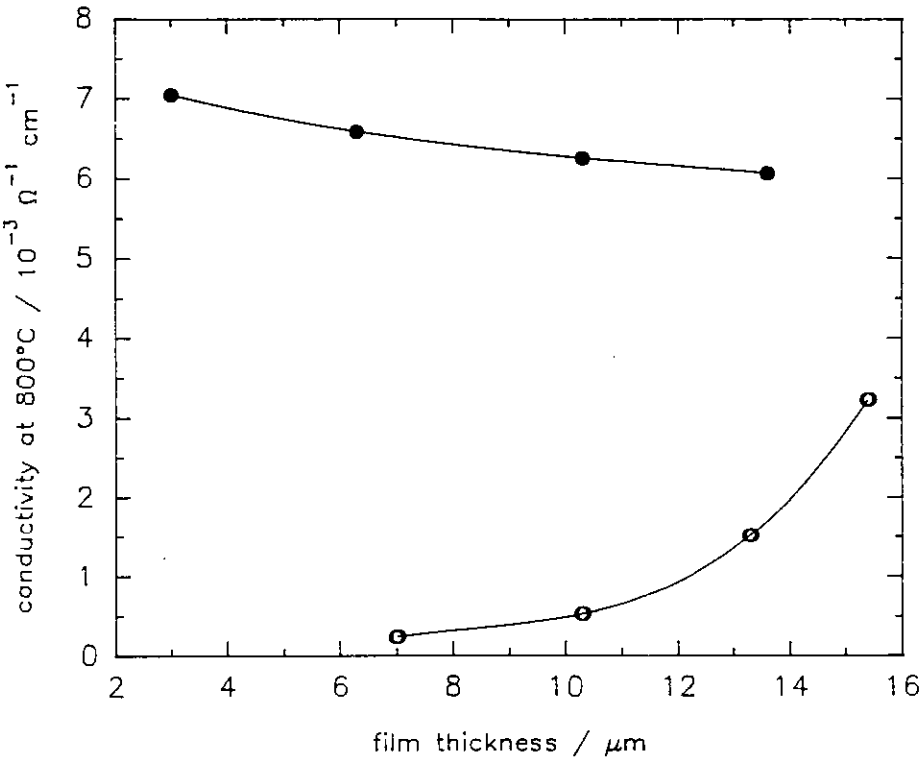

Figure 3.26 *Effect of the ionic conductivity (measured at 800°C) with variation in film thickness of 3Y zirconia thick-films sintered on:* O; *96% and* ●; *99.6% alumina substrates.*

sintered on 99.6% alumina at 1400°C for 1 hour there was little dependence with film thickness in the range 3-15 μm on the conductivity (Fig. 3.26). An invariant conductivity with the film thickness is typical of bulk materials. The film may have achieved a density close to the maximum when sintered at a temperature between 1300°C and 1400°C.

In contrast to the films sintered on 99.6% alumina, those sintered on 96% alumina showed highest conductivities when sintered at 1300°C (Fig. 3.25). Increasing the firing temperature resulted in a continuous conductivity decrease in the zirconia thick-film; furthermore, the conductivity of the films sintered at 1400°C decreased with decreasing thickness (Fig. 3.26). The effects observed on 96% alumina could be explained in terms of impurity diffusion from the 96% alumina into the zirconia,

causing an increase in the grain size (§ 3.3.3.1) and resulting in a tetragonal to monoclinic transformation (§ 3.3.3.2). It is well known that zirconias composed of monoclinic phase have poor ionic conductivities compared to those composed of tetragonal and / or cubic phases [187]. Films on 99.6% alumina sintered at 1400°C which showed little variation of conductivity with thickness also showed little grain growth (Fig. 3.16) and were composed of more than 95% tetragonal phase (Figs. 3.20 and 3.21).

At firing temperatures of 1400°C and above the conductivities of films deposited on 99.6% alumina were higher than those obtained on the lower purity substrate; at 1300°C the reverse was the case (Fig. 3.25). This lower firing temperature may have caused a smaller impurity dissolution from the substrate into the film. The lower impurity concentration was insufficient in this case to cause a t→m transformation (Fig. 3.20) but was sufficient to promote sintering of the zirconia films sintered on 96% alumina compared to those sintered on 99.6% alumina. In such cases the conductivities were higher for films sintered on the less pure substrate.

In general the diffusion of substrate impurities from the 96% alumina into the films at the higher temperatures had deleterious effects on the ionic conductivities. Other workers [140,141,142], have also reported negative effects due to glassy phases on the ionic conductivity of bulk zirconia. The conductivity decrease correlates with an increase in the grain size of the deposit. It can be concluded that the drastic deterioration of the ionic conductivity of zirconia films fired at temperatures above 1300°C on substrates containing nominally 96% alumina was primarily due to the presence of a high percentage of monoclinic phase (§ 3.3.3.2).

Activation energies associated with the total conductivity of the thick film electrolyte were obtained from the data shown in Fig. 3.27 (Table 3.2). The values are on the whole comparable to the activation energy of bulk zirconia reported in the literature of 104 kJ mol^{-1} [165]. Generally the activation energies for ionic conductivity of zirconia thick-films were higher when sintered on 96% alumina than when sintered on 99.6%. A value for the activation energy of 164 kJ mol^{-1} was obtained for a zirconia film (10 μm thick) sintered at 1600°C for 1 hour (Table 3.2);

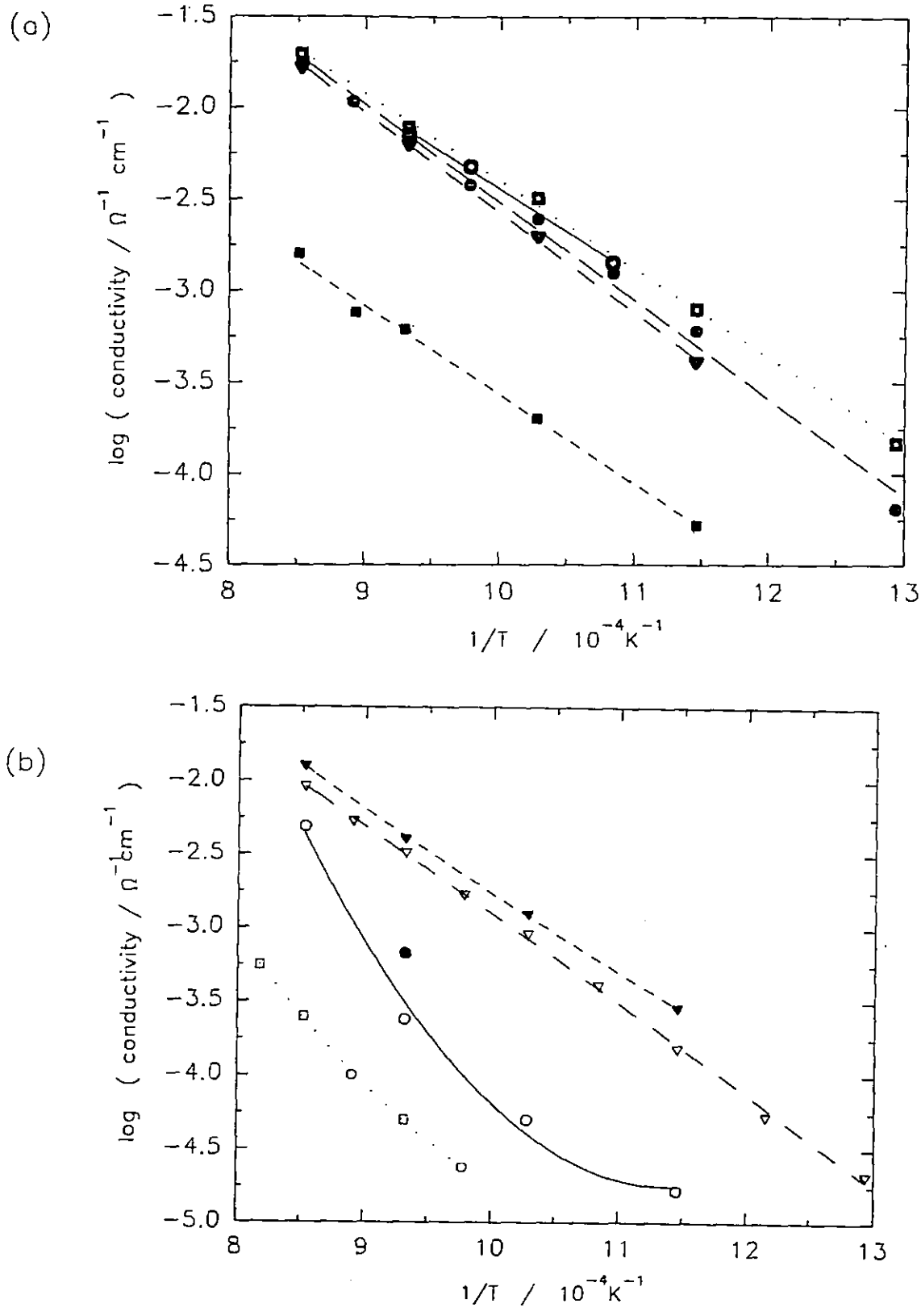

Figure 3.27 *Ionic conductivity vs reciprocal temperature for various zirconia thick films sintered for 1 hour on: (a) 99.6% alumina and (b) on 96% alumina. Thickness/sintering temperature : (a) ○,3μm/1400°C; ●,6.2μm/1400°C; ▾,10.8μm/1400°C; ■, 6.2μm/1300°C; □, 6μm/1600°C, (b) ○,7μm/1400°C; ●,10.2μm/1400°C; ▽,15.3μm/1400°C; ▾, 10.5μm/1300°C; □,10.5μm/1600°C.*

this film is expected to be almost totally monoclinic (§ 3.3.3.2). Films comprising the highest content of monoclinic phase also showed the highest activation energies. Further work is required to establish whether the activation energy for ionic motion is higher in monoclinic than in tetragonal zirconia as this does not appear to have been reported in the literature.

Sintering temperature for 1 hour	Film thickness / μm	Activation energy kJ mol^{-1}	
		Alumina substrate purity	
		96%	99.6%
1300°C	6.2		95
	11.0	108	
1400°C	3.0		93
	6.2		103
	10.8		104
	7.0	120	
	15.3	116	
1600°C	6.0		95
	10.5	164	

Table 3.2 *Activation energies of 3Y zirconia thick-films having various thicknesses and sintered at various temperatures.*

3.4 SUMMARY

The processes and requirements for producing zirconia thick films of low connected porosity (<0.1%) on alumina substrates with no loss of adhesion from the substrate or cracking of the film have been investigated and specified. It was found that this required the preparation of an ink with full dispersion of agglomerates of particles of sub-micron size. Dispersal was achieved using a triple-roll mill and was checked using viscosity measurements. Very viscous pastes did not level out after printing while low viscosity pastes tended to run and lose pattern edge definition. The mix used throughout the work contained 40% by weight of tetragonal zirconia powder (Toyo-Soda 3Y), the remainder being ESL 400, a commercial organic vehicle.

Films were dried using an infra-red dryer which enabled a crack-free deposit to be prepared. Where required, film thickness could be built-up by successive print-dry cycles, drying each layer at 150, 450 and 700°C for 10 minutes at each temperature. The final firing of single or multilayers was done at 1300-1550°C to sinter the deposit. This sintering temperature was approached at a ramp rate of 3°C min^{-1}. The state of dispersion in the pastes had an important influence on the development of the green microstructure and subsequent sintering behaviour.

Thick films of zirconia printed onto 96% alumina substrates and fired at 1400°C or above showed substantial grain growth; there was little grain growth when an intervening layer of platinum was included. Grain growth in the absence of platinum increased as the thickness of the zirconia layer was decreased. Repeating the work on 99.6% alumina revealed little grain growth irrespective of film thickness. Clearly grain growth was accelerated by the transfer of impurities from the substrate to the zirconia film. An intervening layer of platinum either blocked the trasnsfer of impurities or itself acted as a grain growth inhibitor.

Tetragonal zirconia spontaneously transforms to the monoclinic structure. However, the tetragonal phase is metastable if the grain size remains small (<0.5 μm). X-ray diffraction studies of the zirconia thick films, indicated that where grain growth occurred (to > 1 μm) a transformation to the monoclinic form did take place.

It is also well-known that the ionic conductivity of the monoclinic form of zirconia is much lower than that of the tetragonal form. Thus AC impedance measurements were made on the zirconia thick films. These showed the expected substantial decrease in the ionic conductivity for those films in which grain growth had occurred (> 1 μm) and for which X-ray diffraction indicated the tetragonal to monoclinic transformation.

CHAPTER 4

SCREEN–PRINTED PLATINUM–ZIRCONIA CERMET ELECTRODES

4.1 INTRODUCTION

Ceramic-metal mixtures conveniently referred to as cermets have found a variety of uses which include antistatic coatings, film resistors for the electronics industry [188], nickel-zirconia electrodes for solid oxide fuel cells [189] and chemo-resistive platinum-zirconia oxygen sensors [48,49].

In this study planar zirconia amperometric oxygen sensors have been constructed using thick-films technology exclusively (Chapter 5 and [190,191]). Sensor construction involved succesive lamination of electrode (cathode), electrolyte and electrode (anode) layers onto an alumina substrate. This necessitated co-firing of at least the cathode with the electrolyte. The elevated temperatures required to sinter the electrolyte (>1300°C) can lead to low electrode activities. Furthermore such high firing temperatures induce stresses (upon cooling from the firing temperature) between electrode and electrolyte due to the thermal expansion difference between them. Such stresses can result in cracking of the electrolyte layer which is detrimental to the sensor operation. In response to these problems cermet electrodes comprising a mixture of platinum and zirconia have been used [192]. Progressively improved thermal expansion compatibility is expected with increasing content of the ceramic phase in the electrodes. On the other hand, electrochemical considerations suggest that it is important to have an electronically continuous electrode with as high an electronic conductivity in the electrode as possible [193].

In this chapter cermets with various yttria stabilised zirconia to platinum (YSZ:Pt) ratios were investigated in respect of electrode performance and microstructure in order to achieve improvements in the performance of screen-printed amperometric oxygen gas sensors.

The minimum temperature at which an amperometric zirconia oxygen sensor can operate satisfactorily is generally dependent upon the kinetics of the electrode reaction (which become slow at temperatures below 400°C) [194,195,196, 197]. The electrode reaction is normally considered to take place at the electrode/electrolyte/gas *three-phase boundary (TPB)* [198] as it is only here that

the exchange between oxygen gas and oxygen ions can occur (the oxygen ions can then be transferred by the ion conductor and the simultaneously required electrons can be delivered by the electronic conductor). As a consequence increasing the length of the *TPB* should increase the activity of the electrode. Two possible methods of increasing this boundary length are (i) mixing the electrode material with that of the electrolyte thus imitating the electrode structure of liquid electrolyte fuel cells [193,199], and (ii) altering the morphology of the electrode by prolonged current passage so as to increase the number of point contacts with the electrolyte [200].

4.2 EXPERIMENTAL

4.2.1 Preparation of platinum-yttria stabilised zirconia (Pt–YSZ) cermets

Cermet pastes were made by mixing fritless platinum ink (type 5542) with a zirconia ink previously prepared (paste number 4d, Table 3.1, § 3.3.2.2) to maintain the same volume fraction of solids and similar viscosity as the platinum ink. The initial mixing of the pastes was done in an agate pestle and mortar and then intimate mixing was achieved using the triple–roll mill. Cermets pastes containing YSZ:Pt volume ratios of nominally 3:2, 4:5, 2:3, 1:2, 2:5, 1:4, were prepared. These pastes (as well as one containing no YSZ) were screen-printed, dried, and fired at 1000°C for 10 minutes as an initial treatment; the resulting layers were all in the range 6±0.2 μm thick.

4.2.2 Determination of metal, ceramic and void phases in printed and fired cermet films

The respective volume fractions of metal, ceramic and void phases of the screen-printed cermet films (fired at 1000°C for 10 minutes) were calculated (Appendix A) using values for densities (at zero porosity) of platinum and zirconia of 21.4 and 6.05 g cm^{-3} [201] respectively. These calculations also required determination of the amount of metallic phase present (determined using the atomic absorption technique described in § 2.3.10) together with the cross-sectional area (using the Alpha–step technique described in § 2.3.1) of the screen–printed cermets.

4.2.3 Electrical resistance characteristics of the cermets

The cermet compositions were printed onto 96 and 99.6% alumina substrates as strips of 400 µm width and 25 mm length. Ten strips were accommodated onto one substrate as shown in Fig. 4.1a. The resistance of each strip was then measured at ambient temperatures using a four point probe (§ 2.3.8). The measured values were normalised to the same temperature of 20°C using the following relation:

$$R_{20} = R_m (1+\alpha_r\{T_m-20\})^{-1} \quad (4.1)$$

where R_m is the resistance at the measurement temperature T_m (in °C) and R_{20} is the normalised resistance corrected to 20°C. The temperature coefficient of resistance α_r (at 20°C) was determined (using the same experimental arrangement described in § 6.2.5) and taken as 3600 ppm $°C^{-1}$. The initial values of R_{20} were denoted as R_i. The films were then treated at temperatures up to 1500°C for various times and their resistances at 20°C were measured after each treatment.

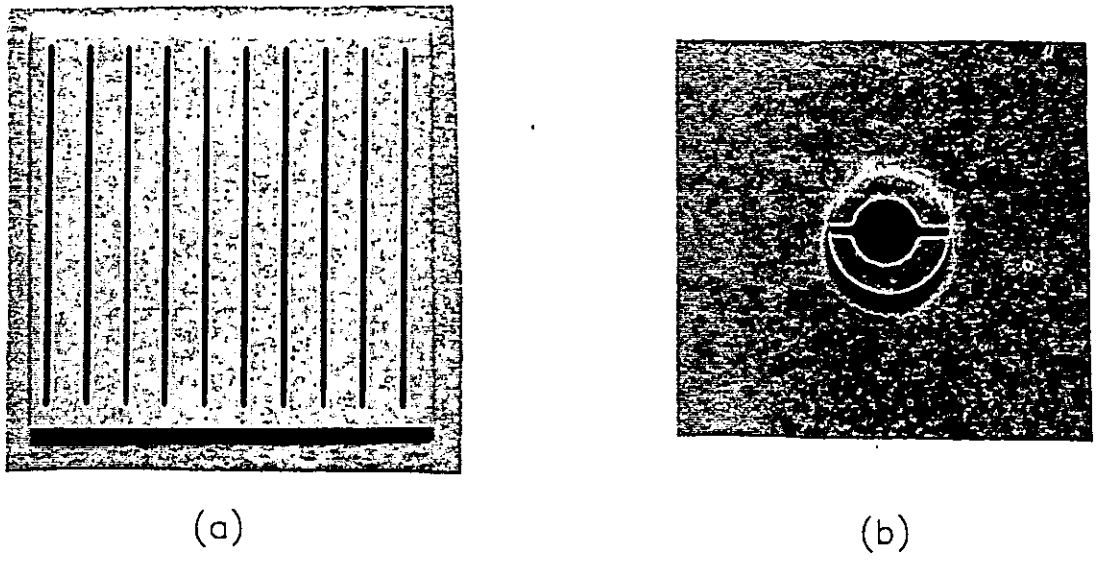

Figure 4.1 *(a) Photograph of cermet strips used to measure resistance changes, (b) Photograph of a cermet electrode on a zirconia disc.*

4.2.4 Current-voltage characteristics of the cermet electrodes

Discs were punched from '8Y zirconia green sheets (ICI material) and sintered at 1500°C for 1hr supported on 99.6% alumina substrates; the temperature ramp rate used was 10°C min^{-1}. The resulting discs were flat with a smooth appearance and diameter 7.8mm and thickness 275 μm.

Electrodes were deposited by screen–printing the required cermet paste onto both sides of the pre-sintered zirconia discs, followed by the relevant firing cycle (1 hour at temperatures between 900 and 1450°C). This resulted in each disc having electrodes of different composition, with individual discs having identical electrodes (size and composition) centrally located on opposite faces of the disc (Fig. 4.1b). A third electrode to be used as a reference electrode, was painted onto a peripheral area of the disc using a brush. Pt wires (100 μm in diameter) used for electrical connection, were attached to the three electrodes using fritless Pt paste.

The potential of the reference electrode was set by the partial pressure of the oxygen in the surrounding atmosphere. Since the reference electrode and the working electrodes (i.e anode and cathode) were exposed to the same atmosphere, the potential difference between them was the overvoltage (plus the IR contribution) of the working electrode. As described below this overvoltage was determined by using the current interruption method [202] to eliminate the ohmic loss (IR) across the electrolyte.

The gaseous environment and temperature of the cells were controlled by the gas mixing apparatus and furnace arrangement described in § 2.3.12. Fixed voltages were then applied (using a Times Electronics constant voltage source) across the cell and the current flowing was measured (Fig. 4.2); stable values of the current I, were usually achieved within 5 minutes of applying the fixed voltage. The total applied voltage (constant voltage source) was varied to vary V_2. The potential difference V_1 (a measure of the potential of electrode 1 relative to the reference electrode) was measured with electrode 1 operated either as an anode or as a cathode depending

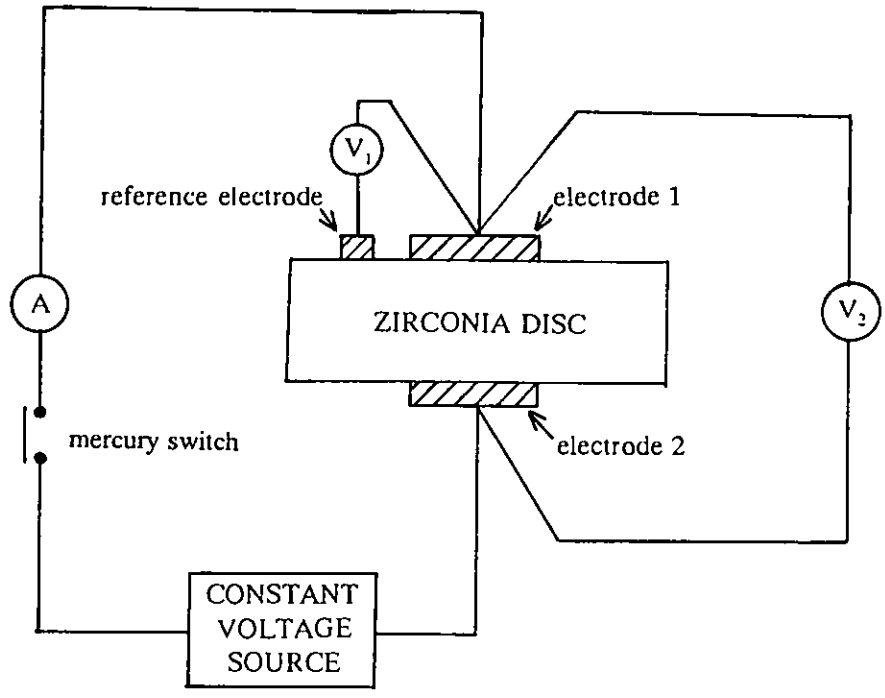

Figure 4.2 *Electrical arrangement used for obtaining current - voltage characteristics.*

upon the current direction; $(V_2–V_1)$ was a measure of the potential of electrode 2 relative to the reference electrode. The cathodic and anodic overvoltages η_c and η_a respectively for each electrode and for the total cell were obtained by subtracting the contribution, IR_E, due to the electrolyte resistance, R_E. The electrolyte resistance between the reference and both other electrodes as well as between the two working electrodes were obtained using a current interruption technique. The electrolyte resistance between the reference and working electrode measured by the current interruption technique was verified by A–C impedance measurements. Prior to making the measurements, a conditioning treatment was given in order to obtain reproducible current–voltage characteristics. This conditioning treatment comprised a series of potential sweeps (from 0 to +900 mV at 100 mV per minute) followed by the application for 30 minutes of a continuous voltage of +900 mV across the cell; this was repeated with the current flowing in the opposite direction.

The potential drop, V_2 across the electrolyte was equal to the ohmic drop (IR) across the electrolyte plus the magnitude of the overpotentials of electrode 1 (η_1) and 2 (η_2), as shown in Eq. (4.2).

$$V_2 = IR_E + \eta_1 + \eta_2 \qquad (4.2)$$

The ohmic drop was proportional to the current I, flowing and the electrolyte resistance R_E.

Current interruption technique

The application of a voltage resulted in an eventual steady current flowing through the cell; the total voltage drop between the electrodes was displayed on an oscilloscope. The current flow was then interrupted (using a mercury switch to ensure bounce-free operation); the IR component showed an immediate drop (~ <1 μs) whereas the electrodes took longer for the overvoltage to decay. This sudden drop was measured using the cursor of the oscilloscope and by relating it to the steady current flow prior the interruption the resistance due to the electrolyte was calculated (using Ohms law).

4.3 RESULTS AND DISCUSSION

4.3.1 Composition of printed cermets

Printed cermet films can be characterised by the respective volume fractions of metallic, ceramic and void phases. These are referred to as *volume film fractions* (VFF), of the respective phases; the volume film fraction of platinum is denoted below as V_f. Quantitative determination of the amount of platinum present (atomic absorption technique) together with the cross-sectional area (Alpha–step technique) of the screen–printed cermets (initialised at 1000°C for 10 minutes) enabled calculation of V_f (Appendix A). The respective volume film fractions of ceramic and void phases were calculated from knowledge of the Pt-YSZ ratio (Appendix A). The results obtained for the cermet films screen–printed on 99.6% alumina and fired at 1000°C for 1 hour are shown in Table 4.1. This treatment resulted in value of V_f in the range 17-40% and a volume film fraction of void phase in the range 53-60%.

Cermet №	YSZ:Pt ratio	Pt content in cermet mix (volume %) ‡	Film fraction of Zirconia (vol %) ‡‡	Void phase in film (vol%) ‡‡	Film fraction of Pt (V_f) in cermet (vol %) ‡‡
1	pure Pt	100.0	0.0	60	40.0
2	1:4	80.0	9.0	56	35.5
3	2:5	71.6	13.2	53	34.0
4	1:2	67.4	14.0	58	28.2
5	2:3	60.0	19.0	53	28.2
6	2:5	55.6	19.0	57	23.5
7	3:2	40.0	27	56	17.0

‡, refers to volume fraction of platinum in a paste considering only a matrix of platinum and zirconia and ignoring other constituents (i.e the carrier vehicle)

‡‡, refers to a volume fraction of the respective phase in the printed and fired film and includes all three phases (i.e platinum, zirconia and void)

Table 4.1 *Composition of Pt–YSZ (3Y) cermets screen–printed on 99.6% alumina and fired at 1000°C for 10 minutes.*

4.3.2 Microstructure

4.3.2.1 Fired at 1000°C for 10 minutes

Examination of the microstructure of the screen-printed cermet films (Fig. 4.3) revealed that they were composed partially of three dimensional (3D) (small metal and ceramic grain size compared to film dimensions) and partially two dimensional (2D) regions (arising from the presence of through voids). Through voids are those which traversed the film thickness.

The scanning electron micrographs of the cermet films at 1000°C (Fig. 4.3) also revealed an inhibiting effect on the grain growth of the platinum phase by the zirconia phase; suppression of grain growth increased with increasing additions of ceramic phase in the cermet. This is because the ceramic grains inhibit the migration of the metallic grain boundaries. This effect is often referred to as "pinning" in the literature and was originally pointed out by Zener [203] who said that grain

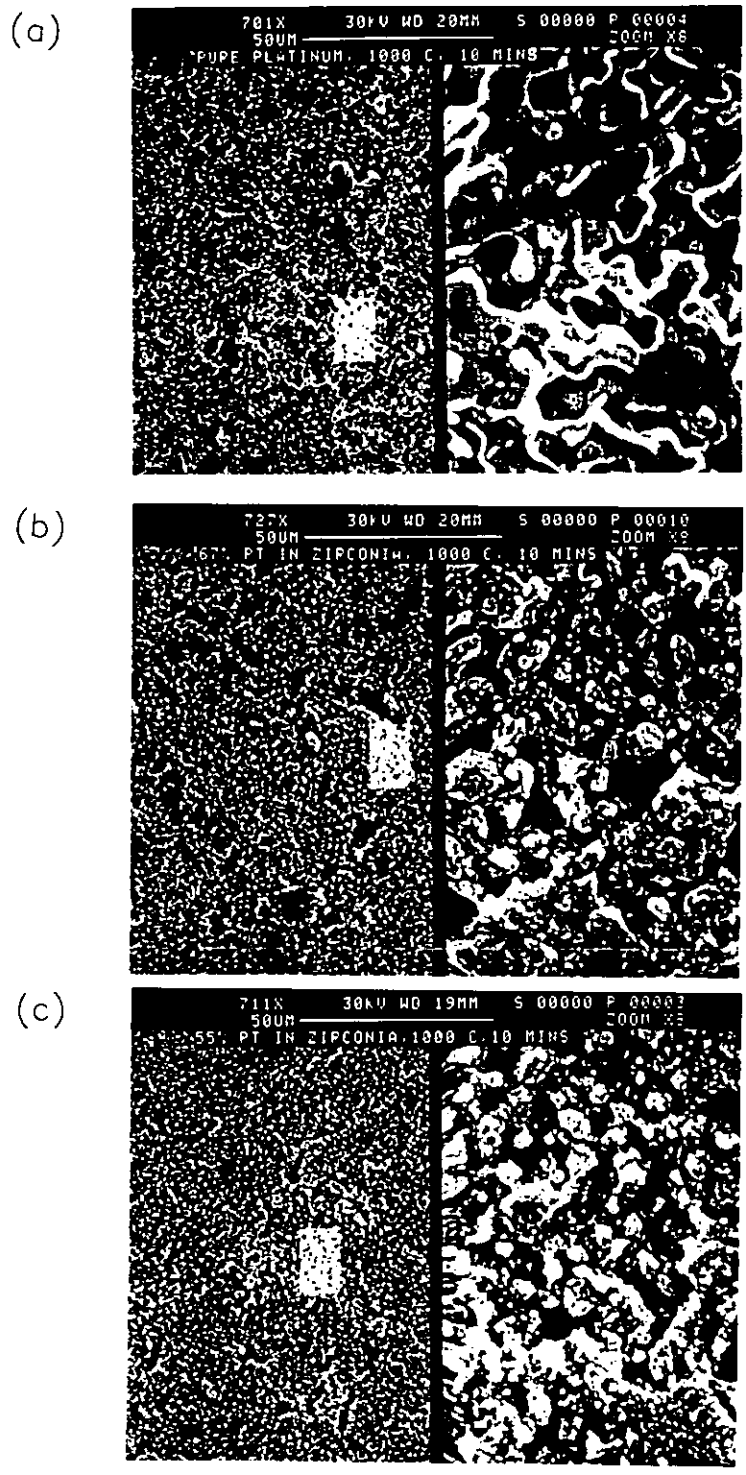

Figure 4.3 *Micrographs of zirconia-platinum thick film cermets (6μm thick) fired on 99.6% alumina at 1000°C for 10 minutes. Percent platinum in zirconia (a) 100%; (b) 67%; (c) 55%. Cursor lengths show the magnifications and refer to the left half of each micrograph. The highlighted area in the left half is shown to the right at eightfold magnification.*

boundaries would be held back by any second phase inclusion. Since then it has been observed in the sintering of many multiphase solids [204].

4.3.2.2 Prolonged firing at temperatures above 1000°C

Prolonged firing times at temperatures above 1000°C showed a progressive growth of through voids with time within the cermet film; the rate of void growth increased with increasing firing temperatures (Fig. 4.4). Void growth was probably due to the effect of grain growth, and loss of platinum metal by evaporation (Chapter 6).

Propagation of void growth and sintering effects resulted in a tendency for the films to switch progressively from primarily a 3D structure to become increasingly 2D because the size of the voids and platinum grains became comparable to the film thickness.

4.3.3 The influence of elevated firing temperatures on the electronic resistance of the cermets

4.3.3.1 General

The electrical resistance of cermets may be related to volume film fraction, distribution and nature of contact of the metallic phase; these were modified by thermal treatments.

4.3.3.2 As printed

Deposition and drying (at 150°C) of the cermet film resulted in electrical non–continuity. This was presumably due to a low overall metallic volume fraction resulting from a high void fraction and the presence of organic binder in the film not permitting continuity of the metallic phase. As the organic vehicle and binder were removed at ~500°C the films became electrically continuous. No sintering of either the metallic or of the ceramic phase was expected at this temperature and consequently the conductivity of the matrix depended only upon the metallic inter–particle contact which necessarily resulted in high resistances.

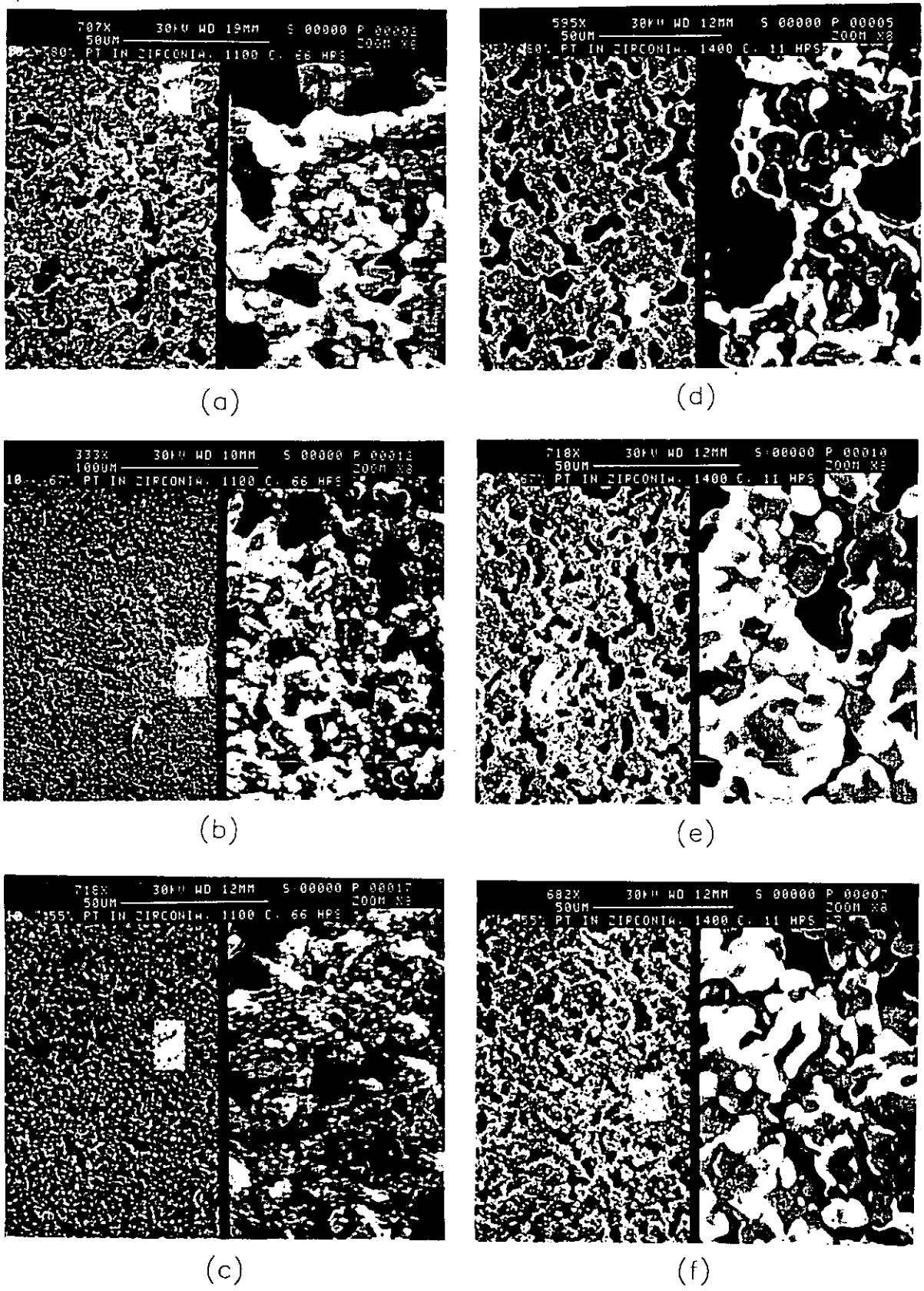

Figure 4.4 *Micrographs of platinum zirconia thick-film cermets (6μm thick) fired on 99.6% alumina. Percent platinum in zirconia fired at 1100°C for 66 hours (a) 80%; (b) 67%; (c) 55% and fired at 1400°C for 11 hours (d) 80%; (e) 67%; (f) 55%. Cursor lengths show the magnifications and refer to the left half of each micrograph. The highlighted area in the left half is shown to the right at eightfold magnification.*

4.3.3.3 Fired at 1000°C for 10 minutes

As the ceramic phase should act as an electrical insulator at 20°C the only conduction path in the cermet was that of electrons through the metal phase. The cermet may therefore be treated as a two phase conductor–insulator electrical system at ambient temperatures where the platinum is the conducting phase and the the zirconia and voids make up the insulting phase.

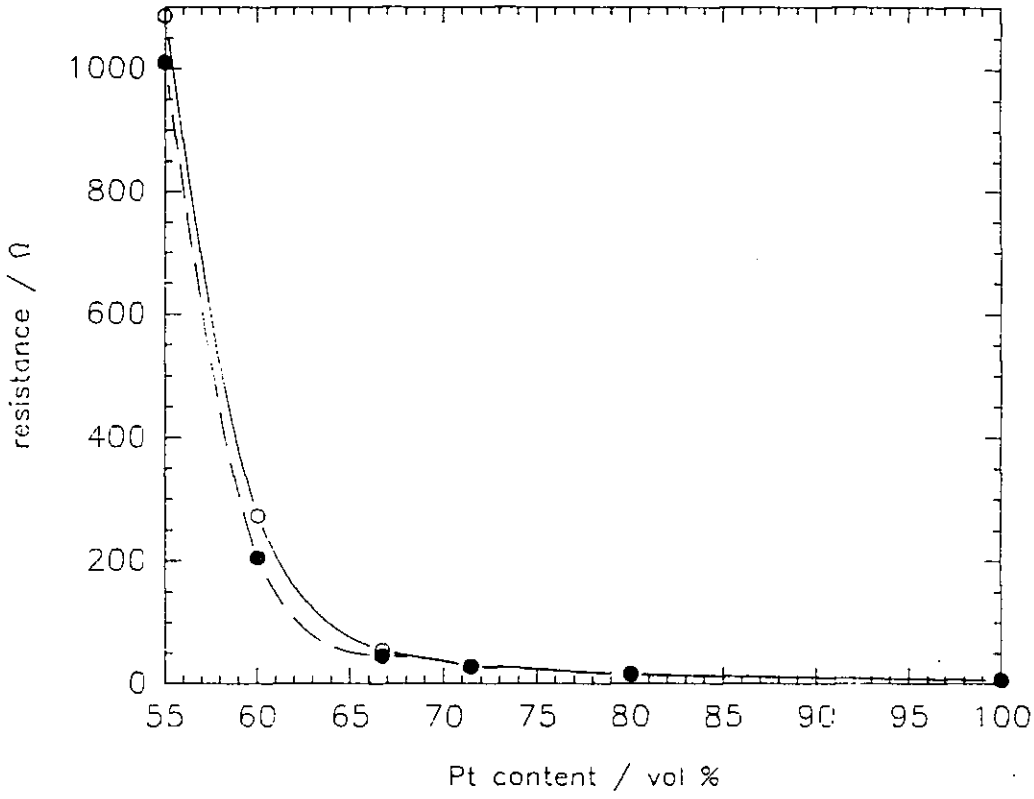

Figure 4.5 *Electrical resistance versus volume fraction of platinum in cermet pastes printed and fired at 1000°C for 1 hour on:* ○, *96% and* ●, *99.6% alumina substrates.*

The electrical resistances corrected to 20°C (R_{20}), versus volume fraction of platinum (‡, Table 4.1) of the cermet paste are shown in Fig. 4.5. The slope of the curve is high near the point of electrical discontinuity (somewhere below 55% and above 40 % Pt) as expected for a two-phase conductor–insulator system [188,205]. The steepness of the slope presented by the data of Fig. 4.5 suggests that electrical discontinuity occurred at a volume fraction of platinum (‡, i.e. not including voids) much closer to 55% than 40%. From Table 4.1 at 55% (‡) the

volume fraction of platinum in the printed cermet film (‡‡, i.e. including voids) corresponded to 24%. This critical volume fraction of conducting phase V_c required for electronic conduction in the printed cermet films of ~0.24 lies between the theoretical values of 0.15 and 0.5 for 3D and 2D two–phase conductor–insulator systems respectively [206]; this may be due to the microstructure of the film being composed of partially 2D and 3D regions (§ 4.3.2.1). However agreement between theoretical and experimental values of V_c, has rarely been quantitatively achievable; as well as dimensionality, variables such as size ratio between the conducting and insulating particles, film geometry and distribution of metallic phase influence the observed value of V_c [207].

Theory and previous experimental investigations on two–phase conductor–insulator systems [205,208] suggest that plotting the data as as $\log_{10}(\sigma/\sigma_o)$ versus $\log_{10}(V_f-V_c)$, according to the following equation (derived from percolation theory which is discussed in further detail in § 6.3.6.3)

$$\sigma = \sigma_o (V_f-V_c)^s \qquad (4.3)$$

should yield a straight line in the region where the volume fraction V falls between V_c and V_c+0.2. Furthermore the observed slope (called the percolation exponent, here denoted as s should fall within the ranges 1.6–2.0 and 1.0–1.4 for a 3D and a 2D system respectively [206]. The experimental data are shown in Fig. 4.6 plotted according to Eq. (4.3) (as described above) using the experimentally derived value for V_c of ~0.24. These showed good linearity and a slope (s) of the line of best fit, s =~1.6 was just within the range expected from percolation theory for electrical conduction in a 3D conductor–insulator system. The fact that the value of s was at the low end of the range predicted for a 3D system and close to the values predicted by a 2D system may indicate partial two dimensionality of the film. These data suggest that percolation theory is applicable to screen–printed cermets, composed of platinum and YSZ, fired at 1000°C and that the resistance increase near the conduction threshold was due to the corresponding small probability of forming continuous conducting paths, becoming negligible below that point.

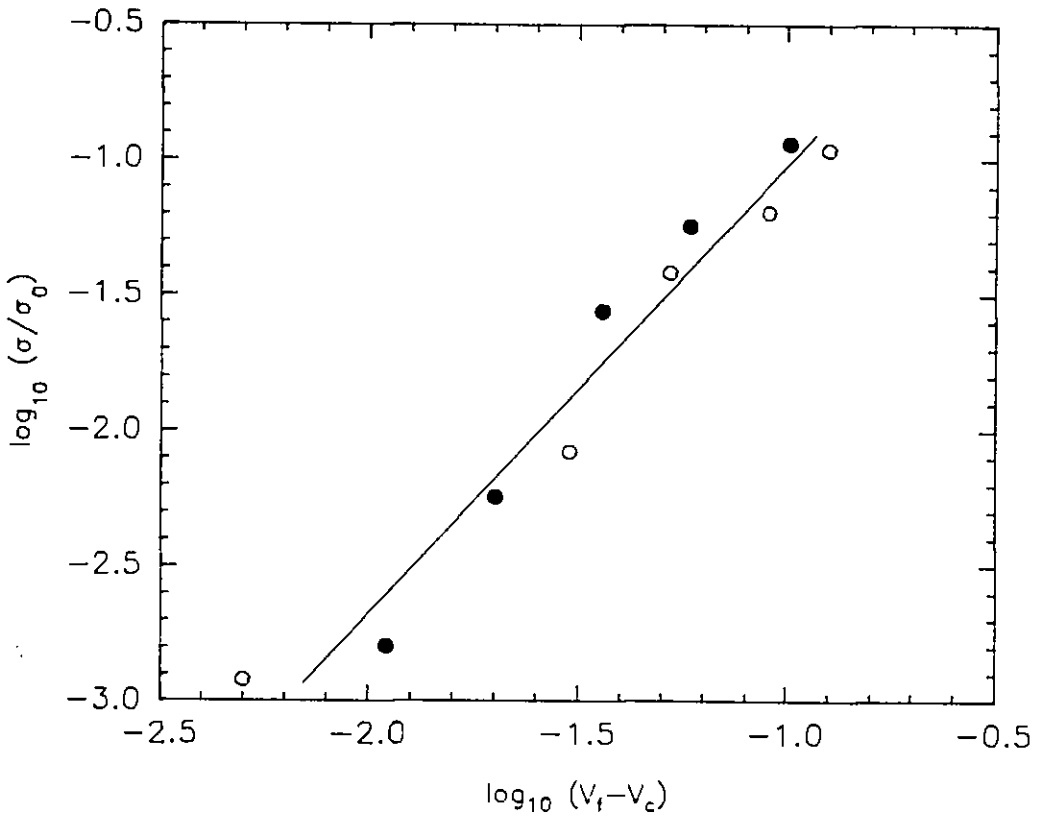

Figure 4.6 *$Log_{10}(\sigma/\sigma_0)$ vs $log_{10}(V_f-V_c)$ for cermet strips fired at 1000°C for 1 hour on: ●, 96% and ○, 99.6% alumina substrates.*

4.3.3.4 Prolonged firing at temperatures above 1000°C

Discontinuity of the electronic path after firing at 1100°C for 1 hour was observed in cermets 5 and 6. This period of time at 1100°C was insufficient to cause significant metal loss (§ 6.3.2) implying that the discontinuity was a result of microstructural changes that caused an increase in the experimental value of V_c required for electrical continuity. An increase in the experimental value of V_c could have resulted from the tendency of the films to switch progressively from primarily a 3D system (where V_c=0.15) to become increasingly 2D (where V_c=0.5) as shown by the micrographs (§ 4.3.2.2).

The resistance data (at 20°C) obtained at time t, (R_t), were normalised with respect to the initial resistance (R_i) and are shown as the normalised resistance r_N (where $r_N = R_t / R_i$). Changes in the normalised electrical resistance of cermet 2 at

various firing temperatures, with firing time are shown in Fig. 4.7. It is evident from this figure that following an initial resistance decrease (resulting in a resistance minimum), the resistance of the cermet films increased with firing time resulting in eventual electrical discontinuity of the films. A comparison of changes in normalised electrical resistance of the various cermet compositions at one temperature (1400°C) is given in figure 4.8.

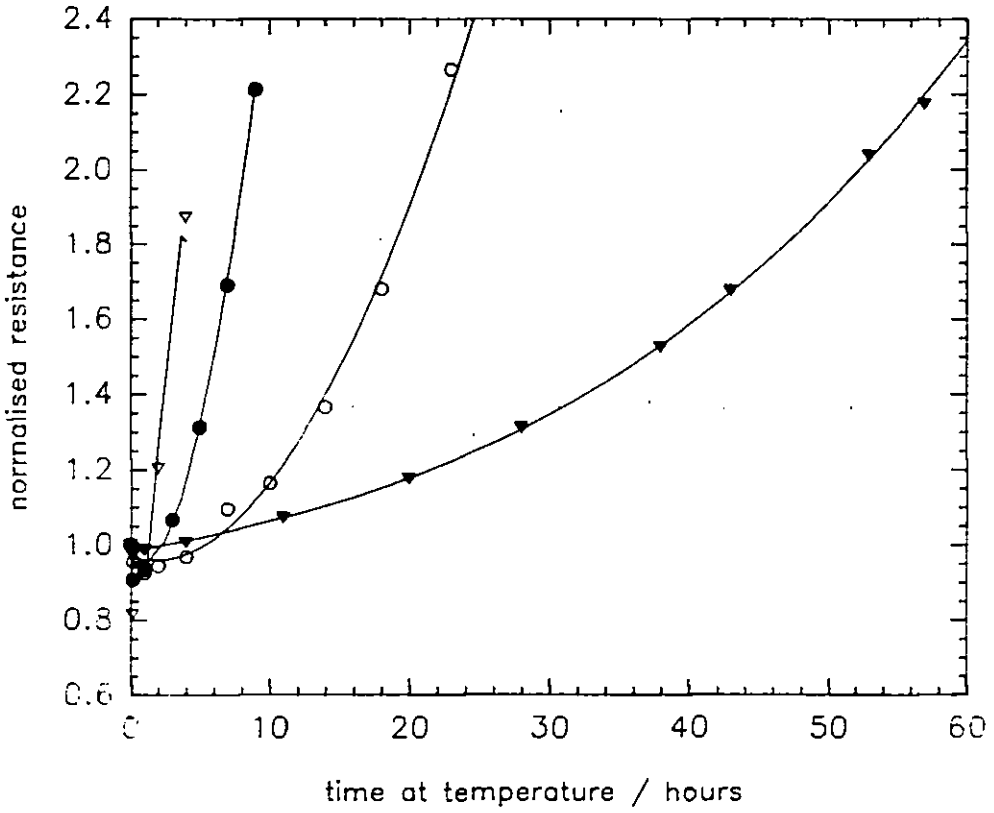

Figure 4.7 Normalised resistance vs time for cermet 2 fired on 99.6% alumina at various temperatures. ▾ *,1100°C;* O*,1200°C;* ●*,1300°C;* ▿*,1400°C.*

The normalised resistance data were also plotted against normalised time (time was normalised with respect to the time taken to reach $1.5R_i$); an example of the outcome is shown in Fig. 4.9. These plots featured a minimum in normalised resistance ($r_{N(min)}$) for each film. The $r_{N(min)}$ values as a function of cermet composition at various firing temperatures are shown in Fig. 4.10. It is evident that increases in the firing temperature of the cermets resulted in decreases in the value of $r_{N(min)}$; furthermore these decreases were increasingly pronounced in cermets with

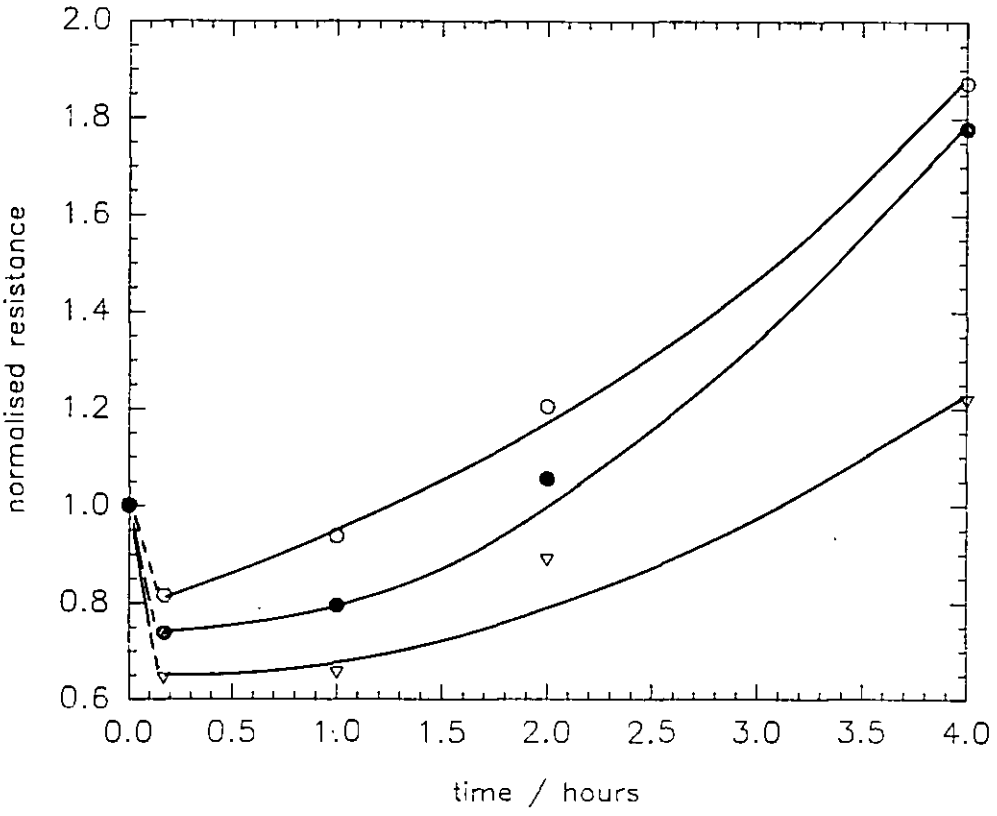

Figure 4.8 *Normalised resistance vs time at 1400°C for printed cermet compositions fired on 99.6% alumina. ○,80%; ●,72%; and ▽,66.7% platinum by volume in 3Y zirconia.*

decreasing fractions of metallic phase. The finding that the R_i data showed a percolative transition suggests that the platinum-to-platinum connections were partially broken by the zirconia additions (§ 4.3.3.3). In addition, sintering inhibition of the metallic phase by the ceramic phase was also observed (§ 4.3.2.1). Both previously mentioned effects could have prevented improvement of electrical contact within the metal following initial treatment which would result in "tortuosity" [209] of the metallic conduction path. An increasing "tortuosity" was thus expected with increasing volume fractions of ceramic phase present. The results of Fig. 4.10 could be explained on the basis that sintering at increasing temperatures improves the metal-metal contact thus reducing the tortuosity of the metallic path.

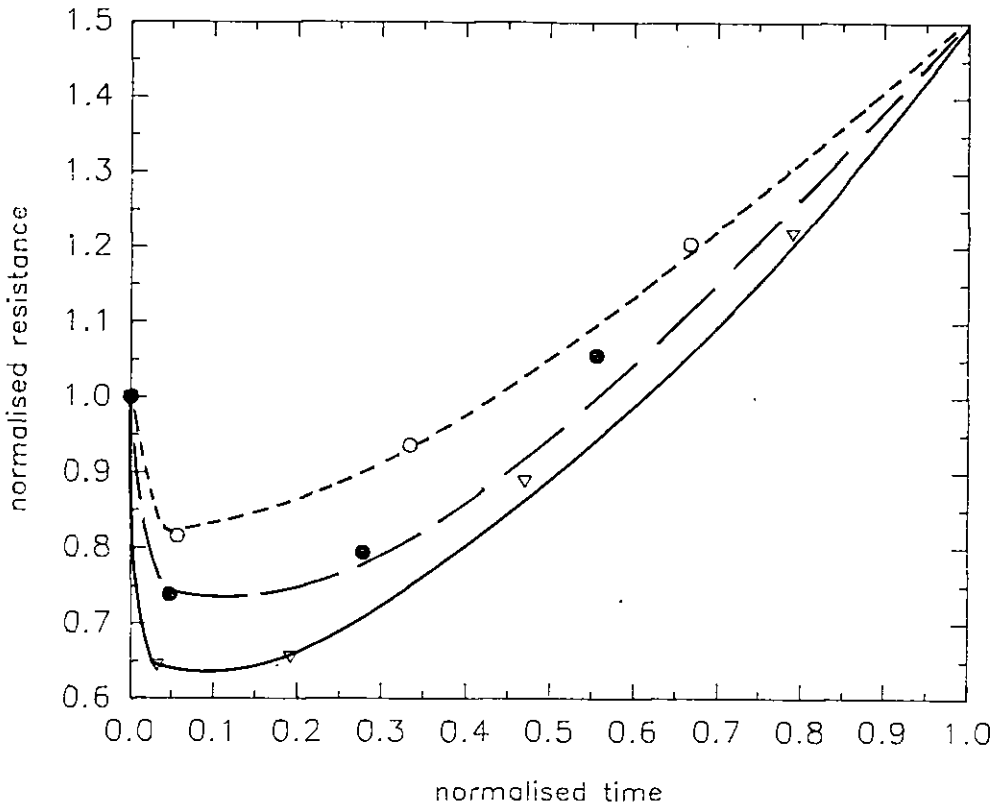

Figure 4.9 *Normalised (resistance vs time) at 1400°C for cermet compositions printed and fired on 99.6% alumina. O,80%; ●,72%; and ▽,66.7% platinum by volume in 3Y zirconia.*

It is likely that the initial resistance decrease (Figs. 4.7 & 4.8) was due to sintering of the metallic phase. The subsequent resistance increase may have been a result of the formation and growth of open voids in the cermet structure (§ 4.3.2.2); these processes could have resulted in the observed resistance increase due to loss of continuity of conduction paths (evidenced by the conformity of the results with percolation effects) and to the increasing conduction path length due to the intervening voids.

Plots of the natural logarithm of the time taken to reach one and a half times the initial resistance ($\ln t_{1.5R_o}$) versus the reciprocal temperature (Fig. 4.11) show that a similar overall activation energy of ~180 kJ mol^{-1} accompanied the rate of resistance increase of all the cermet compositions. Similarity between the activation energies indicates that the same physical processes were probably responsible for the observed

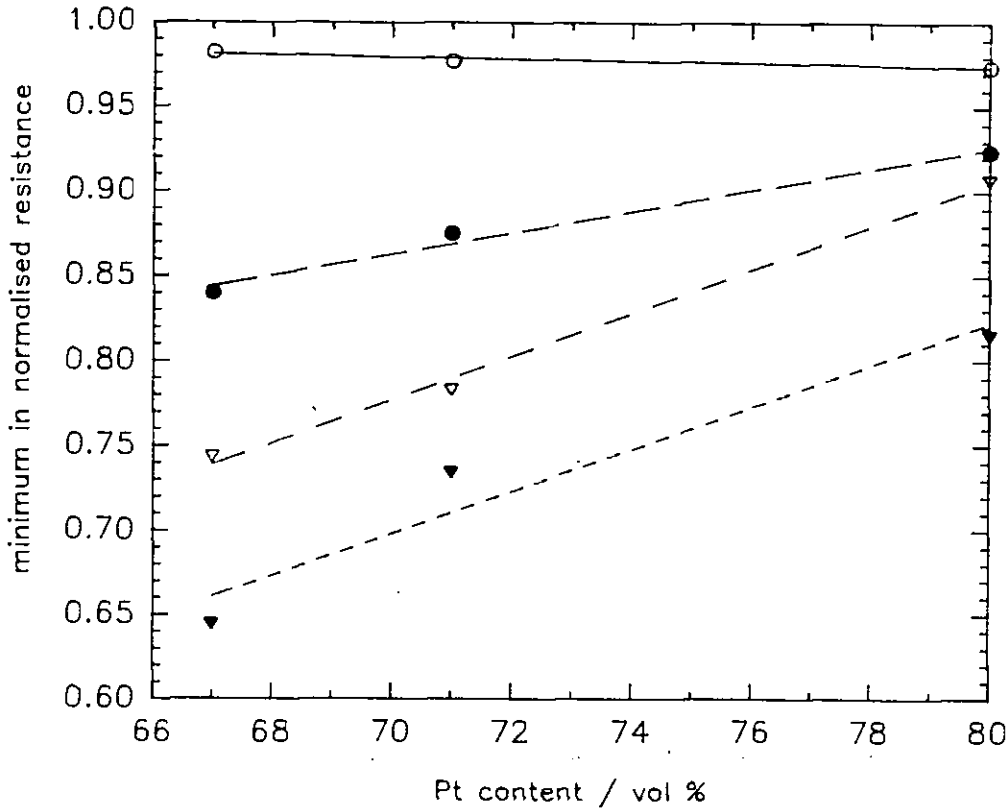

Figure 4.10 *Minimum in normalised resistance vs volume percent platinum in cermets fired on 99.6% alumina at:* ○; *1100°C,* ●; *1200°C,* ▽; *1300°C,* ▼ ; *1400°C.*

resistance increase in each cermet composition. Furthermore the value of the activation energy for the resistance increase of ~180 kJ mol^{-1} for the cermets is higher than the figure obtained for platinum (§ 6.3.1) of ~130 kJ mol^{-1} and suggests that the cermets indicated enhanced microstructural stability. This is important where a minimum deterioration of the electrodes is required with time which is of particular importance for electrodes of solid oxide fuel cells which normally operate at high temperatures (typically around 1000°C).

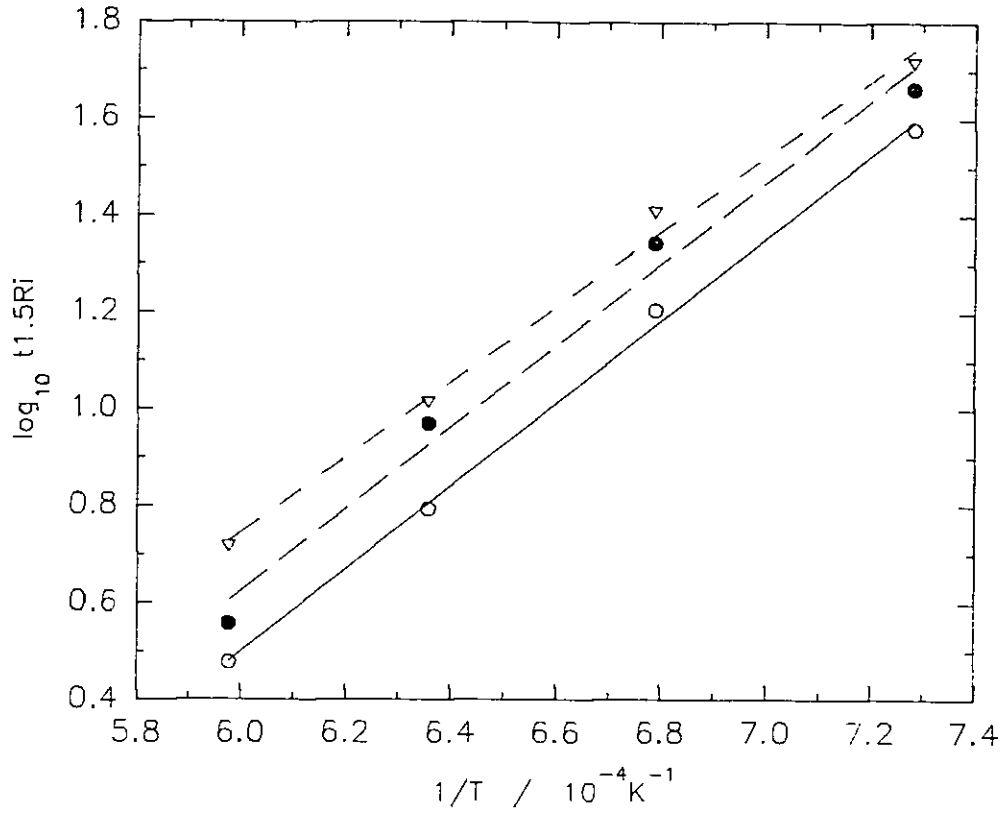

Figure 4.11 *Log$_e$ of time to 1.5R_0 vs reciprocal temperature for cermets containing ▽,66.7%; ●,72% and ○,80% by volume of platinum.*

4.3.4 Current-voltage characteristics of cermets

4.3.4.1 General

This section is concerned with electrode characteristics in the range of applied potentials and temperatures relevant to amperometric zirconia oxygen gas sensors, i.e between 0.5–1.0V and 500–700°C respectively. The ability to operate at high current densities is advantageous and hence the relevant factors were investigated. Furthermore, a literature search revealed nothing on comparison of the characteristics of practical screen-printed Pt–YSZ cermet electrodes. Differences in nature between Pt–YSZ (cermet) and platinum electrodes are considered below prior to discussion of the results obtained.

In a pure platinum porous electrode, electrochemical reaction sites can only exist at the three phase boundary interface between the bulk electrolyte, the metal and the

gas. In porous cermet electrodes the situation may differ on the basis that the ceramic may form continuous ionic paths that traverse (at least in part) the electrode thickness and connect to the bulk of the electrolyte. This could generate additional electrochemical reaction sites at metal-ceramic interfaces within the electrode provided there existed continuous electronic paths to the current collector and continuous ionic paths from this interface to the bulk electrolyte.

4.3.4.2 Current densities for the combined electrode system

General

Sensor operation in the amperometric mode involves the electrochemical pumping of oxygen across an electrolyte by the application of a voltage between two electrodes. The magnitude of the resulting current is an indication of the amount of oxygen transferred across the electrolyte.

Data presented in this section were performed on discs having essentially identical electrodes (composition, size and firing conditions) on opposing faces of the disc. Different electrode compositions were provided on separate discs.

Fired at 1000°C for 1 hour.

Figure 4.13 shows the current density (current per unit geometrical area of the electrode) at 700°C vs the sum of the magnitude of the overpotentials (denoted as η_T, where $\eta_T = |\eta_a| + |\eta_c|$) across the screen-printed cermet electrodes which had been fired at 1000°C for 1 hour. These results were obtained using the experimental arrangement shown in figure 4.2 without use of the reference electrode; the IR component was measured using the current interruption technique. The value of η_T was calculated according to the following equation

$$\eta_T = V_2 - IR_T \qquad (4.4)$$

where I is the steady current flowing through the cell and R_T is the resistance of the electrolyte between electrodes 1 and 2 (Fig. 4.2). The results of figure 4.12 are better clarified by a plot of the current density achieved at various fixed overvoltages across the cell as a function of the volume fraction of Pt in the cermet (Fig. 4.13). The current densities obtained increased with increasing additions of ceramic phase in the electrodes as compared to electrodes of pure platinum; the highest current density

was measured for cermet 4 (67% Pt by volume, excluding voids). Further zirconia additions (i.e cermets containing 60 and 55% platinum) resulted in a decrease in the attainable current density. Electrical continuity in the electrodes was tested (using a multimeter) and revealed that cermets containing volume fractions of platinum of 67% and above were electrically continuous whereas cermets containing volume

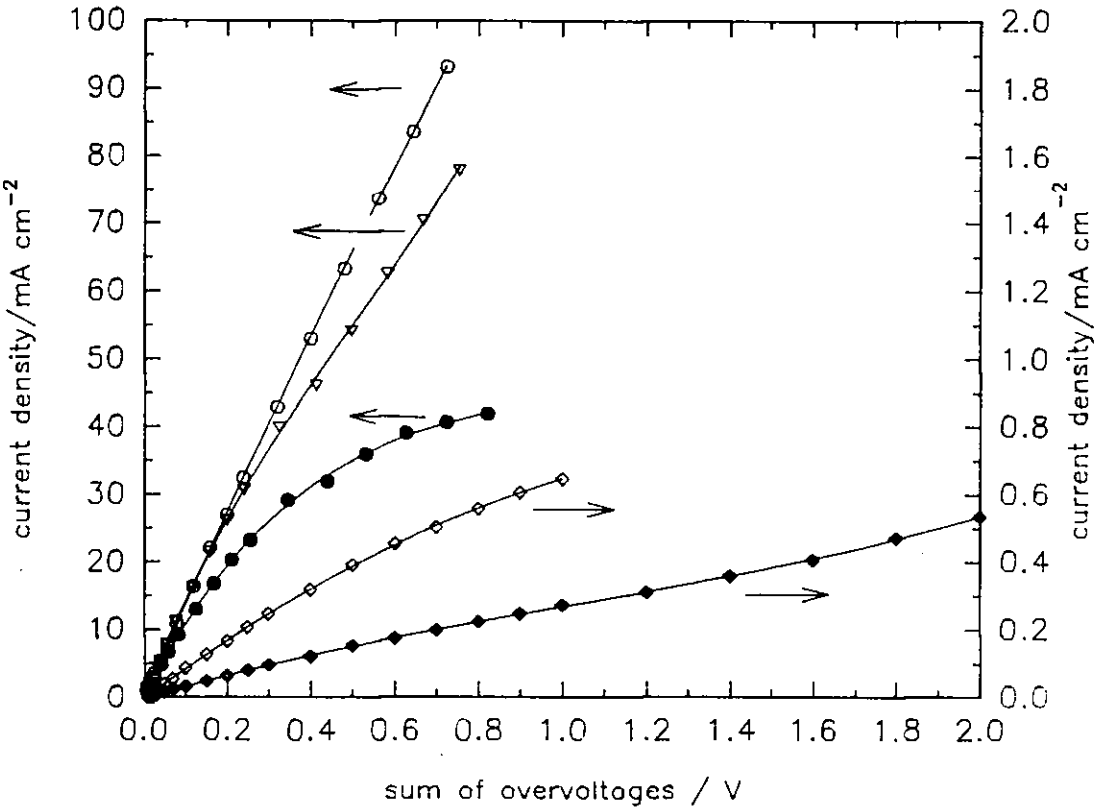

Figure 4.12 *Current density vs η_T across both electrodes for various cermets fired at 1000°C for 1 hour on zirconia discs. Cermet number (Table 4.1): ○,4; ▽,3; ●,2; ◊,5; ♦,6. Tests were performed in air at 700°C.*

fractions of platinum of 60% and below (i.e cermets 5, 6 and 7) were electrically discontinuous at room temperature. Thus the dramatic decrease in electrode current density at fixed overpotential for cermet electrodes containing platinum volume fractions of 60% and below (Fig. 4.13) was due to electronic discontinuity in the cermet.

The previous finding that electronic conductivity at ambient temperatures showed a percolative transition (§ 4.3.3.3) suggests that the platinum-to-platinum connections

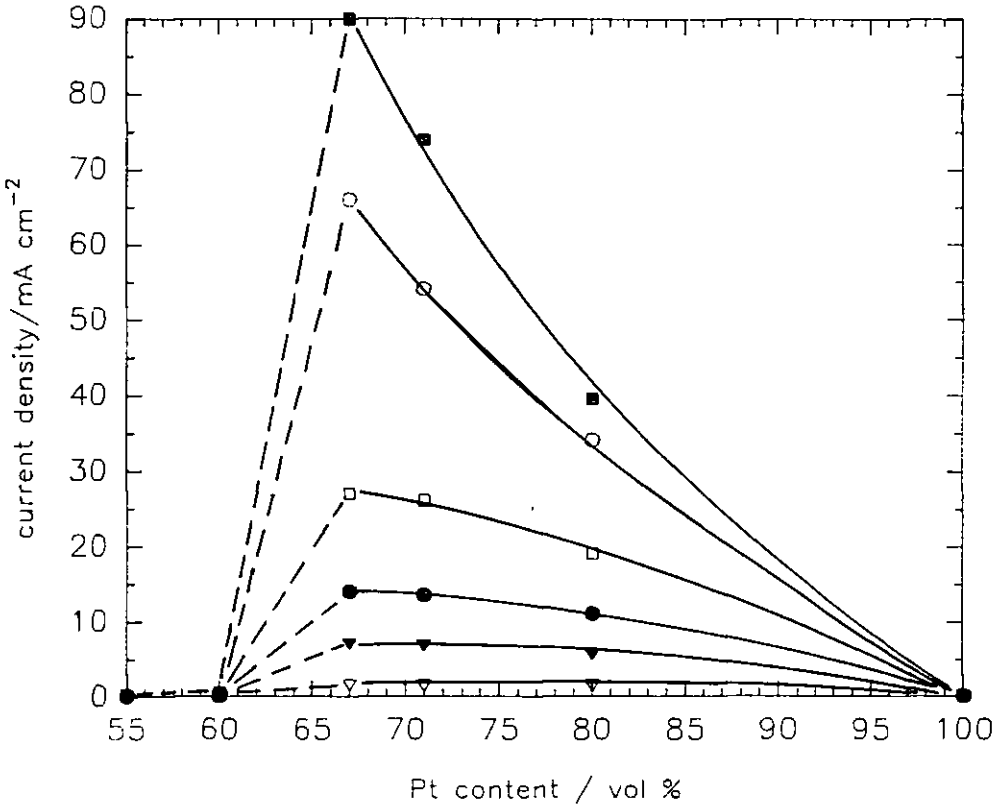

Figure 4.13 *Current density at various values of η_T vs platinum content, by volume, in cermet fired at 1000°C for 1 hour on zirconia discs. η_T: ■,700mV, ○,500mV; □,200mV; ●,100mV; ▾ ,50mV; ▽,10mV. Tests were done at 700°C in air. The data reported were interpolated from current density vs η_T plots.*

were partially broken by the oxide additions. An electrode having some isolated platinum particles should have a reduced three-phase-boundary (TPB) length compared to an electrode where all the platinum particles are connected and as a result would be expected to deliver a lower current density at a fixed overpotential. Unexpectedly however electrically continuous electrodes with some isolated platinum particles showed a higher current density at fixed overvoltage than those having a greater number of connected particles (as explained in the previous paragraph and shown in Fig. 4.13); this should be due to an increase in the *TPB* length. Such an increase in *TPB* length could have arisen in two ways, (a) the generation of additional *TPBs* at the metal-oxide interfaces within the electrode; it is possible that the number of such metal-oxide interfaces increased when larger proportions of electrolyte were present in the electrode and (b) an increase in the length of the *TPB*

due to the larger perimeter generated from smaller particle size of the platinum; it has already been shown that increasing electrolyte additions resulted in grain growth inhibition of the platinum (§ 4.3.2.1).

The electrode best suited for amperometric devices (operating above ~500°C and 100 mV) where the electrodes may be fired at 1000°C was provided by cermet 4.

Effect of firing temperature

The construction of screen–printed zirconia amperometric devices [192] necessitated firing of at least the cathode at temperatures above 1300°C because it had to be co-fired with an overprinted electrolyte layer which required such high temperatures to sinter sufficiently. The effect of firing temperature was investigated by firing the cermet containing 80% platinum by volume at various temperatures in the range 900-1450°C for 1 hour. The observed decrease in the current density with firing temperature (Fig. 4.14), (at 700 mV was ~2 orders of magnitude when the firing temperature was raised from 900 to 1450°C) could not this time be attributed to a discontinuous metallic path in the electrode (continuity was checked using a multimeter). In fact it was shown previously (§ 4.3.3.4) that the electronic resistance of the electrodes decreased with increasing firing temperature.

In relation to the work on the electrical resistance characteristics (R_{20}) (§ 4.3.3), it appears that the firing processes that decreased the electrical resistance of the cermet also decreased electrode current densities at a fixed overpotential. Clearly the electrochemically active area of the electrodes was determined not only by the amount, but distribution and porous nature of the constituent phases within the electrode. The decreasing current density at a single value of η_T (Fig. 4.14) with increasing firing temperature was probably due to a shorter TPB length resulting from platinum grain growth (compare figures 4.4(i) and 4.4(iv)). Sintering of the cermet electrodes may also have reduced the total length of platinum-zirconia boundaries within the electrode.

Firing the cermets at a temperature of 1300°C (for 1 hour) resulted in the highest current density for the cermet containing 80% platinum (by volume) as opposed to

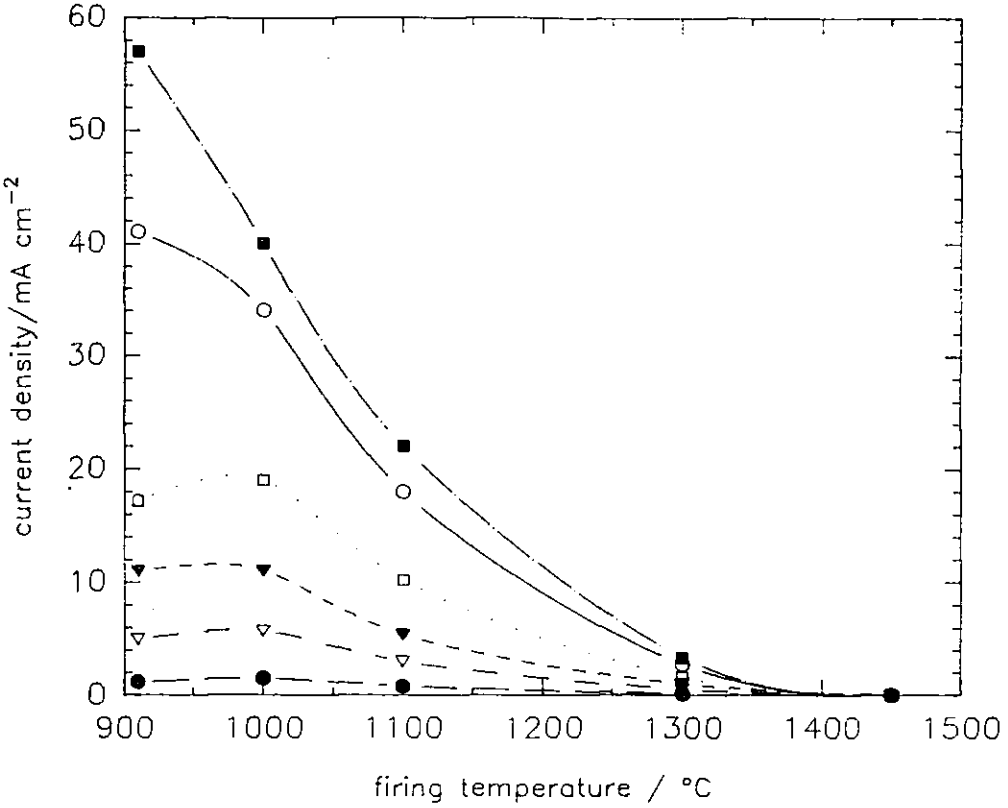

Figure 4.14 *Effect of firing temperature (held for 1 hour) on the current density at various values of* η_T *for the cermet with 80% platinum by volume.* η_T: ■,*700mV;* ○,*500mV;* □,*200mV;* ▾,*100mV;* ▽,*50mV;* ●,*10mV. Tests were done at 700°C in air. The data were interpolated from current density vs* η_T *plots.*

67% platinum when fired at 1000°C for the same period of time (Fig. 4.15). This effect may be due to isolation of a greater part of the metallic skeleton of cermets with lower platinum contents, as a result of high firing temperatures.

4.3.4.3 Single electrode data

In order to try to identify the possible *rate controlling step* for the electrode reaction, the anodic (η_a) and cathodic (η_c) overpotentials from a single electrode were separated; this was done using a reference electrode (§ 4.2.3). Background information of the various reaction steps is provided in Appendix B. The values of $|\eta_a|$ or $|\eta_c|$ (depending on the current direction) were calculated according to the following relations,

For electrode 1 (Fig. 4.2) $|\eta_a|$ or $|\eta_c| = V_1 - IR_1$ (4.5)

For electrode 2 $|\eta_a|$ or $|\eta_c| = V_2 - V_1 - IR_2$ (4.6)

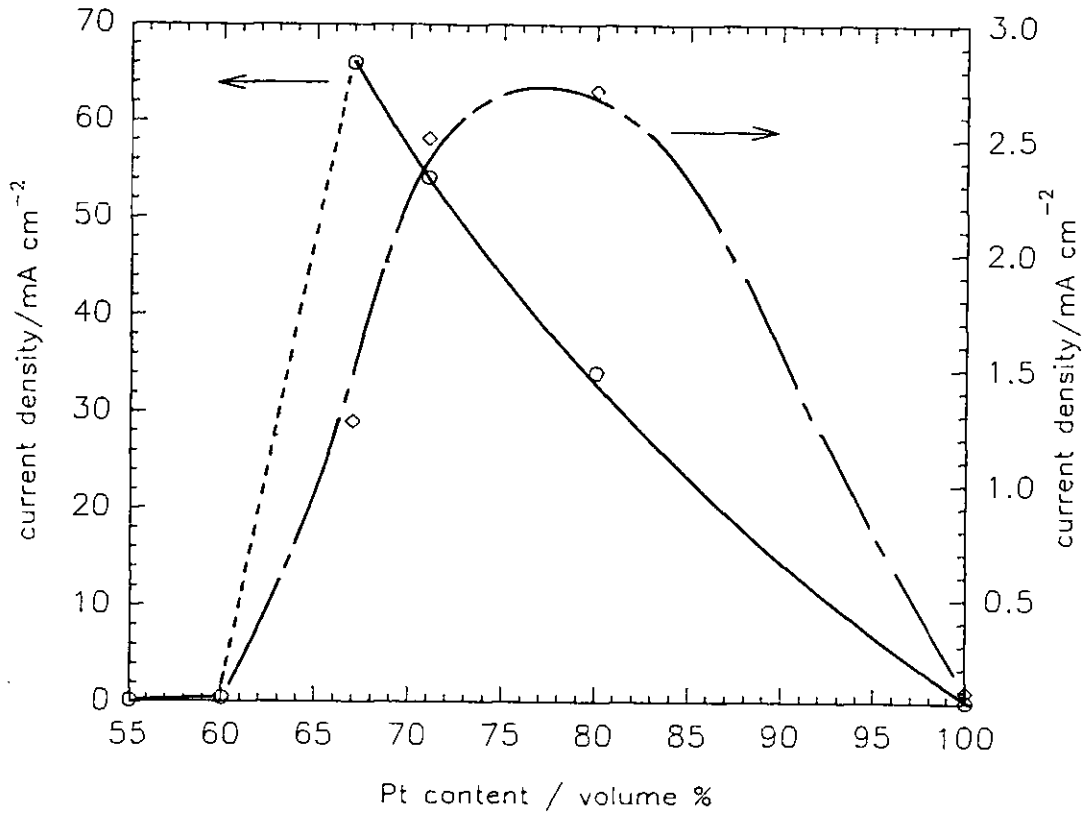

Figure 4.15 *Comparison of current densities at a value of η_T of 500mV (obtained in air at 700°C) for cermet electrodes fired for 1 hour at O,1000°C and ◊,1300°C. The data were interpolated from current density vs η_T plots.*

where I is the steady current flowing through the cell, R_1 and R_2 are the electrolyte resistances between electrode 1 and the reference electrode and electrode 2 and the reference electrode respectively and were measured using the current interruption technique (§ 4.2.4). As electrodes 1 and 2 were prepared to be identical (for each cermet composition) data from both electrodes (obtained at 700°C in air) were compared and found to be essentially the same. Results presented further in this section were obtained using electrode 1 only.

Figure 4.16 shows the natural logarithm of the current density versus the anodic (denoted as positive) and cathodic (denoted as negative) overpotential of an electrode made using cermet 4 at various temperatures. The high overpotential regions ($|\eta|$ >> RT/nF) did not yield linearity. This indicates that charge transfer was probably not the rate controlling step of the electrode reaction [210]. The activation energy

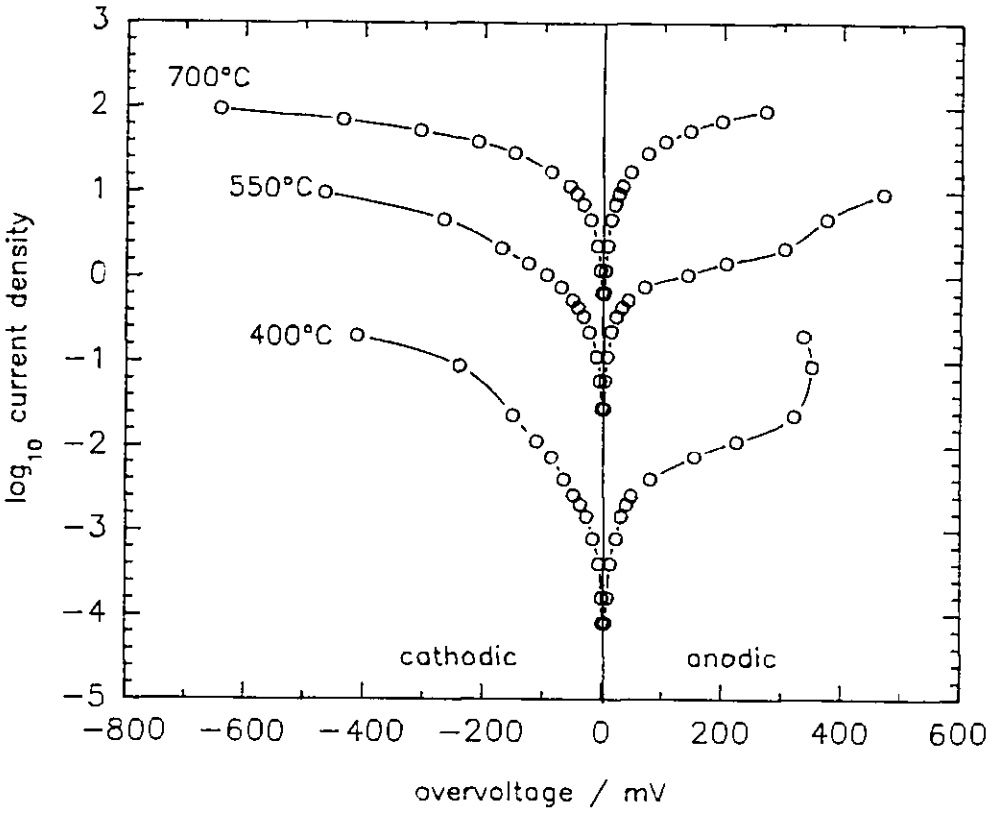

Figure 4.16 *Ln current density vs anodic and cathodic overpotentials (separated using a reference electrode) at various temperatures (in air) for cermet electrode consisting of 66.7% platinum by volume.*

for the electrode reactions was determined from Fig. 4.17 to be ~157 kJ mol^{-1} for the anode and ~125 kJ mol^{-1} for the cathode processes; these are slightly higher than the activation energy for the bulk electrolyte (§ 3.3.2.3). The difference between the anodic and the cathodic activation energies suggests that the rate controlling process was different in the two cases. Such high values of activation energy for the electrode processes eliminates the possibility of gaseous diffusion being rate controlling as this would be expected to show activation energies approximately an order of magnitude lower than those obtained [211]. The value of the activation energy for the anode of 157 kJ mol^{-1} is similar to the activation energy for diffusion of adsorbed oxygen on the surface of platinum [212]. The most probable rate controlling step was diffusion of oxygen atoms across the surface of the platinum to the reaction site [210].

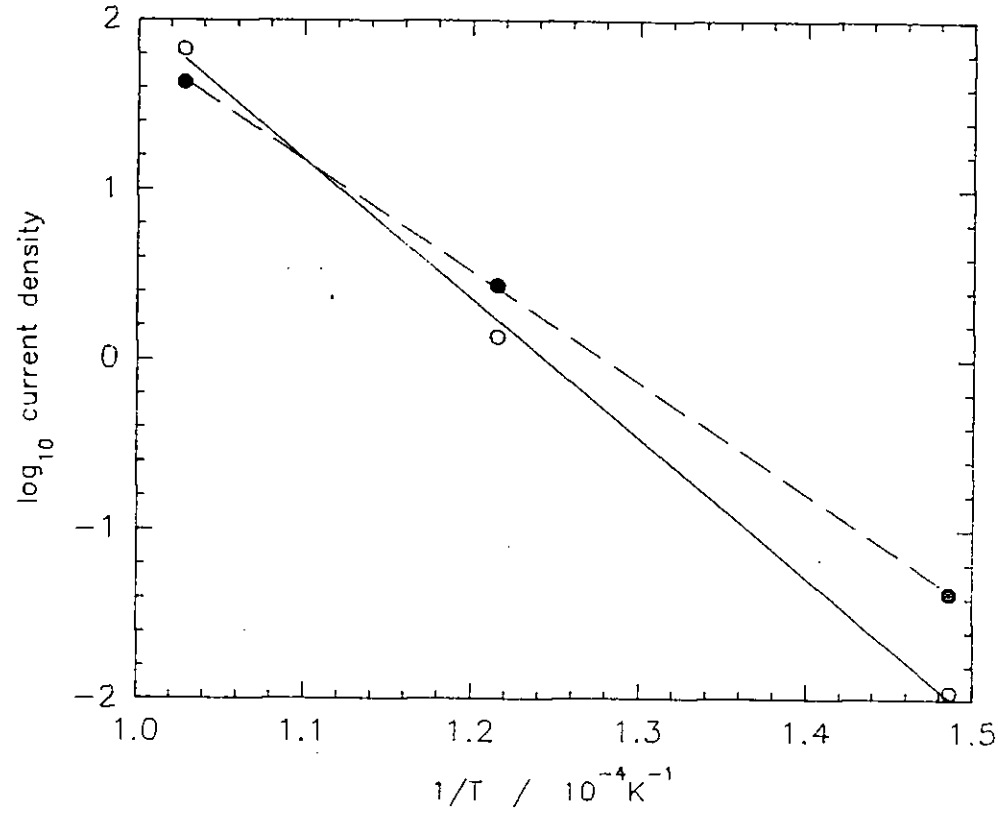

Figure 4.17 *Log of current density at 200mV overpotential vs reciprocal temperature for cermet electrode containing 66.7% platinum by weight.* O; *anodic,* ●; *cathodic.*

Sometimes at high anodic overpotentials (>350 mV) the current began to increase rapidly (as seen in Fig. 4.16). This effect has also been observed by a number of other investigators for platinum [213] and for nickel–zirconia anodes [214]. A rapid increase in the current at high anodic and cathodic overpotentials has been attributed to widening of the *TPB*, possibly by hole and electron injection respectively into the electrolyte [215]. In an air atmosphere hole injection into the electrolyte is expected to occur at much lower overpotentials than electron injection [81] as the latter normally occurs at higher overpotentials than those applied in this work (700 mV cathodic) and much lower oxygen partial pressures ($\sim 10^{-25}$ atm). The observation that a rapid increase in current was observed on the anodic side and not on the cathodic is commensurate with the previous statement.

4.4 SUMMARY

Platinum-yttria stabilised zirconia cermet inks were prepared (by intimately mixing solids and carrier vehicle in a triple-roll mill) for screen-printing onto alumina substrates, zirconia discs and zirconia thick films. Fired films were investigated as possible electrodes for use in thick film sensors.

Scanning electron microscopy revealed that the presence of zirconia in the cermets inhibited grain growth of the platinum. With prolonged firing at temperatures above 1000°C progressive growth of voids was observed.

The electronic resistance of the films at 20°C was measured using a four-point probe. As printed and dried the films were not electronically conducting. On firing at ~500°C the organic binder was removed and electrical continuity was established provided that the platinum content exceeded 55% by volume (zirconia 45%). Prolonged firing above 1000°C progressively increased the electronic resistance of the cermets with firing time after a rapid initial decrease. The increase is thought to have been due to the observed growth of voids of the film and platinum evaporation.

Current densities (per unit geometric electrode area) available at a given overvoltage for electrodes at, for example, 700°C were orders of magnitude higher than those obtainable using porous platinum electrodes and increased with zirconia content of the cermets up to 33% by volume (67% platinum). Current densities also decreased with increasing firing temperature (necessary for preparing a sensor with cofired electrolyte and electrodes).

Measurements on single electrodes, involving the use of a reference electrode, indicated activation energies for the anodic and cathodic processes of 157 and 125 kJ mol^{-1} respectively. The former value suggests that the rate controlling step may have been diffusion of oxygen atoms from the reaction site across the surface of the platinum.

Thus zirconia-platinum cermets have an important role to play in the development of thick-film zirconia oxygen sensors. Besides improving thermal expansion compatibility between the electrode and electrolyte they substantially improved available current densities compared with pure platinum electrodes; this was presumably achieved by the maintenance of a long three-phase boundary length even after treatment at high temperatures (>1300°C) for periods of 1 hour or more.

CHAPTER 5

SCREEN PRINTED AMPEROMETRIC ZIRCONIA OXYGEN GAS SENSORS

5.1 INTRODUCTION

The principles of operation of an amperometric sensor were discussed earlier (§ 1.2.4.3). The sensor normally comprises a non-porous electrolyte separating an anode and a cathode and a diffusion barrier adjacent to the cathode to restrict the diffusion of oxygen from the sample gas. In the screen-printed sensor described below the zirconia thick film performs the functions of both the electrolyte and the diffusion barrier. Such a device has once been previously reported [70]: the resulting sensor operated at concentrations of oxygen up to 0.1% only, indicating that the screen-printed zirconia films were excessively porous.

Zirconia thick films were discussed in chapter 3 and cermet electrodes in chapter 4. In this chapter these components have been laminated by successive print-dry-fire processes to form a working amperometric oxygen sensor.

5.2 THEORY OF OPERATION

A schematic representation of the cross-section of the sensor is shown in Fig. 5.1. In operation a voltage was applied across the electrodes reducing oxygen at the cathode and evolving it at the anode

$$O_2 + 4e \rightleftharpoons 2O^{2-} \qquad (1.2)$$

Thus oxygen was electrochemically pumped from the cathode to the anode via the electrolyte. This created a concentration gradient resulting in the diffusion of oxygen from the sample gas through the porous ceramic to the cathode.

The rate of diffusion of oxygen, J, through the porous electrolyte to the cathode may be expressed in terms of Fick's first law as described in Eq. (5.1),

$$J = -D_1 S \frac{dc}{dx} \qquad (5.1)$$

where D_1 is the molecular diffusion coefficient of oxygen through the total open area S, of the diffusion paths and c is the oxygen concentration at distance, x, from the cathode. This applies in isothermal conditions in the direction of flow. If the type of diffusion in the pores is the same as in the bulk gas, it should be noted that D_1 is

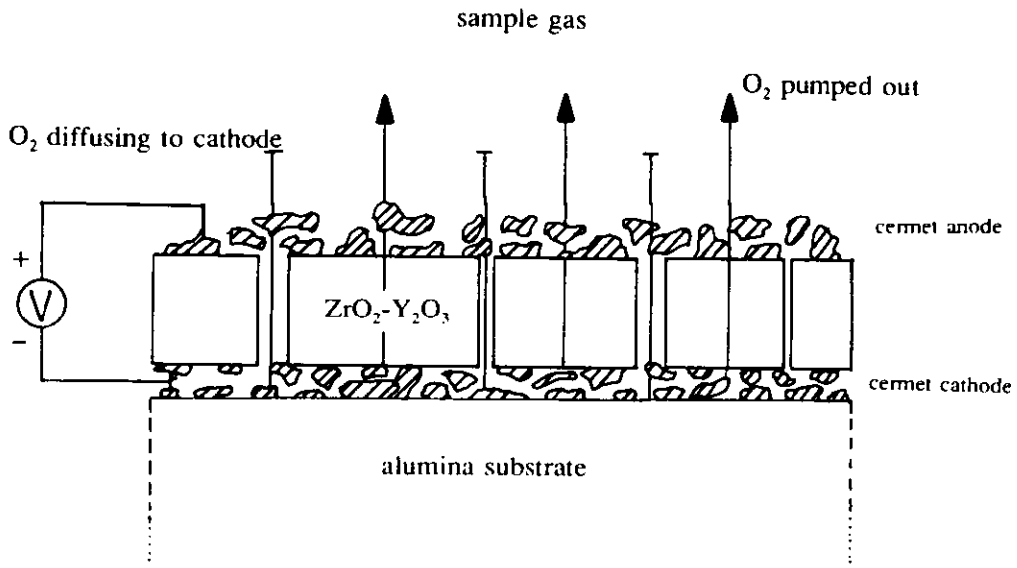

Figure 5.1 *Schematic representation of the cross section of the thick-film amperometric sensor.*

related to D_{O2}, the diffusion coefficient in the bulk gas by

$$D_1 = D_{O2}/\theta^2 \tag{5.2}$$

where θ is the tortuosity of the pores [209]. For gases it is convenient to express concentration in terms of partial pressure. From the ideal gas law the concentration, defined as the number of moles per unit volume, can be expressed as c = P/RT where P,R and T are the pressure, ideal gas constant and temperature respectively. Substituting this and the oxygen concentration boundary conditions into Eq. (5.1) it follows that,

$$J_{O_2} = -\frac{D_1 S}{RT}\frac{dp}{dx} = -\frac{D_1 S}{RT\ell}\left[p_{O2}(sg) - p_{O2}(c)\right] \tag{5.3}$$

where ℓ is the thickness of the electrolyte layer, $p_{O2}(sg)$ and $p_{O2}(c)$ are the oxygen partial pressures of the gas surrounding the sensor and at the cathode respectively (Fig. 5.1). The transfer of one mole of oxygen requires 4 faradays of charge (Eq. (1.2)). The current I, flowing through the electrolyte is then given by Eq. (5.4),

$$I = J\,4F \tag{5.4}$$

In the steady state there is no diffusion of gas from the bulk to the sensor, consequently there is no need to consider a diffusion layer adjacent to the sensor. When a sufficient voltage is applied so that the oxygen partial pressure at the cathode is reduced close to zero, the current reaches a limiting value (§ 1.2.4); it follows that by substitution of Eq. (5.4) in (5.3) and assuming $p_{O2}(c)$ to be essentially zero the current is limited (denoted as I_{lim}) and is described by Eq. (5.5),

$$I_{lim} = -\left(\frac{4FD_1S}{RT\ell}\right) p_{O2}(sg) \tag{5.5}$$

Eq. (5.5) indicates that the limiting current should be proportional to the oxygen partial pressure in the sample gas. Hence at constant barometric pressure the device should enable oxygen concentrations to be determined from a measurement of the pumping current in the limiting region.

5.3 EXPERIMENTAL

5.3.1 Device Fabrication

The cathode of the sensor was first screen-printed using a platinum-YSZ cermet ink onto the substrate as a circular disc with extended pads for electrical connections. This was dried at 150°C and 400°C for 10 minutes at each temperature to remove the organic vehicle and fired at 1000°C for 10 minutes before it was overprinted with the electrolyte paste which was dried and fired to sinter the zirconia as required. Finally, the anode was printed onto the electrolyte using the same cermet composition as that of the cathode, dried and fired for 30 minutes at the same temperature as was the electrolyte. The processing conditions of each layer were as follows. The film was (i) printed and left to settle at room temperature for 10 minutes; (ii) dried at 90°C, 155°C, and 400°C for 10 minutes at each temperature; (iii) fired at 1000°C for 10 minutes prior to receiving the final sintering treatment. A diagram of the sensor is shown in Fig. 5.2a together with a photograph (Fig. 5.2b).

The fired thickness of the electrode layers was in all cases 6 μm. The thickness of the electrolyte layer resulting from a single print-dry-fire cycle was 8-9 μm.

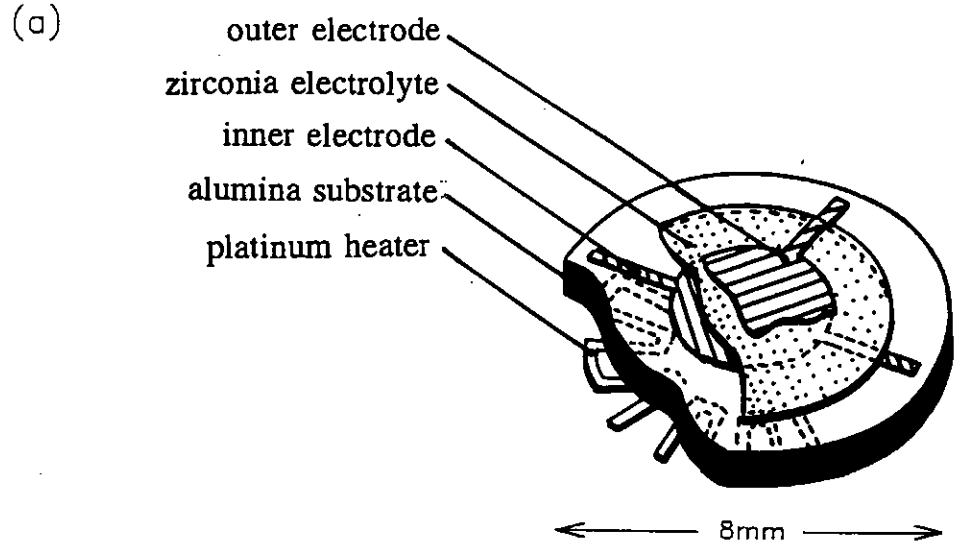

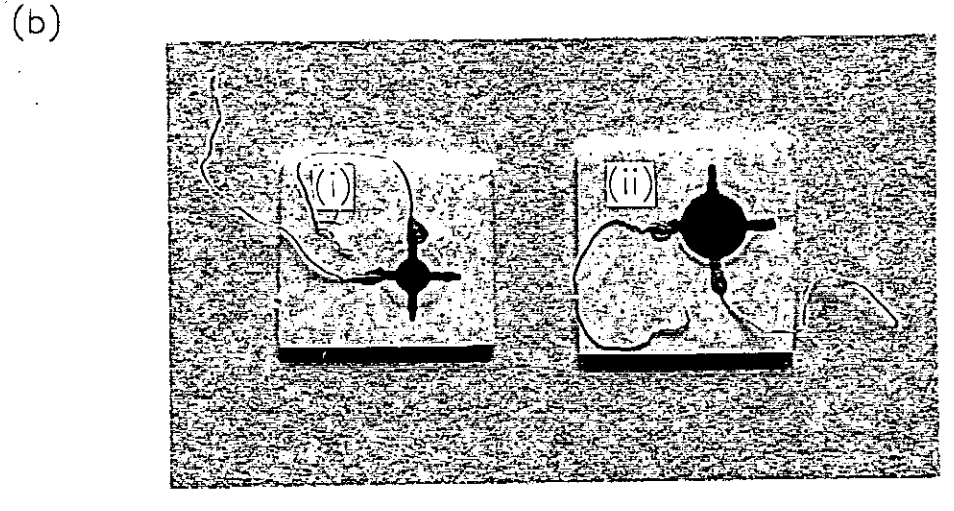

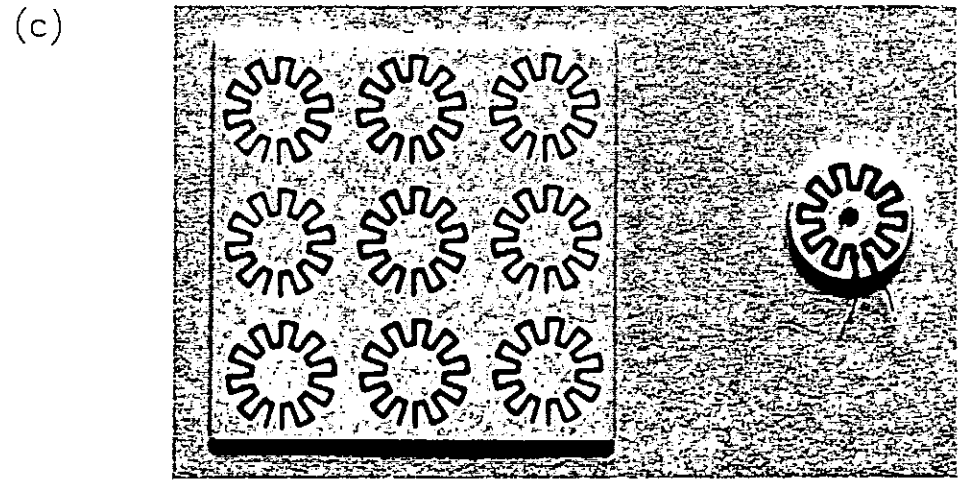

Figure 5.2 *(a) Cutaway perspective view of the thick-film amperometric oxygen gas sensor, (b) photograph of sensor with electrode areas of (i) 0.031 cm^2 and (ii) 0.126 cm^2, (c) photograph of platinum heater.*

Thicker layers were built up by successive print-dry cycles, followed by a single firing step. Platinum wires 100 μm in diameter were then connected to the anode and the cathode using fritless platinum paste which was subsequently sintered (1000°C for 10 minutes) to establish adequate bonding.

The composition and sintering treatments of the various devices prepared are shown in Table 5.1. Note that sensors 1-3 were made using a single zirconia paste (paste 4d consisting of 40% by weight 3Y zirconia mixed with ESL type 400 vehicle); the remaining sensors were made using a zirconia paste of the same composition but prepared at a different time.

Sensor Nº	Electrode composition %Pt in 3Y	Electrode area cm^2	Firing temperature for 1 hour (°C)	Alumina substrate	
				96%	99.6%
1	71.4	0.031	1350	*	
2	71.4	0.031	1400	*	
3	71.4	0.031	1450	*	
4	71.4	0.126	1500	*	
5a	80.0	0.126	1400	*	
5b	80.0	0.031	1400	*	
6a	80.0	0.126	1400		*
6b	80.0	0.031	1400		*
7	80.0	0.031	1400	*	

Table 5.1 Construction and firing cycles of the thick-film devices discussed. In all cases the thickness of the electrode and electrolyte were ~6 and ~30 μm respectively.

Generally devices were brought to the appropriate operating temperature using a furnace (§ 2.3.12). One device (sensor 7) was prepared having an integral thick film heater (Fig. 5.2c) printed onto the reverse side of the alumina substrate; the heater was used to elevate the temperature to an operating value of 700°C eliminating the need for an external furnace in this case. The sensor was mounted on a transistor header which fitted a compatible transistor socket fixed in a brass socket. Connections to the anode, cathode and heater were made using 100 μm platinum wires. A type R (Pt - Pt 13% Rh) thermocouple (made using 40 μm diameter wire) was also attached onto the alumina substrate next to the sensor using platinum paste (subsequently fired to sinter and adhere onto the alumina).

5.3.2 Device characterisation

The devices were tested to check (a) short circuiting between electrodes and (b) electrical discontinuity in any one electrode. The observation of either (a) or (b) above meant that the device could not be operated as described in section 5.2. The devices were characterised at various temperatures and oxygen concentrations using the experimental arrangement described earlier (§ 2.3.13). Tests were conducted in the range of oxygen concentrations from 0–21%. A given DC voltage was applied across the electrodes and the resulting current measured (Fig. 5.1). Sensor 7 was operated both in the laboratory in air-nitrogen mixtures and in a gas burning flue. In the former case the experimental arrangement is shown in Fig. 5.3 and the composition of the gases was controlled using the gas mixing arrangement described in section 2.3.12. The gas mixture flowed through a silicone hose into the internal volume of a brass chamber and out through a bubbler. The silicone hose connecting the mass flow controllers to the sensor chamber was approximately around 40cm long. In the latter case the sensor was exposed to the gases in the exhaust of a gas burning system at British Gas (Watson House Research Station); further details are given in Appendix C.

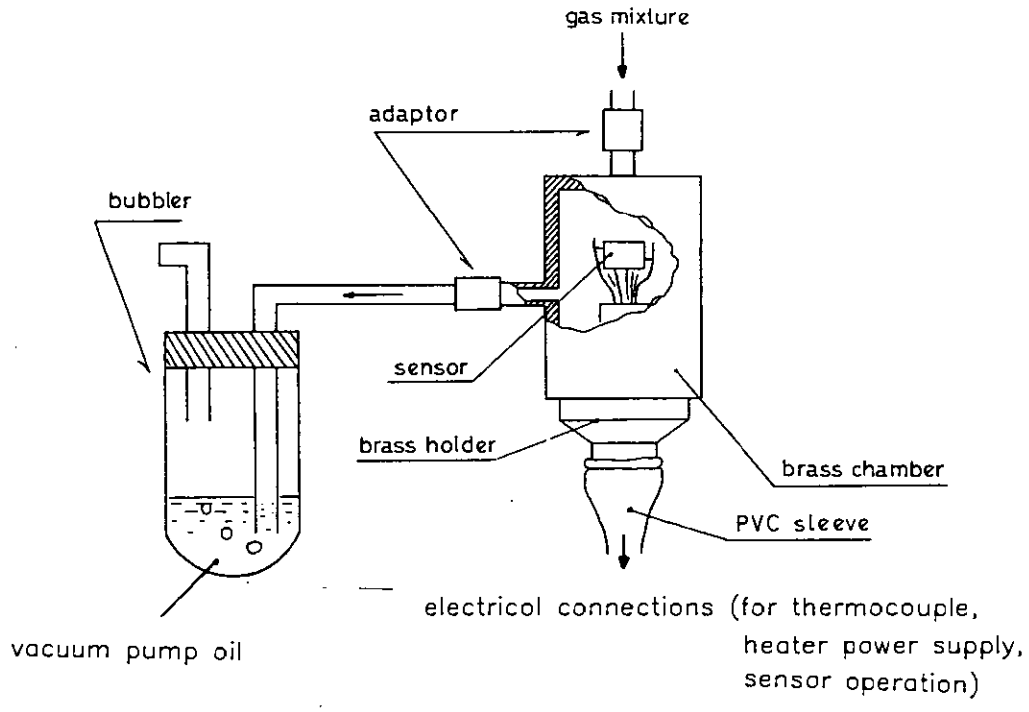

Figure 5.3 Sensor with integral platinum heater, mounted in brass chamber.

5.4 RESULTS AND DISCUSSION

5.4.1 Initial findings

Firing temperatures below 1350°C resulted in short circuiting between the electrodes possibly due to a high level of porosity in the ceramic. Sensors constructed using pure platinum electrodes resulted in cracked electrolytes (possibly the result of the large thermal expansion difference between platinum and zirconia) and poor electrode activities. These problems were overcome by the use of platinum-zirconia cermet electrodes [192].

Electrodes made by screen printing cermets 4-6 (§ 4.3.1, Table 4.1), became electronically discontinuous when overprinted with zirconia electrolyte and fired above 1300°C whereas the same cermet compositions were electronically continuous when not overprinted and fired at temperatures up to 1500°C; this may have been caused by a decrease in the metallic volume fraction of the cermets which could have resulted from inter–diffusion between electrode and electrolyte during co–firing.

5.4.2 Microscopy

The fracture edge of a sensor prepared precisely as sensor 2, examined using scanning electron microscopy, is shown in Fig. 5.4. The individual components can be identified and a low porosity of the sintered zirconia is apparent.

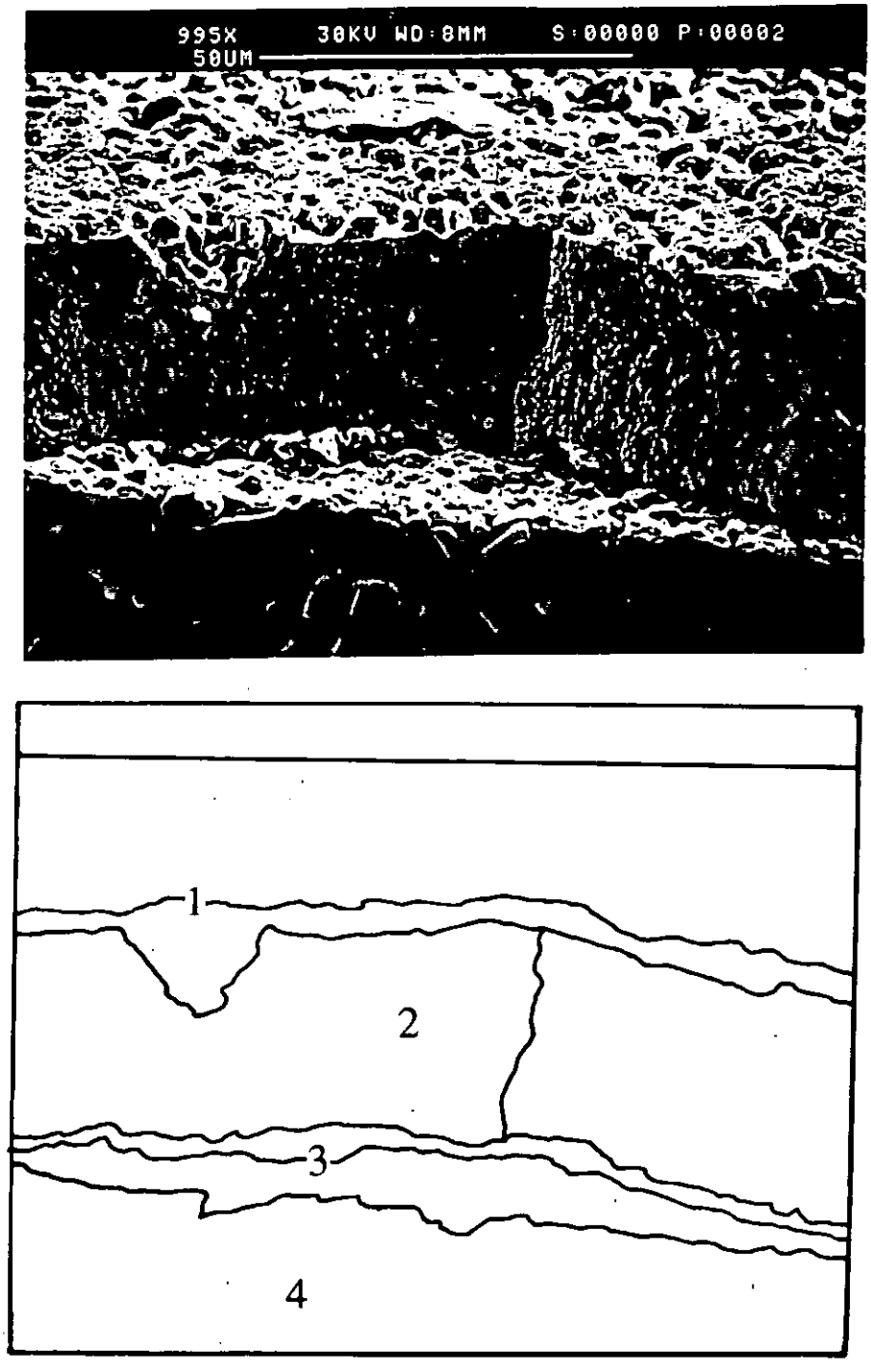

Figure 5.4 Scanning electron micrograph of sensor fracture edge showing: 1; cermet anode, 2; zirconia electrolyte, 3; cermet cathode, 4; alumina substrate.

5.4.3 Current–voltage characteristics

Current-voltage (I–V) characteristics of sensors 1-4 in air-N_2 mixtures are shown in Figs. 5.5–5.8. The shape of the I-V data is similar to that observed for devices constructed from discrete components [24,216]. Clearly the zirconia thick-film was acting both as an electrolyte and as a diffusion barrier [190,191] as was required for satisfactory operation. Oxygen diffused through the pores of the electrolyte to the cathode where it was reduced to O^{2-}. These O^{2-} ions migrated in the electric field to the anode where they underwent charge transfer and were evolved as O_2.

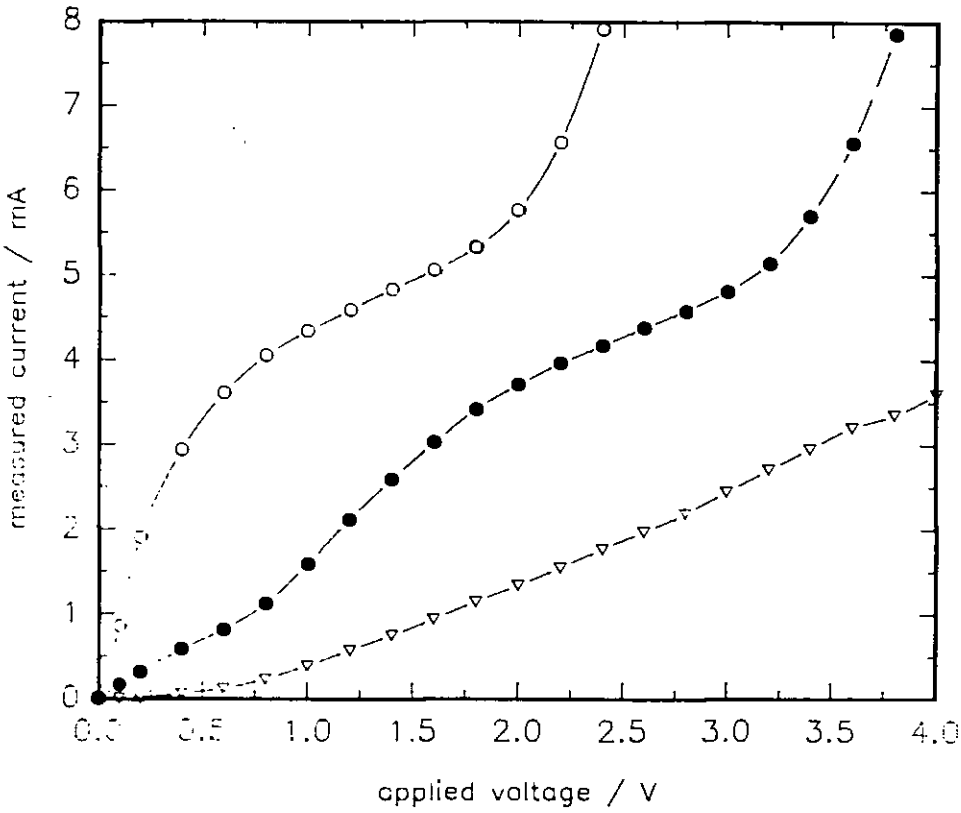

Figure 5.5 Current - voltage characteristic of sensor 1 operated at various temperatures in 2% oxygen. Temperature: ▽,550°C; ●,650°C; ○,700°C.

The I-V curve showed four regions (i to iv) (Fig. 5.9) which were interpreted as follows.

(i). Starting from a small applied voltage it was found that the current increased exponentially, particularly at low temperatures. This indicated that the reactions at

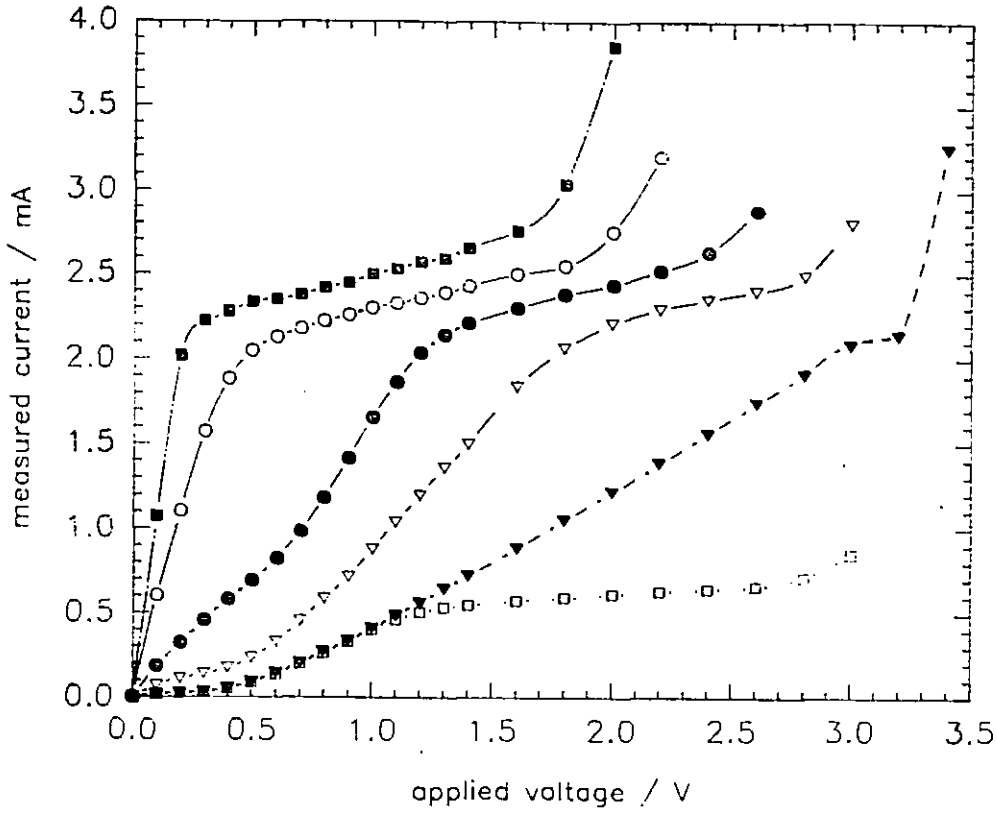

Figure 5.6 *Current voltage characteristics of sensor 2. Operating temperature:* ■; *900°C,* O; *800°C,* ●; *700°C,* ▽; *650°C,* ▼ ,□; *600°C. Oxygen concentration:* ●,O,●,▽,▼; *21%,* □; *6%.*

the electrodes were rate controlling [211,217].

(ii). Increasing the applied voltage further showed an ohmic region; the current increased linearly with the applied voltage as would be expected if the current rise were controlled by the ohmic resistance across the electrolyte (i.e the pump).

(iii). The third region showed a limiting current over a range of applied potentials; the limiting current was proportional to the oxygen concentration (§ 5.4.4) as predicted by the theory of section 5.2.

(iv). Increasing the applied voltage beyond region III produced a rapid increase in the current caused by the onset of electronic conductivity due to the generation of electronic carriers at high cathodic overvoltages [32].

$$O^{x}_{o} \rightleftharpoons \tfrac{1}{2}O_2 + V^{\cdot\cdot}_{o} + 2e' \qquad (1.9)$$

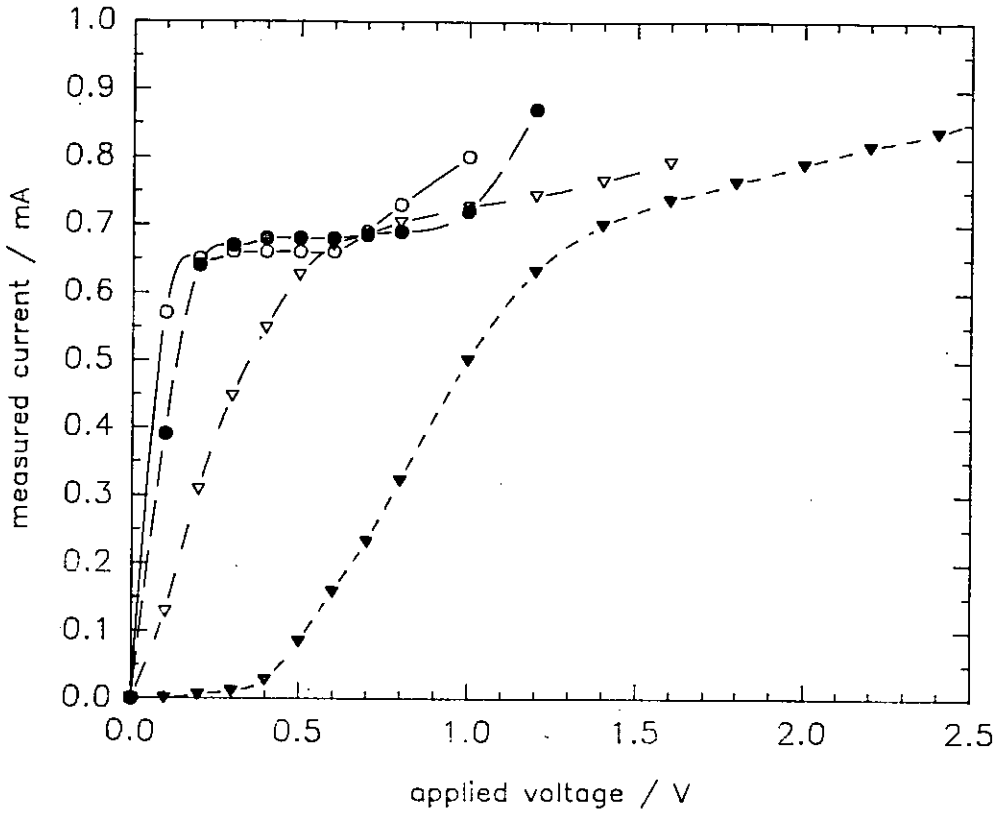

Figure 5.7 *Current voltage characteristics of sensor 3 in 1% oxygen-in-nitrogen. Operating temperature:* ○*,950°C;* ●*,850°C;* ▽*,650°C;* ▼ *,550°C.*

The limiting current plateaux (region (iii)) were in most cases not precisely parallel with the voltage axis indicating the presence of oxygen leakage to the cathode. Leakage may occur by a number of mechanisms such as physical, electrochemical and semipermeability [218]. Electrochemical leakage has been identified to be the most significant in amperometric devices incorporating a metal seal constructed from discrete components [59]. Electrochemical leakage occurs when electrical contacts which form three-phase boundaries both inside (i.e the volume around the cathode) and outside the cell exist. The potential gradient about the sealed volume causes electronic transport in the metal and ionic transport in the ceramic, the net result being the transfer of oxygen from the high to the low partial pressure side (i.e from the outside to the cathode). The thick–film devices described are complex systems and a leakage analysis has not been attempted.

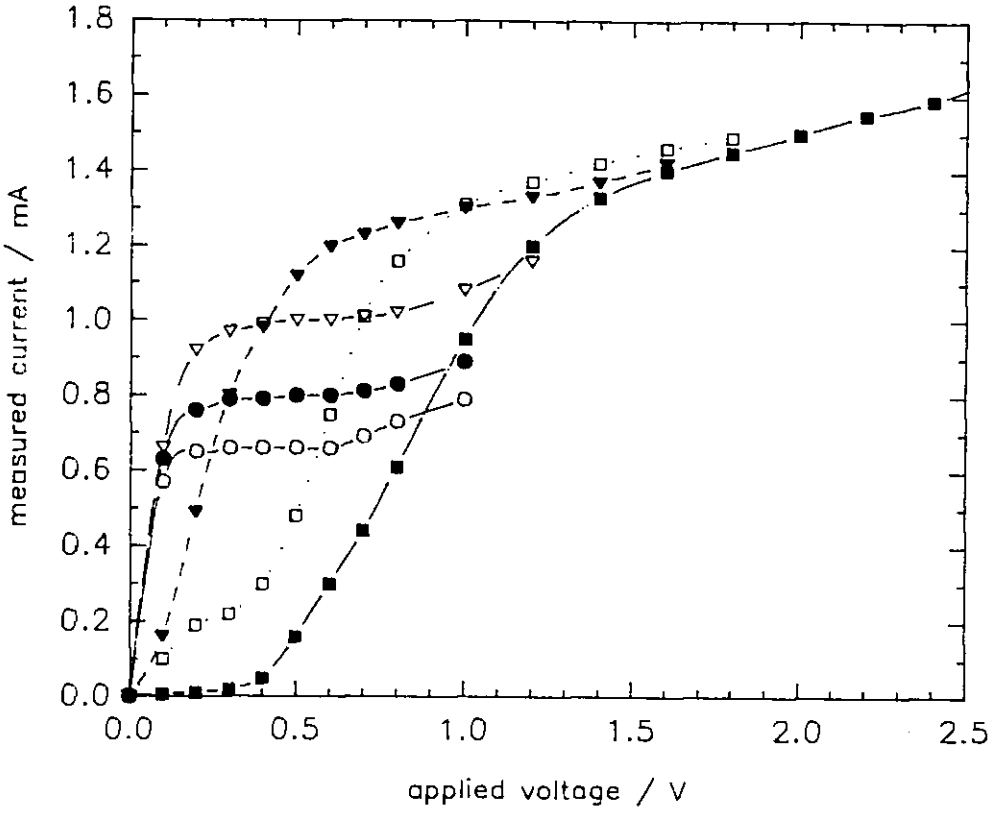

Figure 5.8 *Current voltage characteristics of sensor 4 in 0.5% oxygen. Temperature: 950°C, ●; 850°C, ▽; 750°C, ▼; 650°C, □; 600°C, ■; 550°C.*

5.4.4 Dependence of the limiting current on the oxygen concentration

Theory predicts a limiting current I_{lim} proportional to oxygen concentration of the sample gas, c_{O2}, at a given barometric pressure; however it is difficult to define unbiased criteria for selecting the limiting current value with sloped current plateaus. In the simplest mode of operation, devices would be operated at a fixed applied voltage and the current monitored as an indication of the oxygen concentration. Ideally measurement of the oxygen concentration requires the application of sufficient voltage to measure the current in the limiting condition.

It can be seen from Fig. 5.10 that the current - voltage characteristics were sensitive to the oxygen concentration. The chosen operating pump voltage was a compromise between two factors. A high value (>1.4V) resulted in the onset of electronic conduction in the zirconia of the pump. Conversely a low value (<0.6V) led to a current partially controlled by factors other than diffusion. At an intermediate

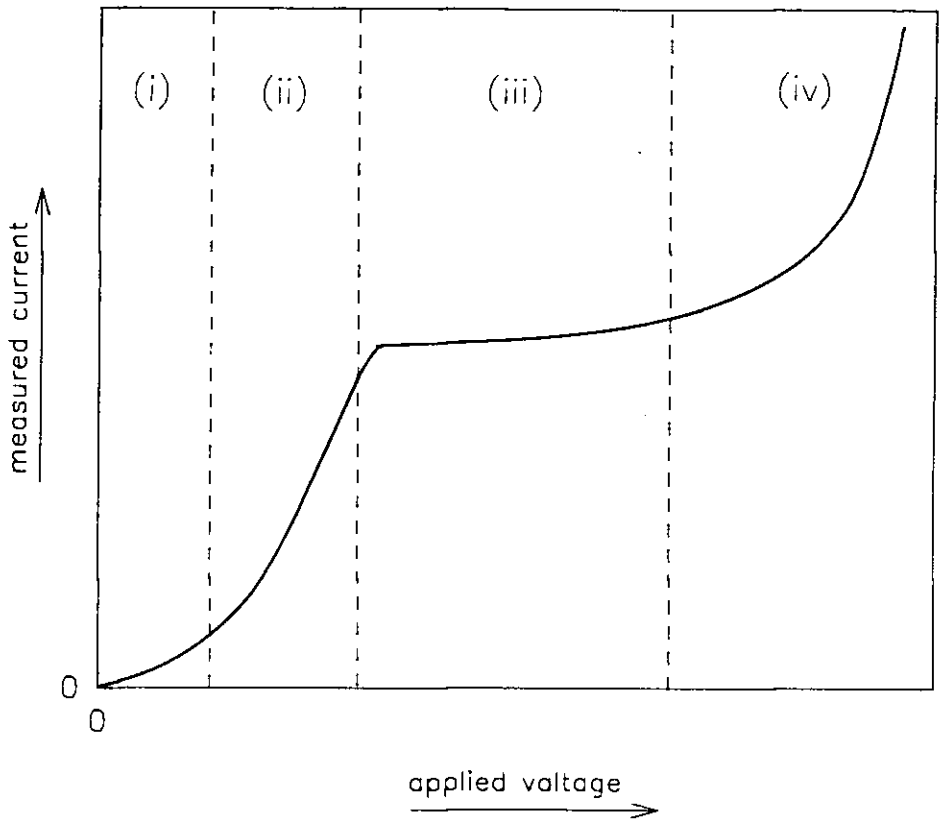

Figure 5.9 *Typical current - voltage characteristic exhibited by the sensor.*

value (0.8-1.2V) the current was primarily controlled by diffusion through the barrier over the range of concentrations shown and resulted in a linear characteristic (Fig. 5.11).

The results of the measured current at fixed applied voltage for sensors 2, 3 and 4 are shown in Fig. 5.11. The linearity was good for all three sensors indicating that they behaved according to the theory described in § 5.2. There was a small deviation from linearity observed at high c_{O2} values due to the applied voltage being insufficient fully to reach the limiting condition. However at a selected fixed applied voltage for each sensor it was possible to measure oxygen concentrations up to 21% which is adequate for most sensor applications. The largest market for oxygen sensing is expected to be in the area of combustion control which normally requires detection in the region of 2-5% oxygen [6]. The fact that the sensors can operate at a fixed applied voltage is advantageous because it enables the use of simple electronics.

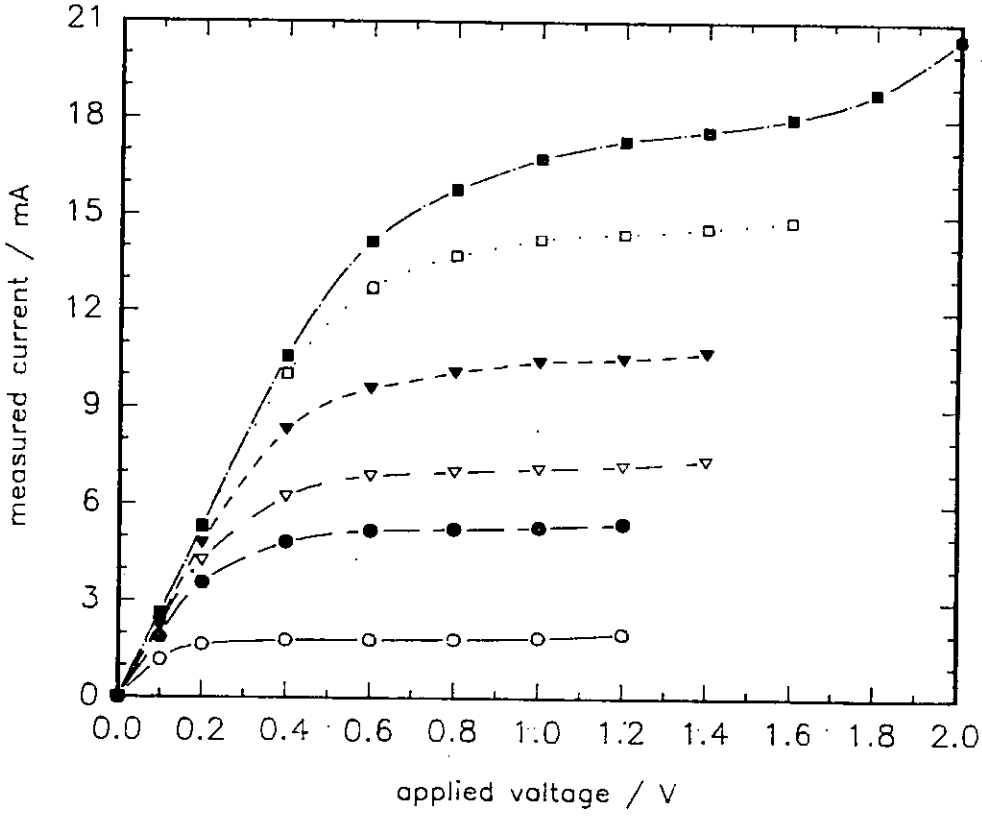

Figure 5.10 Current-voltage characteristic of sensor 4 at 800°C. Oxygen concentration in nitrogen: ○,1%; ●,3%; ▽,4%; ▼,6%; □,8%; ■,10%.

Figure 5.12 shows the current – oxygen concentration characteristic of sensor 7 operated at 1.4V and 700°C. The operating temperature was maintained using a platinum heater printed on the reverse side of the substrate. The linearity was good at low oxygen concentrations but deviated at higher oxygen concentrations; this was because the applied voltage was insufficient to achieve the limiting condition in that region (Fig. 5.13).

5.4.5 Dependence of the limiting current on temperature

Comparison of Figs. 5.5-5.18 indicates that sensor 1 showed a less well-defined transition into the diffusion limited plateau with increasing applied voltage than sensors 2, 3 and 4: furthermore, the plateau for sensor 1 showed a greater slope than for the other sensors. This may indicate the presence of pores with a wide range of sizes due to the lower temperature at which sensor 1 was sintered. Such a spread could possibly result in the characteristics observed on the basis that large pores may

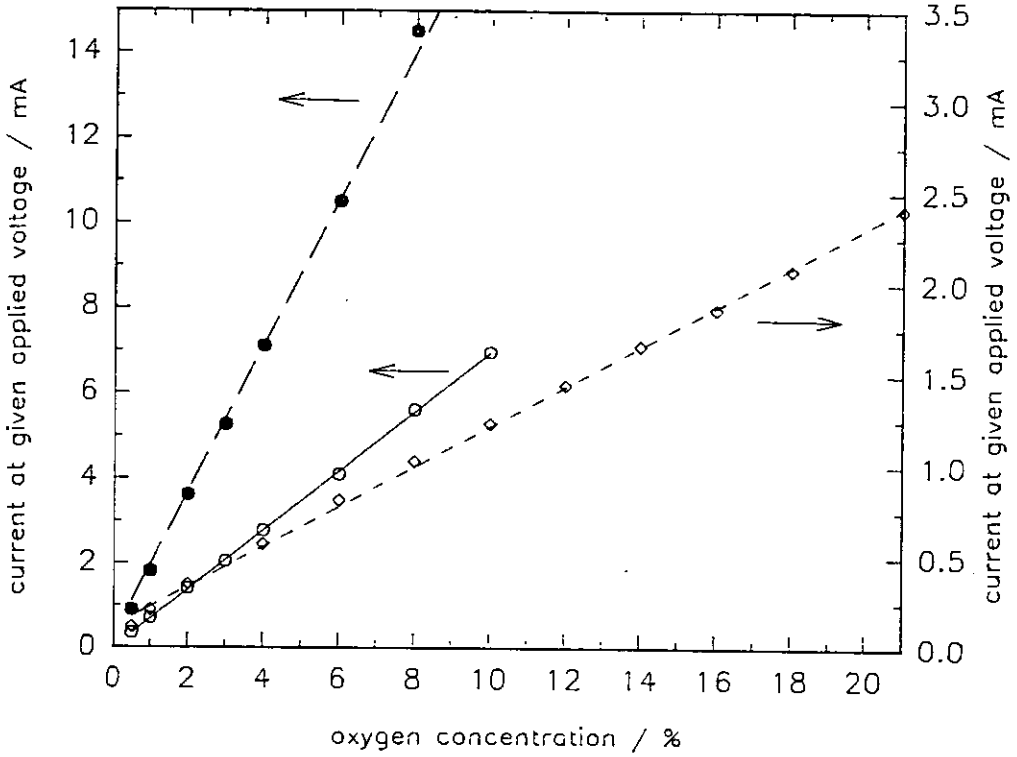

Figure 5.11 *Current vs oxygen concentration for given applied voltages across the cell at 800°C. ♦ ; sensor 2 at 1.0V, O; sensor 3 at 0.8V, ●; sensor 4 at 0.5V.*

require a greater applied voltage to reach the limiting current than small ones: the observed characteristics would be the summation of many such individual curves.

Limiting currents showed only a small dependence upon temperature for sensor 2 as would be expected if the controlling process were gaseous diffusion. An interesting feature of the results was that the limiting current showed an increase with temperature for sensor 2 but a decrease for sensors 3 and 4 (Fig. 5.14 and Table 5.2). A temperature variation was expected due to changes in the diffusion coefficient of oxygen with temperature. It is tempting to speculate that dependences on $T^{0.6}$ and $T^{-0.5}$ for sensors 2 and 3 may indicate predominantly bulk and Knudsen diffusion respectively [33]: however the dependence of the limiting current of $T^{-2.4}$ noted for sensor 4 could not be fitted to this proposition and indicates the need for further investigations. Nonetheless, the switch from a positive to a negative temperature coefficient resulting from a change in sintering conditions offers the prospect of

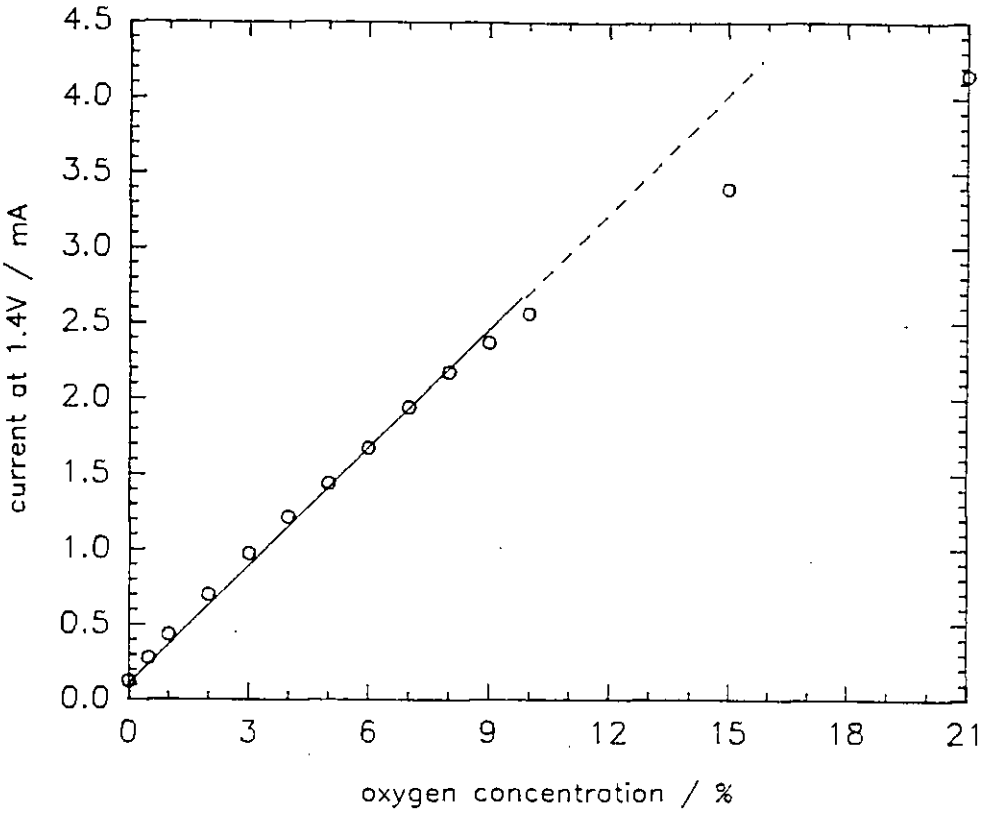

Figure 5.12 *Current vs oxygen concentration for sensor 7 operating at 700°C with an applied voltage of 1.4V.*

designing sensors with a zero temperature coefficient. For sensor 1 the limiting current plateaus were not well defined and indicated a larger positive temperature dependence than could be attributed to bulk diffusion. This may have been due to an ohmic contribution to the total current arising from the presence of large pores that did not act as effective gaseous diffusion barriers (the variation with temperature of the electrolyte resistance is significantly higher than that of gaseous diffusion).

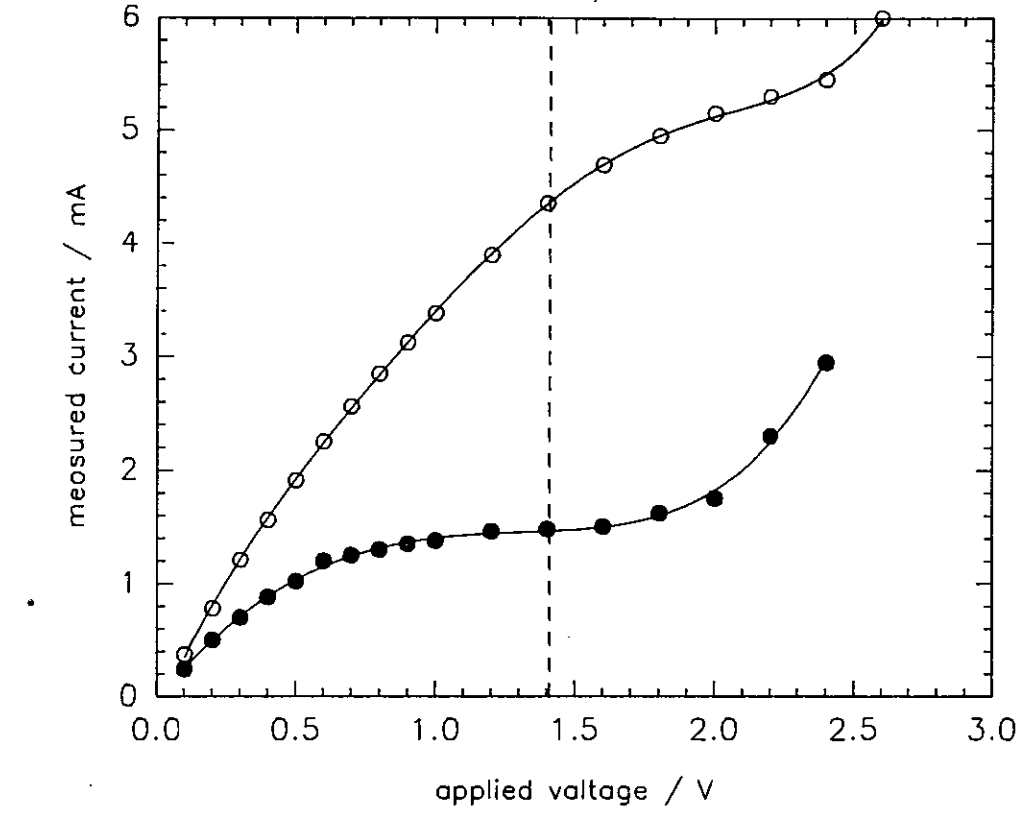

Figure 5.13 *Current-voltage characteristic for sensor 7 operating at 700°C. Oxygen concentration in nitrogen:* O; *6%* , ●; *21% oxygen.*

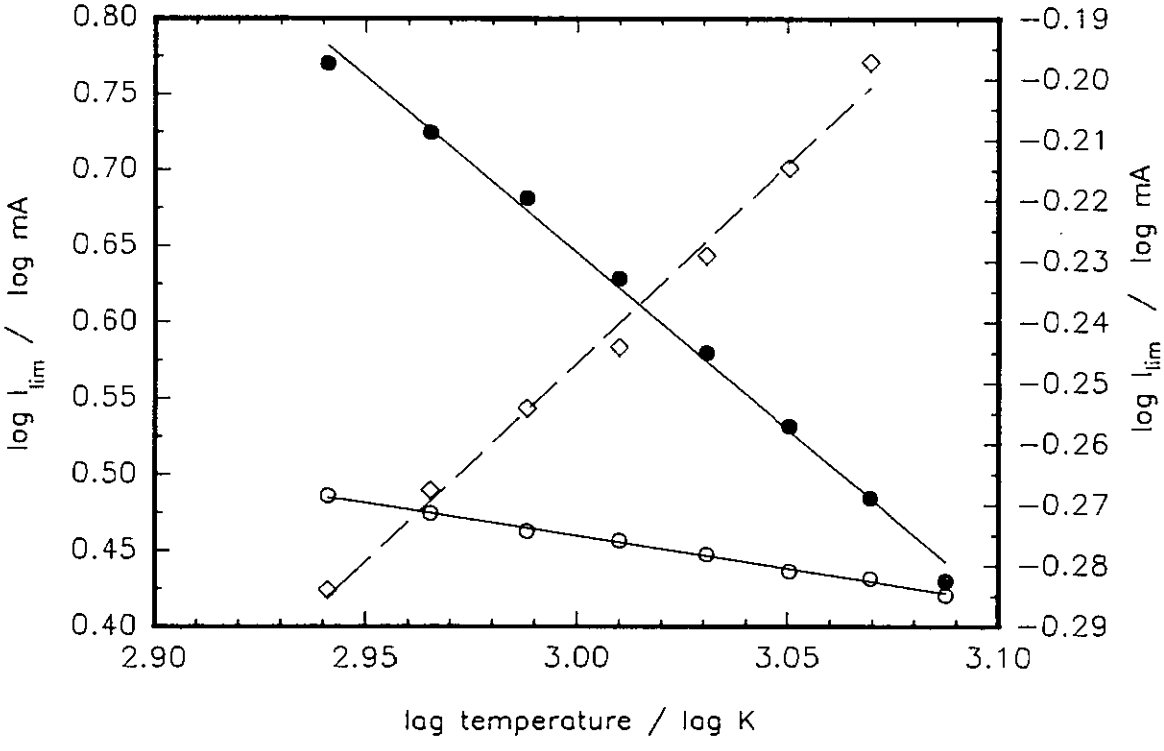

Figure 5.14 *Temperature dependence of the limiting current. Sensor/ oxygen concentration:* ●,*sensor 4 / 2%;* ♦, *sensor 2 / 4%;* O,*sensor 3 / 4%.*

	slope			intercept		
% O_2	sensor 2	sensor 3	sensor 4	sensor 2	sensor 3	sensor 4
0.5			–2.43			7.34
1	0.63	–0.46		–2.6	1.2	
2			–2.33			7.60
4	0.65	–0.45		–2.2	1.8	
8	0.62	–0.44	–2.39	–1.8	2.1	8.35
Average	0.63	–0.45	–2.38			

***Table** 5.2 Effect of temperature on the limiting current. Slope and intercept of plots of log (limiting current) vs log T (current/mA; T/K)*

5.4.6 Effect of substrate composition on the electrode resistance

Complex impedance measurements were performed along the plane of zirconia films deposited onto 96 and 99.6% pure alumina (§ 3.2.4). The electrodes (fritless platinum) were deposited over the zirconia. The influence of substrate composition on the ionic conductivity of the sample was discussed previously (§ 3.3.3.3). The complex impedance plots of two zirconia films of similar thickness (~6 μm) which received identical firing treatment (1400°C for 1 hour) and measured at 800°C in air are shown in Fig. 5.15. It is clear that the resistance attributed to the electrode was higher, very approximately by an order of magnitude for the cell sintered on the less pure substrate. This is presumably due to glassy impurities diffusing from the 96% alumina through the zirconia film to the electrodes. The presence of glassy phases on an electrode has previously been shown physically to block electrochemical reaction sites at the electrode-electrolyte-gas three phase boundary and increase electrode resistance [200].

Although the data reported were not obtained on a complete sensor the electrode responses for the films sintered on the 96 and 99.6% aluminas can still be compared. The observed increase in electrode response on 96% alumina did not seem to detract

from the functionality of complete devices. This may be because lower current densities were required to reach the limiting condition for devices sintered on 96% alumina as opposed to 99.6% alumina due to the corresponding lower porosity of devices made on the former substrates (§ 5.4.7).

5.4.7 Influence of substrate composition and electrode area on the limiting current

Figure 5.16 shows current - voltage characteristics at 4% oxygen-in-nitrogen of devices 5 (a and b) constructed on 96% alumina and 6 (a and b) constructed on 99.6% alumina. The letters a and b represent geometric electrode areas of 0.126cm^2 and 0.031 cm^2 respectively. Differences in the electrode area and alumina substrate aside, the devices were constructed to be identical; further details of their construction are shown in Table 5.1 (§ 5.3.1). The current - voltage characteristics exhibited limiting current behaviour, and for all devices an applied voltage of 1.2V was representative of the limiting current at the illustrated oxygen concentration (4% O_2 in N_2).

Figure 5.17 shows the current measured for various oxygen concentrations during sensor operation with an applied voltage of 1.2V for devices 5 (a and b) and 6 (a and b). The data were linear through the origin of Fig. 5.17 for all four devices indicating that the current measured was the limiting current.

A plot of I_{lim}/p_{O2} versus electrode area derived for devices 5 (a and b) on 96% alumina and 6 (a and b) on 99.6% alumina, from Fig. 5.17, are shown in Fig. 5.18. According to Eq. (5.4) the ratio I_{lim}/p_{O2} should vary in direct proportion to the total open geometric area of the diffusion paths S, provided that the diffusion path length ℓ, remains constant. During sensor operation a concentration gradient was set-up between the cathode and the sample gas; thus oxygen could only diffuse through a geometric area of the electrolyte defined by the area of electrode overlap. The values of the ratio I_{lim}/p_{O2} varied in direct proportion to the geometric area of the electrode supporting the proposition that diffusion was occurring through a multitude of diffusion paths within the electrolyte.

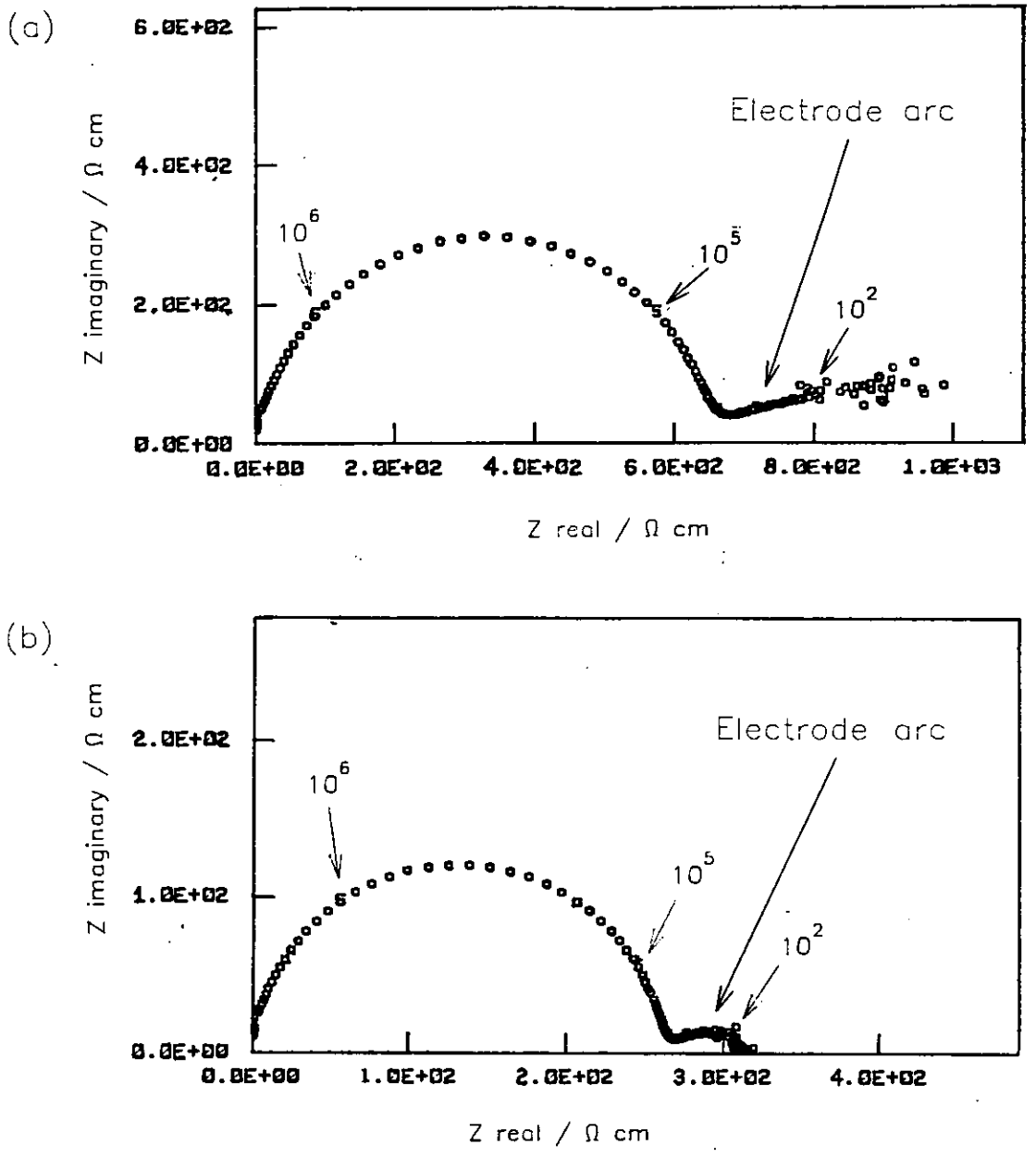

Figure 5.15 *Complex impedance plots at 800°C in air of zirconia films with overprinted cermet electrodes (cermet No. 3, Table 4.1, § 4.3.1). The zirconia was printed and fired under identical conditions (1400°C for 1 hour), onto (a) 96 and (b) 99.6% alumina. The electrodes were fired at 1100°C for 10 minutes. The electrolyte was ~6μm thick. Numbers in powers of 10 denote the measurement frequencies in Hz.*

Limiting current densities were around 4 times greater for devices sintered on 99.6% alumina indicating greater electrolyte porosity compared to devices sintered on 96% alumina (Fig. 5.17). The lower porosity for the latter devices may have been the result of glassy impurities which diffused into the electrolyte from the less pure

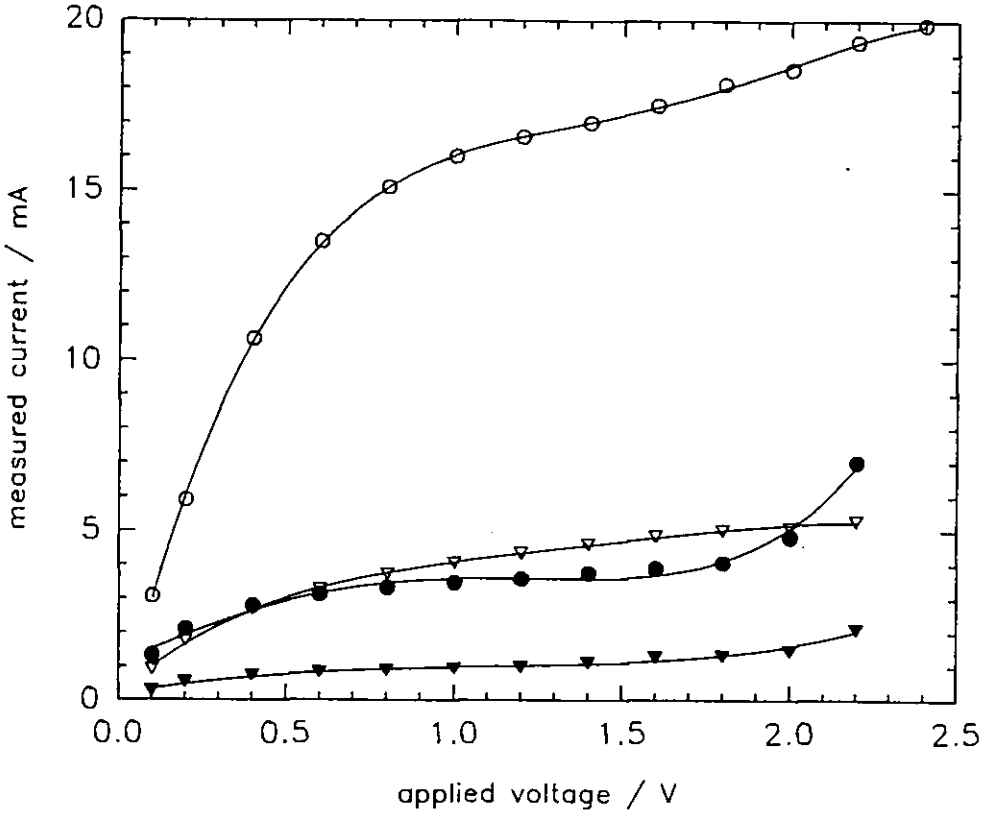

Figure 5.16 Current - voltage characteristics in 4% O_2 in N_2 for sensors operating at 800°C: ▽,sensor 5a; ▼,sensor 5b; ○,sensor 6a; ●,sensor 6b.

substrate (§ 3.3.3.1) aiding sintering of the electrolyte (§ 3.3.3.3) or blocking some gaseous diffusion paths. However an intervening platinum containing layer seemed to block diffusion of impurities to the zirconia (§ 3.3.3.1). Thus any impurity transfer from the substrate to the zirconia with an intervening platinum layer may have occurred via the zirconia directly in contact with the substrate. There is evidence for a little impurity transfer via the previously mentioned route as slightly enhanced grain growth in the zirconia overlayer was observed near the circumference as opposed to near the centre of the disc shaped platinum layer.

5.4.8 Estimation of the through porosity of the electrolyte films.

In order to achieve limiting currents in these sensors the porosity of the ceramic, f_p, due to pores connecting the anode and the cathode must be very small. The following equation was derived [191] based upon the ideal gas equation, Fick's first law of diffusion and Faraday's law and is valid if bulk diffusion were rate

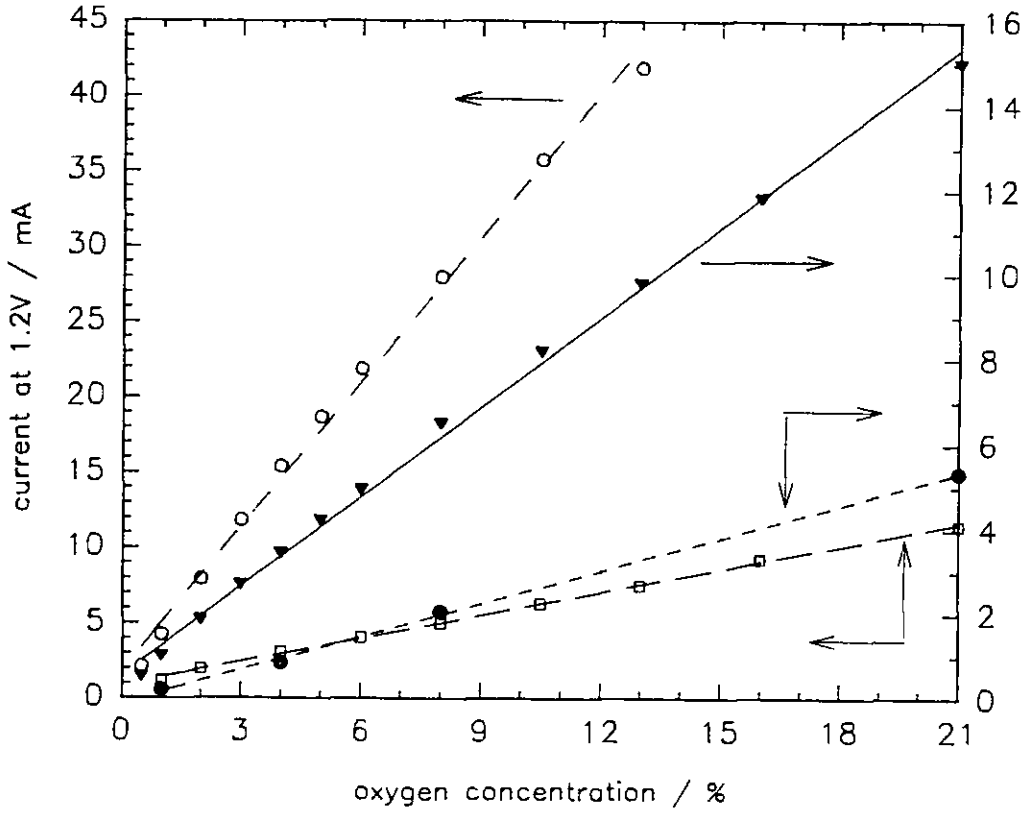

Figure 5.17 Limiting current vs oxygen concentration for sensors operating at 700°C and a fixed voltage of 1.2V: ●,sensor 5a; □,sensor 5b; ○,sensor 6a, ▾,sensor 6b.

determining (Appendix D).

$$f_p = \frac{IRT\ell\theta^2}{4FD_{O_2}A_{el}\,p(O_2)} \qquad (5.6)$$

I is the value of the limiting current at oxygen partial pressure p_{O2}, ℓ and A_{el} are the electrode separation and electrode overlap area respectively, and D_{O2} is the diffusion coefficient of oxygen through the pores. R, T and F have their usual significance. The factor θ was included to take account of the tortuosity of the pores [209]. The following values were substituted into Eq. (5.6) to obtain an estimate of the connected porosity f_p.

D_{O2} in N_2 at 800°C = 1.7×10^{-4} m^2 s^{-1} [219]

$\ell = 3 \times 10^{-5}$ m, $A_{el} = 3.1 \times 10^{-6}$ m^2, $\theta = 1.5$

$F = 9.65 \times 10^4$ C mol^{-1}, $R = 8.2 \times 10^{-5}$ m^3 atm K^{-1} mol^{-1}

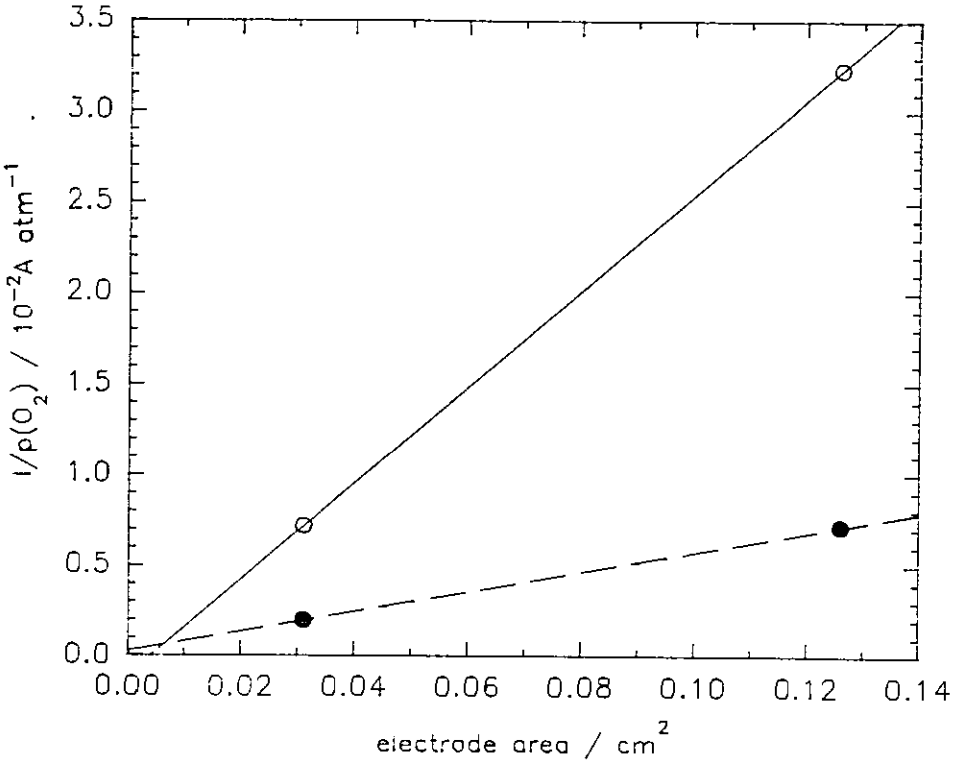

Figure 5.18 *Dependence of the geometric electrode area on the $I_{lim}/c(O_2)$ ratio for some devices operated at 700°C: O; sensors 6 (constructed on 99.6% alumina), ●; sensors 5 (constructed on 96% alumina).*

The value of I/p_{O2} derived from Fig. 5.11 (for sensor 2) was 12 x 10^{-3} A atm^{-1} leading to an estimated connected porosity, f_p, of 0.03%. The derived value of f_p is only an approximation due to the uncertainty of the value of the tortuosity factor and the precise area over which diffusion effectively occurred.

In a previous study [70] devices of a similar construction were characterised; limiting current plateaus were not observed at oxygen concentrations greater than 0.1% suggesting that the electrolyte porosity was higher by 2-3 orders of magnitude than in the present work.

5.4.9 Operation in a gas burning flue

To date very little quantitative information has been published concerning the behaviour of oxygen monitors in combustion gases. The results for operation of

sensor 3 in gases derived from the flue of a gas burning combustion system are shown in Figs. 5.19 and 5.20. The linearity of Fig. 5.20 was good showing that the sensor may be used to monitor the air-to-fuel ratio of such a combustion system. The discrepancy between Fig. 5.20 (at 1% O_2) and Fig. 5.7 may have resulted from errors arising from the calculation of oxygen concentration from the CO_2 measurement: this assumed the natural gas to be pure methane and ignored any condensation of water vapour. Furthermore, the possibility of an air leak into the sampling system is not discounted.

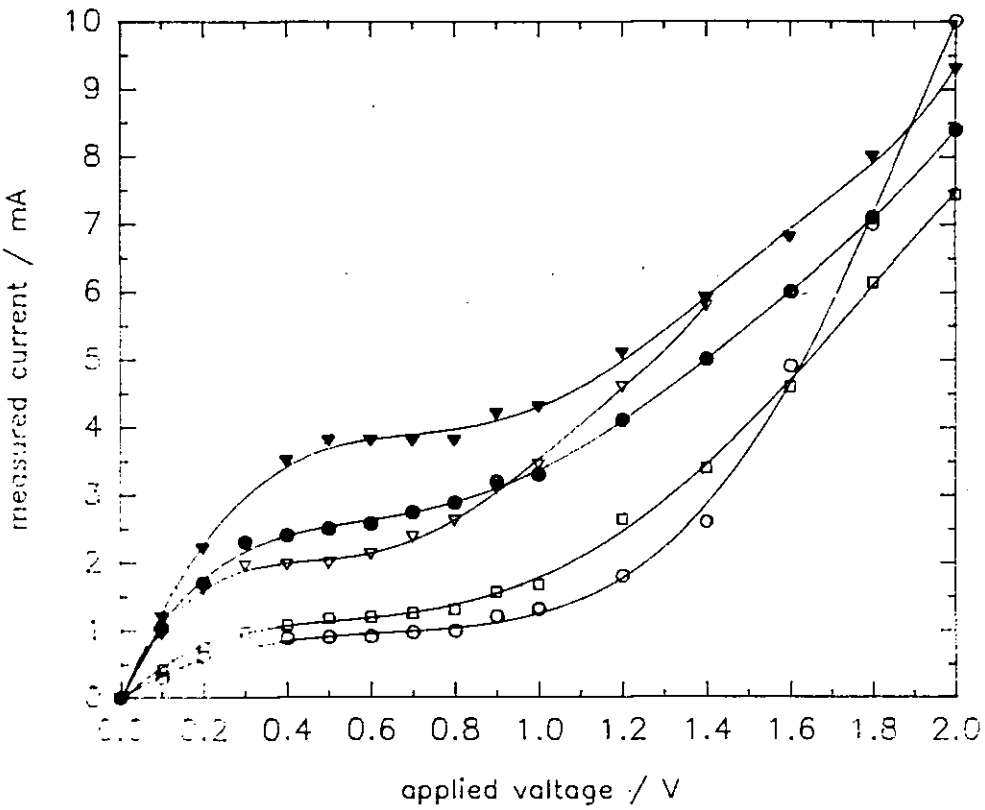

Figure 5.19 Current-voltage characteristics of sensor 3 operating at 800°C in combustion gases. Calculated oxygen concentrations / %: ○,0.9; □,1.4; ▽,2.15; ●,2.45; ▼,3.95.

A detailed study has not been undertaken to establish sensor characteristics with applied voltages in excess of ~1V. The observed sharp increase in the current above ~1V were almost certainly due to the presence of H_2O vapour and CO_2, in the combustion gases. These have been shown to be electroactive on platinum/zirconia interfaces with applied voltages of ~1V as follows:

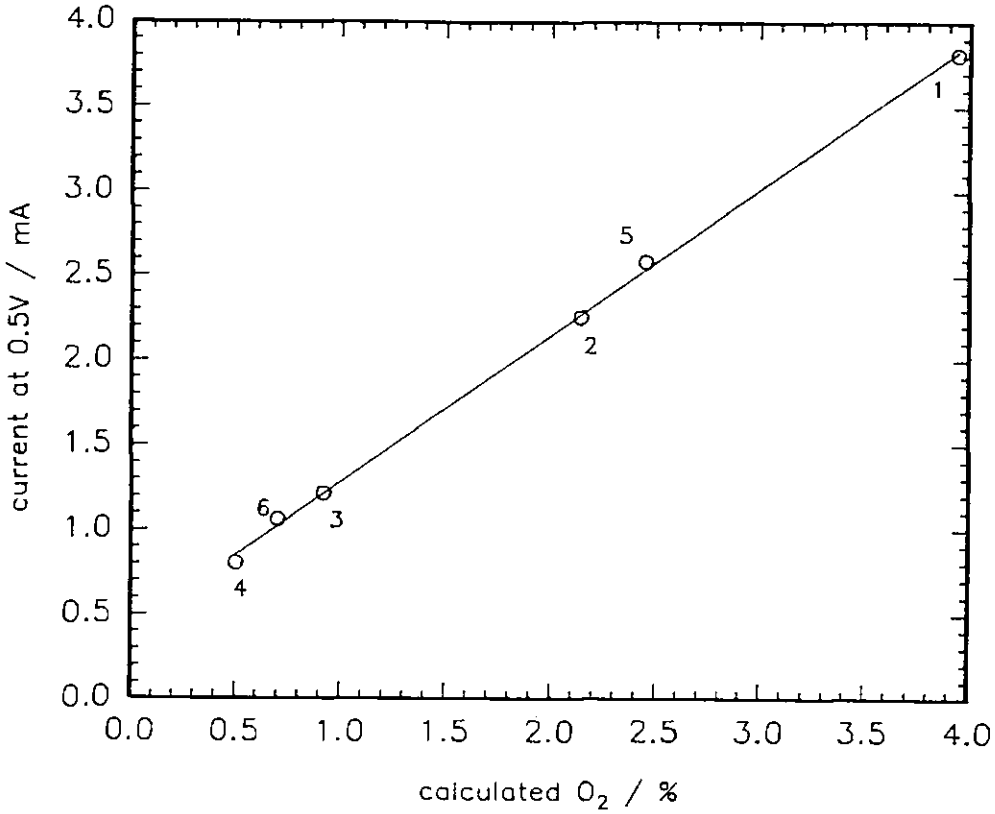

Figure 5.20 *Output of sensor 3 operating at 800°C and 0.5V when exposed to exhaust gases generated in a gas burning flue. Oxygen concentration was calculated from the CO_2 measurement. The data are numbered in the order of measurement.*

$$H_2O + 2e \rightleftharpoons H_2 + O^{2-} \quad (5.7)$$

$$CO_2 + 2e \rightleftharpoons CO + O^{2-} \quad (5.8)$$

thus resulting in an addition to the limiting current plateau above ~1V [29]. During measurement, combustible gases (such as H_2, CO and C_4H_{10}) which can cause a reduction in the observed current [29], were expected to be present in insignificant amounts within the flue.

5.5 SUMMARY

Planar zirconia oxygen sensors were constructed onto 96% alumina using thick films technology exlusively. The cathode was first printed using a platinum-zirconia cermet ink as a circular disc with two protruding radial strips for electrical connections. This was treated at 150, 400 and 1000°C for 10 minutes at each temperature. An electrolyte disc with larger diameter than the cathode was then

printed over the cathode; this was dried and fired to sinter the zirconia typically at 1400°C for 1 hour. Finally the anode cermet disc with the same diameter as the cathode was printed onto the electrolyte, dried and briefly fired at the same temperature as was the electrolyte. Platinum wires were affixed to the electrodes for electrical connections. In one case a thick film heater was applied to the reverse side of the substrate.

Sensors were operated in the amperometric mode at temperatures in the range 550-950 °C. This involved the application of a voltage between the electrodes to reduce oxygen at the cathode and evolve oxygen at the anode. This resulted in the setting up of a concentration profile in the pores of the electrolyte. As the applied voltage was increased the current rose and reached a limiting current value controlled by oxygen diffusion through the anode / electrolyte. At applied voltages above 1.5 V the current increased again due to the generation of electronic carriers in the electrolyte.

It was found, as predicted by theory that the limiting current was proportional to oxygen concentration in the range up to 21% oxygen. This has not previously been achieved with devices of this construction. The temperature dependence of the sensor output was found to vary with the temperature at which the device had been sintered and this requires further study. Nonetheless, it does offer the prospect of designing sensors with a low or negligible temperature coefficient.

Two sensors were also constructed on 99.6% alumina substrates. Limiting currents were a factor of four higher on these substrates compared with otherwise identical sensors on 96% alumina substrates. This suggests that impurity diffusion from the less pure substrates aided sintering of the zirconia electrolyte causing pore constriction. An estimate of connected porosity from limiting currents on 96% substrates revealed a value of less than 0.1%.

Promising results were obtained for a sensor operated in the combustion products from a gas-burning flue. Limiting currents were linearly related to the calculated oxygen concentration.

CHAPTER 6

THICK PLATINUM FILMS SUBJECTED TO EXTENDED TREATMENTS AT TEMPERATURES UP TO 1300°C

6.1 INTRODUCTION

Some sensor types are operated at temperatures above ambient and require convenient, simple and low cost methods of heating. There are numerous examples where thick-film printed heaters have been used to achieve temperatures up to 400°C. However zirconia sensors require to be heated to temperatures in the region of 700°C. At such high temperatures problems are encountered with loss of continuity of the electrical element, drift in the electrical resistance and attachment of leads.

Thick-film heaters have been made using platinum as the conducting material and could be elevated to temperatures as high as 1300°C by the passage of a current. Ideally such a heater would provide a long life (>1 year) under normal operating conditions. Instrumentation has been developed to control the temperature of these heaters precisely using two methods [220]. In the first the temperature of the heaters was monitored with a thermocouple and by using a feedback loop the power to the heater was adjusted to maintain a stable temperature. The second method involved using the heater as a platinum resistance thermometer operating in a Wheatstone bridge arrangement. The power was varied to keep the resistance constant. This was a simpler means which eliminated the use of a thermocouple. Clearly in order to provide temperature control by this means it was essential that at a given temperature the track resistance remained stable over its lifetime.

An object of this study was to determine changes in resistance of the platinum films with time during thermal treatment at elevated temperatures. An attempt was made to relate the resistance of the films to the volume fraction of the conducting phase. Consequently the work involved measurements of the platinum content and cross-sectional area of the films as well as resistance changes, with respect to time.

6.2 EXPERIMENTAL

6.2.1 General

Platinum films were deposited by a screen printing technique onto alumina substrates and treated at elevated temperatures between 800 and 1300°C for various times. The films were characterised subsequent to each heat treatment as follows: a)

resistance measurements at 20°C, b) temperature coefficient of resistance, c) quantification of platinum remaining, d) cross–sectional area, e) scanning electron microscopy and image analysis.

6.2.2 Heater preparation

The design of the printed heater was described [221] previously. Nine heater tracks were screen-printed onto a single substrate (Fig. 6.1).

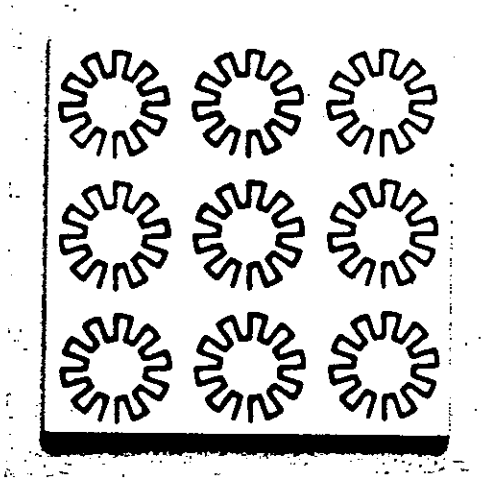

Figure 6.1 Photograph of 9 heater tracks screen-printed onto an alumina substrate. The side of the substrate was 25.4mm long.

All printed heaters produced for this work were screen–printed in a single batch onto 96% alumina substrates. The films were then subsequently dried at 150 ℃ for 10 minutes in order to remove the volatile constituents. This was followed by a firing treatment at 1000°C for 10 minutes to sinter and initialise the film. For attachment to sensors individual heaters were isolated on an 8mm disc of the ceramic using laser cutting (Laser Mitronics Ltd).

6.2.3 Heating cycles

The furnaces used were described earlier (§ 2.3.7). The temperature ramp rate for the firing cycles was set at 50°C min^{-1} until the desired temperature was reached then held for the desired time period before ramping down. The downward ramp was also

50°C min^{-1} until reaching a value of ~700°C when the cooling rate was controlled by the natural cooling rate of the furnace at zero power.

6.2.4 Resistance and cross–sectional area measurement

Resistance measurement was done using the four point probe arrangement described in section 2.3.8. The resistance of each film following heat treatment was measured at room temperature and normalised to 20°C (§ 4.2.2); values below were averages of the resistances of 27 platinum films (9 films on each of three substrates); this resistance is referred to as the initial resistance (R_i).

The value for the cross–sectional area at each point in time was derived from the average of twenty profiles taken across the length of each of 27 films.

6.2.5 Determination of temperature coefficient of resistance (α_r)

Films were selected at random (after various time/temperature cycles) and their resistance was measured between 20 and 300°C. An Heizung HT-301 hotplate was used to heat the substrate including the overprinted film and the film resistance was subsequently measured at various temperatures using the four-point probe (§ 2.3.8). The substrate temperature on the film side was monitored to ±3°C using a Pt/Pt–13%Rh fine wire (40 μm) thermocouple (Type R) bonded to the substrate using Pt paste (type 5544) and subsequently fired. The value of α_r was calculated using the following relation:

$$\alpha_r = \frac{R_1 - R_{20}}{R_{20}(T_1 - 20)} \qquad (6.2)$$

where R_2 is the resistance at temperature T_1 and R_{20} is the resistance at 20°C.

6.2.6 Quantification of platinum on substrate and rate of weight loss

The amount of platinum present on each heater film was quantified, following various thermal treatments, using atomic absorption analysis (§ 2.3.10). The rate of platinum weight loss, per unit area, from the films was determined by quantifying the amount of platinum present following heat treatment at various times at fixed temperatures.

6.2.7 Electron microscopy and Image analysis

The platinum films were examined using the scanning electron microscope (§ 2.3.9) to investigate progressive changes of film microstructure following thermal treatment at various times.

An image of part of the heater encompassing the whole width of the track was obtained at 600X magnification on the SEM. This image was acquired for image analysis using software comprising of two programs. The acquired image was displayed on a remote screen allowing various contrast levels to be ascertained. The sampling count and threshold values were adjusted to match the acquired image with that displayed on the SEM. The various contrast levels were then grouped so as to represent the voids exposing underlying substrate by a different shade to that of the platinum on the film (Fig. 6.2).

The first program (Digiscan) provided feature analysis. Once the voids were obtained as separate distinguishable features the program stored information of each of these voids in terms of the following: (a) area, (b) computer grid points occupied, (c) maximum, minimum and mean void lengths (ferrets). Values of (b) were used to set a minimum size of feature for the program to analyze. This was useful for the elimination of numerous tiny features diagnosed which were not voids.

The second program used (Digipad) allowed measurement of the percentage area of voids within the film that traversed the full thickness of the film in a direction perpendicular to the substrate so that the underlying substrate was visible from above; such voids are referred to below as through–voids. This was based on the determination of the percentage area occupied by each contrast range. These ranges, represented by different colours by the program, were combined so as to represent voids by one colour and platinum by another.

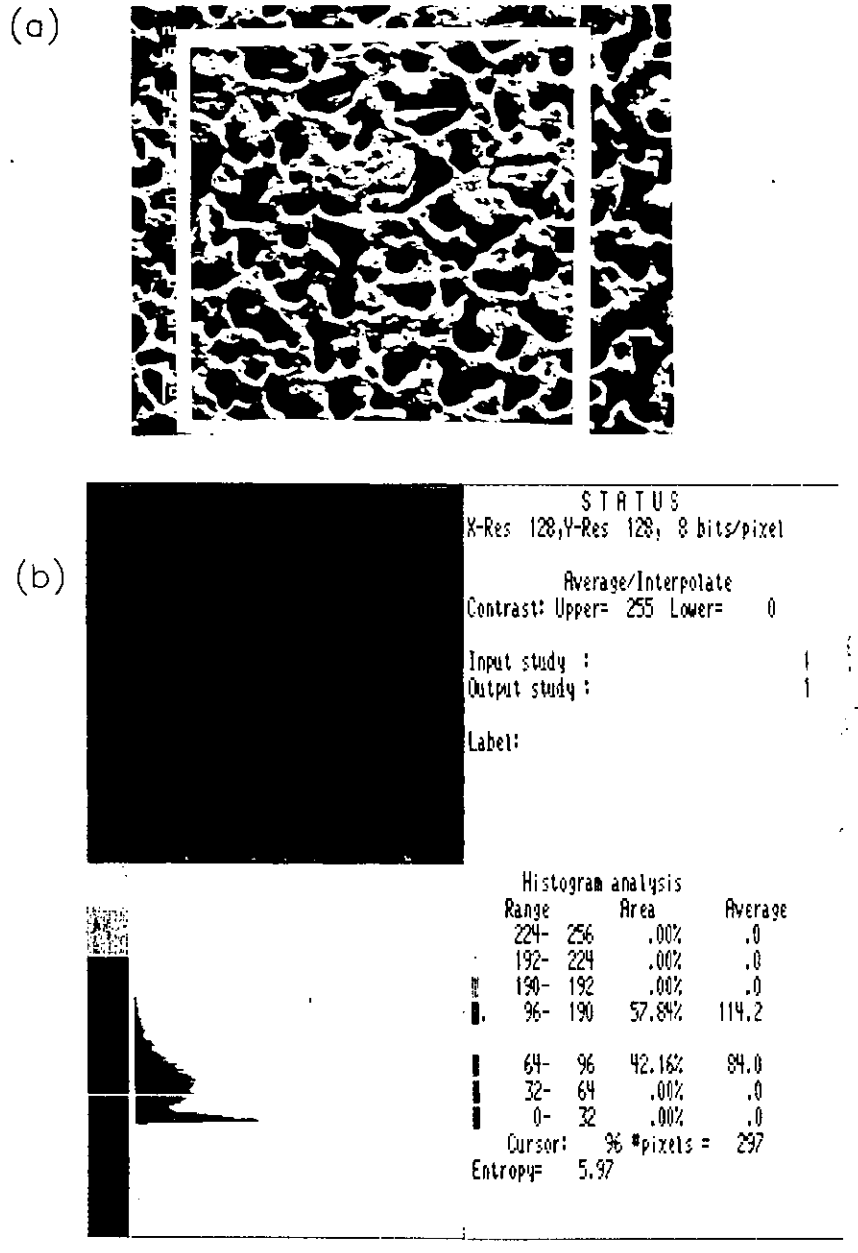

Figure 6.2 *(a) Micrograph of platinum film displayed by video monitor of SEM, (b) Captured part of the micrograph used by image analysis program; area of holes is indicated as 42.16 % in this instance.*

6.3 RESULTS AND DISCUSSION

6.3.1 Electrical resistance changes at elevated temperatures

Typical trends for the changes in electrical resistance at elevated temperatures of two fritless and two fritted platinum films are shown in Fig. 6.3 with reference to the films fired at 1000°C. The initial treatment (1000°C for 10 minutes) produced films

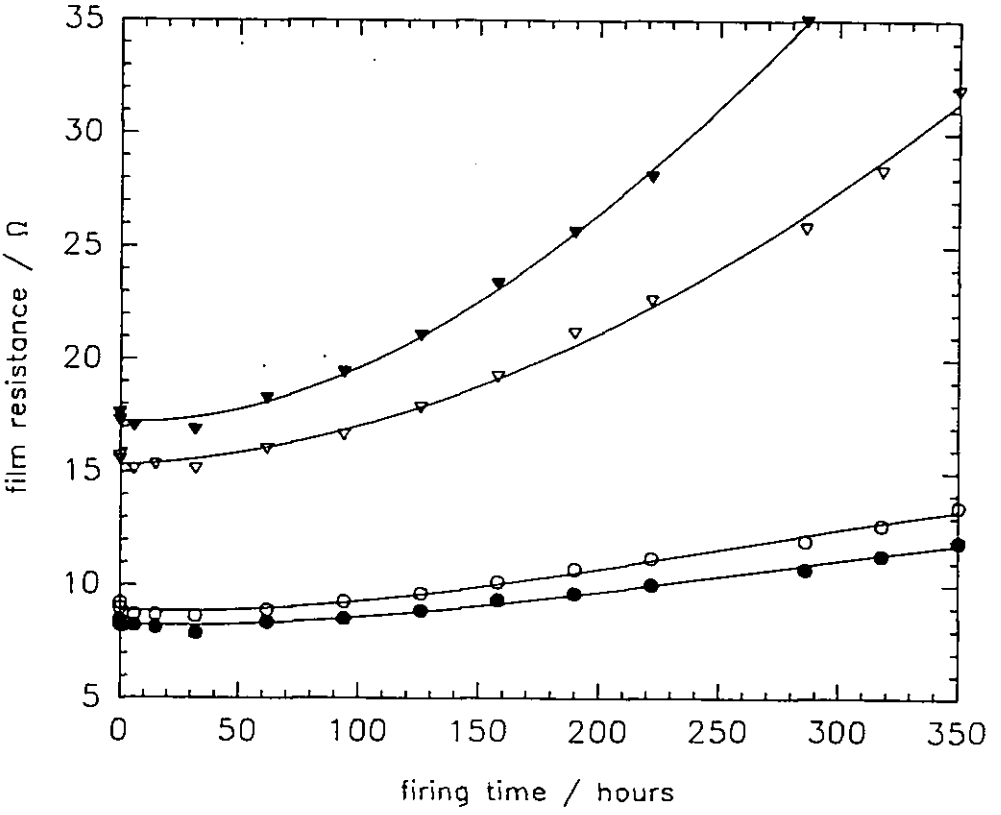

Figure 6.3 *Resistance at various firing times for films fired at 1000°C which had various initial resistances. Film type / initial resistance (Ω): ▽fritless / 15.7; ▼ fritless / 17.6; ● fritted / 8.4; ○ fritted / 9.2.*

with only a small variation in the initial resistance; the values shown in Fig. 6.3 represent the highest and lowest values of the initial resistance measured for 27 films of each type. Initial resistances of the films averaged ~9Ω for the fritted as opposed to ~16Ω for the fritless films: the ratio 1.8:1 correlated with the inverse of that corresponding to the amount of platinum metal deposited of 1:1.8 (see § 6.3.2) indicating that the glass in the fritted films did not play a major part in determining the film resistance which was solely determined by the amount of platinum present in the film. It should be noted here that the neither the heating nor the cooling rate produced observable differences in the heater resistance at 20°C. Films with higher

initial resistances showed a more rapid resistance increase with firing time resulting in earlier electrical discontinuity. Electrical discontinuity in the film is referred to below as film "failure" as the heater could no longer be used to meet its service function.

Changes in the resistance data were more conveniently represented using a normalisation procedure

$$r_N = R_t / R_i \qquad (6.2)$$

where r_N is the normalised resistance, R_i is the resistance of the film following the initial treatment and R_t is the resistance measured following thermal treatment for time t. Changes in r_N with firing time at various temperatures are shown for the fritted films in Fig. 6.4 and for the fritless films in Fig. 6.5. The resistance changes of the tracks show that after an initial decrease there was a subsequent continuous increase in r_N with firing time at elevated temperatures until film failure. The rate of resistance increase was accelerated with increasing temperature and for the fritless films was higher than that of the fritted ones. This may have been associated with the higher initial resistance of the fritless films (Fig. 6.3).

The time taken for the value of r_N to reach 1.5 was taken as an indication of the rate of resistance change; its relation with temperature (Fig. 6.6) was used to calculate an activation energy for resistance change. Such activation energies for fritted and fritless films were found to be similar with a value of ~135 kJ mol^{-1}; this suggests that for both fritted and fritless films the same physical processes may have controlled the observed changes in the electrical resistance. In the sections that follow it is shown that with increasing time at a fixed firing temperature there was an increase in the proportion of each film made up of through voids and that platinum was lost by evaporation from the film. The activation energy obtained for the resistance change of the films of ~135 kJ mol^{-1} compares well with that obtained for the increase of the through voids of ~130 kJ mol^{-1} (§ 6.3.3, Fig. 6.16) but is lower than the value of ~207 kJ mol^{-1} (§ 6.3.2, Fig. 6.10) obtained for the rate of platinum evaporation. This suggests that the overall resistance rise of the films was primarily controlled by the formation and growth of the voids. Extrapolation of the

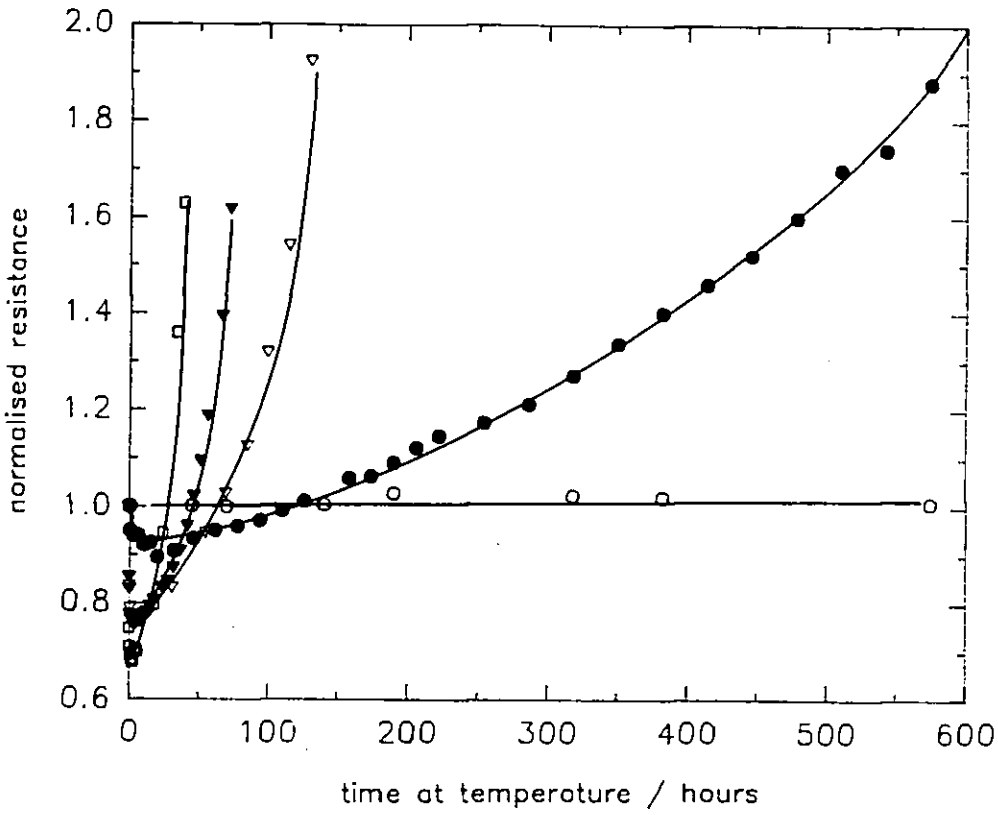

Figure 6.4 *Normalised resistance of fritted platinum films after firing at various times at* ○*,800°C;* ●*,1000°C;* ▽*,1150°C;* ▼ *,1225°C and* □*,1300°C.*

data in figure 6.6, indicate that the fritted film may require 4-5 years at 700°C for its resistance to rise to one and a half times its initial value. It is uncertain however that the factors controlling the resistance rise, and hence the activation energy, at temperatures below 1000°C remain the same as that for temperatures in the range 1000°C to 1300°C.

The initial decrease and subsequent increase in film resistances may be explained with reference to the film microstructure. Sintering, void growth and platinum evaporation were occurring simultaneously. The initial decrease in the film resistance was more rapid than the subsequent increase and was attributed to sintering of the film (§ 6.3.3) improving interparticle contact. The subsequent resistance increase indicates that the processes acting to effect the increase (void growth and platinum evaporation) became dominant over the sintering process. Void growth may have acted to increase the resistance by effecting an increase in the conduction path length

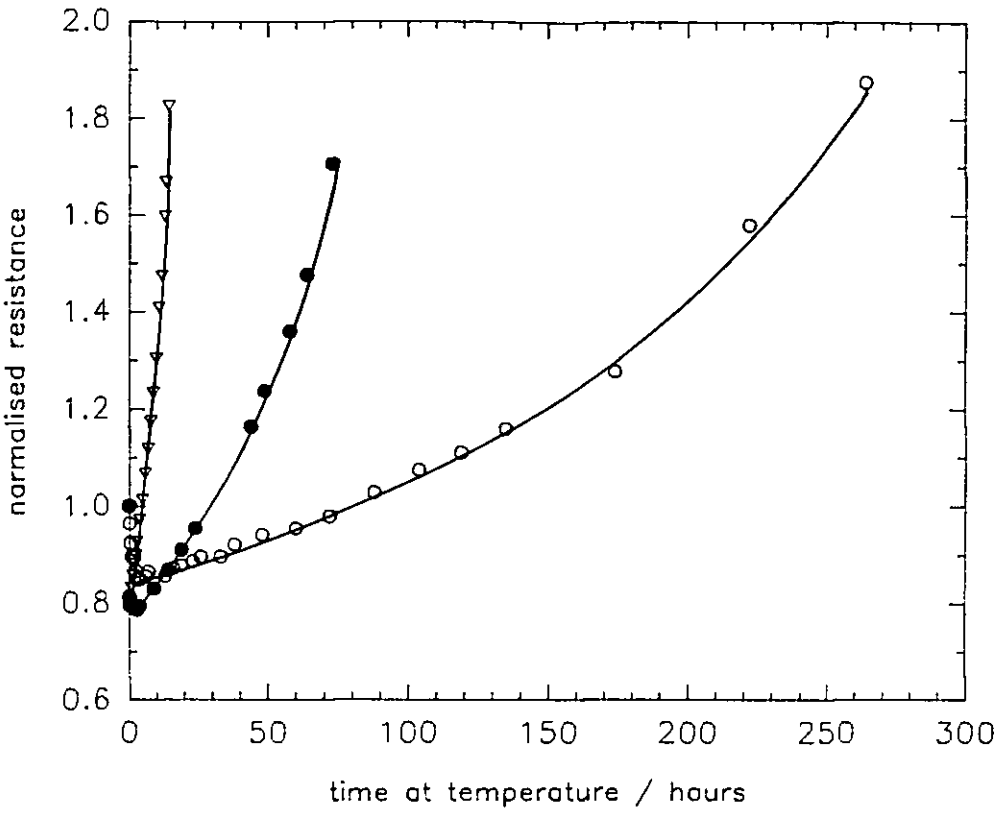

***Figure 6.5** Normalised resistance of fritless platinum films after firing at various times at O;1000°C, ●;1150°C and ▽;1300°C.*

(tortuosity), due to the intervening voids. Platinum evaporation caused an increase in resistance by reducing the amount of platinum available to carry the current.

A further procedure was to normalise time,

$$t_N = t/t_{1.5Ri} \qquad (6.3)$$

where the normalised time t_N is the ratio between the time t and the time taken for r_N to equal 1.5 ($t_{1.5Ri}$). Plots of r_N versus t_N are shown in Fig. 6.7 for the fritted composition and Fig. 6.8 for the fritless composition. It was found that the diversity in the resistance-time relationship between films of the same type (Fig. 6.3), which were the result of differences in their initial resistance disappeared and resulted in a single line on the plot of r_N versus t_N.

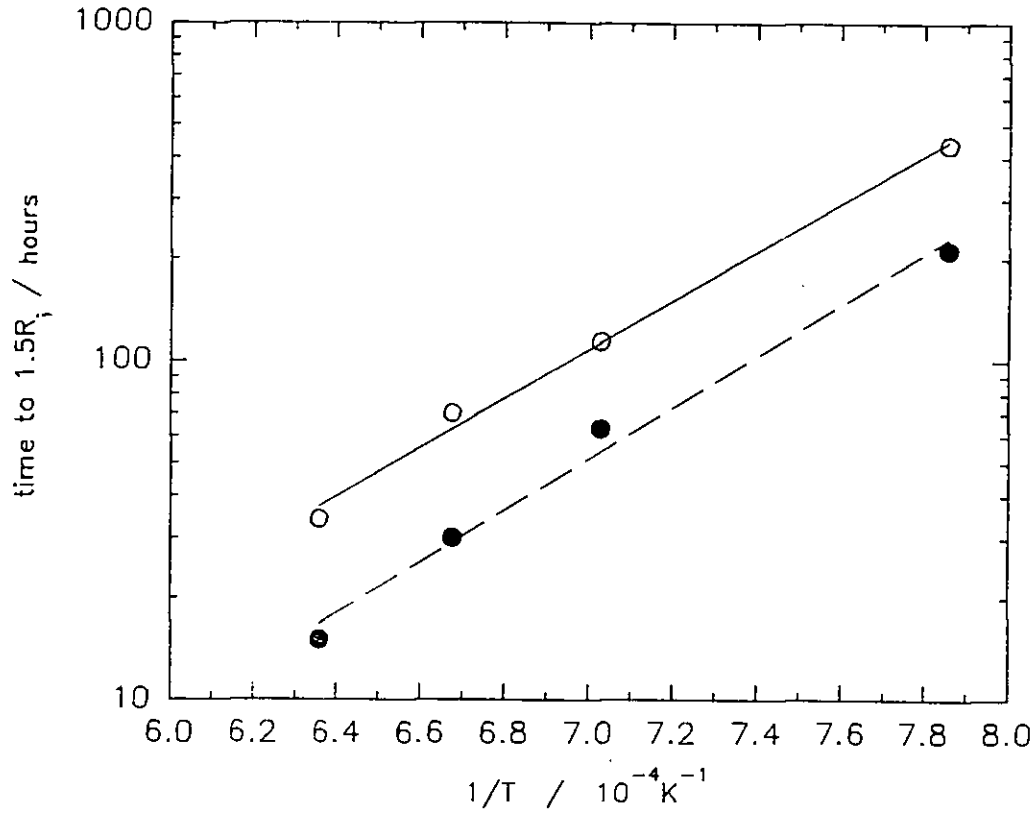

Figure 6.6 *Relation with temperature and time taken for the film to increase its resistance to 1.5 times its initial value.* ○*fritted films;* ●*fritless films.*

Figure 6.7 demonstrates that the sintering effect in the initial period became more dominant compared with void growth for fritted films as the temperature was raised resulting in a lower minimum normalised resistance. This means that the activation energy for sintering of the fritted films was lower than the value of 130 kJ mol^{-1} obtained for void growth. Smaller differences in the minimum normalised resistance with temperature were observed for the fritless films (Fig. 6.8) suggesting that the activation energy for sintering was closer to that of void growth in this case. Differences in activation energies for sintering between fritted and fritless films could mean that the glass present in the former films acted as a sintering aid.

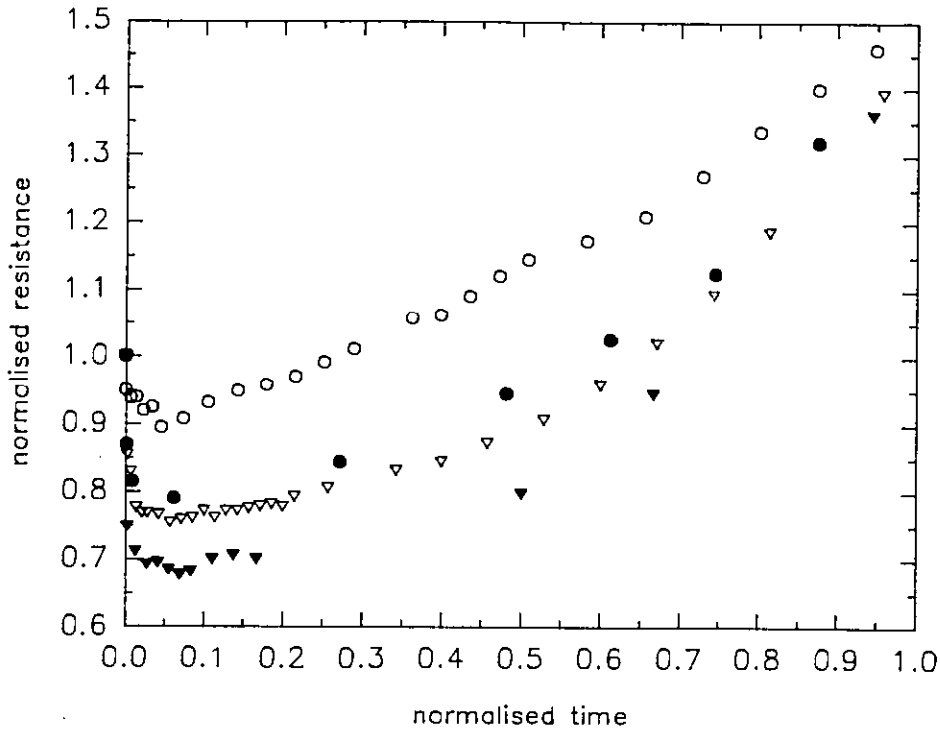

***Figure 6.7** Normalised resistance vs normalised time of fritted platinum films fired for prolonged time periods at O,1000°C; ●,1150°C; ▽,1225°C and ▼,1300°C.*

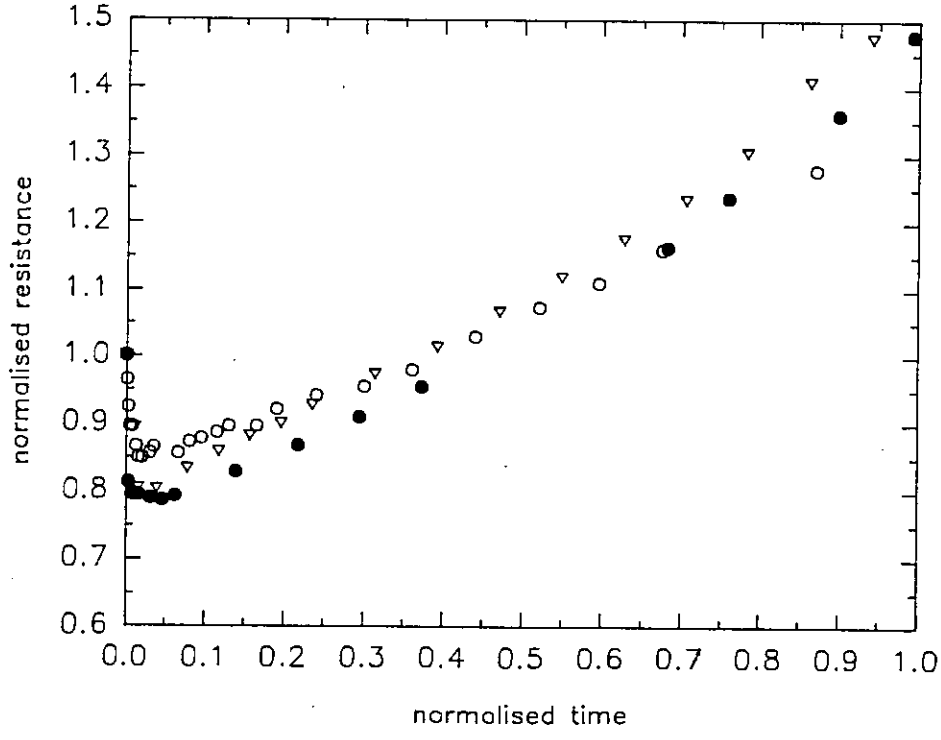

***Figure 6.8** Normalised resistance vs normalised time of fritless films fired at for times indicated at O;1000°C, ●;1150°C and ▽;1225°C.*

6.3.2 Quantification of the amount of platinum deposited on the substrate and the rate of weight loss at elevated temperatures

It is well established that at high temperatures in oxidising environments platinum and other metals in its group, react with oxygen forming volatile oxides [222,223,224,225]. The volatile compounds which evaporate have been shown to be mainly PtO_2 [225], and to a lesser extent PtO and PtO_3 [226]. At atmospheric pressures it has been suggested that the oxidation rate is determined by the transport of the oxide vapour away from the metal through a gaseous boundary layer [227]

$$Pt(s) + \tfrac{1}{2}xO_2 = PtO_x\ (g) \qquad (6.4)$$

where (s) and (g) represent solid and gaseous phases respectively.

The rate of platinum loss from the printed films by evaporation was linear (Fig. 6.9 shows data obtained at 1300°C) throughout the time the track was electrically continuous (i.e < 40 hrs at 1300°C). The average amount of platinum deposited by screen–printing nine heater patterns on one substrate was ~5.1mg when using the fritless ink and ~8.9mg when using the fritted ink. Quantification of the amount of platinum (at each point in time) was undertaken on five randomly selected substrates and the results averaged for each measurement. The spread of the results at any single point in time was ±3%. Verification of this consistency was important as the analytical method was destructive. The most common method for determining the rate of metal weight loss is thermo-gravimetric analysis; this was thought to be an insufficiently accurate technique for measurement of the weight loss of platinum printed onto a 96% alumina substrate. This is because the elevated temperatures (>1000°C) used might cause other volatile constituents, glass for example, to evaporate. The atomic absorption technique however provided a means of quantifying exclusively the rate of platinum weight loss from the printed films.

Rates of platinum weight loss from the films were calculated from plots of the type in Fig. 6.9 and normalised per unit geometric area of the platinum films. These results are compared with previously published data for pure platinum in Table 6.1. The activation energies calculated from figure 6.10 were similar amongst all the sets of the data with a value of ~207 kJ mol^{-1}. Major effects on the rate of platinum loss

may be caused by variations in the specimen dimensions [228] and texture of the platinum surface [223], the oxidising environment [229,229], the gas movement around the sample [224] and temperature of the surrounding gas [229]; non-accountability of such effects are the most probable explanation for the large scatter between the results of various investigators.

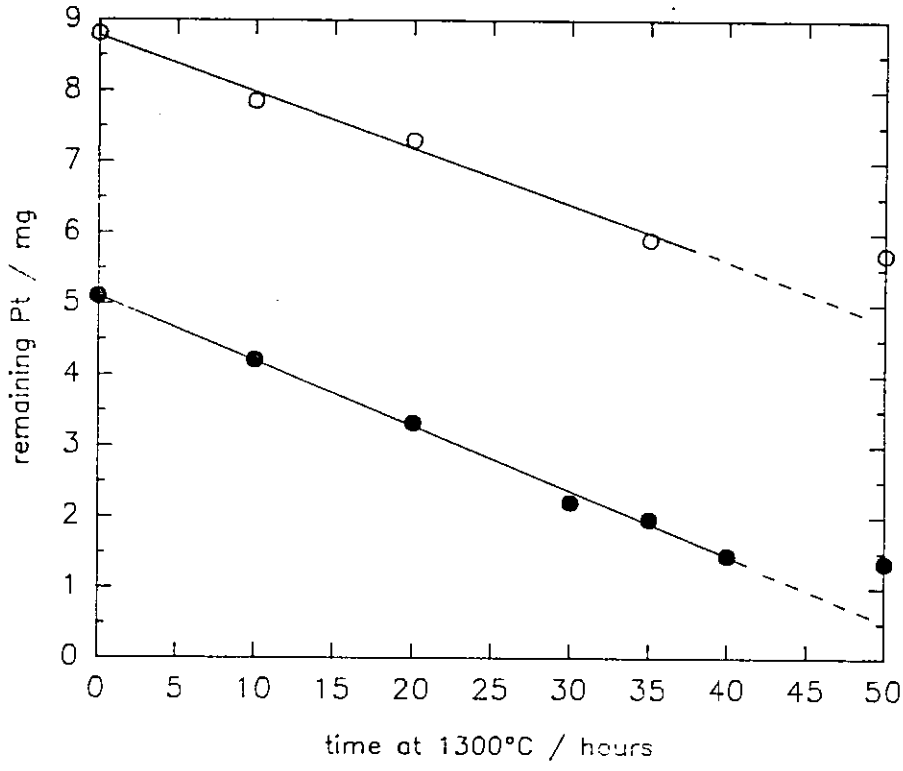

Figure 6.9 *Amount of platinum remaining on substrate (total of 9 heater tracks) following heat treatment at 1300°C for various times.* ○ *fritted films;* ● *fritless films.*

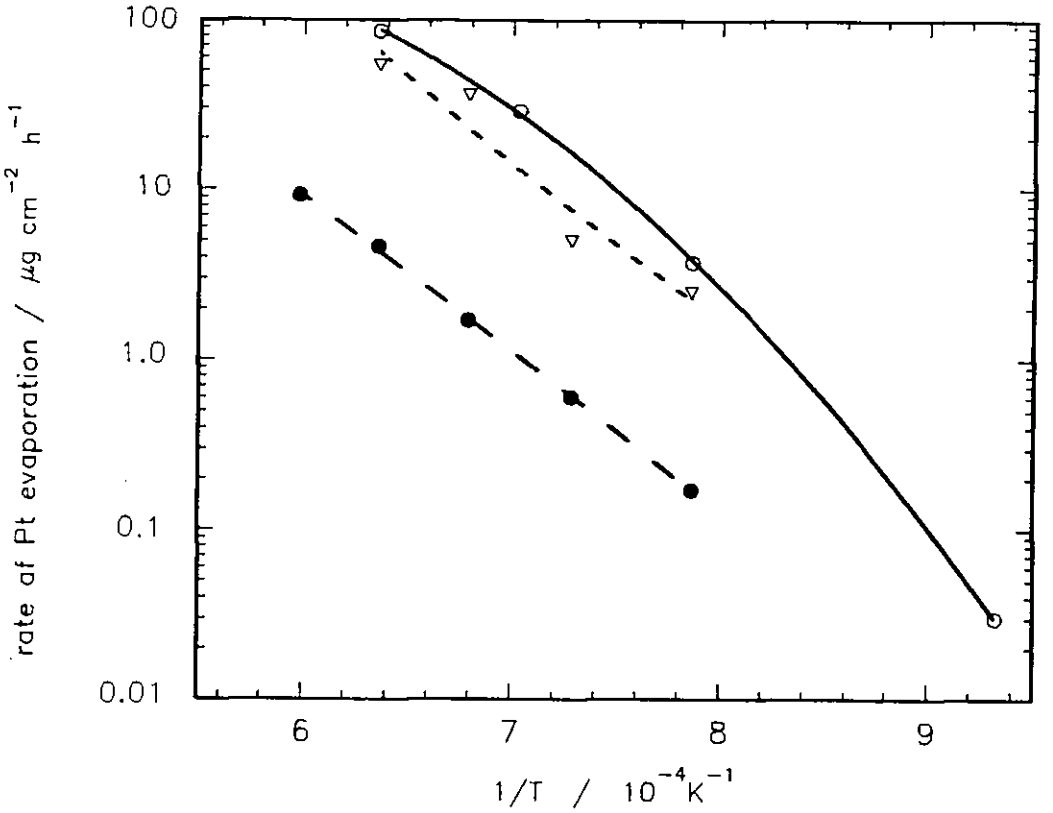

Figure 6.10 *Relation of rate of platinum evaporation with temperature.* ▽ *;Raub and Plate 1957,* ●*; Krier and Jaffee 1963,* ○*; this study (fritless films).*

Investigator	Weight loss at 1300°C / (μg cm^{-2} h^{-1})
This study: Fritted films Fritless films	69±4 78±5
Krier & Jaffee [224]	4.6
Raub & Plate [222]	54

Table 6.1 *Comparison of platinum weight loss data by evaporation at 1300°C in air.*

The rates of platinum evaporation between fritted and fritless films were the same within the range of experimental error, i.e 69±4 and 78±5 μg cm^{-2} h^{-1}. The weight loss of platinum could not be continuously monitored on a single substrate as the technique used for quantification (dissolution followed by atomic absorption) was destructive; this resulted in some uncertainty in the data due to variations of ±3% in the initial amount of platinum deposited.

6.3.3 Microstructural examination and analysis

Scanning electron micrographs

Due to the nature of the screen printing technology some porosity remained in the printed films after firing. Scanning electron micrographs of the fracture edge of both fritted and fritless films following treatment at 980°C for 10 minutes and at the point of electrical discontinuity are shown figure 6.11. These show that the films consisted of a mixture of solid and void phases. Micrographs of the surface of the fritted films following heat treatment at 1300°C for various times (Fig. 6.12) show that sintering and grain growth of the platinum particles and coarsening of the voids were occurring simultaneously; these processes were accelerated with increasing temperature. Sintering caused the platinum particles to coalesce forming at least one continuous cluster between the two ends of the length of the film.

When fired at 980°C for 10 minutes (Fig. 6.11a & 6.12a), individual voids were small compared to film dimensions and a three dimensional (3D) distribution of voids in the film was evident. During growth, voids coalesced and became through-voids (Fig. 6.11b and 6.12c); it is evident that the void distribution in the films was then principally two dimensional (2D). Progression of the void growth caused the through-voids to join and eventually traverse the film width resulting in numerous isolated platinum clusters. Such clusters were first observed at the edges of the film width; this is probably because they were the thinner parts of the films as can be seen from a profile of the film cross section (Fig. 6.13). Void growth was an inevitable consequence of agglomeration of the grains, grain growth and platinum evaporation.

Elemental mapping of the cross-section of the film (using energy dispersive X-ray analysis integral with the scanning electron microscope) indicated negligible diffusion of alumina from the substrate into the platinum film. The glass contained in the fritted samples segregated to form a layer between the platinum and the substrate during the initial stages of sintering. This phenomenon had previously been observed in studies of the structures of screen-printed resistors [230]. In this study there was no evidence that the glass had dissolved into the substrate. Previous in-depth investigations revealed that alumina rapidly dissolves into an overprinted glass layer

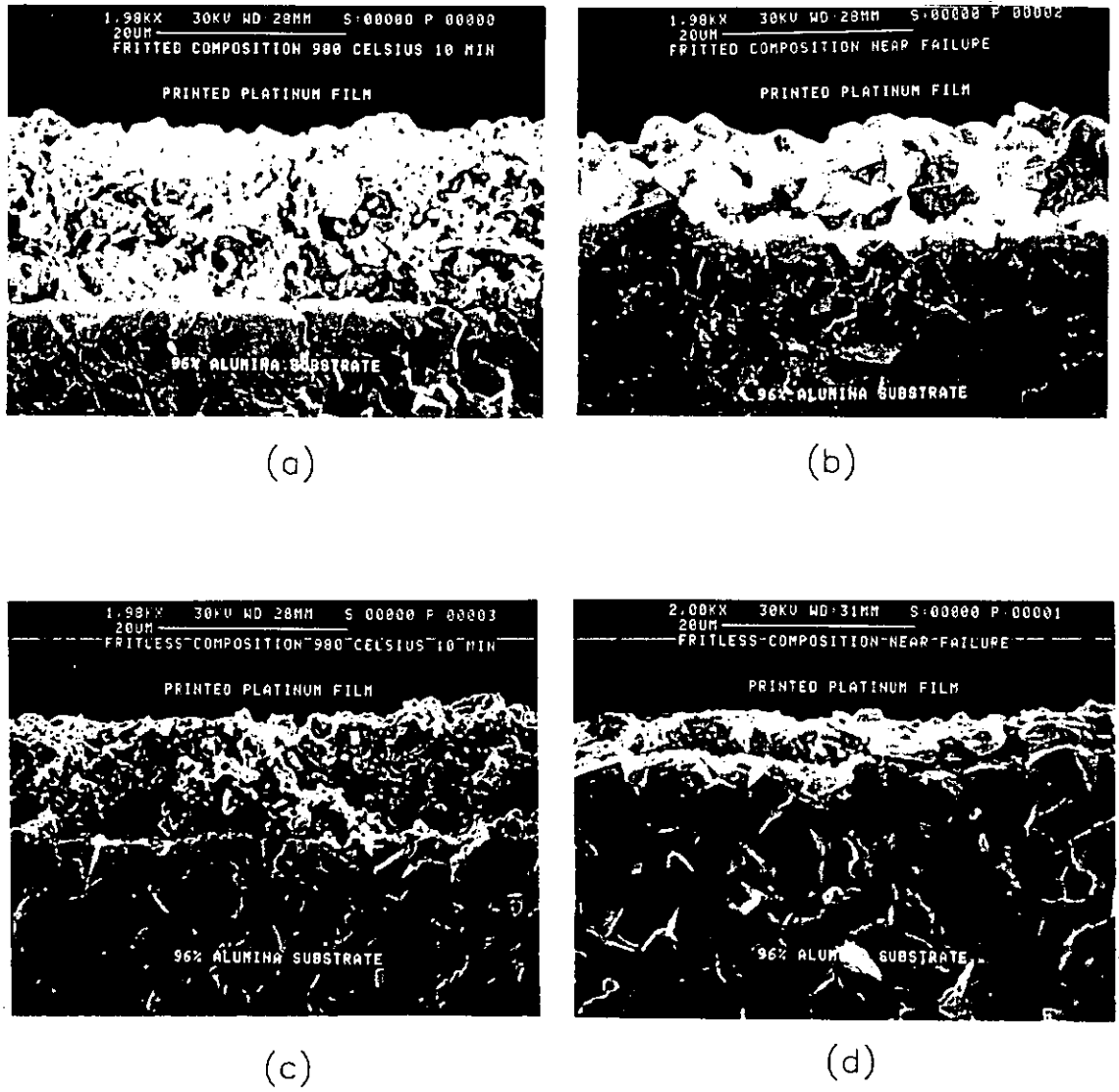

Figure 6.11 *Scanning electron micrographs of the fracture edge of the platinum films: (a) & (b) fritted films, (c) & (d) fritless films. (a) & (c) show films following firing at 980°C for 10 minutes, (b) & (d) show films at the point of electrical discontinuity. Cursor lengths show the magnifications.*

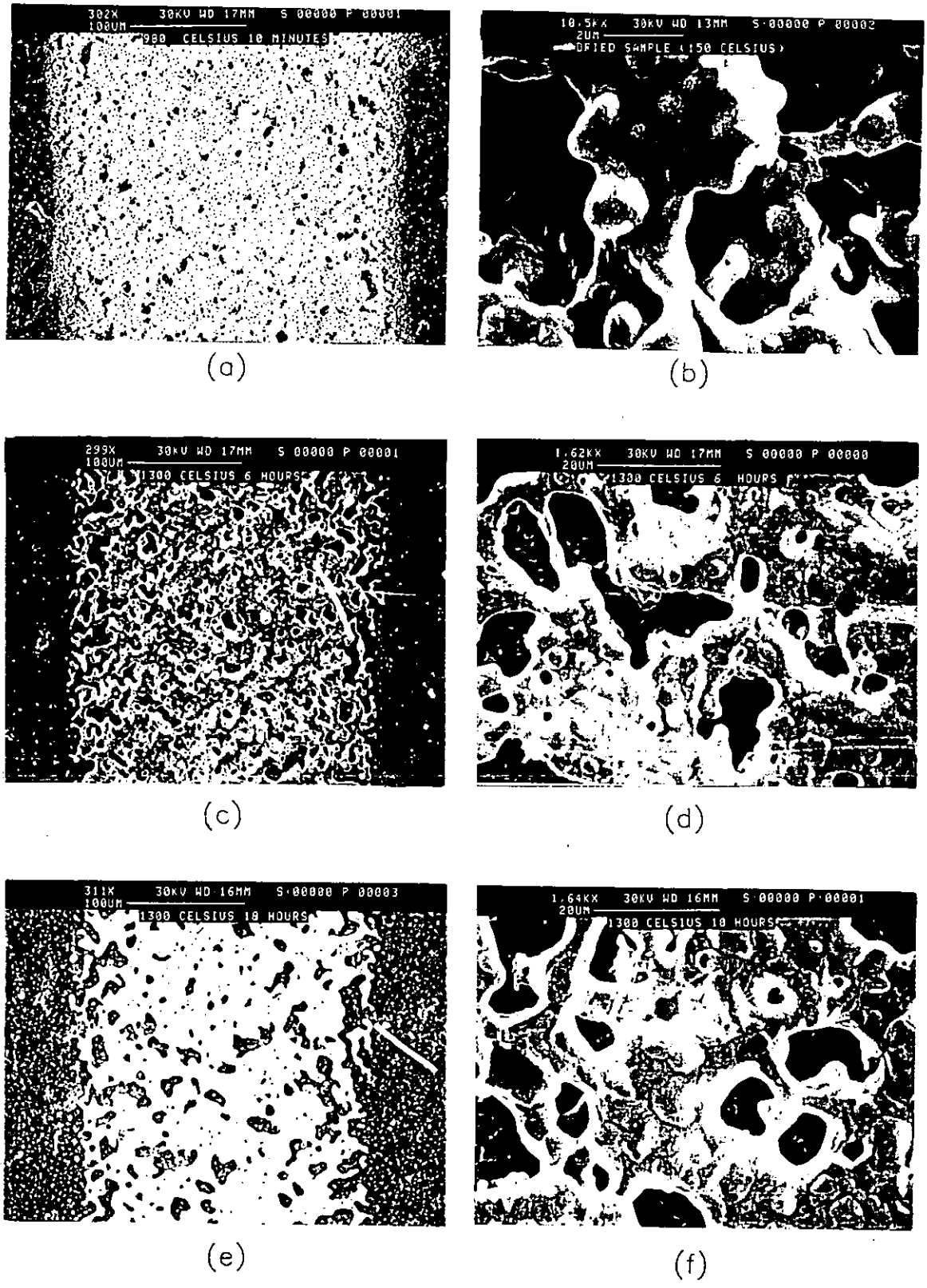

Figure 6.12 *Scanning electron micrographs showing plan views of some of the fritted films fired at temperatures and times indicated on the micrographs: those to the left show void growth and those to the right grain growth. Cursor lengths show the magnifications.*

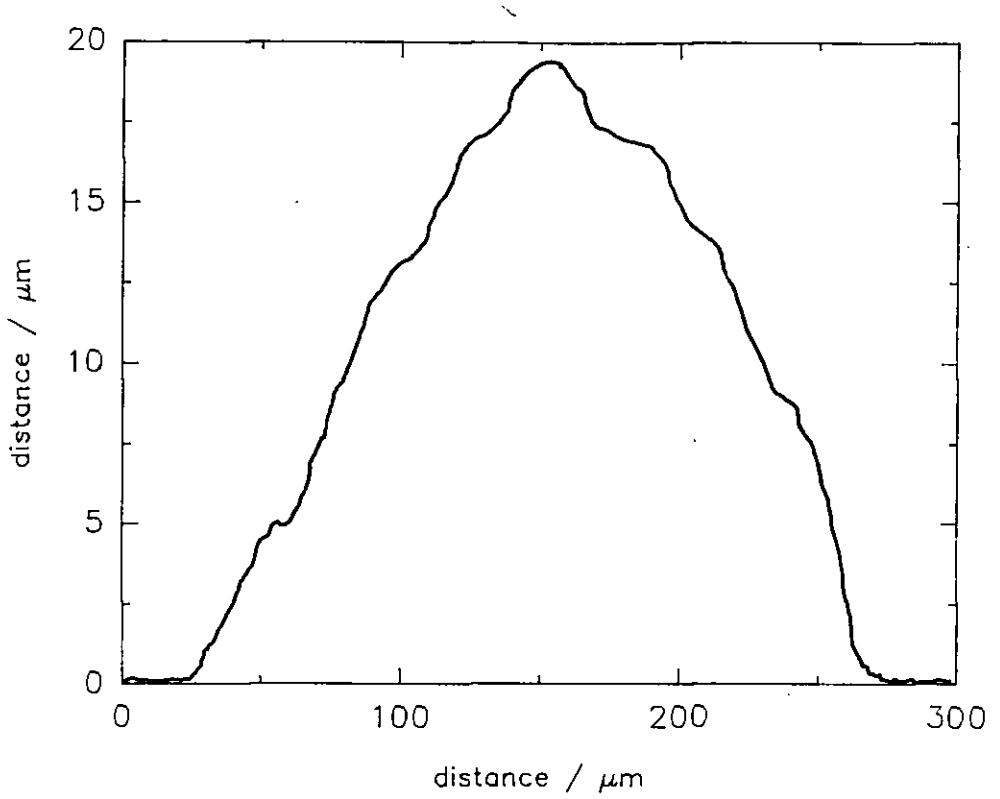

Figure 6.13 *Traced profile of a part of one film (fritted film fired at 980°C for 10 mins). Note the different scales of the axis. Alpha-step output: Cross-sectional area, 3000μm²; film width, 250μm; average height, 15μm.*

following firing at 1000°C [231]; this should increase the viscosity of the glass layer. The segregation of the denser platinum to the surface of the glass may indicate that the interfacial energy between the glass and the alumina was lower than that between the platinum and the alumina.

Image analysis

In this section discussion of the results obtained, is preceded by a discussion of the validity of the image analysis software used, to the application.

A general error could arise in the selection of the particular track area for analysis. It is apparent that if a different area of the film were selected a different result might be obtained. This was considered by analyzing various randomly selected areas on various tracks that had received identical heat treatment; the results were found to be within ± 10%.

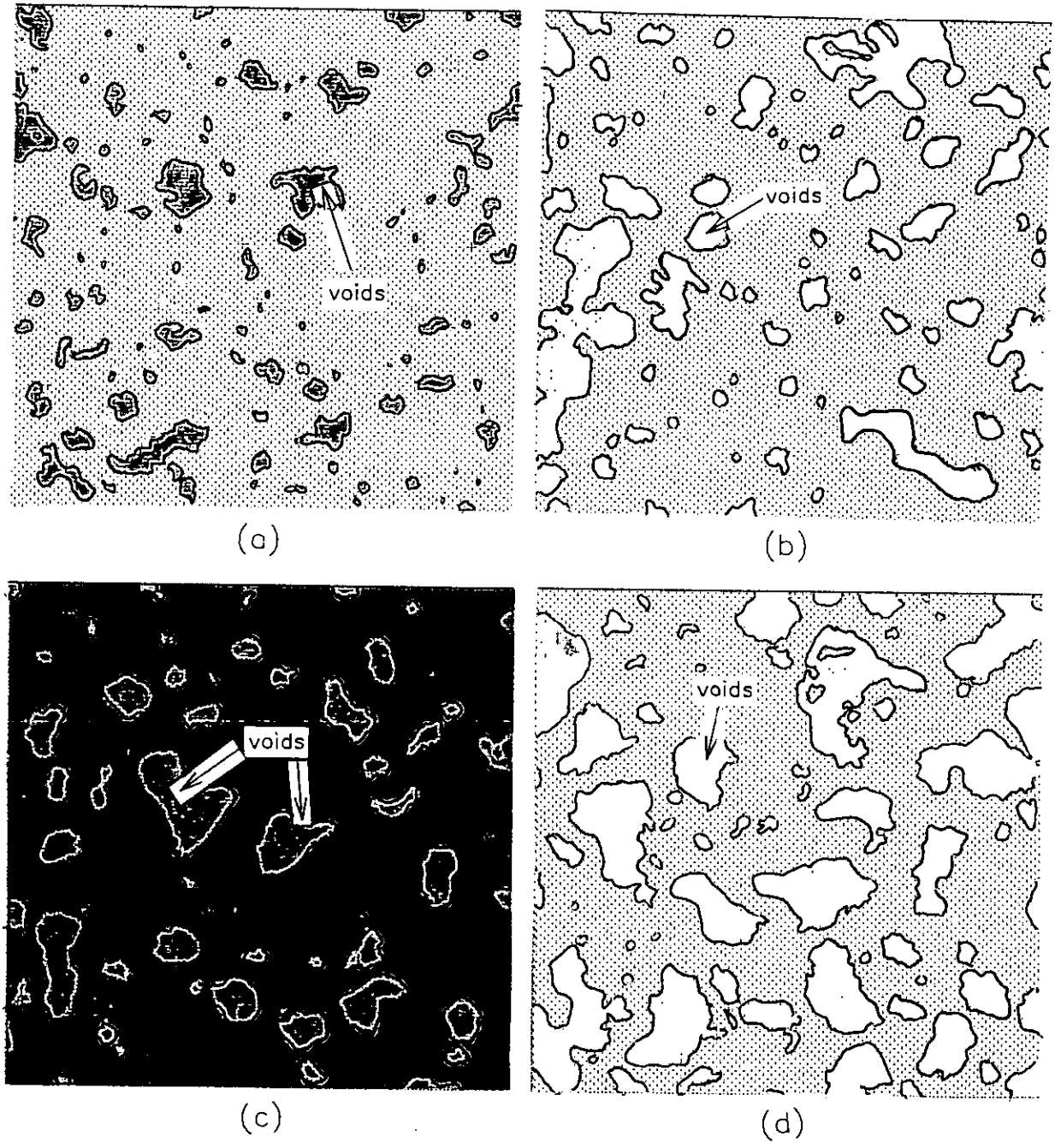

Figure 6.14 Some of the images captured by the analysis program showing void growth and increasing area of holes of fritted films fired at 1300°C for times in hours: (a),3; (b),15; (c),30; (d),50.

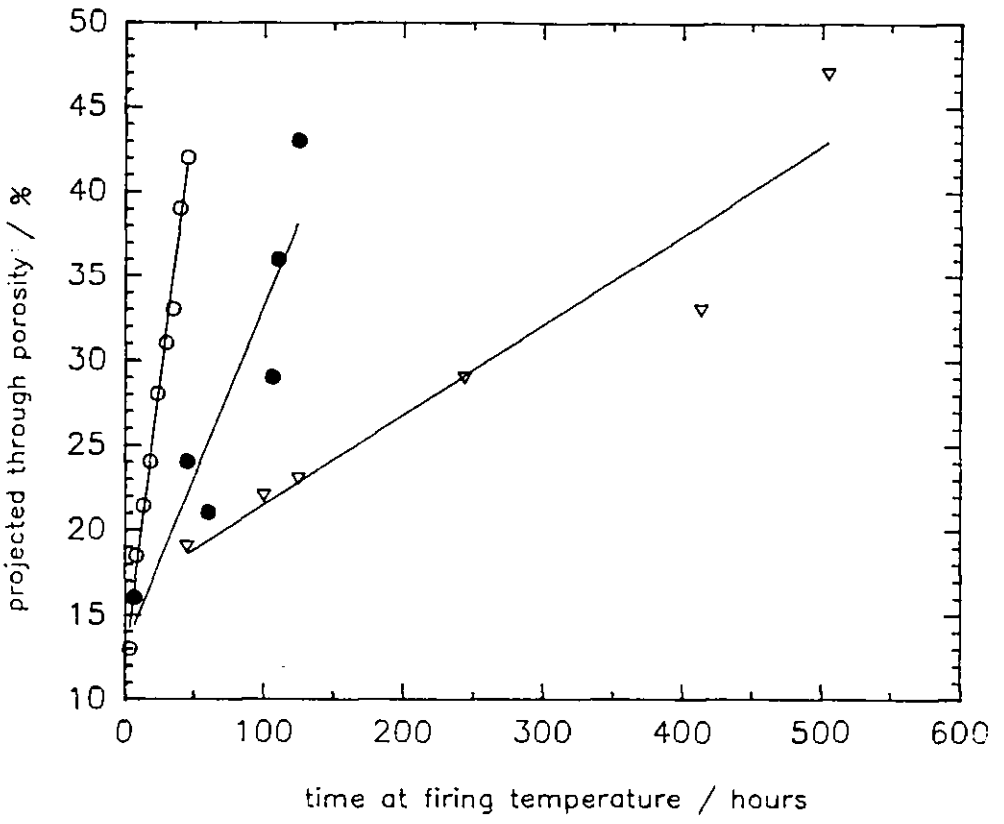

Figure 6.15 *Projected surface porosity in the films (obtained from image analysis) versus firing time at various temperatures.* ▽,*1000°C;* ●,*1150°C;* ○,*1300°C.*

The feature analysis program had one shortcoming in this application. Any clearly defined features in contact with the boundary of the selected area were ignored from the analysis. This was not particularly important when the voids of the sample were small but errors increased as the voids grew and contacted the boundary.

Image analysis of the films (Fig. 6.14 shows fritted platinum film fired at 1300°C) enabled determination of the percentage of the total area occupied by the film exposed as substrate; this area is referred to below as the projected through porosity. These results are summarised in figure 6.15. It was found that electrical discontinuity of the films occurred when the projected through porosity of the film was between 39–50%. This is consistent with the findings of Maskell *et al* [50] who showed that a sputtered platinum film on zirconia achieved electrical continuity at a projected through porosity between 40 and 55%. The relation between the time taken for the

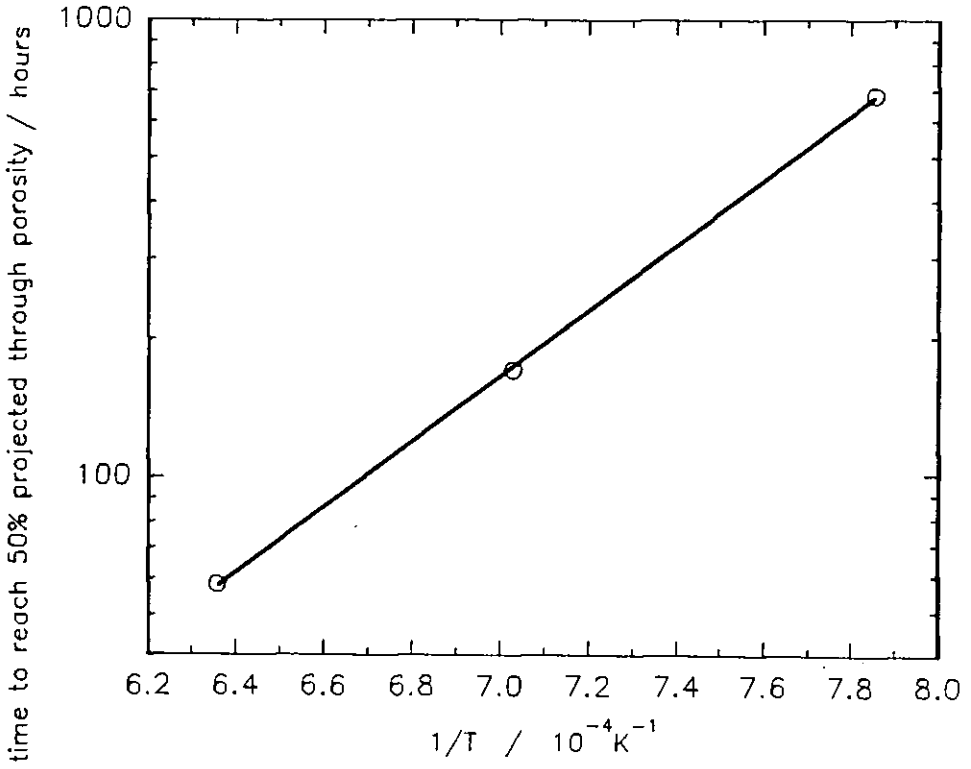

Figure 6.16 *Relation between temperature and time taken to reach a through porosity of 50% for the fritted films.*

fritted films to develop a projected through porosity of 50% and the temperature is shown in figure 6.16; an activation energy calculated from this figure for the growth rate of the through porosity was 130 kJ mol^{-1}.

Void growth

Voids not expelled by sintering were those with a large coordination number; these could only be expelled by grain growth. However the high temperatures required for grain growth also enhance void growth. These voids are also expected to act like impurity inclusions suppressing the rate of platinum grain growth and hence their chance of closure. As the interfaces between particles surrounding the void widen and deepen during sintering, (by equalisation of the chemical potential gradient, which is largest at the grain boundary interface) so the void tends to increase in size. Voids have an interfacial energy which is minimised at the minimum specific perimeter length or area; this may be the cause of the observed

tendency of individual voids to become circular with increased firing time. Coalescence and growth of voids occurred in a similar manner to coalescence of solid particles. Hence it is proposed that void growth is due to the same factors as grain coarsening. Some factors influencing void growth are as follows. When two neighbouring particles have a large size difference there exists a greater chemical potential gradient than when the neighbouring particles have a small size difference and so the void coarsening rate is enhanced. Where the surface of the substrate is curved particles tend to migrate to concave sites [232]. This enhances particle growth rates at the concave and void growth rates at the convex sites. Thus void growth is influenced by the geometry and number of grains enclosing the void and the nature of the substrate surface.

The development and persistence of voids depend upon the ability to form nucleation sites which is associated with the interfacial energy between the film and the substrate; low values of interfacial energy indicate high wettability. The interfacial energies are shown in Table 6.3 and suggest that the platinum atoms execute random walk on the substrate surface at high temperatures until they evaporate or coalesce with larger agglomerates of platinum, leaving sites where nucleation is not favoured void of metal. The glass present in the fritted film presumably wetted the alumina and platinum readily at high temperatures enabling good adherence of the film to the substrate.

Interface	Interfacial energy (in air at 1400°C) $J\ m^{-2}$
Pt – air (void)	2.097 ± 0.05
Pt – Al_2O_3	1.050 ± 0.08
Pt – Pt	0.525 ± 0.035
Al_2O_3 – Al_2O_3	0.065 ± 0.015

***Table 6.3** Interfacial energies between various solids (McLean and Hondros [233])*

6.3.4 Cross-sectional area of the films

These results are shown with reference to the data obtained when firing the films at 1000°C and 1300°C for various times (Fig. 6.17). There was a rapid initial decrease followed by a slower continuous decrease in the cross-sectional area of the platinum films. Electrical discontinuity in the films occurred at similar values of cross-sectional area at treatment temperatures of 1000°C and 1300°C. These values were approximately 1500 and 550 $(\mu m)^2$ for the fritted and fritless films respectively. This is probably because the film formed isolated platinum islands at a particular film thickness which was related to the size of the voids and the islands. This is more clearly understood by considering a process with the reverse effect, like that of sputtering a metal onto a substrate. The sputter process first forms isolated platinum islands which join to form at least one continuous electrical path (between the two extreme ends of the film's length) at a particular thickness (and projected through porosity) of the deposit.

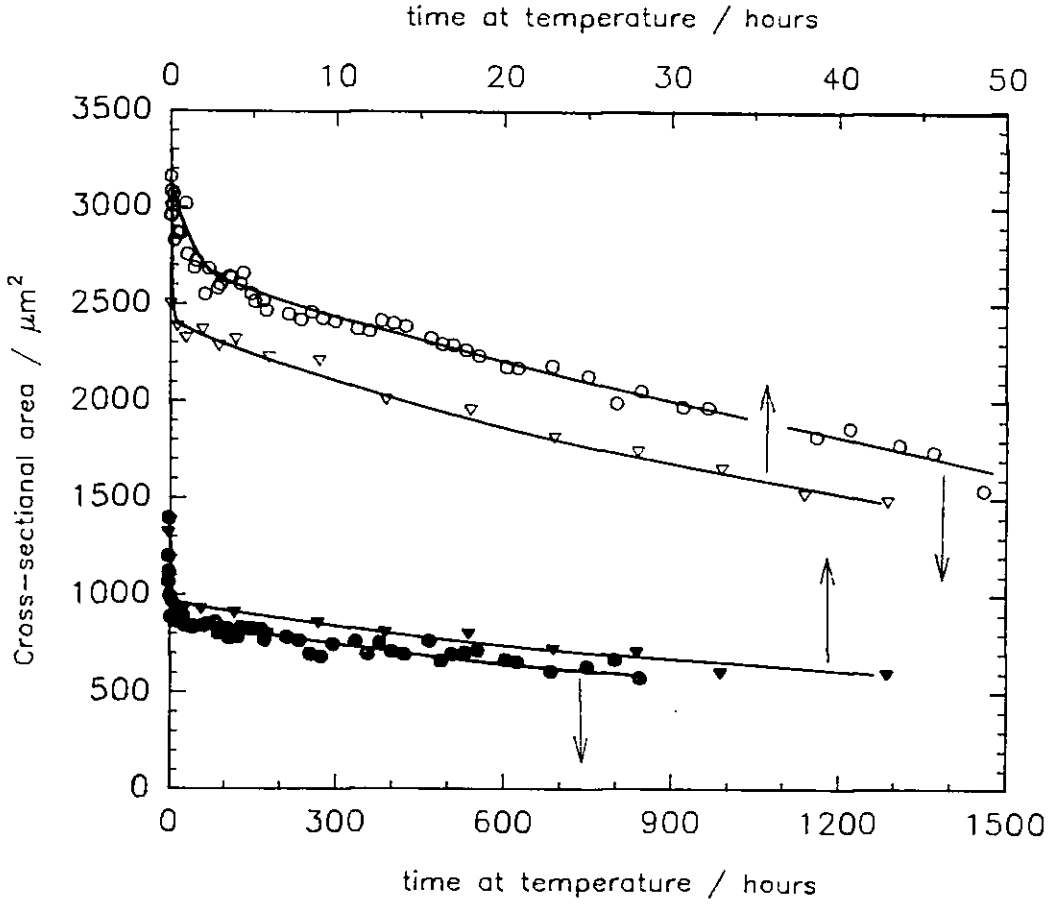

Figure 6.17 Changes in cross-sectional area with time of the platinum films following firing at temperatures indicated. Fritted films: ○,1000°C; ▽,1300°C. Fritless films: ●,1000°C; ▾ ,1300°C.

6.3.5 Temperature coefficient of resistance (α) measurements

Values of α for a number of platinum films were calculated from the variation of resistance with temperature (Fig. 6.18) and compared (Table 3.2) to that of pure bulk platinum and values obtained from the manufacturers data sheet.

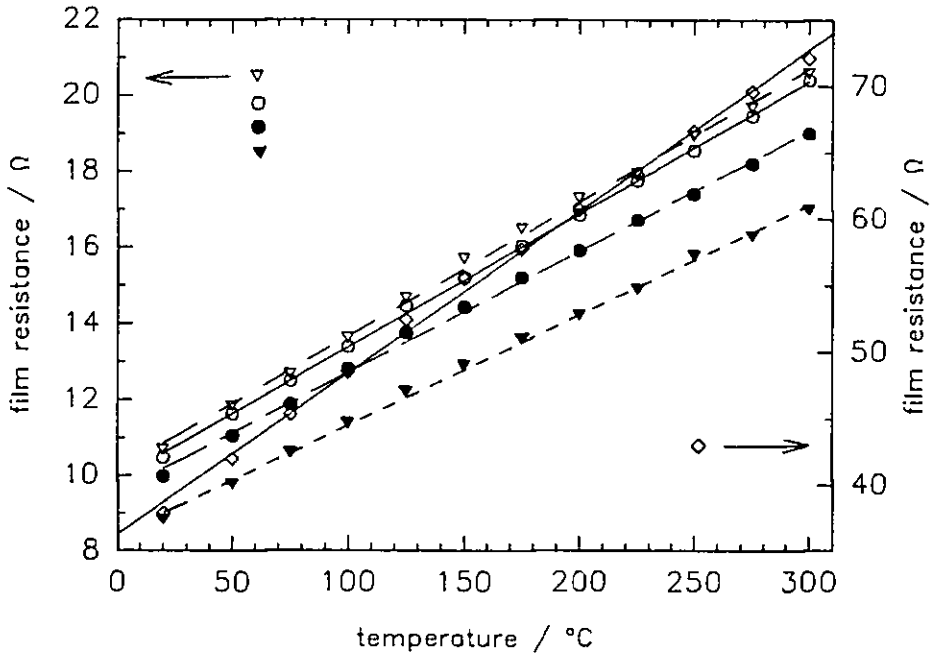

Figure 6.18 The variation of resistance with temperature, enabling calculation of α_f; film type, sintering temperature in °C, time at sintering temperature in hours, R_i in ohms: ▼fritted, 1300, 36, 8.7; ●, fritted, 980, 0.18, 9.9; ○, fritless, 980, 0.18, 10.6; ▽, fritted, 1150, 86, 10.9; ∃, fritless, 1300, 36, 37.5.

Platinum thick film Type/Thermal treatment	α (20-125°C) ppm $°C^{-1}$
fritless/ 980°C; 10 min	3600 ±50
fritted/ 980°C; 10 min	3500 ±50
fritted/ 1150°C; 83hrs	3600 ±50
fritted/ 1300°C; 35hrs	3550 ±50
Bulk platinum[201] (99.2% pure)	3800
Electro-Science Laboratories data sheet	3500 ±200

Table 6.2 Comparison of α values of thick platinum films (α_f) and bulk Pt (α_{Pt}).

The positive α values of the thick platinum films (α_f) and their proximity to that of bulk platinum (α_{Pt}) suggest that conduction was controlled by electrons flowing through the metal; effects such as electron tunnelling [234,235] or electron hopping [236,237] can be neglected as these would yield negative values of α. Computed α_f values were lower than those of α_{Pt} and should be treated with caution at present. The value of α_f may differ from that of bulk platinum because of a difference in the expansion coefficient of the film and the substrate resulting in a strain–gauge effect superimposed on the value for the platinum α_{Pt}. An examination of the thermal expansion coefficients (ε) of the alumina substrate ($\varepsilon_s = 6.3\times10^{-6}$ °C^{-1}) and platinum ($\varepsilon_{Pt} = 9.1\times10^{-6}$ °C^{-1}) reveals that on heating the platinum film tended to be compressed. In fact it has been shown that the value of α of any film, characterised by a certain thermal expansion coefficient (ε_f) and deposited on a substrate with thermal expansion coefficient (ε_s) is given by [238]

$$\alpha = \alpha_\rho - \epsilon_f - \left(2\frac{(\epsilon_f - \epsilon_s)(G_F - 1 - \nu)}{1-\nu}\right) \qquad (6.5)$$

where α_ρ indicates the temperature coefficient of resistivity, G_F is the longitudinal gauge factor of the film and ν is the Poissons modulus for the substrate. This reversible change with temperature has only a small change in the α_f as the value calculated by substituting G_F=2, ν=0.22, $\varepsilon_s = 6.3\times10^{-6}$ °C^{-1}, $\varepsilon_{Pt} = 9.1\times10^{-6}$ °C^{-1}) and α_ρ=3800 ppm °C^{-1}, yielded an α value for the film of ≈3780 ppm °C^{-1} which is still higher than the obtained values for the film (Table 6.2). Thus discrepancies between α_f and α_{Pt} cannot be accounted for by consideration of stresses imposed on the film by the substrate. It may be that the α of the platinum material deposited was altered by the presence of the glass or a chemical interaction with the substrate.

According to Watkins [239], the multiple (α x ρ) for a given material remains constant, so the lower value of α obtained for the platinum conductors suggests they had a higher resistivity ρ, given by,

$$\rho_{film} = \rho_{pure\ Pt}\ (\alpha_{Pt} / \alpha_f) \qquad (6.6)$$

Thus a material will dominate the resistivity (relative to the pure bulk sample), to the same extent as it dominates α; the ratio of the deviation of α_f with α_{Pt} was ~0.93 (at maximum) indicating that the resistivity of the film may have been approximately

(1/0.93) times higher than that of pure bulk platinum. It has been shown by Wert and Thomson [240] that the total resistivity of metals can consist of various additive components

$$\rho_{total} = \rho_{temperature} + \rho_{impurities} + \rho_{deformation} \quad (6.7)$$

where it is implicit that the effects of lattice impurities and lattice structural distortions are both temperature independent. Thus there may be a difference between the resistivity value assumed for the film (that of bulk platinum) in later sections is the true value of the resistivity.

6.3.6 Analysis of the platinum film as a two–phase system

6.3.6.1 General

An insulating phase within a conducting matrix represents a two-phase system. Porous thick film conductor tracks can be modelled as electrical two-phase systems; the sites occupied by the metal phase (platinum in this case) are good electrical conductors and the glass and void phases are electrically insulating. Some properties of multiphase mixtures may be obtained by simply averaging the properties of the pure phases, but the relationship of the thermal and electrical conductance of such mixtures to the conductances of the pure phases represents a problem that has challenged scientists and engineers for over a century. The numerous theories proposed to model the electrical conductivity of heterogeneous media fall into three general categories: a) effective medium theories, b) percolation theories and c) chain theories. Chain theories are not considered relevant in treating the electrical properties of sintered metals because they involve the use of probability arguments to determine how a set of conducting spheres form continuous chains through the sample; they are only mentioned here so that the reader may be aware of their existence.

Knowledge of the width and length of the film, the amount of platinum present and the resistivity of platinum, enabled calculation of $R_{c(t)}$ (Appendix E); this was the resistance expected based on the amount of platinum present at time t, assuming a layer of platinum with uniform cross-section along the length of the film and the absence of voids. The ratio between the measured film resistance at time t (denoted as R_t), and $R_{c(t)}$ (i.e $R_t/R_{c(t)}$) was found to be in the range of 1.8–2.2 (Fig. 6.19)

irrespective of the porosity and thermal treatment given to the film. The fact that this ratio was similar between both fritted and fritless films suggests almost complete segregation at an early stage of the glass and platinum within the fritted films. The ratio $R_t/R_{c(t)}$, which is expected to be unity in the absence of tortuosity indicates a tortuosity factor θ_1 [209] of approximately 1.5 {i.e $\approx(2.2)^{1/2}$} for the films.

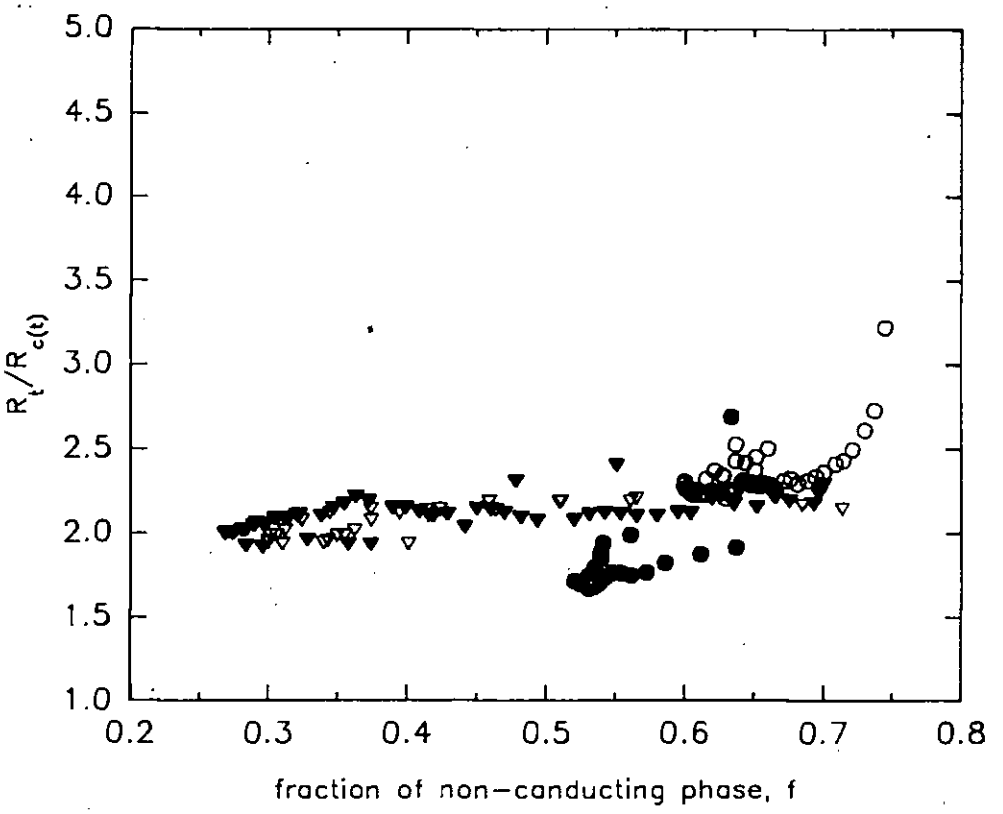

Figure 6.19 *Rt/Rc vs porosity at increasing firing times for fritless films fired at ▼,1000°C; ▽,1300°C and fritted films fired at ○,1000°C; ●,1300°C.*

Films screen-printed and fired on a substrate are subjected to stresses at room temperature caused by differences in thermal expansion coefficients of the film and the substrate on cooling from the sintering temperature. The change (ΔR) in resistance (R) at the measurement temperature (20°C in this case) induced by the stresses can be evaluated by integrating [241] (Eq. (6.5)) to arrive at

$$\frac{\Delta R}{R} = \Delta T \frac{2(\epsilon_f - \epsilon_s)}{1-\nu} (G_p - 1 - \nu) \qquad (6.8)$$

where ΔT is the difference between the peak firing temperature and the measurement

temperature (20°C in this case). Calculations using a peak firing temperature of 1300°C reveal the percentage change in resistance (at 20°C) induced by stresses due to thermal expansion to be minimal at just below 1%.

The data gathered in sections 6.3.1 to 6.3.5, enable the electrical resistance of the films to be portrayed as a function of their porosity for comparison with theoretically derived relations. A dimensionless relation can be defined as a resistance ratio Q,

$$Q = R_t / R_{e(t)} \qquad (6.9)$$

where R_t is the film resistance (at 20°C) following thermal treatment at time t, and $R_{e(t)}$ is the effective resistance of the film at time t, assuming that the non-conducting fraction was also conducting to the same extent as the conducting phase (platinum in this case) of the rest of the film. Relations and parameters used to calculate values of Q are exemplified in Appendix E.

6.3.6.2 Comparison with effective-medium theories

In the effective medium approach a typical element of the mixture is considered to be embedded in a homogeneous medium and expressions for the "effective" properties of the medium developed. Relationships have been developed [242, 243,244,245,246] and shown to apply with excellent accuracy for low concentrations (up to 10% non-conducting fraction) of particles (irrespective of their size distribution) that are small in comparison to the bulk dimensions. The reason for the upper limit of applicability of 10% for these relations lies in the physical consequences of the assumptions used to derive them implying that the lines of flow describing the electric path show no discontinuities, the flow is smooth and that at all points within the system including the boundaries, lines of flow are orthogonal to equipotential surfaces. Concentrated suspensions infer that the particles of the dispersed phase approach each other and the fields surrounding them interact. The models referred to below are simplifications of theoretically derived equations for the special case involving concentrated suspensions of a two-phase conductor-insulator mixture where the non-conducting phase is dispersed in a conducting medium.

Lord Rayleigh [245] used the principle of superposition of potentials, and for a cubic array of equisized non-conducting spheres in a conducting medium, derived an

equation which was further refined by Runge [247] and simplifies to

$$\frac{1}{Q} = 1 - \frac{3f}{2+f-0.3937f^{10/3}} \tag{6.10}$$

where f is the volume fraction occupied by the non-conducting medium. Note that the original relations developed were expressions of the conductivity ratio of the heterogeneous mixture to that of the conducting medium and not the resistivity (or resistance) ratio Q. Meredith and Tobias [248] used a different function for the potential and considered higher terms in the series to obtain

$$\frac{1}{Q} = 1 - \left(\frac{3f}{2 + f - \dfrac{1.315\, f^{10/3}}{\frac{4}{3} + 0.409\, f^{7/3}}}\right) \tag{6.11}$$

Bruggeman [249] used Maxwell's [244] original 3D model and considered the surrounding medium to be a continuum from the point of view of each additional fraction of the dispersed phase, to derive the following approximation

$$Q = (1-f)^{-\frac{3}{2}} \tag{6.12}$$

Bruggeman's equation has been tested experimentally and shown to be a good approximation only when a large range of particle sizes is present in the dispersion [250,251]. It also allows volume fractions approaching f = 1, without contact between adjacent particles and therefore is not limited by close packing fractions.

Fricke [246] obtained a relation to account for a dilute concentration of randomly oriented ellipsoids. Reynolds and Hough [252] extended Fricke's original equation so that it could be valid for a concentrated suspension of ellipsoidal particles; Meredith [253] subsequently corrected an error in the equation of Reynolds and Hough which for non-conducting ellipsoids in a conducting medium reduces to

$$Q = (1-f)^{\frac{-1}{1+\beta+\gamma}} \tag{6.13}$$

where β and γ are purely numerical and are related to the axial ratio of the non-conducting spheroid.

The corresponding three dimensional models described above can be visualised in two dimensions by replacing the spheres in the above model by cylinders. For a square array of equisized parallel cylinders with the field perpendicular to the axis of the cylinders, the conductivity ratio relation derived by Lord Rayleigh reduces to

$$\frac{1}{Q} = 1 - \frac{2f}{1+f-0.3058f^4} \tag{6.14}$$

Runge [247] further refined Eq. (6.14) to read

$$\frac{1}{Q} = 1 - \frac{2f}{1+f-0.3058f^4-0.1334f^8} \tag{6.15}$$

Expressions for concentrated suspensions in two dimensional conductor-insulator dispersions have no physical significance above $\pi/4$ corresponding to the close packing of cylinders, where the conductivity ratio is expected to be infinity; the fact that this is not predicted is due to the approximations involved in the derivations.

The relation for an expression containing a random arrangement of non-conducting cylinders follows from Eq. (6.13), for prolate spheroids as the limiting case where the ratio of the major to the minor axis tends to infinity ($1+\beta+\gamma = 0.6$, Appendix F).

$$Q = (1-f)^{-\frac{1}{0.6}} \tag{6.16}$$

Equation (6.13) reduces to Eq. (6.12) when all the three principal axes of the ellipsoid are equal (i.e for spherical particles); however the equation does not reduce to that Eq. (6.14) or (6.15) concerning a dispersion of parallel rods or cylinders, as the former equation (Eq. 6.13) is based on a model containing a completely random orientation and not a square array.

The resistivity–porosity behaviour of consolidated systems (such as sintered metals, porous ceramics, sandstone etc) owing to their complexity and difficulty in characterisation, has only been treated empirically; various investigators [254,255] have found Archie's law [256] to be valid. Winsauer [257] added an empirical constant, C_1, to Archie's equation which then takes the form,

$$Q = C_1 (1-f)^m \qquad (6.17)$$

where m is also an empirical constant. This equation (Eq. (6.17)) is a general and empirical form of Eq. (6.13) for a two–phase system.

The dimensionless theoretical and empirical relations between Q and f described above are shown together with the experimentally derived data in Figs. 6.20 and 6.21 for the fritless films fired at 1000°C and 1300°C respectively and Figs. 6.22 and 6.23 for the fritted films. Previously diverse data at the various temperatures (§ 6.3.1) are seen to be grouped, following a similar relationship and showing an increasing value of Q with increasing porosity. The fact that little scatter was observed in each set of results is due to the averaging of a large number of data. Uncertainty in the data was lower with decreasing porosity fractions but increased towards failure because of the magnification of errors (i.e rate of platinum weight loss and rate of decrease in cross-sectional area) with time.

Figures 6.20-6.24 enable certain generalisations to be made. Two distinct Q-f types of behaviour are evident in each set of experimental data; both are associated with a high resistivity ratio at high fractions of non-conducting phase. One type of behaviour is between points 1 and 2 and relates to sintering of the film (thus expelling some of its porosity) until a minimum porosity was reached at point 2 where the conducting part of the film may have already reached a maximum in density. The other relation is between points 2 and 3 and relates to the growth of voids within the sintered film. These relations show that the microstructure of the film influenced the resistivity-porosity relationship. A possible explanation is that at point 1 where the films first became electrically continuous by joining of the platinum particles there may have been a large resistance due to the existence of narrow necks between particles, thus increasing the measured film resistance.

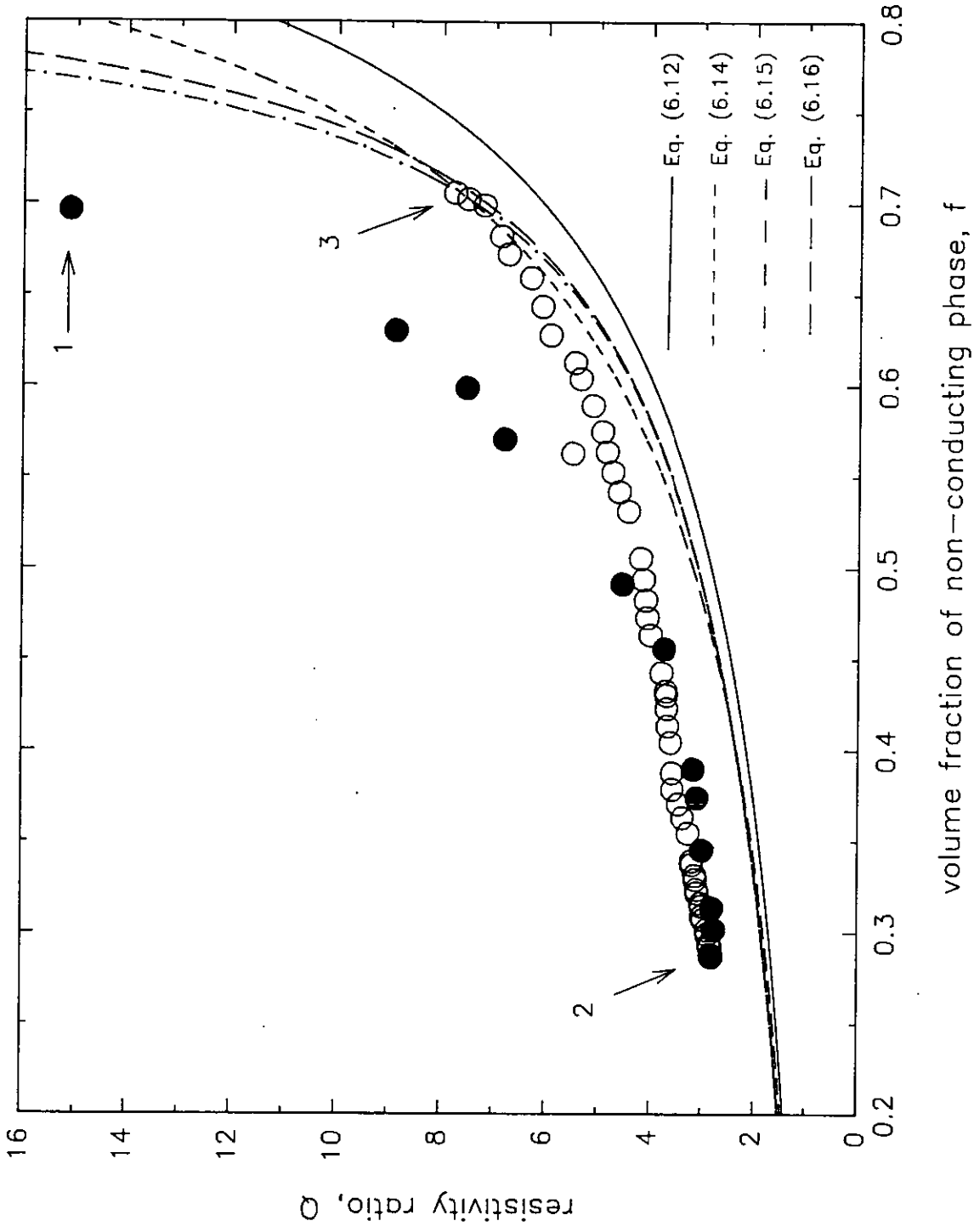

Figure 6.20 *Resistivity ratio vs porosity for fritless films fired at 1000°C; ●,represent data during the resistance decrease phase; ○,represent data during the resistance increasing phase. Lines represent theoretical relations and are marked with their corresponding equation numbers as they appear in the text.*

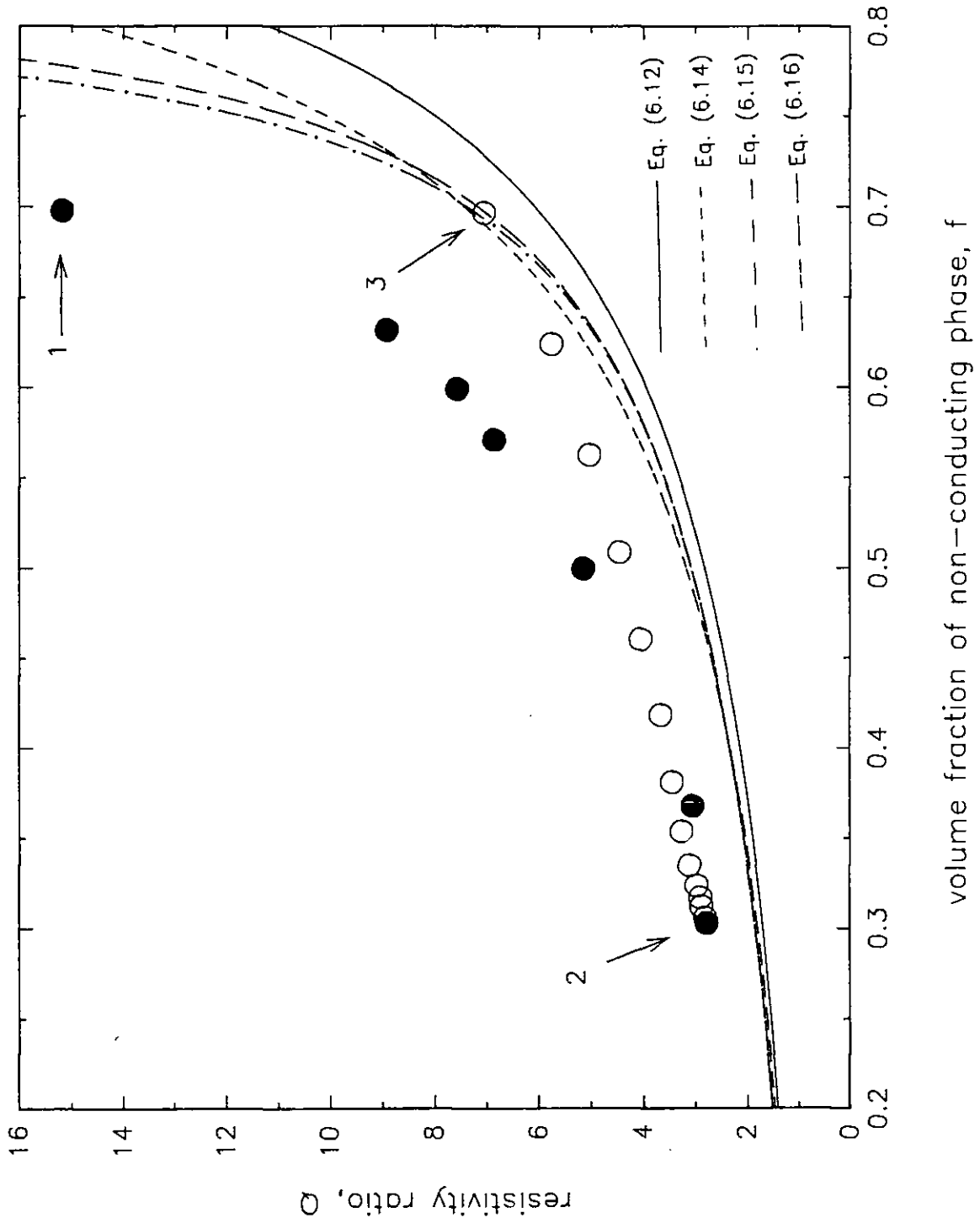

***Figure 6.21** Resistivity ratio vs porosity for fritless films fired at 1300°C; ●, represent data during the resistance decreasing phase; ○, represent data during the resistance increase phase. Lines represent theoretical relations and are marked with their corresponding equation numbers as they appear in the text.*

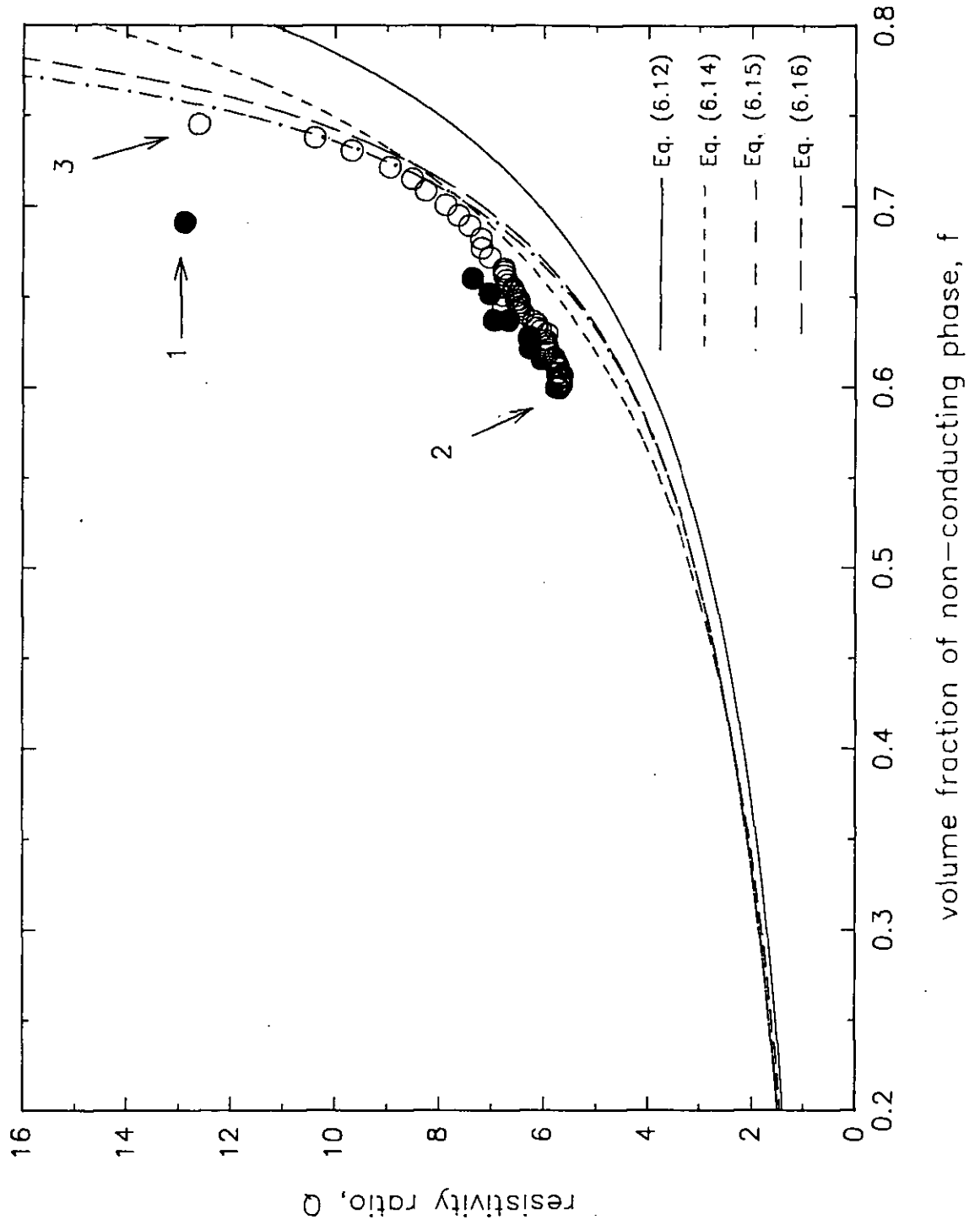

***Figure 6.22** Resistivity ratio vs porosity for fritted films fired at 1000°C; ● represent data during the resistance increasing stage; O represent data during the resistance increasing stage. Lines represent theoretical relations and are marked with their corresponding equation numbers as they appear in the text.*

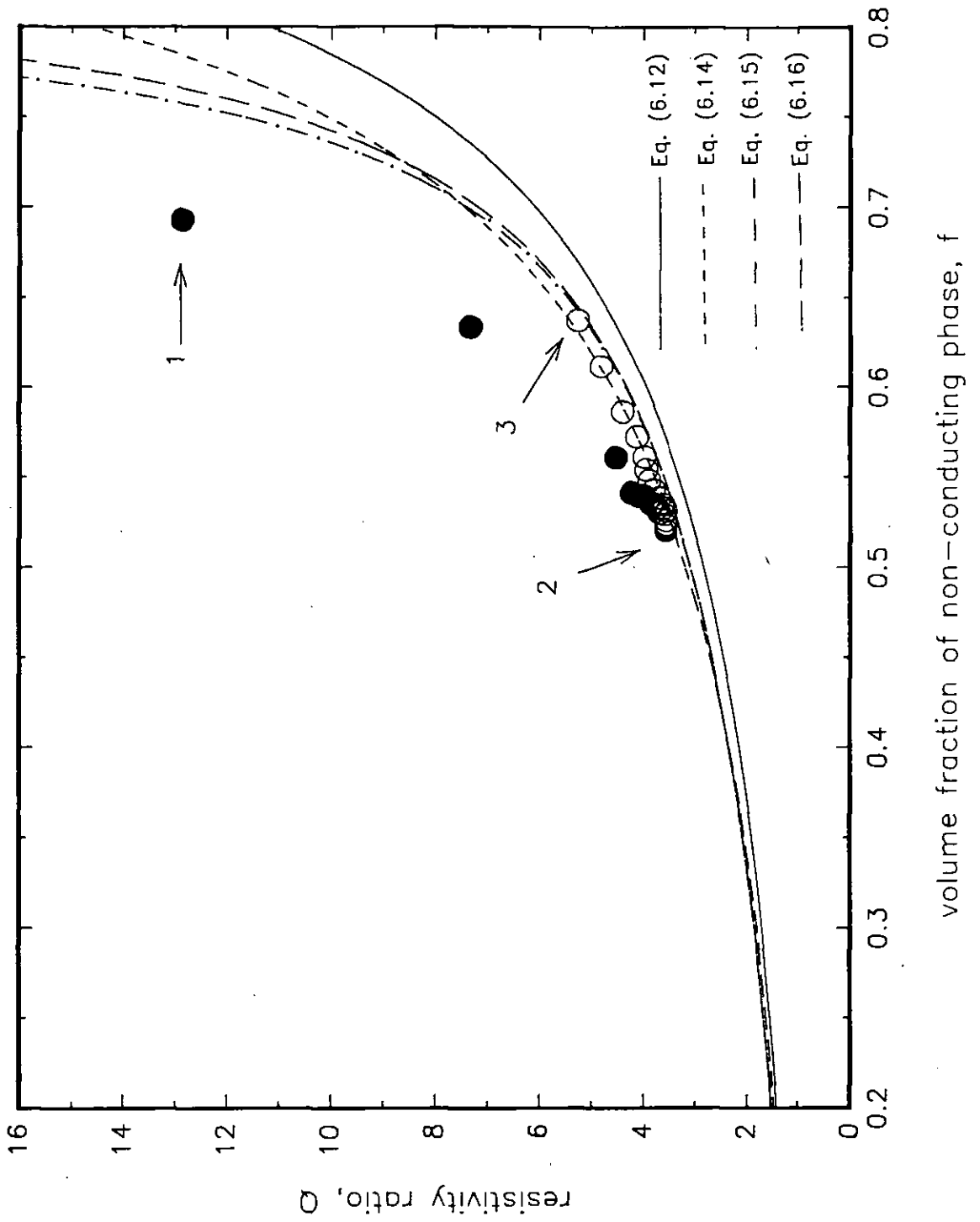

Figure 6.23 *Resistivity ratio vs porosity for fritted films fired at 1300°C; ●, represent data during the resistance decreasing stage; ○, represents data during the resistance increasing stage. Lines represent theoretical relations and are marked with their corresponding equation numbers as they appear in the text.*

Fritless films reached a lower value of f than fritted films (compare Figs. 6.20 & 6.21 with 6.22 & 6.23); this can be explained by the presence of the glass frit in the latter films. Fritted films demonstrated a lower value of f when fired at 1300°C as opposed to 1000°C; this may have beeen partly due to the removal of a larger amount of glass from the film when sintered at 1300°C and partly due to increased sintering of the platinum phase. A smaller difference in the minimum value of f reached was demonstrated by the fritless films, the curves obtained at 1000°C and 1300°C being virtually superimposed; this is consistent with the absence of glass from the film. The times at which the minimum values of f were reached coincided with the times of the normalised resistance minima in Fig. 6.7 and hence it may be concluded that the lower resistance minima of the films fired at higher temperatures was due to the lower porosity achieved. The subsequent rise in film resistance that followed the minimum resistance noted in figure 6.7 was due to an increase in porosity caused by void growth.

The theoretical equations that most closely fit the experimental data (Figs. 6.20-6.24) are those based upon the two dimensional case (such as equations 6.14-6.16) i.e non-conducting cylinders dispersed in a conducting medium. This is consistent with microstructural observations within the film (§ 6.3.3) which show that the through voids (which were non-conducting) resemble embedded cylinders. It is necessary to recognise that the theoretical models were developed for perfect cylinders and that the voids in the film are not perfectly cylindrical. In fact closer agreement between theory and experiment is observed with increasing fraction of non-conducting phase; it is possible that this could result from the tendency of the through voids to become increasingly more cylindrical with firing time (§ 6.3.3). Thus the voids more closely resembled the theoretical model causing a progressive shift of the Q-f behaviour towards the theoretical curve for embedded cylinders with increasing firing time. The random nature in the dispersion of the through voids suggests that Eq. (6.16) should more closely match the experimental data than Eq. (6.14) or (6.15).

The general theoretical equation (Eq. (6.13)) indicates that a dependence upon pore geometry should be expected. Interestingly the variation of the resistivity ratio

with porosity, (Q–f) relation, observed experimentally can be fitted by Eq. (6.13) [253] by choosing for each point a void shape (axial ratio) in order to set the exponent value of the equation. Changes in the void shape were observed with time, although the voids were irregular (i.e did not resemble perfect spheroids or cylinders) and insufficiently well characterised; thus a theoretical treatment was unjustifiable. It may be possible to pursue an explanation of the Q-f data by undertaking computer simulations [258] to investigate the effect of various sized irregular voids embedded in a conducting medium on the resistivity of the matrix.

The results for the fritted system at 1000°C, after approaching the theoretical curve for embedded cylinders show a steep rise away from it; this is consistent with a tendency towards a value for Q of infinity at $\pi/4$, not predicted by the theoretical relation for the conductivity of a matrix with embedded cylinders due to the approximations made in its derivation. An interesting feature within the curve for the fritless films at 1000°C (Fig. 6.22) is the clustering of the data points into sets that follow different slopes; this effect may be related to the breaking of the conduction paths by void coalescence, briefly changing their axial ratio.

A plot of the data in order to yield values of m and C_1 of Eq. (6.17) (Table 6.3) for fritless and fritted films fired at 1000°C and 1300°C is shown in Fig. 6.24; linearity of the plot suggests that the modified Archie equation can be used to model changes in resistivity ratio with porosity for porous sintered thick film conductors. Data obtained during initial sintering (points 1 to 2 on Fig. 6.24) showed a value of m of ~-2.2 which was higher than the value of -1.2 corresponding to prolonged treatment times (points 2 to 3) at temperatures of 1000°C and 1300°C. Values for m of -1.3 for unconsolidated sand and -1.8 to -2.0 for sandstones was reported by Archie [256].

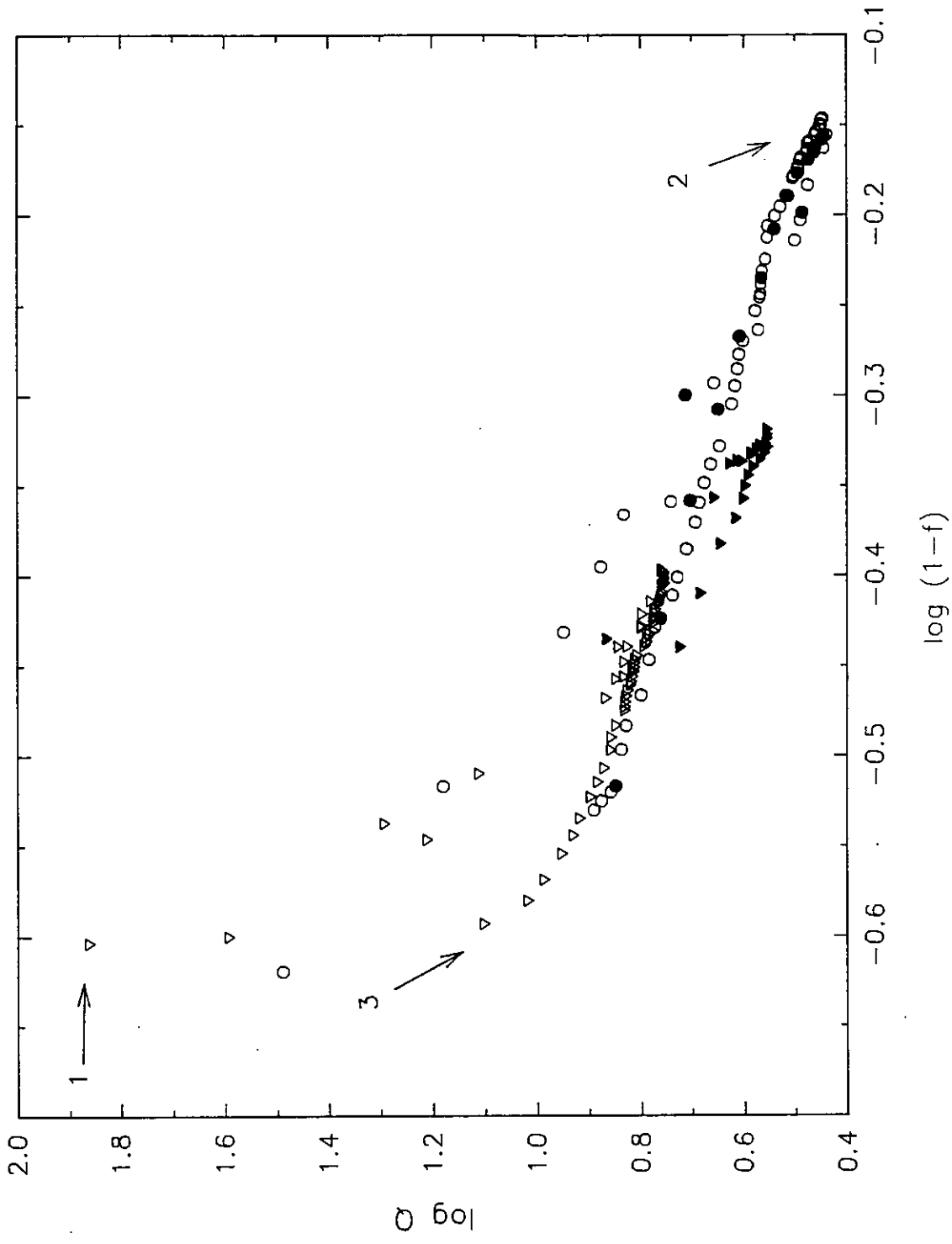

Figure 6.24 *Log_{10} Q vs Log_{10} (1-f) for platinum films printed on alumina substrates and fired for prolonged periods. Film type/firing temperature (°C); ○ fritless/1000; ● fritless/1300; ▽ fritted/1000; ▼ fritted/1300.*

Film type / firing temperature	m	C_1
Fritless / 1000°C and 1300°C	–1.2	1.8
Fritted / 1000°C	-1.2	1.8
Fritted / 1300°C	-1.7	1.0
All data during initial sintering	–2.2	1.2

Table 6.3 *Empirical values of the constants m and C_1 ,from Eq. (6.17)(Archies equation) for fritted and fritless platinum films sintered on 96% alumina.*

6.3.6.3 Comparison with percolation theories

With appropriate representation percolation models are useful for characterising a multitude of disordered phenomena as diverse as galactic structure, forest fires, measles epidemics and more relevantly random two-phase systems. Recently a considerable amount of literature has built up. For an introduction the reader is referred to Clerc *et al* [259] and for applications to Zallen [260].

The approach is usually to define the proportion, p, of sites or bonds present on the lattice. The key factor in percolation theory is the existence of a percolation threshold, namely a critical value of the occupation probability of the bonds, p_c. When the probability p is less than p_c the occupied bonds form finite clusters. A cluster is any set of vertices connected to each other by occupied bonds. For $p>p_c$ there exists at least one cluster that connects opposite sides of the whole sample together with a distribution of finite clusters.

Previous workers have modelled the conductivity of inhomogeneous conducting materials by random resistor networks with the emphasis on the binary case, modelling a random mixture of two materials with very different conductivities [261,262,263,264]. This was done by relating the probability p, with the volume fraction of conducting phase, V_f (V_f = 1-f). Monte-Carlo simulations [258], analog experiments [265,266,267] and series expansions [268] have shown that near the conduction threshold (generally in the range $V_c < V_f < V_c+0.2$)

the following relationship is valid:

$$\sigma = \sigma_o (V_f - V_c)^s \quad (4.3)$$

where σ and σ_o are the conductivity of the two-phase system and conducting component respectively; V_f, is the volume or area fraction of conducting component (for 3D and 2D systems respectively), and V_c, is the critical volume or area fraction required for continuity

for the 3-D case $s = 1.6$ to 2.0 , $V_c = \sim 0.15$

for the 2-D case $s = 1.0$ to 1.4 , $V_c = \sim 0.5$

Note that the value of the critical exponent s, is a novel universal characteristic of the electrical percolation problem.

Scher and Zallen [269] have proposed an empirical relation, $V_c P_F = 0.154$, to calculate the value of V_c if the packing fraction (P_F) is known. This relation is not universally valid [270] and it is now widely recognised that there exist large variations of the critical volume fraction ranging between 2-60% which may be due to differences in system microstructure [271] as well as film dimensionality. The value of V_c can be treated as an adjustable parameter in the absence of other insights into the conduction threshold [272].

The experimental electrical resistance data are shown in Fig. 6.25 plotted according to Eq. (4.3) (above) as $\log_{10}(\sigma/\sigma_o)$ versus $\log_{10}(V_f - V_c)$ using a value for V_c of 0.15. It appears that both fritted and fritless films fired at 1000°C and 1300°C are characterised by similar slopes (Fig. 6.23). Furthermore two distinct slopes are apparent (Fig. 6.25), one between points 1 and 2 and the other between points 2 and 3. The slopes provide values for the percolation exponent, s. The data were plotted using various values for V_c and the resulting exponent values are shown in Table 6.4. The two distinct slopes (Fig. 6.25) are interesting as they may provide evidence of a change in the dimensionality of the system. The clear change from a higher to a lower exponent value (obtained from the slope) and the magnitude of that change, is typical of the change expected if the film had changed dimensionality from 3D (points 1 to 2) to 2D (points 2 to 3). Such a change in dimensionality is supported

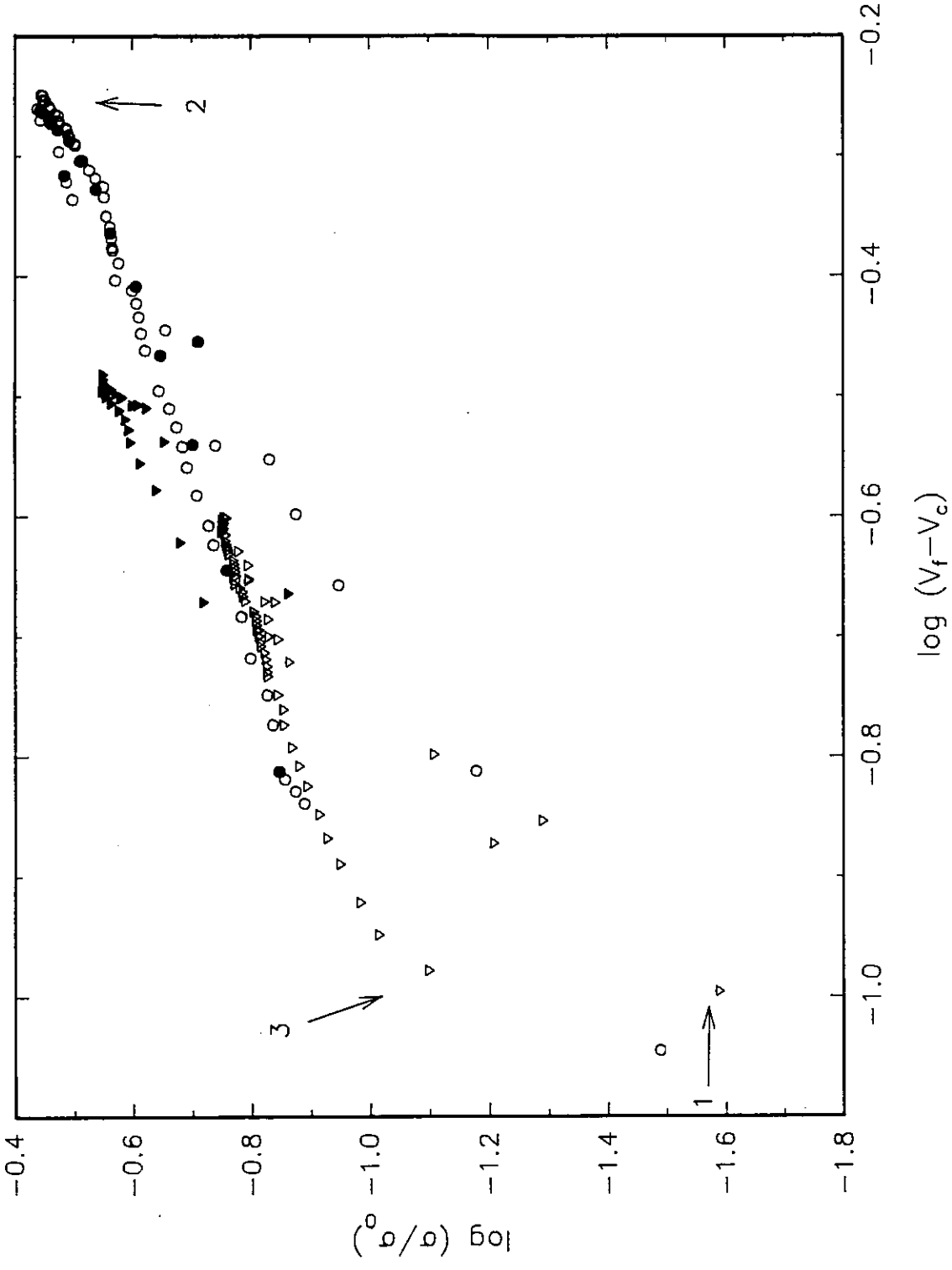

Figure 6.25 *Log_{10} ((σ/σ_0) vs (V_f-V_c)) for fritted films fired at: ▽,1000°C; ▼,1300°C and fritless films fired at ○,1000°C; ●,1300°C.*

by the scanning electron micrographs (§ 6.3.3). In order to derive values of s in the range predicted by percolation theory it is clear that the value of V_c must be taken to be in the region between 0 and 0.1; however these values are lower than those obtained experimentally i.e ~0.23.

The expected percolative transition, (i.e a sudden rise in resistance vs porosity near the critical volume fraction V_c), was not observed for all films. This may have been due to dimensional variations along the film; failure inevitably tended to occur at the thinner and less dense regions (i.e failure was localised and not homogeneous). Localised failure renders a higher observed value of V_c than the true value which otherwise would have been obtained if the system had arrived homogeneously at a percolation threshold; this could also be an explanation for the discrepancy between the experimentally observed value of V_c (~0.23) and that used to obtain a more meaningful critical exponent t, i.e $V_c = 0$ to 0.1. Furthermore the value of V_c for this system may not be fixed and may continuously change in line with microstructural changes. Consequently the results did not yield the value of the exponent expected for electrical conduction in a two–phase metal–insulator.

Value of V_c assumed	Value of exponent "s" obtained (between V_c and V_c+0.2)	
	During initial sintering (between points 1 and 2 on Fig. 6.25)	During void growth (between points 2 and 3 on Fig. 6.25)
0.00	2.0	1.1
0.05	1.8	1.0
0.10	1.7	1.0
0.15	1.4	0.8
0.23	0.9	0.5

Table 6.4 *Percolative exponents for various assumed values of V_c*

Archie's equation is analogous to that of the limiting case of percolation theory, where the percolation threshold occurs at zero porosity; this has been shown to be realistic for consolidated systems [255,254].

It is fairly certain that between points 1 and 2 (Fig 6.25) the resistance changes are due to sintering and improvement in contacts between particles (§ 6.3.1 & § 6.3.6.2). This effect was expected to be modelled by percolation theory yet the analysis was disappointing as in order to achieve a percolation exponent s, expected for a three-dimensional two-phase system a value for the critical volume fraction V_c lower than that obtained experimentally had to be used. Furthermore the resistance increase near failure could not be explained by the 2D or the 3D case of percolation theory.

6.3.7 Actual operation of heater

The above data all relate to heat treatment of thick films in an environment of uniform temperature. In actual use on sensors the films were heated by the traversal of an electric current. Operating in the current passage mode showed that for a given temperature, failure of the films occurred much earlier and the time to failure was less predictable than when heated by a furnace. This was presumably because heat was preferentially liberated in a high resistance section of the film causing uneven heating hence faster deterioration at such points.

Data obtained by heating the films in a furnace suggested that failure was a result of increased porosity (due to growth of voids and loss of metal by evaporation) and was accelerated when less metal was deposited. Thus it should be possible to increase the lifetime of a practical heater by satisfying one or more of the following, (i) printing films with lower porosity and / or higher platinum content, (ii) the inclusion of platinum grain growth suppressors, and (iii) overprinting with a material that will retard the rate of platinum weight loss.

6.4 SUMMARY

Zirconia oxygen sensors operate at elevated temperatures, typically 650°C, and integral thick film heaters have been developed to maintain this temperature. The heater can be used simultaneously as a resistance thermometer for temperature control: in this instance it is important that the heater resistance remains constant at a given temperature. Operating life of the heater is also important as it may limit sensor life.

Thick film platinum heaters printed onto alumina substrates using either fritted or unfritted inks, were examined after extended treatments in a furnace at temperatures in the range 800-1300°C. Values above the normal operating temperature were chosen to accelerate ageing effects. At 1000°C and above there was an initial reduction in resistance (measured at 20°C) followed by a progressive increase until eventual discontinuity. The time taken for the resistances to increase to 1.5 times the initial values indicated an activation energy for both fritted and fritless films of 135 kJ mol^{-1}.

Evaporation rates of platinum from the substrates were measured by dissolution of the remaining metal and atomic absorption spectroscopy of the resulting solutions. Rates were 0.7-0.8 g m^2 h^{-1} at 1300°C in air for both fritted and fritless films with an activation energy of 207 kJ mol^{-1}.

Microstructural analysis using a scanning electron microscope revealed grain growth of platinum and also growth of voids within the films. It seems likely that the initial decrease in resistance was due to sintering of the platinum particles and the subsequent increase was due to platinum evaporation and growth of voids. Initially the porous structure was 3-dimensional (3D) but progressively it became 2-dimensional (2D) with the large voids revealing the substrate beneath. Eventually voids coallesced and traversed the width of the film resulting in electrical discontinuity.

The fractional area of the tracks revealing exposed substrate was measured using automated image analysis equipment. This fraction was found to be linearly related

to the firing time with an activation energy (for firing to reach 50% exposure) of 130 kJ mol^{-1}. This was the same (within experimental error) as the activation energy for resistance increase suggesting that the dominant factor in the resistance increase was the growth of voids rather than the metal evaporation.

The cross - sectional area of the films treated at 1000 and 1300°C was measured. There was a rapid initial decrease followed by a slower progressive decrease. These data together with the platinum loss information enabled the fractional electronic and non-electronic volumes within the films to be quantified. The non-electronic component was the voidage but also included glass where present. It was found that initially, during the resistance decrease phase, the fractional volume of electronic component was increasing. This was reversed during the resistance increase phase.

An attempt was made to understand the resistance vs time behaviour in terms of the fractional volume of the metallic component by applying effective medium theories which quantify the blocking effect of the non-metallic components. Various theoretical relationships between resistance and fractional non-conducting component were compared with the experimental data.

During the initial phase when the resistance of the films was decreasing the resistance values were substantially higher than the theoretical ones. This indicates that during this phase the resistance was controlled by factors other than obstruction effects. It is probable that the governing factor was the high resistance of narrow necks at which points particles had begun sintering.

During the subsequent phase, when the resistance of the films was increasing, resistance values remained greater than theoretical ones but progressively approached the latter as the volume fraction of conducting phase decreased.

The theoretical expressions most closely fitting the data were those based upon a 2D structure, e.g. non-conducting cylinders with their axis perpendicular to the direction of the applied field. In fact this was approximately the microstructure observed during the later parts of the ageing periods with voids exposing substrate

and resembling embedded cylinders.

Percolation theory was also considered for modelling the resistance behaviour but was less succesful. There was difficulty in defining the value of the critical volume of conducting phase between continuity and discontinuity. The value measured of 0.23 led to an unlikely value for the critical exponent.

CHAPTER 7

CONCLUSIONS AND RECOMMENDATIONS FOR FURTHER WORK

7.1 CONCLUSIONS

7.1.1 Introduction

The work concerned the development and characterisation of thick film amperometric zirconia oxygen sensors. The devices had a laminated structure in which a cathode, an electrolyte and an anode were printed, in that order, onto a planar alumina substrate. The anode and electrolyte were porous and acted as a diffusion barrier, restricting the rate of oxygen diffusion to the cathode.

In order to construct devices, investigations were carried out to optimise and characterise the individual components, prior to assembly of complete sensors.

The following sections 7.1.2 - 7.1.5 are a compilation of the summaries from the individual chapters.

7.1.2 Thick Zirconia Films

The processes and requirements for producing zirconia thick films of low connected porosity (<0.1%) on alumina substrates with no loss of adhesion from the substrate or cracking of the film have been investigated and specified. It was found that this required the preparation of an ink with full dispersion of agglomerates of particles of sub-micron size. Dispersal was achieved using a triple-roll mill and was checked using viscosity measurements. Very viscous pastes did not level out after printing while low viscosity pastes tended to run and lose pattern edge definition. The mix used throughout the work contained 40% by weight of tetragonal zirconia powder (Toyo-Soda 3Y), the remainder being ESL 400, a commercial organic vehicle.

Films were dried using an infra-red dryer which enabled a crack-free deposit to be prepared. Where required, film thickness could be built-up by successive print-dry cycles, drying each layer at 150, 450 and 700°C for 10 minutes at each temperature. The final firing of single or multilayers was done at 1300-1550°C to sinter the deposit. This sintering temperature was approached at a ramp rate of 3 °C min^{-1}. The state of dispersion in the pastes had an important influence on the development of the green microstructure and subsequent sintering behaviour.

Thick films of zirconia printed onto 96% alumina substrates and fired at 1400°C or above showed substantial grain growth; there was little grain growth when an intervening layer of platinum was included. Grain growth in the absence of platinum increased as the thickness of the zirconia layer was decreased. Repeating the work on 99.6% alumina revealed little grain growth irrespective of film thickness. Clearly grain growth was accelerated by the transfer of impurities from the substrate to the zirconia film. An intervening layer of platinum either blocked the trasnsfer of impurities or itself acted as a grain growth inhibitor.

Tetragonal zirconia spontaneously transforms to the monoclinic structure. However, the tetragonal phase is metastable if the grain size remains small (<0.5 μm). X-ray diffraction studies of the zirconia thick films, indicated that where grain growth occurred (to > 1 μm) a transformation to the monoclinic form did take place.

It is also well-known that the ionic conductivity of the monoclinic form of zirconia is much lower than that of the tetragonal form. Thus AC impedance measurements were made on the zirconia thick films. These showed the expected substantial decrease in the ionic conductivity for those films in which grain growth had occurred (> 1 μm) and for which X-ray diffraction indicated the tetragonal to monoclinic transformation.

7.1.3 Platinum Zirconia Cermets

Platinum-yttria stabilised zirconia cermet inks were prepared (by intimately mixing solids and carrier vehicle in a triple-roll mill) for screen-printing onto alumina substrates, zirconia discs and zirconia thick films. Fired films were investigated as possible electrodes for use in thick film sensors.

Scanning electron microscopy revealed that the presence of zirconia in the cermets inhibited grain growth of the platinum. With prolonged firing at temperatures above 1000°C progressive growth of voids was observed.

The electronic resistance of the films at 20°C was measured using a four-point probe. As printed and dried the films were not electronically conducting. On firing

at ~500°C the organic binder was removed and electrical continuity was established provided that the platinum content exceeded 55% by volume (zirconia 45%). Prolonged firing above 1000°C progressively increased the electronic resistance of the cermets with firing time after a rapid initial decrease. The increase is thought to have been due to the observed growth of voids of the film and platinum evaporation.

Current densities (per unit geometric electrode area) available at a given overvoltage for electrodes at, for example, 700°C were orders of magnitude higher than those obtainable using porous platinum electrodes and increased with zirconia content of the cermets up to 33% by volume (67% platinum). Current densities also decreased with increasing firing temperature (necessary for preparing a sensor with cofired electrolyte and electrodes).

Measurements on single electrodes, involving the use of a reference electrode, indicated activation energies for the anodic and cathodic processes of 157 and 125 kJ mol^{-1} respectively. The former value suggests that the rate controlling step may have been diffusion of oxygen atoms from the reaction site across the surface of the platinum.

Thus zirconia-platinum cermets have an important role to play in the development of thick-film zirconia oxygen sensors. Besides improving thermal expansion compatibility between the electrode and electrolyte they substantially improved available current densities compared with pure platinum electrodes; this was presumably achieved by the maintenance of a long three-phase boundary length even after treatment at high temperatures (>1300°C) for periods of 1 hour or more.

7.1.4 Amperometric Zirconia Oxygen Sensors

Planar zirconia oxygen sensors were constructed onto 96% alumina using thick films technology exlusively. The cathode was first printed using a platinum-zirconia cermet ink as a circular disc with two protruding radial strips for electrical connections. This was treated at 150, 400 and 1000°C for 10 minutes at each temperature. An electrolyte disc with larger diameter than the cathode was then printed over the cathode; this was dried and fired to sinter the zirconia typically at

1400°C for 1 hour. Finally the anode cermet disc with the same diameter as the cathode was printed onto the electrolyte, dried and briefly fired at the same temperature as was the electrolyte. Platinum wires were affixed to the electrodes for electrical connections. In one case a thick film heater was applied to the reverse side of the substrate.

Sensors were operated in the amperometric mode at temperatures in the range 550-950 °C. This involved the application of a voltage between the electrodes to reduce oxygen at the cathode and evolve oxygen at the anode. This resulted in the setting up of a concentration profile in the pores of the electrolyte. As the applied voltage was increased the current rose and reached a limiting current value controlled by oxygen diffusion through the anode / electrolyte. At applied voltages above 1.5 V the current increased again due to the generation of electronic carriers in the electrolyte.

It was found, as predicted by theory that the limiting current was proportional to oxygen concentration in the range up to 21% oxygen. This has not previously been achieved with devices of this construction. The temperature dependence of the sensor output was found to vary with the temperature at which the device had been sintered and this requires further study. Nonetheless, it does offer the prospect of designing sensors with a low or negligible temperature coefficient.

Two sensors were also constructed on 99.6% alumina substrates. Limiting currents were a factor of four higher on these substrates compared with otherwise identical sensors on 96% alumina substrates. This suggests that impurity diffusion from the less pure substrates aided sintering of the zirconia electrolyte causing pore constriction. An estimate of connected porosity from limiting currents on 96% substrates revealed a value of less than 0.1%.

Promising results were obtained for a sensor operated in the combustion products from a gas-burning flue. Limiting currents were linearly related to the calculated oxygen concentration.

7.1.5 Thick Film Platinum Heaters

Zirconia oxygen sensors operate at elevated temperatures, typically 650°C, and integral thick film heaters have been developed to maintain this temperature. The heater can be used simultaneously as a resistance thermometer for temperature control: in this instance it is important that the heater resistance remains constant at a given temperature. Operating life of the heater is also important as it may limit sensor life.

Thick film platinum heaters printed onto alumina substrates using either fritted or unfritted inks, were examined after extended treatments in a furnace at temperatures in the range 800-1300°C. Values above the normal operating temperature were chosen to accelerate ageing effects. At 1000°C and above there was an initial reduction in resistance (measured at 20°C) followed by a progressive increase until eventual discontinuity. The time taken for the resistances to increase to 1.5 times the initial values indicated an activation energy for both fritted and fritless films of 135 kJ mol^{-1}.

Evaporation rates of platinum from the substrates were measured by dissolution of the remaining metal and atomic absorption spectroscopy of the resulting solutions. Rates were 0.7-0.8 g m^2 h^{-1} at 1300°C in air for both fritted and fritless films with an activation energy of 207 kJ mol^{-1}.

Microstructural analysis using a scanning electron microscope revealed grain growth of platinum and also growth of voids within the films. It seems likely that the initial decrease in resistance was due to sintering of the platinum particles and the subsequent increase was due to platinum evaporation and growth of voids. Initially the porous structure was 3-dimensional (3D) but progressively it became 2-dimensional (2D) with the large voids revealing the substrate beneath. Eventually voids coallesced and traversed the width of the film resulting in electrical discontinuity.

The fractional area of the tracks revealing exposed substrate was measured using automated image analysis equipment. This fraction was found to be linearly related

to the firing time with anactivation energy (for firing to reach 50% exposure) of 130 kJ mol^{-1}. This was the same (within experimental error) as the activation energy for resistance increasesuggesting that the dominant factor in the resistance increase was the growth of voids rather than the metal evaporation.

The cross - sectional area of the films treated at 1000 and 1300°C was measured. There was a rapid initial decrease followed by a slower progressive decrease. These data together with the platinum loss information enabled the fractional electronic and non-electronic volumes within the films to be quantified. The non-electronic component was the voidage but also included glass where present. It was found that initially, during the resistance decrease phase, the fractional volume of electronic component was increasing. This was reversed during the resistance increase phase.

An attempt was made to understand the resistance vs time behaviour in terms of the fractional volume of the metallic component by applying effective medium theories which quantify the blocking effect of the non-metallic components. Various theoretical relationships between resistance and fractional non-conducting component were compared with the experimental data.

During the initial phase when the resistance of the films was decreasing the resistance values were substantially higher than the theoretical ones. This indicates that during this phase the resistance was controlled by factors other than obstruction effects. It is probable that the governing factor was the high resistance of narrow necks at which points particles had begun sintering.

During the subsequent phase, when the resistance of the films was increasing, resistance values remained greater than theoretical ones but progressively approached the latter as the volume fraction of conducting phase decreased.

The theoretical expressions most closely fitting the data were those based upon a 2D structure, e.g. non-conducting cylinders with their axis perpendicular to the direction of the applied field. In fact this was approximately the microstructure observed during the later parts of the ageing periods with voids exposing substrate and resembling embedded cylinders.

Percolation theory was also considered for modelling the resistance behaviour but was less succesful. There was difficulty in defining the value of the critical volume of conducting phase between continuity and discontinuity. The value measured of 0.23 led to an unlikely value for the critical exponent.

7.1.6 Final Comments

A sensor of simple construction and potentially very low cost has been developed and demonstrated. Important advancements were made in the formulation and preparation of the printing inks for the electrodes and electrolyte. By careful optimisation of processing conditions cracking of layers was eliminated: this was made particularly difficult by the substantial difference in the thermal expansion coefficients of zirconia and alumina.

It is anticipated that after further development and testing sensors of this construction will be widely incorporated into combustion systems and internal combustion engines for monitoring and control of air-to-fuel ratio.

7.2 RECOMMENDATIONS FOR FURTHER WORK

Testing of sensors constructed in this work suggested than when the electrolyte was fired at high temperatures (1400-1450°C), the pore size of the ceramic became sufficiently small so that the diffusion of gases through the ceramic changed from bulk to Knudsen type. The temperature dependence of the limiting current measured at a range of barometric pressures would provide additional information of the diffusion mechanism involved.

It might be advantageous to construct devices that have lower electrolyte porosities than those produced in this work. Further work should therefore be aimed at obtaining detailed knowledge of the factors controlling the porosity of the zirconia thick-films. Parameters to be investigated include firing temperature/time, starting particle size and size distribution, and the addition of sintering fluxes. An important objective of this work would be the construction of devices with a reproducible characteristic.

Detailed studies of and the interrelation between microstructure, crystalline structure and electrical impedance of tetragonal (3Y) zirconia films printed and sintered onto alumina substrates of varying purity have been reported here. These require repeating using the fully-stabilised cubic (8Y) form. This would be carried out in parallel with the construction and testing of devices using either the fully-stabilised or a mixture of tetragonal and fully-stabilised zirconia.

Characteristics of thick-film devices have only been demonstrated for sensor operation in lean-burn combustion gases. Further work should involve testing of the devices in sub-stoichiometric exhaust gases: an understanding of the behaviour in such gases would be aided by operation in other mixtures of gases such as CO/CO_2 and H_2/H_2O mixtures.

Factors relating to resistance changes of platinum heater films following heat treatment in an environment of uniform temperature were investigated in chapter 6. In actual use on sensors the platinum films were heated by the traversal of an electric current through the film and this requires further investigation.

REFERENCES

[1] Calvert WR, *MATLAB* 1968 p.275

[2] Stein RL, *BuMines*-RI-8102, 1976

[3] Fairbank LH, *Heat Treatment Metals* **4** 1977 p.95

[4] William DS and Paul JR, *Research and Development* (Nov. 1989) pp.79-82

[5] Franx C, 1984, *Proc. Sensors and Actuators Symposium*, Nov. 1-2, (Kluwer, Deventer, The Netherlands).

[6] Hargreaves KJA, Ovenden NA, Sauba RN and Cotton JA, in *"Sensors: Technology Systems and Applications"* KTV Grattan (ed) (Adam Hilger, Bristol) 1991 pp.183-188

[7] Soejima S and Mase S, *SAE Conf. Sensors and Actuators*, paper 850378 1985

[8] Matsushita S, Inoue T, Nakanishi K, Kato K, Kobayashi N, *SAE paper 850044* 1985

[9] Kocache RMA, *J. Phys. E: Sci. Instrum.* 19 1986 pp.401–412

[10] Twisselham L and Gast Th, *Feinwerktechnik und Messtechnik* **85** 1977 pp.218-222

[11] Munday CW, *Proc. Int. Conf. Sponsored by SIT Swansea*, (London, Butterworth) 1958 pp.104-117

[12] Dietz H, Haecker W and Jahnke H, *Advances in Electrochemistry and Electrochemical Engineering, vol 10* H Gerischer and CW Tobias (eds) (New York, Wiley Interscience) 1977 pp.1-90

[13] Bergman I, *UK Patent 1200595*, 1970

[14] Bergman I, *UK Patent 1344616*, 1974

[15] Takami A, Matsuura T, Miyata S, Furusaki K and Watanabe Y, *SAE Conf. Sensors and Actuators* 1987

[16] Beie HJ and Gnorich A, *Sensors and Actuators B* **4** 1991 pp.393-399

[17] Tragut CH. and Hardtl KH, *Sensors and Actuators B* **4** 1991 pp.425-429

[18] Fleischer M and Meixner H, *Sensors and Actuators B*, **4** 1991 pp.437-441

[19] Gutman EY and Myasnikov IA, *Sensors and Actuators B* **1** 1990 pp.210-214

[20] Bransky J and Whimmer JM, *J. Phys. Chem. Solids* **33** 1972 p.801

[21] Logothetis EM, Park K, Meitzler AH and Land KR, *Applied Phys. Lett.* **26** 1975 p.209

[22] Kocache RMA, A review of the evolution and development of solid state oxygen sensors, *Trans. Inst. MC* **6** 1984 pp.67-76

[23] Kiukkola K, Wagner C, *J. Electrochem. Soc.* **104** 1957 pp.379-387

[24] Maskell WC, *J. Phys. E: Sci. Instrum.* **20** 1987 pp.1156-1168

[25] Maskell WC and Steele BCH, *J. Appl. Electrochem.* **16** 1986 pp.475-489

[26] Fouletier J, *Sensors and Actuators* **3** 1982/3 pp.295-314

[27] Williams D E and McGeehin P, in *"Electrochemistry - Solid State Gas Sensors and Monitors"* D Pletcher (ed) **9** 1984 pp.246-290

[28] Okamoto H, Obayashi H and Kudo T, *Solid State Ionics* **1** 1980 pp.319-326

[29] Takahashi H, Saji K, Kondo H, Takeuchi T, Igarashi I, *Proc. 5th Sensor Symposium* 1985 pp.133-137.

[30] Usui T, Kurumiya Y, Nuri K and Nakazawa M, *Sensors and Actuators* **16** 1989 pp.345-358

[31] Deportes CH, Henault MPS, Tasset F and Vitter GRP, *US Pat. 4045319* 1977

[32] Yuan D and Kroger FA, *J. Electrochem. Soc.* **116** 1969 pp.594

[33] Dietz H, *Solid State Ionics* **6** 1982 pp.175-183

[34] Ioannou AS and Maskell WC, Factors Influencing the Response time of Oxygen Sensors, *Proc. Solid State Ionics for Sensors and Electrochromics,* (International School of Materials Science and Technology (Erice-Sicily) 1-12 July 1992

[35] Crank J, in *"The Mathematics of Diffusion"* (Oxford: Oxford University press) 1956 p.48

[36] Heyne L, in *"Measurement of oxygen"*, Degn H et al (eds) (Proc. Int. Symp. Odense Univ. 26–27 Sept. 1974, Elsevier, Amsterdam) 1976 pp.65–88

[37] Beekmans NM and Heyne L, *Philips Tech. Rev.* **31** 1970 pp.112

[38] Agrawal YK, Short DW, Gruenke R, Rapp RA, *J. Electrochem. Soc.* **121** 1974 pp.354–360

[39] Haaland DM, *Analytical Chemistry* 49 **12** 1977 pp.1813–1817

[40] Hetrick RE, Fate WA and Vassell WC, *IEEE Trans. on Electron Devices* **29** 1982 pp.129–132

[41] DeJong HL, *US Patent.* 4.384.935, 1983

[42] Benammar M, *PhD Thesis, Middlesex Polytechnic (CNAA)* 1991

[43] Benammar M and Maskell WC, in *"Sensors: Technology, Systems and Applications"* KTV Grattan (ed), (Adam Hilger: Bristol) 1991, pp.113-119.

[44] Benammar M and Maskell WC, *Solid State Ionics* in press 1992

[45] Benammar M and Maskell WC, *J. Smart Materials and Structures* in press 1992

[46] Benammar M and Maskell WC, *Measurement of oxygen partial pressure using fully-sealed zirconia pump-gauge devices operated in the Tracking Mode. Part 2.* to be presented in EUROSENSORS VI conf, 5-7 Oct 1992, San Sebastian, Spain.

[47] Badwal SPS and De Bruin HJ, *Aust. Chem. Eng.* **20** 1979 pp.9–12

[48] Isenberg AO, *US Patent 4.138.881*, 1979

[49] Goge M, Maniette Y, Heggestad K and Gouet M, *Brit. Ceram. Proceedings* **38** 1986 pp.227-230

[50] Maskell WC, Sammes NM and Steele BCH, *J. Phys D: Appl. Phys.* **20** 1987 pp.99-104

[51] Verkerk MJ and Burgraaf AJ, *J. Electrochem. Soc: Solid State Sci. & Technol.* **130** 1983 pp.70-84

[52] Clifford R K, *Proceedings of the International Meeting on Chemical Sensors*, Fukuoka Japan (Sept 1983) p.153

[53] Maskell WC, *UK Patent No: GB 2 208 007 B*, 1991

[54] Kocache RMA and Holman DF, *UK Patent 1604445* 1978

[55] Kocache RMA and Holman DF, *UK Patent 2052751* 1979

[56] Ruka RJ, *US Patent 4088543* 1978

[57] Maskell WC and Steele BCH, *Solid State Ionics* **28-30** 1988 pp.1677-1681

[58] Usui T, Asada A, Nakazawa M and Osanai H, *J. Electrochem. Soc.* **136** 1989 pp.534-542

[59] Kaneko H, Maskell WC and Steele BCH, *Solid State Ionics* **22** 1987 pp.161-172

[60] Bailey FP and Black KJT, *J. Mater. Sci.* **13** 1987 pp.1045-1052 and pp.1606-1608

[61] Wheelan PT and Borbidge WE, *Solid State Ionics* **9&10** 1983 pp.1263-1272

[62] Usui T, Yamamoto H, Ishibashi K and Nakazawa M, *Jap. J. Appl. Phys.* 29 **3** 1990 pp.606-610

[63] Liaw BY and Weppner W, *J. Electrochem. Soc.: Solid State Sci. & Technol.* 138, **8** (1991) pp.2478-2483

[64] Velasco G, Schnell JP, Crozet M, *Sensors and Actuators* **2** 1982 pp.371-384

[65] Velasco G, *Solid State Ionics* **9-10** 1983 pp.783-792

[66] Goge M, Bauza D and Velasco M, *Proceedings Siame Conference, Paris Capteurs* June 1984 pp.88-93

[67] Isenberg AO, *US Patent 4.428.817*, 1984

[68] Kondo H, Takahashi H, Saji H, Takeuchi T and Igarashi I, *6th Sensor Sympasium, Japan* 1986

[69] Velasco G and Pribat D, *Proc. 2nd Int. Meeting on Chemical Sensors*, Bordaux, France, 1986

[70] Chu WF, Leonhard V, Erdmann H, Ilgenstein M, *Sensors and Actuators B* **4** 1991 pp.321-324

[71] Nissan Motor Cy, *Jap. Pat 54-89243 & 54-168084*, 1979

[72] Oh S, Chhokar S, Joseph J and Madou M, *Presented at 8th Int. Conference in Solid State Ionics*, Lake Louise, Calgary, Canada 20-26 Oct 1991. In pss Solid State Ionics, 1992

[73] Prudenziati M, *Sensors and Actuators A: Physical Sensors* **25-27** 1991 pp.227-234

[74] Steele BCH, Drennan J, Slotwinski RK, Bonanos N and Butler EP, *Advances in Ceramics, vol 3* AH Heuer and LW Hobbs (eds) (Columbus, Ohio, Amer. Ceram. Soc.) 1981 pp.286-309

[75] Nowick AS and Park DS, in *"Superionic conductors"*, Mahan GD and Roth WL (eds), Plenum Press, New York, 1976 pp.395

[76] Etsell TH and Flengas SN, *Chem. Rev.* **70** 1970 pp.339

[77] Subbarao EC and Maiti HS, *Solid State Ionics* **11** 1984 pp.317

[78] Verkerk MJ and Burgraaf AJ, *J. Appl. Electrochem.* **10** 1980 pp.677

[79] Takahashi T, Esaka T and Iwahara H, *J. Appl. Electrochem.* **7** 1977 pp.303-308

[80] Blumenthal RN, Brugner FS and Garnier JE, *J. Electrochem. Soc.: Solid State Sci. & Technol.* **120** 1973 pp.1230-1237

[81] Steele BCH, in *"Transport-Structure Relations in Fast Ion and Mixed Conductors"*, FW Poulsen et al (eds), 6th Riso Int. Symp. Met. and Mat.Sci., (Riso National Lab.) 1985 pp.79-92

[82] Kriven WM, Fraser WL and Kennedy SW, *Advances in Ceramics, vol 3* AH Heuer and LW Hobbs (eds) (Columbus, Ohio, Amer Ceram Soc) 1981 pp.82-97.

[83] Subbarao EC, *Advances in Ceramics, vol 3* AH Heuer and LW Hobbs (eds) (Columbus, Ohio, Amer Ceram Soc) 1981 pp.1-24

[84] Weppner W and Schubert H, *Advances in Ceramics, vol 24B* S Somiya et al (eds) (Westerville, Ohio, Amer Ceram Soc) 1987 pp.837-843

[85] Duran P, Recio P, Pascual C, Jurado JR and Moure C, *J. Mater. Sci.* **23** 1988

[86] Rajendran S, Swain MV and Rossell HJ, *J. Mater. Sci.* **23** 1988 pp.1805

[87] Sato T, Ohtaki S and Shimada M, *J. Mater. Sci.* **20** 1985 pp.1466

[88] Watanabe M, Iio S and Fakuura I, *Adv. Ceram.* **12** 1984 pp.391

[89] Baurle J E and Hrizo J, *J. Phys. Chem. Solids* **30** 1969 pp.565

[90] Steele BCH, in *"Electrode Processes in Solid State Ionics"*, M. Kleitz and J. Dupey (eds), (Reidel, Dordrecht) 1976 pp.711-728

[91] Garvie RC, *"High Temperature Oxides", vol.2,* AM Alper (ed), (Academic, New York, 1970) p.117

[92] Brook RJ, *Advances in Ceramics vol 3*, AH Heuer and LW Hobbs (eds) (Columbus, Ohio, Amer Ceram Soc) 1981 pp.272-285

[93] Burkin AR, Saricimen H and Steele BCH, *Trans. J. Brit. Ceram. Soc.* **79** 1980 p.105

[94] Haberko K and Pyda W, *Advances in Ceramics, vol 12* (Columbus, Ohio, Amer. Ceram. Soc.) 1985 pp.714-726

[95] Mazdiyasni KS, *High Tech Ceramics*, P Vincenzini (ed) (Elsevier Science Publishers B.V., Amsterdam) 1987 pp.693-706

[96] Mazdiyasni KS, Lynch CT and Smith JS, *J. Amer. Ceram. Soc.* 48, **7** 1965 pp.372-375

[97] Mazdiyasni KS, Lynch CT and Smith JS, *J. Amer. Ceram. Soc.* 50, **10** 1967 pp.532-536

[98] Marcilly C, Conty P and Delmon B, *J. Amer. Ceram. Soc.* 53, **1** 1970 pp.56-57

[99] Van de Graaf MACG and Burggraaf AJ, *Advances in Ceramics vol.12*, AH Heuer and LW Hobbs (eds) (Columbus, Ohio, Amer Ceram Soc) 1984 pp.744-765

[100] Ramamurthi DS, Xu Z and Payne DA, *J. Amer. Ceram. Soc.* **73** 1990 pp.2769-2763

[101] Haberko K, Ciesla A and Pron A, *Ceramurgia Int.* 1, **3** 1975 pp.111-116

[102] Haberko K, *Ceramurgia Int.* 5, **4** 1979 pp.148-154

[103] Thompson MA, Young DR and McCartney R, *J. Amer. Ceram. Soc.* **56** 1973 p.648

[104] Ready MJ, Lee RR, Halloran JW and Heuer H, *J. Amer. Ceram. Soc.* 73, **6** 1990 pp.1499-1503

[105] Scott CE and Reed JS, *Amer. Ceram. Soc. Bull.* **58** 1979 p.587

[106] Balog M, Schieber M, Michman M and Patai S, *Thin Solid Films* **47** 1977 pp.109-120

[107] Blocher M Jr and Whithers JC (eds), *Proc. 2nd Int. Conf. on Chemical Vapor Deposition*, Los Angeles (Electrochemical Society: Princeton N.J.) 1970 p.619

[108] Schoonman J, Dekker JP, Broers JW and Kiwiet NJ, *Solid State Ionics* **46** 1991 pp.299-308

[109] Kao AS and Gorman GL, *J. Appl. Phys.* **67** 1990 p.3826

[110] Jones F, *J. Vac. Sci. Technol.* **A6** 1988 p.3088

[111] Grosz F, Zegers P, Singhal SC and Yamamoto O, *Proc. 2nd Int. Symp. on SOFC*, July 1991, Athens (Commission of the European Communities: Luxemburg)

[112] Iwamoto N, Umesaki N and Endo S, *Thin Solid Films* **127** 1985 pp.129-137

[113] Grot AS and Martyn JK, *Am. Ceram. Soc., Bull.* **60** 1981 p.807

[114] Bauza D, Especel D and Gouet M, *Brit. Ceram. Proc.*, **38** 1986 pp.197-201

[115] Tseng TY, Huang JM, Lin JG and Lin YL, *J. Mater. Sci.* **24** 1989 pp.2735-2738

[116] Hashiba M, Okamoto H, Nurishi Y and Hiramatsu K, *J. Mater. Sci.* **24** (1989) pp.873-876

[117] Herring C, *J. Appl. Phys.* **21** 1950 p.301

[118] Kingery WD and Francois B, in *"Sintering and Related Phenomena"* GC Kuczynski et al (eds) (Gordon and Breach Science, New York) 1967 p.471

[119] Lange FF, *J. Am. Ceram. Soc.* 67 **2** 1984 pp.83-89

[120] Duran P, Recio P, Jurado JR, Pascual C and Moure C, *J. Mater. Sci.* **23** pp.4349-4356

[121] Barringer EA and Bowen HK, *J. Am. Ceram. Soc.* 65 **12** 1982 C.199-C.201

[122] Barringer EA, Jubb N, Fegley B, Pober RL and Bowen HK, *"Ultrastructure processing of Ceramics, Glasses and Composites"* LL Hench and DR Ulrich (eds), (Wiley: New York) 1984 pp.315-333

[123] Coble RL, *J. Amer. Ceram. Soc.* 56 9 1973 pp.461-466

[124] O'Hara MJ and Cutler IB, *Proc. Br. Ceram. Soc.* **12** 1969 pp.145-155

[125] Handwerker CA, Cannon RM and Coble RM, *Adv. in Ceramics* **10** 1984 pp.619-643

[126] Harmer MP, *Adv. in Ceramics* **10** 1984 pp.679-696

[127] Wu JM and Wu CH, *J. Mater. Sci.* **23** 1988 pp.3290-3299

[128] Rumpf H and Shubert H, in *"Ceramic Processing Before Firing"* GY Onoda and LL Hench (eds) (Wiley) 1978 p.338

[129] Evans PE, *J. Amer. Ceram. Soc.* **53** 1970 pp.365

[130] Wu S and Brook RJ, *Trans. J. Br. Ceram. Soc.* **82** 1983 pp.200

[131] Jorgensen P, *"Sintering and Related Phenomena"*, GC Kuczynski (ed) (Gordon and Breach, New York) 1967 pp.401

[132] Rhodes WH, *J. Amer. Ceram. Soc.* **64** 1981 pp.19-22

[133] Roosen A and Hausner H, *Ceram For Intern/Ber Dt Keram Ges* **4/5** 1985 p.184

[134] Thompson MA, Young DR and McCartney R, *J. Amer. Ceram. Soc.* **56** 1973 p.648

[135] Gnoheim NM and Hanna SB, *J. Mat. Sci.* **25** 1990 pp.5192-5198

[136] Kilner JA and Brook RJ, *Solid State Ionics* 3, **6** 1982 pp.237-252

[137] Steele BCH, *Science of Ceramics* **12** 1983 pp.697

[138] Onoda GY and Hench LL, *"Ceramic Processing Before Firing"* (Wiley, New York) 1978

[139] Bernard H, *PhD Thesis, Grenoble* 1980

[140] Kleitz M, Bernard H, Fernandez E and Schouler E, *Advances in Ceramics vol.3* 1981 pp.310-336

[141] Chaim R, Brandon DG and Heuer AH, *Acta Metall.* **34** 1986 p.1933

[142] Whalen PJ, Reidinger F, Correale ST, and Marti J, *J. Mater. Sci.* **22** 1987 pp.446

[143] Yamamoto O, Takeda Y, Imanishi N, Kawahara T, Shen GQ, Mori M and Abe T, *Proc. 2nd Int Symp on SOFC*, (Commission of the European Communities: Luxembourg) Athens, July 1991

[144] Radford KC and Bratton RJ, *J. Mat. Sci.* **14** 1979 p.59

[145] Ishitsuka M, Sato T, Endo T amd Shimada M, *J. Mater. Sci. Lett.* **24** 1989 pp.4057-4061

[146] Miyayama M, Yanagida H and Asada A, *Am. Ceram. Soc. Bull.* **64** 1985 pp.660-664

[147] Butler EP and Drennan J, *J. Amer. Ceram. Soc.* **65** 1982 pp.474

[148] Savage J, in *"Handbook of Thick Film Technology"* (Electrochemical Publications) 1976 p.55

[149] Cramer SD, *PhD Thesis, University of Maryland*, College Park, 1968

[150] Casson N, *"Rheology of Disperse systems"* C.C.Mills (ed), (Pergamon Press: New York) 1959

[151] Pierce PE, *Journal of Paint Technology* **43** 557 (June 1971) pp.35-43

[152] Usui T, Yamamoto H, Ishibashi K and Nakazawa M, *Jap. J. Appl. Phys.* 29, **3** 1990 pp.606-610

[153] Cunningham RE and Williams RJJ, in *"Diffusion in Gases and Porous Media"* (New York: Plenum Press) 1980

[154] Treybal RE, in *"Mass transfer operations" 2nd ed.* (McGraw and Hill) 1968 p.87

[155] Evans RB, Watson GM and Mason EA, *J. Chem. Phys.* **33** 1961 p.2076

[156] Cussler EL, in *"Diffusion; Mass Transfer in Fluid Systems"* (Cambridge University Press) 1984

[157] Sherwood TK, Pigford RL and Wilke CR, in *"Mass Trasfer"* (McGraw and Hill) 1975 p.42

[158] Barrer RM, in *"Diffusion in and through Solids"* (Cambridge University Press: London) 1941

[159] Pitt KEG, *Electronic Prod.* 1982 pp.52-54.

[160] Horowitz and Hill, *"The Art of Electronics"*, (Cambridge University Press) 1980 p.144

[161] Torayo H, Yoshimura M and Somiya S, *J. Amer. Ceram. Soc.* **67** 1984 C-119

[162] Bauerle JE, *J Phys Chem Solids* **30** 1969 pp.2657-2670

[163] Armstrong RD, *J. Electroanal. Chem. and Interfacial Electrochem.* **52** 1974 pp.413-419

[164] Schouler EJL and Isaacs HS, *Solid State Ionics* **5** 1981 pp.555-558

[165] Bonanos N, Slotwinski RK, Steele BCH and Butler EP, *J. Mater. Sci. Lett.* **3** 1984 pp.245-248

[166] Groot Zevert WFM, Winnburst AJA, Theunissen GSAM and Burgrgraf AJ, *J. Electrochem. Soc.* **137** 1990 pp.3449-3455

[167] Takahashi M, Suzuki S, Nitanada H and Arai E, *J. Amer. Ceram. Soc.* 71 **12** 1988 pp.1093-99

[168] Trease RE and Dietz RL, *Solid State Technology* **15/1** 1972 p.39

[169] Fennelly TJ and Reed JS, *J. Am. Ceram. Soc.* 55 **5** 1972 pp.264-268

[170] Prochazka S and Coble RS, *Phys. Sintering.* 2 **2** 1970 pp.15-34

[171] Kuczynski GC (ed), *Sintering and Related Phenomena"* (Plenum Press) 1973

[172] Lange FF and Metcalf M, *J. Am. Ceram. Soc.* 66 **6** 1983 pp.398-406

[173] Kellett BJ and Lange FF, *J. Amer. Ceram. Soc.* **72** 1989 p.725

[174] Ioannou AS and Maskell WC, *J. Mater. Sci. Lett.* in press July 1992

[175] Scherer GW and Garino TJ, *J. Am. Ceram. Soc.* 68 **4** 1985 pp.216-220

[176] Mitsuhashi T, Ichihara M, Tatsuke U, *J. Amer. Ceram. Soc.* **57** 1974 pp.97

[177] Garvie RC, Hannink RH and Pasceo RT, *Nature* **258** 1975 pp.703

[178] Gupta TK, Bechtold JH, Kuznicki RC, Cadoff LH, and Rossing BR, *J. Mater. Sci.* **12** 1977 pp.2421-2426

[179] Shengli AN, Weijang WU and Qingguo LIU, *Solid State Ionics* **28-30** 1988 pp.546-549

[180] Lange FF, Dunlop GL and Davis BI, *J. Amer. Ceram. Soc.* **69** 1986 pp.237

[181] Matsui M, Soma T and Oda I, *Advances in Ceramics vol.12*, N Claussen (ed) (Columbus, Ohio, Amer. Ceram. Soc) pp 352-370

[182] Kleitz M et al in *"Advances in ceramics"* AH Heuer and LW Hobbs (eds) (American Ceramic Soc., Columbus Ohio) 1981 p.310

[183] Vest RW and Tallan NM, *J. Amer. Ceram. Soc.* **48** 1965 p.472

[184] Kofsad P and Ruzicka DK, *J. Electrochem. Soc.* **110** 1963 p.181

[185] Van Dijk T and Burggraaf AJ, *Phys. Status Solidii A* **63** 1981 p.229

[186] Butler EP, Slotwinski RK, Bonanos N, Drennan J and Steele BCH, *Advances in Ceramics vol 3* AH Heuer and LW Hobbs (eds) (Columbus Ohio, Amer. Ceram. Soc) 1984 pp.272-285

[187] Bonanos N and Butler EP, *J. Mater. Sci. Lett.* **4** 1985 pp.561-564

[188] Pike GE and Seager CH, *J. Appl. Phys.* **48** 1977 pp.5152

[189] Dees DW, Claar TD, Eastler TE, Fee DC and Mrazek FC, *J. Electrochem. Soc.* 134 **9** 1987 pp.2141-2146

[190] Ioannou AS and Maskell WC, in *"Sensors: Technology Systems and Applications"* KTV Grattan (ed) (Adam Hilger: Bristol) 1991 pp.157-161

[191] Ioannou AS and Maskell WC, *Solid State Ionics*, in press 1992

[192] Ioannou AS and Maskell WC, *UK Patent Application No: 9116385.7* 1991

[193] Kenjo T, Osawa S and Fujikawa K, *J. Electrochem. Soc.* 138 2 1991 pp.349-355

[194] Isaacs HS and Olmer LJ, *J. Electrochem. Soc.* **129** 1982 pp.436

[195] Sasaki J, Mizusaki J, Yamauchi S and Fueki K, *Bull. Chem. Soc. Japan* **54** 1981 pp.1688

[196] Pizzini S, *"Fast ion transport in solids"* W. van Gool (ed), North Holland, Amsterdam) 1973 p.461

[197] Badwal SPS and Ciacchi FT, *J. Appl. Electrochem.* **17** 1987 pp.495-504

[198] Karpachov S and Filajev A, *Z. Phys. Chem.* **238** 1968 pp.284

[199] Sakaguchi M, Uematsu K, Sakata A, Sato Y and Sato M, *Electrochim. Acta*, **34** 1989 p.625

[200] Gur TM, Raistrick ID and Huggins RA, *Electrochem. Sci. & Technol.* **127** 1980 pp.2620-2628

[201] RC Weast and MJ Astle (eds), *CRC Handbook of Chemistry and Physics*, 62nd edn (CRC Press, Boca Raton, Florida) 1981

[202] Badwal SPS and Nardella N, *Solid State Ionics* **40/41** 1990 pp.878-881

[203] Zener C, J. Appl. Phys., **20** 1949 p.950

[204] Martin JW and Doherty RD, *"Stability of Microstructure in Metallic Systems"*, (Cambridge University Press: Cambridge) 1976

[205] Abeles B, Pinch HL and Gittleman GI, *Phys. Rev. Lett.* **35** 1976 p.247

[206] Deutscher G, Zallen R and Alder J (eds), *"Percolation Structures and Processes"* (Adam Hilger: Bristol) 1983

[207] Kusy RP, *J. Appl. Phys.* 48 **12** 1977 pp.5301-5305

[208] Deutscher G, Rappaport M and Ovadyahu Z, *Solid State Commun.* **28** 1978 p.593

[209] Lee JA, Maskell WC and Tye FL, *Membrane Separation Processes*, P Meares (ed) (Elsevier, Amsterdam) 1976 pp.399-476

[210] Van Hassell BA, Boukamp BA and Burggraaf, *Solid State Ionics* **48** 1991 pp. 139-154

[211] Van Hassel, Boukamp BA and Burggraaf, *Solid State Ionics* **48** 1991 pp.155-171

[212] Mizusaki J, Amano K, Yamauchi S and Fueki K, *Solid State Ionics* 22 1987 pp 313-322 and 323-330

[213] Schouler EJL and Kleitz M, *Solid State Ionics* **134** 1987 p.1045

[214] Kawada T, Sakai N, Yokokawa H, Dokiya M, Mori M, Iwata T, *J.Electrochem. Soc.* 137 **10** 1990

[215] Robertson NL and Michaels JN, *J. Electrochem. Soc* **137** 1990 p.1

[216] Asada A, Yamamoto H, Nakazawa M and Osanai H, *Sensors and Actuators B* **1** 1990 pp.312-318

[217] Wang DY, *J. Electrochem. Soc.*, 137 **11** 1990 pp.3660-3666

[218] Heyne L and Beekmans NM, *Proc. Brit. Ceram. Soc* **19** 1971 p.229

[219] Fate WA, Hetrick RE and Vassell WC, *Appl. Phys. Lett.*, 39 **11** 1981 pp 294-296

[220] Benammar M and Maskell WC, *J. Phys. E: Sci. Instrum.* 22 1989 pp.933-936

[221] Maskell WC, *UK Registered Design N.1053348* 1988

[222] Raub E and Plate W, *Z. Metallk* 48 **10** 1957 pp.529-539

[223] Fryburg GC and Petrus HM, *J. Electrochem. Soc.* June 1961 pp.496-502

[224] Krier CA and Jaffee RI, *J. Less Comm. Metals* **5** 1963 pp.411-431

[225] Alcock CB and Cooper GW, *Proc., Royal Soc., London* **254A** 1960 pp.551-556

[226] Olivei A, *J. Less Common Metals* 29 1972 pp.11-23

[227] Bartlett RW, *J. Electrochem. Soc.* **114** 1967 pp.547-550

[228] Fryburg GC, *Trans. Metallk. Soc. AIME,* **233** 1965 pp.1986-1989

[229] Fryburg CG and Murphy HM, *Trans. AIME,* 212, **5** 1958 pp.411-431

[230] Kusy A, *Thin Solid Films* **43** 1977 p.243

[231] Palanisamy, *PhD Thesis, Purdue University* Dec. 1979.

[232] Ahn TM, *PhD Thesis, Columbia University* 1978

[233] McLean M and Hondros ED, *J. Mater. Sci.* **6** 1971 pp.19-24

[234] Neugebauer CA and Webb MB, *J. Appl. Phys.* **33** 1962 pp.174

[235] Herman DS and Rhodin TN, *J. Appl. Phys.* 37 **4** 1966 pp.1594

[236] Forlani S and Prudenziati S, *Electrocomp. Sci. Tech.* **3** 1977 p.77

[237] Jacobini C, Prudenziati M and Rizzi A, *Proc. ISHM*, Avignon, 1981 pp.11-18

[238] Verma BS and Sharma SK, *Thin Solid Films* **5** 1970 R44-R46

[239] Watkins J, *Modern Electronic Materials* (Butterworth) 1972

[240] Wert CA and Thomson RM, *Physics of Solids* (2nd Edition), (McGraw Hill) 1970

[241] Cattaneo A, Pirozzi L, Morten B and Prudenziati M, *Conference ISHM* Ghent 1979

[242] Lorentz HA, *Wied. Ann.* **11** 1880 p.70

[243] Lorentz L, *Wied. Ann.* **9** 1880 p.641

[244] Maxwell JC, *A Treatise on Electricity and Magnetism*, 2nd ed, vol.1, (Clarendon Press: Oxford) 1881 p.435

[245] Lord Rayleigh, *Phil. Mag.* **34** 1892 p.481

[246] Fricke H, *Phys. Rev.* **24** 1924 p.575

[247] Runge I, *Z. Teck. Phys.* **6** 1925 p.61

[248] Meredith RE and Tobias CW, *J. Appl. Phys.* **31** 1960 p.1270

[249] Bruggeman DAG, *Ann. Physik* **24** 1935 p.636

[250] De La Rue RM and Tobias CW, *J. Electrochem. Soc.* **106** 1959 p.827

[251] Meredith RE and Tobias CW, *Advances in Electrochemistry and Electrochemical Engineering* vol.2 (Wiley, New York) 1962 pp.15-47

[252] Reynolds JA and Hough JM, *Proc. Phys. Soc.* (London) **B70** 1957 pp.769

[253] Meredith RE, *Studies on the Conductivities of Dispersions*, Lawrence Radiation Report UCRL-8667, 1959

[254] Stroud G, Milton GW and De BR, *Phys. Rev. B* **34** 1986 p.5145

[255] Brouers F and Ramsamugh A, *J. Phys C.* **21** 1988 p.1839

[256] Archie G.E, *Trans. Amer. Inst. Mining Met. Engrs (AIME)* **146** 1942 p.54

[257] Winsauer WO, *Bull. Amer. Ass. Petrol. Geologists*, **36** 1952 p.253

[258] Coutts TJ and Hopewell B, *Thin Solid Films* **9** 1971 p.37

[259] Clerc JP, Giraud G, Laugier JM and Luck JM, *Europhysics Journal*, vol 39, 3 1990 pp.193-221.

[260] Zallen R (ed), *"Physics of Amorphous Solids"* (John Wiley & Son: New York) 1983

[261] Kirkpatrick S, *Rev. Mod. Phys* **45** 1973 p.574

[262] Webman I, Jortner J, Cohen MH, *Phys. Rev.* **B11** 1975 p.2885

[263] Efros A L ,Shklovskii BI, *Phys. Stat. Sol (b)* **76** 1976 p.475

[264] Bergman DJ, Imry Y, *Phys. Rev. Lett* **39** 1977 p.1222

[265] Watson BP and Leath PL, *Phys. Rev., Sect. B* **9** 1974 p.4893

[266] Last BJ and Thouless DJ, *Phys. Rev. Lett.* **27** 1971 p.1719

[267] Stauffer D, *Phys. Reports* **54** 1979 p.1

[268] Sykes MF and Essam JW, *Phys. Rev. Sect. A.* **133** 1964 p.310

[269] Scher H and Zallen R, *J Chem Phys* **53** 1970 pp.3759-3761

[270] Ottavi H, Clerc J, Giraud G, Guyon J and Mitescu CD, *J. Phys. C* **11** 1978 p.1311

[271] Seager CH and Pike GE, *Phys. Rev. B10* **4** 1974 pp.1435-46

[272] Straley JP, *"Electrical Transport and Optical Properties in Inhomogeneous media"* (AIP, New York) 1978 p.40

[273] Verkerk MJ, Hammink MWJ and Burggraaf AJ, *J. Electrochem. Soc.: Solid State Sci. & Technol.* **130** 1983 pp.70-77

[274] Nguyen BC, Rincon-Rubio LM, and Mason DM, *J. Electrochem. Soc.* 127, **12** 1987, p.2620

[275] Wang DY, *Solid State Ionics* **40/41** 1990 pp.849-856

[276] Thirsk HR and Harrison AJ, *"A Guide to the Study of electrode kinetics"* (Academic Press: London and New York) 1972

[277] Wang DY and Nowick AS, *J. Electrochem. Soc.* **126** 1979 p.1155

[278] Wang DY and Nowick AS, *J. Electrochem. Soc.* **128** 1981 p.56

[279] Jones HRN, *"Domestic Gas Burner Design"* (E & FN Spon Ltd) 1989 pp 8-9

APPENDICES

APPENDIX A : Calculation of the volume fractions of platinum zirconia and voids in the printed cermet films

Calculation of the relative amount of platinum, zirconia and void phases present in the screen-printed cermets required knowledge of the following i) the weight of platinum present in a film, W_{Pt}, measured using the atomic absorption technique (§ 2.3.10), ii) the cross-sectional area of the film, X_f, measured using the Alpha-step (§ 2.3.1), iii) the length of the film and iv) the YSZ:Pt ratio of the cermets.

A cross-sectional area was calculated (X_{Pt}) based upon the amount of platinum present only as

$$X_{Pt} = W_{Pt} / d_{Pt}\, \ell_f \qquad (A.1)$$

where d_{Pt} is the density of platinum at zero porosity and ℓ_f is the length of the cermet film.

The volume percentage of platinum present V_f, in the printed film was then determined by

$$V_f = 100\, X_{Pt} / X_f \qquad (A.2)$$

The volume percentage of zirconia (YSZ) present was then determined from knowledge of the YSZ:Pt volume ratio of the cermet paste (Table 4.1 § 4.3.1). It is safe to assume the absence of significant amounts of other phases besides voidage and thus the fraction not attributed to platinum or zirconia was assumed to be made up of voids.

APPENDIX B : Rate controlling steps of the electrode reaction

The overall electrode reaction (involving porous platinum electrodes on zirconia) of Eq. (1.2) occurring at the reaction site is thought to comprise three steps [196]:

i) Dissociative adsorption of molecular oxygen to form chemisorbed oxygen atoms,

ii) Migration of chemisorbed oxygen across the surface of the electrode material to the electrode/electrolyte/gas three-phase boundary (*TPB*),

iii) The charge transfer reaction. The formation of oxygen ions which involves the uptake of two electrons. (the oxygen ions O_o^x are then free to diffuse through the electrolyte).

Controversy in the literature concerns the various rate determining steps for the electrode reaction. Possible steps are: gas–phase diffusion in the electrode, diffusion on the electrode surface to the *TPB*, and charge transfer [273,200,274,212]. These contradictions are believed to result from the difference in electrode morphology of the samples studied and from the methods of data analysis [275].

If the charge transfer process is rate limiting then electrode overpotential is described by the Butler–Volmer equation [276]

$$I = I_o \left[\exp\left(\frac{\alpha_a \eta nF}{RT}\right) - \exp\left(\frac{-\alpha_c \eta nF}{RT}\right)\right] \qquad (B.1)$$

where I_o is the exchange current density, α_a and α_c are the anodic and cathodic charge transfer coefficients, $\eta F/RT$, is a dimensionless potential η is the electrode overpotential and n is the number of charges transferred (for the overall electrode reaction n = 4). The sum of α_a and α_c is always equal to 1 for the reaction of Eq. (1.2) [277,278]. At low overpotentials ($|\eta| << RT/nF$) the Butler-Volmer equation can be simplified into an ohmic behaviour

$$I = I_o \left(\frac{\eta nF}{RT}\right) \qquad (B.2)$$

At high overpotentials ($|\eta| >> RT/nF$) the Butler-Volmer equation becomes the Tafel equation [276]

$$|\eta| = \left(\frac{RT}{\alpha nF}\right) \ln \left|\frac{I}{I_o}\right| \qquad (B.3)$$

When plotting $\ln|I|$ vs the anodic or cathodic overpotential the Tafel slope of $(RT/nF)(1/\alpha_a)$ for the anodic process and $(RT/nF)(1/\alpha_c)$ for the cathodic process is expected. The slope should be linear and well defined; extrapolation of the line to zero overpotential yields a value for I_o and from the slope calculation of the charge transfer coefficients can be made.

APPENDIX C : Testing in a gas-burning flue

The sensor was field tested in a gas burning flue at British Gas (Watson House). The gas used for combustion in the boiler was natural gas A (NGA) containing 92–96% methane (the remaining 4-8% split approximately equally between nitrogen and propane). The analysis of the NGA used as certified by British Gas on the day of testing (using gas chromatography) was as follows:

Calorific Value (CV) = 38.2 MJ m^{-3}

Net Calorific Value (NCV) = 34.5 MJ m^{-3}

Wobbe Number = 49.7

Total Air Requirement (TAR) = 9.67

The TAR is the volumetric ratio of air to gas required for stoichiometric combustion of the NGA used in these tests.

The heat input of the boiler was maintained at 5 KW by fixing the gas flow rate at 0.47m^3 hr^{-1} calculated from the equation below;

$$\text{Heat Input} = \text{Flow rate} * \text{CV} * 0.2778 \qquad \text{(C.1)}$$

where the value of the constant is based upon the units of flow rate of m^3 hr^{-1} and calorific value of MJ m^{-3}.

The total Aeration was calculated using the following equation:

$$\text{Total Aeration} = \frac{V_{fr}(\text{air})}{V_{fr}(\text{gas})} * \text{TAR} \qquad \text{(C.2)}$$

where V_{fr} is the volume flow rate. The air flow rate was adjusted accordingly to achieve various values of aeration ranging from 60% to stoichiometric (100%) and up to 170% in the lean burning region. Values outside this range are unlikely to be encountered in normal operation of the boiler. Values above 170% aeration caused cooling and the flame could not be sustained; values below stoichiometric caused rapid overheating of the burner and, at 60% aeration could not be maintained for periods longer than about a minute.

The following equations were used to calculate the theoretical excess air and wet oxygen and required the knowledge of CO_2 in the combustion gases [279]:

$$\text{excess air } \% = \left(\frac{1044}{\text{dry } CO_2\%}\right) - 89 \tag{C.3}$$

$$\text{wet } O_2 \% = \frac{\left(\frac{2088}{\text{dry } CO_2\%}\right) - 178}{\left(\frac{99.18}{\text{dry } CO_2\%}\right) + 2.065} \tag{C.4}$$

These equations strictly apply only for the burning of pure methane gas, so the results can only be accurate to ~±5%. The CO_2 concentration in the flue was continuously monitored using a Siemens Ultramat 22P infra red instrument.

APPENDIX D : Estimation of through porosity of a zirconia layer

It has already been shown for this device (see § 5.2) that the limiting current, I, can be calculated using the following equation,

$$I = -\left(\frac{4FD_1S}{RT\ell}\right) p(O_2)_{sg} \qquad (5.5)$$

During sensor operation it is assumed that oxygen will diffuse through the electrolyte to the cathode and that a concentration gradient can only occur around the overlap area of the electrodes. Only a fraction of the surface is open to the gas. This fraction, f_p, (relating to the pores that allow diffusion of the gas through the ceramic) can be related to the electrode area, A_{el} by the following equation:

$$S = A_{el} * f_p.$$

In practice the capillaries leading through the porous ceramic may not be of constant diameter and their average length is on average some multiple of the ceramic thickness. A tortuosity factor θ needs to be introduced into the equation to account for this probable tortuous nature of the gas diffusion paths. The real effective gas diffusion path through the ceramic becomes an apparent increased thickness normal to the ceramic of $\ell\theta^2$.

$$\theta = \frac{\text{mean gas diffusion path length}}{\text{ceramic thickness}} > 1 \qquad (D.1)$$

A value of the tortuosity of 1.5, is taken from experimentally derived values, from consolidated sands and porous rocks [256].

Substituting for S and introducing θ into the above equation and rearranging, the fractional porosity is now related to:

$$f_p = \frac{IRT\ell\theta^2}{4FD_{O_2}A_{el}\,p(O_2)} \qquad (5.6)$$

working a single value for the constants 4F, D, θ and R in consistent units for the whole equation it now becomes:

$$f_p = 3.471 \times 10^{-6} \frac{IT\ell}{A_{cl} P_{O_2}} \qquad (D.2)$$

The following values were used for the constants:

$F = 9.64846 \times 10^4$ C mol^{-1}

$R = 8.20575 \times 10^{-5}$ m^3 atm K^{-1} mol^{-1}

$D(O_2)$ in N_2 at 20°C = 1.6×10^{-5} m^2 s^{-1}

N_2 at 700°C = 1.51×10^{-4} m^2 s^{-1}

Due to the uncertainty of the value of the tortuosity factor and the precise area over which diffusion effectively occurs the value of f_p is only an approximation.

APPENDIX E : Calculation of the resistance ratio Q, and fraction of non-conducting phase f.

The experimental data were represented on dimensionless plots where possible in order to explain the physical processes occurring. In order to do this a conductivity ratio and an overall porosity have been defined for the track. The conductivity ratio is obtained by relating the measured experimental resistance values (R_t) to calculated ones. Knowledge of the following was required throughout the films continuity: i) cross-sectional area of the films obtained from data of the type in Fig. 3.3, ii) amount of platinum deposited, iii) rate of platinum evaporation, iv) film resistance, R_t and v) film dimensions. The assumption was also made that the resistivity of the film was the same as that of pure bulk platinum. Two calculated values were used. One has been derived from the assumption that the whole measured cross-section of the track is composed of pure bulk platinum assuming the absence of voids ($R_{e(t)}$), and the other from the expected resistance due to the volume of platinum metal remaining on the track ($R_{c(t)}$),

$$R_{e(t)} = \rho_{Pt}(\ell_f/A_{m(t)}) \quad \text{and} \quad R_{c(t)} = \rho_{Pt}(\ell_f/A_{c(t)})$$

where

ρ_{Pt} = resistivity of pure bulk platinum

ℓ_f = length of track

$A_{m(t)}$ = measured cross-sectional area of the film at time t.

$A_{c(t)}$ = cross-sectional area calculated from the volume of platinum present at time t assuming it formed an evenly deposited bulk film over the whole track length.

$A_{c(t)} = W_{Pt}/(d_{Pt}\ell_f)$

W_{Pt} = weight of platinum on track

d_{Pt} = density of bulk platinum

An overall fractional porosity in the printed composition was calculated as the total fraction of cross-sectional area not occupied by platinum,

$f = 1-(A_{c(t)}/A_{m(t)})$

The resistance ratio Q is described as

$Q = R_t/R_{e(t)}$

APPENDIX F : Spheroid analysis of Fricke

The values of β and γ for Eq. (6.13) are defined as follows

$$\beta = \frac{3L(1-2L)}{(3L-2)} \tag{F.1}$$

$$\gamma = \frac{2(3L-1)^2}{(3L-2)(3L+1)} \tag{F.2}$$

where the L terms in the equations involve elliptic integrals of the second kind. Designating the three principal axis of a spheroid as a,b and c (where b = c), the values of L may be obtained from the table below [251]

Type of particle	b/a	Value of L	1+β+γ
Rods	0	0.5	0.6
Prolate spheroids	1/6	0.4784	0.6148
	1/5	0.472	0.6189
	1/4	0.4624	0.6248
	1/3	0.4465	0.6338
	1/2	0.4134	0.6495
Spheres	1/1	0.3333	0.6667
Oblate spheroids	2	0.2383	0.6351
	3	0.1823	0.5782
	4	0.1477	0.5234
	5	0.1245	0.4762
	6	0.1077	0.4358
Discs	∞	0	0

Table A1 Values of L for spheroids (c = b)